KU LEUVEN

ARENBERG DOCTORAL SCHOOL
Faculty of Science

Visualization and localization of defects by Nonlinear Elastic Wave Spectroscopy techniques

Jan Hettler

Supervisor:
Prof. dr. K. Van Den Abeele

Dissertation presented in partial
fulfillment of the requirements for the
degree of Doctor of Science (PhD):
Physics

November 2016

Visualization and localization of defects by Nonlinear Elastic Wave Spectroscopy techniques

Jan HETTLER

Examination committee:
Prof. dr. D. Dudal, chair
Prof. dr. K. Van Den Abeele, supervisor
Prof. dr. ir. H. De Gersem, assessor
dr. E. Blomme, assessor (VIVES)
dr. H. Pfeiffer
Prof. dr. O. Bou Matar
(Ecole Centrale de Lille)
Ing. Z. Převorovský, CSc.
(Institute of Thermomechanics, CAS)

Dissertation presented in partial fulfillment of the requirements for the degree of Doctor of Science (PhD): Physics

November 2016

Uitgegeven in eigen beheer, Jan Hettler, Etienne Sabbelaan 53, B-8500 Kortrijk (Belgium)

Preface

First, I would like to thank to my supervisor and assessors, Koen Van Den Abeele, Herbert De Gersem and Erik Blomme, for all their support and for the great opportunity they have given me. It was a great pleasure to work with all of them and to learn from them. I will always remember Koen Van Den Abeele as a great boss with almost intoxicating enthusiasm. As a matter of fact, I can hardly recall him in bad mood. He has always been great source of inspiration as a brilliant researcher and a great person.

Many thanks go also to my colleagues at KU Leuven Kulak that helped me to adapt to the new country, environment and bier-drinking habits. They made me feel in Kortrijk like in my second home. I have never worked in a greater and more friendly environment. Thank you all.

I would also like to thank to my family for their support and understanding. I would never be able to get that far without their help, advice and encouragement. Above all, I would like to thank my girlfriend Pavla for unconditional love and support. She has been my anchor in the difficult times and encouraged me all the time. She had sacrificed a lot for me, so I can fulfil my dream and I will be always grateful to her for that.

I would also like to thank the ALAMSA project partners that provided me with lot of help and stimulated the research with many intricate questions.

Thank you all,
Jan

Abstract

The importance of non-conventional nondestructive testing (NDT) methods has been exponentially growing in the past few decades. This development has been driven mainly by the increasing usage of advanced and complex new materials in key industrial sectors including the automotive and aerospace industry. For example, carbon-fiber-reinforced polymer (CFRP), which used to be an exclusive material for high-tech aerospace structures due to its cost and manufacturing complexity, is now a common material in automotive or sports-goods industry. Hence, previously select materials drift from high-tech to low-tech industries, and as their usage spreads, quality control ensurance becomes increasingly important. Regrettably, the existing conventional NDT methods are often insufficient to inspect these complex materials. Therefore, both the high-tech and the low-tech industry are searching for a more reliable, more versatile and more affordable NDT inspection methods that will allow them to inspect the mass-produced composite parts as well as special one-off parts. In addition, there is also a strong call from the aviation industry for a real-time structural health monitoring (SHM) method that will enable even safer operation and better maintenance planning.

The present work deals with application of nonlinear elastic wave spectroscopy (NEWS) to boost up the classically used ultrasonic guided waves (GW) NDT. It is mainly focused on the detection and visualization of damage in thin plate-like composite structures that are typically used in the aerospace industry. A baseline-free method for imaging of defects, such as delaminations and disbonds is described and demonstrated both in numerical simulation as well as in experiment. Advantages and pitfalls of nonlinear guided wave imaging in anisotropic plates are addressed and discussed. In particular, we mention the fact that the new methodology eliminates inconvenient influences arising from environmental factors. Moreover, a new way of data fusion for better experimental determination of GW dispersion curves is described. In the future, this can be used to improve the excitation and sensing of GW or to invert the elastic properties of the tested sample from the experimental data.

The second major part of the work deals with the local defect resonance (LDR). Several improvements, including the automatic LDR frequency detection and iterative sizing, are proposed and verified in simulation and in experiment. The proposed advancements can greatly improve the applicability of the method in a real-world environment. This is further demonstrated by experimental results on a variety of different engineering materials, such as composite sandwich structures, glass-fiber-reinforced polymer and ionomeric self-healing plates.

Beknopte samenvatting

Het belang van niet-conventionele technieken voor niet destructief testen (NDT) van materialen is in de voorbije decennia exponentieel gegroeid. Deze ontwikkeling werd gedreven door het toegenomen gebruik van meer geavanceerde en complexere nieuwe materialen in vooraanstaande industriële sectoren zoals de automobiel- en luchtvaartindustrie. Koolstof-vezelversterkte kunststoffen (CFRP) werden bijvoorbeeld in het verleden nagenoeg exclusief gebruikt voor high-tech toepassingen in de luchtvaart omwille van hun kostenplaatje en de productiecomplexiteit, maar vormen tegenwoordig een veeleer alledaags basismateriaal voor de automobielindustrie en de sportwereld. Dus, materialen die vroeger heel selectief gebruikt werden, ondergaan momenteel een significante verschuiving van hoog-technologisch gebruik naar laag-technologische toepassingen, en, met het toenemend gebruik ervan, wordt ook een verzekerde kwaliteitscontrole van deze materialen alsmaar belangrijker. Helaas zijn de bestaande en conventionele NDT technieken in vele gevallen niet voldoende aangepast om deze nieuwe types van materialen te inspecteren. Daardoor bestaat er bij zowel de hoog- als laag-technologische bedrijven een grote interesse in de ontwikkeling van meer betrouwbare, flexibelere en meer betaalbare NDT systemen en methodologieën die hen in staat stellen om grote productievolumes aan composieten te inspecteren, evenals om de kwaliteit van speciale eenmalige componenten te controleren. Bovendien is er ook de relevante vraag van de luchtvaartindustrie naar een instantane monitoring van de structurele integriteit van componenten in het kader van een veiligere operationaliteit en een betere onderhoudsplanning van vliegtuigen. Het onderzoek handelt over het toepassen van niet-lineaire elastische golfvoortplanting (Engels: Nonlinear Elastic Wave Spectroscopy, NEWS) met als doel de klassiek gebruikte Niet-Destructieve Test (NDT) technieken gebaseerd op geleide golven (Engels: Guided Waves, GW) te optimaliseren. Dit werk is voornamelijk gericht op het detecteren en visualiseren van schade in dunne plaatvormige composietstructuren die doorgaans gebruikt worden in de luchtvaartindustrie. Een referentie-vrije methode voor het in

beeld brengen van defecten, zoals delaminaties en zwakke verbindingen, wordt beschreven en geïllustreerd aan de hand van zowel numerieke simulaties als experimentele metingen. Voor- en nadelen van deze niet-lineaire GW techniek voor schadelokalisatie worden aangehaald en besproken. In het bijzonder vermelden we hier het feit dat deze nieuwe methodologie storende variaties omwille van omgevingsomstandigheden buiten spel zet. In de marge van deze studie wordt bovendien ook een nieuwe datafusie methode besproken die toelaat om op een betere manier experimenteel de dispersie krommen van geleide golven te bepalen. In de toekomst kan deze methode gebruikt worden voor het verbeteren van zowel excitatie als detectie van geleide golven, alsook om elastische parameters van onderzochte materialen te bepalen via een inverse studie van de experimentele data.

Het tweede deel van dit onderzoek handelt over Lokale Defect Resonanties (LDR). Verschillende verbeteringen, zoals het automatisch detecteren van de LDR frequentie en de bepaling van de grootte van het defect, worden voorgesteld en gestaafd aan de hand van zowel numerieke simulaties als experimenten. De voorgestelde aanpassingen kunnen leiden tot een grotere toepasbaarheid van de methode in concrete toepassingen. Dit wordt geïllustreerd aan de hand van experimentele studies uitgevoerd op verschillende materialen, zoals composiet sandwich structuren, glasvezel polymeren en zichzelf herstellende ionomeer platen.

Abbreviations

ACU Air-coupled ultrasound.

ALAMSA A Life-cycle Autonomous Modular System for Aircraft Material State Evaluation and Restoring System, FP7 project.

ASLC Adaptive Signal Length Correction.

AWG Arbitrary Waveform Generator.

BC Boundary Conditions.

BSS Baseline Signal Stretch.

BVID Barely Visible Impact Damage.

CAN Contact Acoustic Nonlinearity.

CFRP Carbon-Fiber-Reinforced Polymer.

EFIT Elastodynamic Finite Integration Technique.

EMAT Electromagnetic Acoustic Transducer.

FBG Fiber Bragg Grating.

FBH Flat Bottom Hole.

FEM Finite Element Method.

FFT Fast Fourier Transform.

FWHM Full Width at Half Maximum.

GFRP Glass-Fiber-Reinforced plastic.

GMT Global Matrix Technique.

GPU Graphical Processing Unit.

GUIGUW Graphical User Interface for Guided Ultrasonic Waves.

GW Guided Waves.

IR Infrared.

LDR Local Defect Resonance.

LDV Laser Doppler Vibrometry.

LHS Left-hand Side of Equation.

LRB Low Reflecting Boundaries.

MPM Matrix Pencil Method.

NDE Nondestructive Evaluation.

NDT Nondestructive Testing.

NEWS Nonlinear Elastic Wave Spectroscopy.

NWMS Nonlinear Wave Modulation Spectroscopy.

OBS Optimal baseline selection.

ODE Ordinary Differential Equation.

PM Preisach-Mayergoyz space.

PMMA Polymethyl methacrylate.

POD Probability of Detection.

PZT Piezoceramic Transducer.

RAPID Reconstruction Algorithm for Probabilistic Inspection of Damage.

RHS Right-hand Side of Equation.

ROI Region of Interest.

SAFE Semi-Analytical Finite Elements.

SARISTU Smart Intelligent Aircraft Structures (FP7 project).

SD Standard Deviation.

SDC Signal Difference Coefficient.

SEM Strip Element Method.

SH Shear Horizontal Waves.

SHM Structural Health Monitoring.

SNR Signal-to-Noise Ratio (SNR).

SSM Scaling Subtraction Method.

SV Shear Vertical Waves.

SVD Singular Value Decomposition.

T-R Transmitter-Receiver Pair.

TMT Transfer Matrix Technique.

TOF Time of Flight.

μ**CT** Microfocus Computed Tomography.

UPS Ultrasonic Polar Scan.

UT Ultrasonic Testing.

VT Visual Testing.

List of Symbols

$\vec{n}$ Normal vector to the surface [m].

ν Poisson's ratio.

λ Wavelength [m].

ρ Material density [$\mathrm{kg\,m^{-3}}$].

ϕ Scalar potential in Helmholtz's decomposition.

ω Angular frequency [$\mathrm{rad\,s^{-1}}$].

φ Rotation/propagation angle [rad].

θ Angle of propagation [rad].

γ Parameter of nonlinear delamination model [$\mathrm{N\,s\,m^{-3}}$].

λ, μ Lamé constants.

$\theta(A)$ SSM parameter.

Ω_d Damaged area.

ε_{ij} Infinitesimal strain tensor.

τ_{ij} Stress tensor [Pa].

δ_{ij} Kronecker symbol (operator).

Δx Spatial step in x-direction [m].

Δy Spatial step in y-direction [m].

A Amplitude.

A_B Amplitude of the baseline signal [V].

A_D Amplitude of the current (damaged) signal [V].

A_{lin} Amplitude of the linear signal [V].

B Signal bandwidth [Hz].

C_{ijkl} Stiffness tensor [Pa].

C_{ijklmn} 3rd order elastic tensor [Pa].

D_{ij} Sparse array signals collected in the damaged state.

E Young's modulus [Pa].

E_{eff} Effective stiffness of the FBH.

F_{d_b} Damping force at the delamination's bottom interface [N].

F_{d_t} Damping force at the delamination's top interface [N].

F_{s_b} Spring force at the delamination's top interface [N].

F_{s_t} Spring force at the delamination's bottom interface [N].

$H(\varepsilon)$ Heaviside function.

M_{eff} Effective mass of the FBH [kg].

Q Quality factor.

$R_{ij}(x, y)$ Geometrical function.

SDC_{ij} Signal difference coefficient.

T Duration of a signal, period of a signal [s].

W Elastic strain energy.

Z_0 Distance between delamination interfaces at rest [m].

c_1 Longitudinal wave velocity [$\mathrm{m\,s^{-1}}$].

c_2 Shear wave velocity [$\mathrm{m\,s^{-1}}$].

c_g Group velocity [$\mathrm{m\,s^{-1}}$].

c_{ph} Phase velocity [$\mathrm{m\,s^{-1}}$].

d Diameter, plate thickness, depth of defect [m].

f Frequency [Hz].

f_e LDR frequency [Hz].

f_i Body forces.

f_s Sampling frequency [Hz].

f_t Analytical LDR frequency [Hz].

$g(f)$ Gain function [dB].

h Thickness of a plate [m].

h_i Thickness of a layer in layered laminate [m].

i Imaginary unit.

k Wavenumber $[\mathrm{rad\,m^{-1}}]$.

$k_1,\ k_2, k_3$ Virtual generalized spring constants $[\mathrm{N\,m^{-3}}]$.

k_s SSM scaling coefficient.

l Degree of Legendre polynomial.

m Number of signals.

n_c Number of cycles.

n_e Number of sparse array elements.

n_l Number of layers.

n_s Number of samples.

p MPM model order.

q Number of independent modes in MPM method.

r Radius of a circle [m].

r_e Estimated radius of a defect [m].

$s_{ij}(x, y)$ a priory probability distribution function.

t_P Damage index $(P(x, y))$ threshold.

t_{SDC} SDC threshold.

u_i Displacement tensor.

u_z z-component of displacement [m].

$v_A(t)$ High amplitude signal in Scaling Subtraction Method.

v_{lin} Low amplitude linear signal in Scaling Subtraction Method.

v_{ref} Scaled signal in Scaling Subtraction Method.

$w_A(t)$ SSM signal.

$\vec{\alpha}$ Polarization vector.

α_{dM} Damping coefficient.

$\vec{A}$ Vector of partial wave amplitude $\vec{A} = [A_1, A_2, A_3, A_4, A_5, A_6]$.

$\mathbf{A}$ State matrix.

β Shape factor in RAPID algorithm.

$\hat{\beta}$ Stretch factor.

β_{dK} Stiffness damping factor.

$\mathbf{B}$ System matrix in the partial wave technique.

B_{ij} Sparse array signals collected in the baseline (intact) state.

$\mathbf{C}$ Stiffness matrix.

$\mathbf{S}$ Compliance matrix.

δ 4th order elastic parameter.

Δt Time step, sampling interval [s].

$\mathbf{D}$ Field matrix.

ε_c Contact strain threshold.

E_0 Constant Young's modulus in weakly nonlinear system [Pa].

$\mathbf{G}$ Global matrix in the Global Matrix Technique.

$\mathbf{I_p}$ Unit matrix.

$\vec{k}$ Wave vector.

$\mathbf{L}$ Transfer matrix.

$\vec{n}$ Direction cosines.

N_i Order of the Legendre polynomial approximation.

$\boldsymbol{\psi}$ Vector potential in Helmholtz's decomposition.

ψ Skew angle in anisotropic material [rad].

$P(x, y)$ Damage index.

ρ_{ij} Correlation coefficient for a specific T-R pair.

$\vec{T}$ State vector $[u_1, u_2, u_3, \tau_{13}, \tau_{23}, \tau_{33}]^T$.

$\boldsymbol{u}$ Displacement vector field $\boldsymbol{u} = [u_1, u_2, u_3]$.

Δz Delamination gap distance [m].

Contents

List of Figures

List of Tables

Chapter 1

Introduction

1.1 Context

Guided waves based testing has been steadily coming into the spotlight of the ultrasonic Nondestructive Testing (NDT) in the last two decades. The main reason for this interest is the steeply increasing usage of Carbon-Fiber-Reinforced Polymers (CFRP) and thin metallic structures in a broad range of engineering applications spanning from aerospace industry to the manufacturing of sport accessories. This boom of CFRP usage has also radically stimulated the development of novel nondestructive inspection techniques, because the traditional approaches, such as Visual Testing (VT) and Ultrasonic Testing (UT), proved to be costly, time ineffective and sometimes unsuitable for this new generation of composite structural parts with very complicated shapes [1, 2, 3, 4, 5]. The typical properties of guided waves, such as their low attenuation, long propagation distances and damage sensitivity, made them suitable not only for in-situ scheduled inspection with hand-held devices, but also for Structural Health Monitoring (SHM) of plate-like composite structures using embedded sensors [6, 7]. This application is further supported by the relatively cheap and simple Guided Waves (GW) instrumentation compared to other inspection techniques like active thermography or shearography. These two facts, the small, cheap and nonintrusive instrumentation together with favourable wave properties, made guided waves widespread and popular. On the other hand, this experimental accessibility is compensated by a far more complex post-processing and evaluation when compared to other NDT methods. Due to the nature of guided waves, more than one wave mode typically propagates through the structure and the propagating modes can have very different phase and group velocities [8, 9]. To make it even more complicated, the propagation velocities in anisotropic samples, such as CFRP, are direction dependent. Therefore, the phase and group velocities, displacement profiles and other main characteristics of the guided waves have to be known before the actual NDT takes place.

With this fact in mind, the basic numerical simulation methods for predicting the guided wave propagation characteristics are introduced and described in the first part of the present work. They are applied to real-world test samples to predict and identify the best guided wave mode, excitation frequency and other important parameters that will enable successful detection of damage. Hence, numerical simulations represent an extremely important first step in every NDT inspection task and especially in GW techniques.

Next, when the detailed propagation and dispersion characteristics are known, they can be used to establish an optimized input for the experimental measurements and inspection. This type of tuned GW inspection has several advantages, some of them were highlighted in the opening paragraph and the rest is summarized in the following list

- long range inspection
- lower number of small transducers
- low attenuation of the propagating wave
- good damage sensitivity (proportional to the wavelength)
- inspection free of moving mechanical parts.

On the other hand, the GW testing suffers from a few significant drawbacks. First of all, it is extremely difficult, with a few exceptions such as long pipes and large plates, to directly identify the presence of damage from the backscatter signal [10, 11]. This signal is often buried in the edge-reflected and mode converted waves and it is a complex task to recover it [12]. A typical approach to this problem is to employ the so called *baseline* signal that was recorded on the same sample prior to the damage introduction. If the baseline signal is subtracted from the signal that was acquired in the damaged state, only the waves scattered from the defect will remain. It is apparent that this baseline-dependence is the weakest spot of the current GW inspection. This and other notable drawbacks are summarized in the following list.

- baseline-dependent analysis

- difficult inspection of more complex structures: stringers, I-beams, etc.
- complex synchronization of input-output circuitry.

The last drawback can nowadays be solved rather easily using high density digitizers with tight synchronization that are becoming more and more affordable and are perfectly suited for such an application. Using the multiplexed multichannel digitizers, the acquisition times can be reduced to order of seconds for very large arrays with several hundreds of channels.

1.2 Research goal and objectives

The present thesis attempts to tackle and solve the problems related to baseline-dependent GW inspection techniques. A novel method is sought that will be able to replace the intact baseline with another input that can be acquired on-line and under the same circumstances. By eliminating the need for an intact baseline, the method should be more robust and versatile, and more easily applied throughout the designed operation lifetime of the inspected specimen. Moreover, the new measurement concept should be sufficiently immune towards changes in external environmental conditions, such as temperature, humidity and pressure. Hence, the proposed method should be ready to match the requirements for a reliable SHM method.

Since the simple wave scattering, that is the working principle of the baseline-dependent methods, cannot be obviously used for such a purpose, the attention is turning to the application of Nonlinear Elastic Wave Spectroscopy (NEWS). This class of nonlinear spectroscopic methods represents one of the future directions of NDT and as such, we would like to harness their potential and use them as a backbone for a new baseline-independent method. Therefore, the goals of the first major part of the thesis are

- to propose a novel baseline-independent method based on NEWS.
- to carry out numerical simulations to test the performance of the proposed method.
- to test the method on realistic samples provided by the ALAMSA[1] project partners.

Although other excitation and receiving methods, such as Fibre Bragg Grating (FBG) [13, 14] or laser sensing [15, 16, 17], can be used for sensing propagating

---

[1] `http://cordis.europa.eu/project/rcn/103931_en.html`

waves, simple leave-in-place Piezoceramic Transducer (PZT) patches are used throughout the thesis. Ultrasonic imaging using an array of such sensors is beneficial, because their unit price is very low and they do not require any special fabrication steps. Moreover, they can be easily integrated in the structure before or simply after its manufacturing.

The second part of the present work is dedicated to the application and improvement of the Local Defect Resonance (LDR) technique. We attempt to broaden the application scope of the LDR from ordinary aluminum alloys via CFRP to sandwich composites by automating the LDR frequency detection. In order to do that, the local resonance phenomena have to be properly and quantitatively described, and its main characteristics have to be analyzed. To itemize the goals of the second part:

- to develop the LDR detection algorithm.
- to test the proposed algorithm in numerical simulations.
- to apply the algorithm to the samples and assess its performance.

1.3 Outline of the thesis

The present thesis is divided into seven chapters. In the second chapter of the thesis, an overview of the theory of elastic waves in solids is given. Special attention is paid to guided waves and more specifically to Lamb waves that propagate in thin flat plate-like structures. An analytical derivation of the governing Lamb-Rayleigh dispersion relations is presented and the corresponding solutions are numerically calculated and visualized to provide a better insight into the typical behaviour of the symmetric and asymmetric Lamb waves.

The third chapter further expands on the topic of guided wave propagation in layered structures. This is of great importance for understanding the dispersion and wave propagation characteristics in CFRP. Three most common solution strategies for this problem are presented and their precision and complexity is studied. In addition to this topic, two methods for experimental dispersion analysis are described. Furthermore, it will be demonstrated that the fusion of the outputs of these two algorithms yields better results with lower amount of noise.

The fourth section is then dedicated to the NEWS phenomena that creates the backbone of the newly proposed GW baseline-free inspection technique. A short overview of the most important nonlinear elastic wave effects is given and described.

Chapters five and six deal with the proposed baseline-independent nonlinear GW inspection technique and advancements in the LDR applicability respectively. The two sections summarizes the most important findings of this thesis and present several new ideas.

The thesis concludes with a discussion of the results and findings in section 7. The future prospects and outlook on the use of guided waves based NDT and SHM are also summarized in this section.

Chapter 2

Elastic Waves in Solids

Elastic waves in solids are the cornerstone of ultrasonic NDT, because they are used to probe the interior of the sample and carry the information to the receiver. As such, the understanding of their fundamentals is crucial. Elastic wave characteristics can be derived from the fundamental laws of elasticity and the equations of motion. Therefore, the essential pieces of the theory of elasticity and elastodynamics are introduced in the following section. First, the general geometric and constitutive equations are recapitulated. The fundamental isotropic symmetry is discussed followed by other symmetry classes that are important for NDT of thin layered composites. Then, using the equation of motion, the wave equation for isotropic solids is derived and the bulk wave solution is presented. Guided waves and especially Lamb waves are another important solution of the wave equation with specific boundary conditions imposed by the finite thickness waveguides. This type of elastic waves is of utmost importance for this work and therefore, it is presented in greater detail.

2.1 General equations of elasticity and elastostatics

The fundamental equations of elasticity are the common starting point for the derivation of all types of elastic waves that propagate in solids and liquids too. As such, they are outlined in this section and they will be referred to throughout the rest of the present manuscript. The first corner stone is the general theory of linear (*infinitesimal*) elasticity. The strain tensor ε_{ij} is in this case reduced

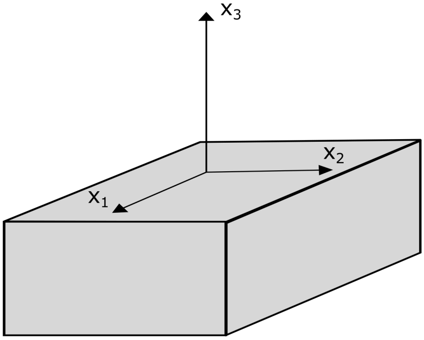

Figure 2.1: General right-hand coordinate system.

to the linear terms by excluding the second order mixed term from

$$\varepsilon_{ij} = \frac{1}{2}(u_{i,j} + u_{j,i} + u_{k,i}u_{k,j}), \tag{2.1}$$

where u_i denotes the displacement tensor. Einstein's notation, as described in Appendix A, is used throughout the manuscript to simplify the tensor notation. This leads to the classic infinitesimal strain tensor

$$\varepsilon_{ij} = \frac{1}{2}(u_{i,j} + u_{j,i}), \tag{2.2}$$

The tensor notation will be used in cases where it simplifies the formulas, otherwise it will be replaced by a vector notation for clarity and detailed description. The general rules of tensor notation can be found in Appendix A. The general coordinate system is represented in Fig. 2.1.

The second foundation of the theory of elasticity is the constitutive equation. It is this relation that couples together the stress and strain tensors in a *linearly or nonlinearly elastic* solid with arbitrary class of symmetry. In case nonlinearity can be ignored, the generalized Hooke's law states that the components of the stress tensor can be expressed as a linear function of the strain tensor components using the following formula

$$\tau_{ij} = C_{ijkl}\varepsilon_{kl}, \tag{2.3}$$

where τ_{ij} is the stress tensor and C_{ijkl} is the stiffness (elasticity) tensor [18]. Although C_{ijkl} is a rank 4 tensor with $3^4 = 81$ components in total, it can be proven, using symmetry and energy considerations, that there are only 21 independent coefficients [19]. Using these 21 coefficients, a generally anisotropic body can be described [20]. Details regarding the symmetric properties of C_{ijkl} as well as the derivation of the stiffness tensor for different symmetry classes can be found, for example in [20]. Since only 21 coefficients are independent, the stiffness tensor and the constitutive equation is most commonly represented in a matrix form as

$$\begin{bmatrix} \tau_{11} \\ \tau_{22} \\ \tau_{33} \\ \tau_{23} \\ \tau_{13} \\ \tau_{12} \end{bmatrix} = \begin{bmatrix} C_{11} & C_{12} & C_{13} & C_{14} & C_{15} & C_{16} \\ & C_{22} & C_{23} & C_{24} & C_{25} & C_{26} \\ & & C_{33} & C_{34} & C_{35} & C_{36} \\ & & & C_{44} & C_{45} & C_{46} \\ & & sym & & C_{55} & C_{56} \\ & & & & & C_{66} \end{bmatrix} \begin{bmatrix} \varepsilon_{11} \\ \varepsilon_{22} \\ \varepsilon_{33} \\ 2\varepsilon_{23} \\ 2\varepsilon_{13} \\ 2\varepsilon_{12} \end{bmatrix}, \tag{2.4}$$

which can be further simplified using the Voigt's notation (see Appendix B.2). Hence, equation (2.4) can be rewritten in a more concise form as

$$\vec{\tau} = \mathbf{C}\vec{\varepsilon}, \tag{2.5}$$

where $\mathbf{C}$ is the stiffness matrix. As mentioned above, the stiffness tensor is symmetric. Therefore, the contracted $\mathbf{C}$ matrix is also symmetric ($\mathbf{C}_{ij} = \mathbf{C}_{ji}$).

A generally anisotropic medium is a rather scarce sight in nature. Most of the naturally occurring and also man-made materials possess a higher order symmetry, typically isotropic, transversely isotropic or orthotropic symmetry class. These three symmetry classes are widespread, because most of the engineering materials, and composites especially, can be described by them.

In some cases, it is beneficial to represent the constitutive relation in the inverse form as a function of stress. The stiffness matrix is then replaced by its inverse, the *compliance matrix*

$$\vec{\varepsilon} = \mathbf{S}\vec{\tau}, \tag{2.6}$$

where $\mathbf{S} = \mathbf{C}^{-1}$. The compliance matrix $\mathbf{S}$ exhibits the same properties as $\mathbf{C}$, most notably the symmetry property $\mathbf{S}_{ij} = \mathbf{S}_{ji}$.

Combined with the appropriate boundary conditions, equations (2.3) and (2.2) are instrumental in solving the linear elastostatic problems. In the following sections, the most common symmetry classes are described in detail. The stiffness matrices as well as their relation to the engineering constants are presented.

2.1.1 Orthotropic material

A material with two mutually orthogonal symmetry planes is called *orthotropic*. The presence of two planes of symmetry directly implies that symmetry exists with respect to a plane that is orthogonal to the original symmetry planes. In this case, the constitutive relation is fully defined by nine independent elastic constants. In the principal material directions [1], the stiffness matrix can be expressed in as

$$\mathbf{C} = \begin{bmatrix} C_{11} & C_{12} & C_{13} & 0 & 0 & 0 \\ & C_{22} & C_{23} & 0 & 0 & 0 \\ & & C_{33} & & 0 & 0 \\ & & & C_{44} & 0 & 0 \\ & & sym & & C_{55} & 0 \\ & & & & & C_{66} \end{bmatrix}. \tag{2.7}$$

Note that, in orthotropic materials, there is neither *extension-shear*, nor *shear-shear* coupling in the principal directions. However, if the direction of loading is not aligned with one of the principal directions, the stiffness matrix becomes more populated and extra shear-extension coupling is introduced.

The samples in the present work are mostly characterized in terms of their engineering constants, because those are the values that can be experimentally measured, unlike the coefficients of the stiffness matrix **C**. Therefore, it is necessary to shortly introduce these constants and relate them to the computational stiffness and compliance matrices. In engineering applications, an orthotropic material is described by nine engineering constants. To introduce these constants, it is more favourable to start with the compliance matrix, since it offers a more intuitive insight in the physical meaning of these constants and directly describes the deformation behaviour. For orthotropic materials,

$$\mathbf{S} = \begin{bmatrix} \frac{1}{E_1} & -\frac{\nu_{21}}{E_2} & -\frac{\nu_{31}}{E_2} & 0 & 0 & 0 \\ -\frac{\nu_{12}}{E_1} & \frac{1}{E_2} & -\frac{\nu_{32}}{E_3} & 0 & 0 & 0 \\ -\frac{\nu_{13}}{E_1} & -\frac{\nu_{23}}{E_2} & \frac{1}{E_3} & 0 & 0 & 0 \\ 0 & 0 & 0 & \frac{1}{G_{23}} & 0 & 0 \\ 0 & 0 & 0 & 0 & \frac{1}{G_{31}} & 0 \\ 0 & 0 & 0 & 0 & 0 & \frac{1}{G_{12}} \end{bmatrix}, \tag{2.8}$$

where $E_i,\ (i = 1, 2, 3)$ are the Young's moduli in the directions of axis x_1, x_2, x_3, respectively, and can be seen as extensions from the standard (direction independent) Young's modulus in an isotropic solid. ν_{ij} are the Poisson's ratios defined as

$$\nu_{ij} = -\frac{\varepsilon_i}{\varepsilon_j}, \quad i, j = 1, 2, 3 \quad i \neq j, \tag{2.9}$$

---

[1] Principal material directions are directions parallel to the intersections of the three orthogonal planes of material symmetry. The principal material coordinate system is defined by the principal material directions [20].

where i represents the direction in which the stress is applied and j denotes the transverse (perpendicular) direction. In short, ν_{ij} describes the ratio of induced strain in the transverse direction to the strain in the direction in which the stress is being applied. G_{23}, G_{31} and G_{12} are the shear moduli in the planes defined by the subscripts. These are the shear moduli in particular directions. The coefficients of the stiffness matrix $\mathbf{C}$ can be analytically expressed by inverting $\mathbf{S}$ as follows

$$C_{11} = \frac{1-\nu_{23}\nu_{32}}{E_2E_3\Delta} \qquad C_{22} = \frac{1-\nu_{13}\nu_{31}}{E_1E_3\Delta} \qquad C_{33} = \frac{1-\nu_{12}\nu_{21}}{E_1E_2\Delta} \tag{2.10}$$

$$C_{12} = \frac{\nu_{21}+\nu_{31}\nu_{23}}{E_2E_3\Delta} \qquad C_{13} = \frac{\nu_{31}+\nu_{21}\nu_{32}}{E_2E_3\Delta} \qquad C_{23} = \frac{\nu_{32}+\nu_{12}\nu_{31}}{E_1E_3\Delta} \tag{2.11}$$

$$C_{44} = G_{23} \qquad C_{55} = G_{31} \qquad C_{66} = G_{12} \tag{2.12}$$

$$\tag{2.13}$$

where

$$\Delta = \frac{1-\nu_{12}\nu_{21}-\nu_{23}\nu_{32}-\nu_{31}\nu_{13}-2\nu_{12}\nu_{23}\nu_{31}}{E_1E_2E_3}. \tag{2.14}$$

It is very difficult to experimentally measure all the engineering constants of the orthotropic material. However, several sophisticated methods how to directly populate the stiffness matrix of such a material have been published. Among the most interesting is the Ultrasonic Polar Scan (UPS) developed at University of Gent [21, 22].

Now that the basis for the analysis of the orthotropic materials has been laid, we can proceed to other important type of materials with slightly higher symmetry class, the *transversely isotropic materials*.

2.1.2 Transversely isotropic material

If there is a plane in which the elastic properties of the material are equal in all direction, the material is said to be *transversely isotropic* and its elastic behaviour can be defined by five independent elastic constants. The symmetry of such a material is demonstrated in Fig. 2.2 using a unidirectional fibre composite with fibres aligned with the axis x_1. If $x_2 - x_3$ is the plane of isotropy in the

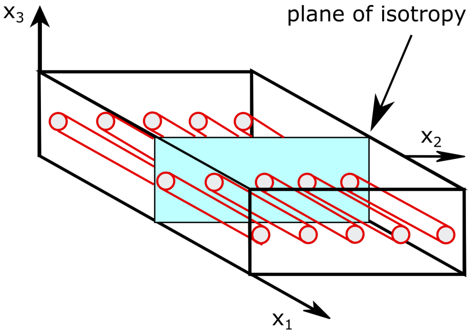

Figure 2.2: Transversely isotropic material and its plane of isotropic symmetry $x_2 - x_3$.

studied sample, then the stiffness matrix takes on the form of

$$\mathbf{C} = \begin{bmatrix} C_{11} & C_{12} & C_{12} & 0 & 0 & 0 \\ & C_{22} & C_{23} & 0 & 0 & 0 \\ & & C_{22} & & 0 & 0 \\ & & & \frac{C_{22}-C_{23}}{2} & 0 & 0 \\ & & sym & & C_{55} & 0 \\ & & & & & C_{55} \end{bmatrix}. \tag{2.15}$$

Like in an orthothropic material, there is no shear-extension or shear-shear coupling for a *transversely isotropic* material, if oriented in the principal material directions. If we assume the orientation of the sample as shown in Fig. 2.2, the compliance matrix can be expressed in terms of five engineering elastic constants $[E_1, E_2, \nu_{12}, \nu_{23}, G_{12}]$ as

$$\mathbf{S} = \begin{bmatrix} \frac{1}{E_1} & -\frac{\nu_{21}}{E_2} & -\frac{\nu_{21}}{E_2} & 0 & 0 & 0 \\ -\frac{\nu_{12}}{E_1} & \frac{1}{E_2} & -\frac{\nu_{32}}{E_2} & 0 & 0 & 0 \\ -\frac{\nu_{12}}{E_1} & -\frac{\nu_{23}}{E_2} & \frac{1}{E_2} & 0 & 0 & 0 \\ 0 & 0 & 0 & \frac{1}{G_{23}} & 0 & 0 \\ 0 & 0 & 0 & 0 & \frac{1}{G_{12}} & 0 \\ 0 & 0 & 0 & 0 & 0 & \frac{1}{G_{12}} \end{bmatrix}, \tag{2.16}$$

where the following identities hold: $G_{23} = \frac{E_2}{2(1+\nu_{23})}$, $\nu_{12} = \nu_{13}$, $E_2 = E_3$ [23, 24]. The symmetry of the compliance matrix further results in following relations $\frac{\nu_{12}}{E_1} = \frac{\nu_{21}}{E_2}$. However, it is important to realize that the values of ν_{12} and ν_{21} can be significantly different [25].

However, if the direction of loading is not aligned with the principal axis of the transversely isotropic material, the stiffness/compliance matrices become more populated and extra shear-extension coupling is introduced.

2.1.3 Isotropic material

Isotropic materials exhibit the highest class of symmetry. All properties are the same in all directions. In case of isotropy, the number of independent coefficients in the stiffness matrix is reduced down to two. The elastic properties are identical in all directions and the extensional (or longitudinal) and shear components are decoupled. These are usually represented as the Young's modulus E, and the Poisson coefficient ν in engineering applications or by the *Lamé constants* (λ, μ) in computational elasticity. Nonetheless, it is very easy to convert from one pair of constants to the other.

$$\lambda = \frac{E\nu}{(1+\nu)(1-2\nu)}, \qquad \mu = \frac{E}{2(1+\nu)} \tag{2.17}$$

Using the *Lamé constants*, the constitutive equation (2.3) can be easily simplified to

$$\tau_{ij} = \lambda \varepsilon_{kk} \sigma_{ij} + 2\mu \varepsilon_{ij} \tag{2.18}$$

or in terms of Voigt's notation using $C_{11} = \lambda + 2\mu$ and $C_{12} = \lambda$

$$\begin{bmatrix} \tau_1 \\ \tau_2 \\ \tau_3 \\ \tau_4 \\ \tau_5 \\ \tau_6 \end{bmatrix} = \begin{bmatrix} C_{11} & C_{12} & C_{12} & 0 & 0 & 0 \\ & C_{11} & C_{12} & 0 & 0 & 0 \\ & & C_{11} & & 0 & 0 \\ & & & \frac{C_{11}-C_{12}}{2} & 0 & 0 \\ & & sym & & \frac{C_{11}-C_{12}}{2} & 0 \\ & & & & & \frac{C_{11}-C_{12}}{2} \end{bmatrix} \begin{bmatrix} \varepsilon_1 \\ \varepsilon_2 \\ \varepsilon_3 \\ \varepsilon_4 \\ \varepsilon_5 \\ \varepsilon_6 \end{bmatrix}. \tag{2.19}$$

It follows that the stiffness matrix can be subsequently expressed as

$$\mathbf{C} = \begin{bmatrix} \lambda + 2\mu & \lambda & \lambda & 0 & 0 & 0 \\ & \lambda + 2\mu & \lambda & 0 & 0 & 0 \\ & & \lambda + 2\mu & & 0 & 0 \\ & & & \mu & 0 & 0 \\ & & sym & & \mu & 0 \\ & & & & & \mu \end{bmatrix}. \tag{2.20}$$

Most of the metals and homogeneous polymeric materials are generally isotropic and it is sufficient to describe them using the linear isotropic model. However, the usage of composites and tailored materials has been growing significantly in past decades and these materials cannot be easily described using the isotropic model anymore. Therefore, a lower symmetry classes, such as transversely isotropic or orthotropic symmetries, have to be used to properly analyse the elastic behaviour of such materials.

The two previously mentioned symmetry classes are especially helpful when describing the elastic behaviour, deformation and wave propagation in fibre-composite materials and laminated structures, e.g. laminated plates and pipes [19].

2.2 Elastodynamics and bulk waves

Bulk wave propagation describes the elastodynamic wave propagation in an infinite or semi-infinite unbounded medium. The solution does not require any additional boundary conditions (BC) and can be solved directly from (2.22). The infinite media assumption can be also applied to wave propagation in samples with smallest spatial dimension d much greater then the typical wavelength λ of the propagating waves, the limit value being $d \geq 5\lambda$. Therefore, bulk waves have been absolutely crucial for ultrasonic NDT, since most of the inspected samples can be thought of as infinite with respect to the applied wavelengths.

So far, only the equations of static elasticity have been introduced. In order to solve a typical elastodynamic wave propagation problem, the equation of motion needs to be added. This can be derived for generally anisotropic homogeneous media using Newton's second law as

$$\tau_{ij,j} + \rho f_i = \rho \ddot{u}_i, \tag{2.21}$$

where ρ stands for the density of a homogeneous continuous medium and f_i represents the external body forces acting on the sample. The equation (2.21) is given in terms of stress and displacement tensors. If the constitutive and strain-displacement equations ((2.2) and (2.5) respectively) are applied, the equation of motion can be expressed in terms of the displacement vector components u_i as:

$$\frac{\partial}{\partial x_j}\left(C_{ijkl}\frac{1}{2}(u_{k,l} + u_{l,k})\right) + \rho f_i = \rho \ddot{u}_i \quad . \tag{2.22}$$

This fundamental wave equation is valid for any linear elastic material with arbitrary class of symmetry. It is used as a common starting point for the analysis of a variety of elastic wave propagation problems including bulk, surface and guided waves. Considering bulk waves in infinite media exclusively for now, the next two sections describe the bulk wave propagation in isotropic and anisotropic media.

2.2.1 Isotropic material

First, let us assume the case of an unbounded homogeneous isotropic medium. Hence, (2.3) simplifies to

$$\tau_{ij} = \lambda\varepsilon_{kk}\delta_{ij} + 2\mu\varepsilon_{ij} \tag{2.23}$$

and (2.21) yields

$$(\lambda + \mu)u_{j,ij} + \mu u_{i,jj} + \rho f_i = \rho\ddot{u}_i, \tag{2.24}$$

where λ, μ are the Lamé constants and δ_{ij} stands for the Kronecker delta. In terms of stiffness matrix components: $C_{11} = \lambda + 2\mu$, $C_{12} = \mu$. Similarly, assuming that there are no external forces acting in the system $f_i = 0$, the previous equation can be written using the vector notation as

$$(\lambda + \mu)\nabla(\nabla \cdot \boldsymbol{u}) + \mu\nabla^2\boldsymbol{u} = \rho\frac{\partial^2\boldsymbol{u}}{\partial t^2}, \tag{2.25}$$

where ∇, ∇^2 stands for the gradient and Laplace operator, respectively (see Appendix A). Several methods for solving equation (2.25) are discussed by several authors in distinguished textbooks, for example by Auld [18] or Achenbach [26]. One of the most frequently used methods is the method of potentials or, as it is more commonly known, the *Helmholtz decomposition.* Using the Helmholtz decomposition the displacement vector field can be written as a sum of the gradient of a scalar potential ϕ and the curl of a vector potential $\boldsymbol{\psi}$

$$\boldsymbol{u} = \nabla\phi + \nabla \times \boldsymbol{\psi}. \tag{2.26}$$

If the decomposed vector field $\boldsymbol{u}$ is substituted in (2.24) and the following identities $\nabla \cdot \nabla\phi = \nabla^2\phi$ and $\nabla \cdot \nabla \times \boldsymbol{\psi} = 0$ are taken into account, then (2.24) is reduced to

$$\nabla[(\lambda + 2\mu)\,\nabla^2\,\phi - \rho\ddot{\phi}] + \nabla \times [\mu\,\nabla^2\,\boldsymbol{\psi} - \rho\ddot{\boldsymbol{\psi}}] = 0. \tag{2.27}$$

This equation is true, if both expressions in brackets are equal to zero, which leads to two decoupled equations

$$\nabla^2\,\phi - \frac{1}{c_1^2}\ddot{\phi} = 0, \tag{2.28}$$

$$\nabla^2\,\boldsymbol{\psi} - \frac{1}{c_2^2}\ddot{\boldsymbol{\psi}} = \boldsymbol{0}, \tag{2.29}$$

where

$$c_1^2 = \frac{\lambda + 2\mu}{\rho}, \qquad c_2^2 = \frac{\mu}{\rho}. \tag{2.30}$$

In the previous equation, c_1 represents the *longitudinal wave (P-wave)* velocity and the c_2 stands for the *shear wave (S-wave)* velocity. It follows that Eq. (2.26) is a solution of the general problem posed by (2.25) if it satisfies the two decoupled equations (2.28) and (2.29).

Let us first assume that $\nabla \times \boldsymbol{\psi} = \mathbf{0}$ and $\boldsymbol{u} = \nabla \phi$, then (2.28) reduces to

$$\nabla^2 \boldsymbol{u} = \frac{1}{c_1^2} \ddot{\boldsymbol{u}}, \tag{2.31}$$

which represents the *longitudinal waves* in homogeneous isotropic medium. Similarly, if $\boldsymbol{u}$ contains only the rotational part $\boldsymbol{u} = \nabla \times \boldsymbol{\psi}$, then (2.29) becomes

$$\nabla^2 \boldsymbol{u} = \frac{1}{c_2^2} \ddot{\boldsymbol{u}} \tag{2.32}$$

and represents the *shear* waves in the medium. As a result of Helmholtz decomposition, the wave equation has been decoupled in two separate parts with different velocities and different profile of particle motion. In case of *longitudinal waves*, the particles move in the direction parallel to the wavefront propagation direction[2]. On the contrary, transverse *S-waves* have a particle motion in the plane perpendicular to the direction of propagation (wavefront). For the shear waves, two distinct versions can exist and are called Shear Horizontal (SH) and Shear Vertical (SV), respectively. The above derived longitudinal and shear waves do not have to fulfil any BC in infinite unbounded media. Hence, the two fundamental modes are completely decoupled in this case.

2.2.2 Anisotropic material

In isotropic media, the two types of elastic waves are clearly decoupled and separated from each other. The situation is far more complex for anisotropic solids. In this section, a short overview of the most important results and properties related to anisotropic solids will be presented. The topic has already been extensively studied by several authors and the details regarding the phenomena as well as the mathematical treatment can be found in several reference textbooks, e.g. [18, 27, 28, 29].

Let us assume an anisotropic medium with elastic tensor C_{ijkl}. We start the analysis using the general equation (2.22). No special assumptions, except for the linearity of the constitutive relation, were considered when deriving this equation and, therefore, it is valid even for the case of general anisotropy. Firstly,

---

[2] *Wavefront* is defined as a moving surface that separates the disturbed from undisturbed part of the elastic body or a locus of points with the same phase [26].

we omit the body forces and apply the spatial derivatives to the displacement tensor, yielding

$$\frac{1}{2}C_{ijkl}(u_{k,lj}+u_{l,kj})=\rho\ddot{u}_i, \tag{2.33}$$

where Einstein summation is assumed.

Secondly, let us assume a *harmonic plane wave* propagating in a direction given by the wave vector $\vec{k}$ (k_i in component notation)

$$u_i=A_i\exp\left[i(k_ix_i-\omega t)\right], \tag{2.34}$$

where the amplitudes A_i can be conveniently expressed using the polarization vector $\vec{\alpha}$ as $A_i=|A|\alpha_i$. It is obvious that substituting (2.34) into the right-hand side (RHS) of (2.33), which contains the time derivative results in

$$\rho\ddot{u}_i=-\rho\omega^2u_i, \tag{2.35}$$

where ω stands for the angular velocity. Similarly, it can be easily shown that the second derivative with space yields a $u_{k,jl}=-k_jk_lu_k$ factor. Therefore, the left-hand side (LHS) of (2.33) can be rewritten as

$$-C_{ijkl}k_jk_ku_l. \tag{2.36}$$

Hence, the original equation (2.33) can be recast into a more compact form as

$$C_{ijkl}k_jk_ku_l-\rho\omega^2u_i=0. \tag{2.37}$$

Finally, if the displacement tensor u_i is expressed using the Kronecker symbol as $u_i=u_l\delta_{il}$, then the previous equation takes the form of the famous *Christoffel equation*

$$(C_{ijkl}k_jk_k-\rho\omega^2\delta_{il})u_l=0. \tag{2.38}$$

In order to better understand the equation itself, it is beneficial to use $c_{ph}^2=\frac{\omega^2}{k^2}$ and replace the angular velocity ω with the phase velocity c_{ph}. Furthermore, the components of the wave vector can be replaced using the direction cosines and the scalar wavenumber as $k_j=kn_j$

$$\vec{k}=\begin{bmatrix}k_1\\k_2\\k_3\end{bmatrix}=k\begin{bmatrix}n_1\\n_2\\n_3\end{bmatrix}=k\vec{n}, \tag{2.39}$$

simplifying the Christoffel equation to

$$(\Gamma_{il}-\rho c_{ph}^2\delta_{il})u_l=0, \tag{2.40}$$

where $\Gamma_{il}=C_{ijkl}n_jn_k$ denotes the *Christoffel tensor*.

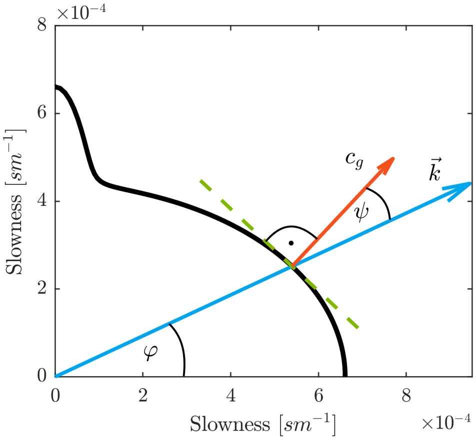

Figure 2.3: Graphical representation of the slowness curve $\frac{1}{c_{ph}}$, phase velocity c_g and skew angle ψ for an anisotropic medium. The black line represents the slowness surface.

The Christoffel equation describes the propagation of elastic waves in generally anisotropic material. For a given direction of propagation, defined by the wave vector $\vec{k}$ and its direction cosines $\vec{n}$, it returns three specific wave velocities c_{ph}. This can be inferred from (2.40), for which a nonzero solution for u_i exists if and only if the determinant of the matrix is zero

$$\det(\Gamma_{il} - \rho c_{ph}^2 \delta_{il}) = 0. \tag{2.41}$$

This results in a sixth order polynomial equation with only even powers in c_{ph}, thus it will lead to 3 solutions for c_{ph}^2, which represent three waves propagating either in positive or negative direction.

These are the solutions of the eigenvalue problem posed by (2.40) for c_{ph}^2. It is apparent that the resulting velocities are functions of both, the elastic constants and the direction of propagation. Therefore, it is more common to express the solution of (2.40) in a form of slowness surface, where slowness is defined as $\frac{1}{c_{ph}}$ (see Fig. 2.3). As can be seen from Fig. 2.4, the anisotropy also results in the appearance of a *skew angle* ψ between the direction of the wave vector and propagation direction, or alternatively, the manifestation of a nonzero angle between the phase c_{ph} and group velocity c_g.

The slowness representation has several advantages. First, it is independent of ω. Second, the direction of the group velocity can be easily determined as a normal to the slowness surface through a given point (see Fig. 2.3). The group

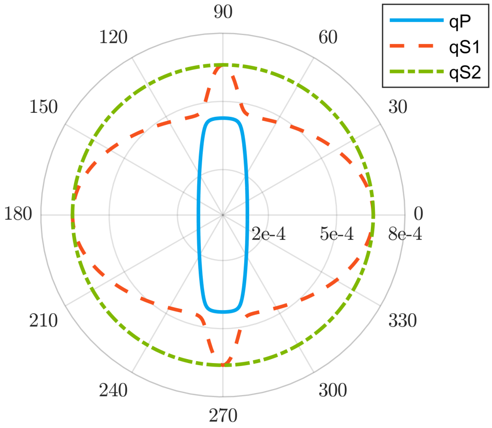

Figure 2.4: Slowness curves $\frac{1}{c_{ph}}$ for a transversely isotropic material.

velocity can then be calculated from the phase velocity taking into account the skewing angle ψ as explained in [18]

$$c_{ph} = c_g \cos \psi. \tag{2.42}$$

In the most general case three different modes are excited: two quasi-transverse (qS_1, qS_2) with mostly a transverse polarization and one quasi-longitudinal (qP) which is mostly longitudinal polarized and with none of the modes having a full longitudinal or transverse motion. However, if the propagation direction is aligned with one of the principal material axes, then a pure mode can be generated and the polarization vector is parallel or perpendicular (depending on whether it is a longitudinal or shear mode) to the wavefront normal $\psi = 0$ (see Fig. 2.4).

It is apparent that the wave propagation in anisotropic media is significantly more complicated that in the isotropic case. The group velocity direction can differ significantly from the wave vector (propagation) direction which may pose difficulties and this fact has to be taken into account when trying to launch waves in a particular direction. In addition, when dealing with anisotropic media, special attention has to be paid to the dispersion analysis that can provide us with valuable information about the sample's symmetry class and to the dependence of the phase velocity c_{ph} on the launch angle.

While it is straightforward to use the Christoffel equation to simulate the forward problem, i.e. the wave propagation in anisotropic solids. The inverse problem of determining the elastic constants from the experimentally measured data is very challenging. Notable approaches to invert the C-tensor from bulk wave measurements include, for example the ultrasonic pulsed polar scan [30] and laser ultrasonics [31].

2.3 Guided waves

Another important type of waves propagating in solids are the guided waves that propagate along/inside a particular waveguide, e.g. a thin plate, a pipe, or a shell structure. They are primarily characterized by a particle motion that is a combination of components which are parallel and perpendicular to the main propagation direction. In fact, guided waves can be seen as a combination of longitudinal and shear waves that are internally reflecting and constructively interfering inside the waveguide [8, 32].

Mathematically, guided waves are not only solutions of the fundamental elastodynamic wave equation, but they also have to satisfy certain boundary conditions imposed on the external boundaries of the waveguide. In contrast, bulk waves only satisfy the wave equation, since the medium in which they propagate is considered to be infinite. In other words, bulk waves do not 'feel' the influence of remote boundaries. It is this requirement - to fulfil the specific boundary conditions - that renders the analytical solution of some guided wave problems extremely difficult. In spite of this difficulty, several special cases have been solved successfully and these solutions carry the names of their authors, e.g. Lamb waves, Rayleigh waves. Lamb waves, for example, are representing the solution that applies in the case of a free thin plate in vacuum under condition of plane strain. This elegant solution was presented by H. Lamb in 1917 [33]. Another example is the case of free waves on the boundary of a semi-infinite solid solved by late Baron Rayleigh [34] and Stoneley waves on the interface between two semi-infinite solids [35]. In addition to these more commonly employed guided waves, the last type of guided waves that can be successfully used in the GW ultrasonic NDT are the SH waves [18].

The starting point for the mathematical description and derivation of all the above mentioned types of guided waves is common: the elastodynamic equations consisting of the equation of motion, the constitutive equation and the strain-displacement relation. The different solutions for each individual type types of guided waves are obtained by enforcing and assuming different boundary conditions and stress state. This will be demonstrated in the following sections.

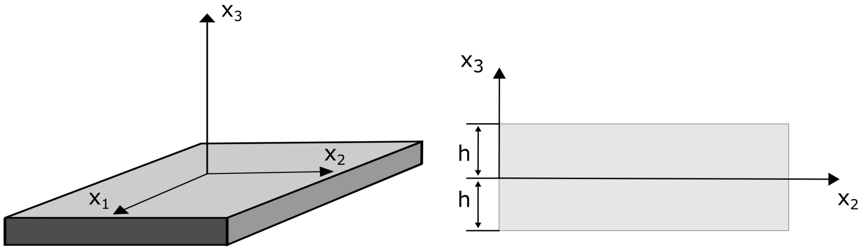

(a) Coordinate system (b) Cross-section

Figure 2.5: General coordinate system and dimensions used for deriving solution for Lamb waves in a free plate.

2.3.1 Lamb waves in isotropic free plates

As mentioned above, Lamb waves propagate in thin plate-like structures, such as simple plates or pipes with diameters significantly greater than the wavelength. They are a combination of longitudinal and shear waves propagating along the lateral direction of the plate. Let us derive the classic solution for the Lamb waves in a free plate. Several approaches can be used to calculate this case, e.g. method of displacement potentials or the partial wave technique [36]. Here, we will use the method of potentials combined with the transverse resonance assumption.

Let us assume a free thin plate of thickness $d = 2h$ oriented with respect to an orthogonal coordinate system as depicted in Fig. 2.5b. The plate is assumed to be homogeneous and isotropic for the sake of simplicity and the upper and lower surfaces are traction-free (normal and tangential components of the stress are zero). Firstly, using the Helmholtz decomposition we can write the displacement vector as a sum of the gradient of the scalar potential ϕ and the curl of the vector potential $\boldsymbol{\psi}$. This part follows exactly the elaborate derivation presented in section 2.2.1. Therefore, the details can be omitted and we can skip directly to the final result: two separate decoupled waves as described by equations (2.28) and (2.29).

Secondly, we assume that the plate is large enough and it is in a state of plain strain with respect to the x_1 direction. This implies that all field variables are independent of x_1 and the displacement component u_1 is zero [26]. The motion takes place in the $x_2 - x_3$ plane only. Hence, the vector field $\boldsymbol{\psi}$ from the Helmholtz decomposition contains only one non-zero component ψ_1 pointing in the direction orthogonal to the plane defined by x_2 and x_3. Using the above mentioned assumptions, (2.26) can be reduced from the general formulation

$$\begin{bmatrix} u_1 \\ u_2 \\ u_3 \end{bmatrix} = \begin{bmatrix} \frac{\partial\phi}{\partial x_1} + \frac{\partial\psi_3}{\partial x_2} - \frac{\partial\psi_2}{\partial x_3} \\ \frac{\partial\phi}{\partial x_2} + \frac{\partial\psi_1}{\partial x_3} - \frac{\partial\psi_3}{\partial x_1} \\ \frac{\partial\phi}{\partial x_3} + \frac{\partial\psi_2}{\partial x_1} - \frac{\partial\psi_1}{\partial x_2} \end{bmatrix} \tag{2.43}$$

to a much simpler system solution

$$\begin{bmatrix} u_1 \\ u_2 \\ u_3 \end{bmatrix} = \begin{bmatrix} 0 \\ \frac{\partial\phi}{\partial x_2} + \frac{\partial\psi_1}{\partial x_3} \\ \frac{\partial\phi}{\partial x_3} - \frac{\partial\psi_1}{\partial x_2} \end{bmatrix}. \tag{2.44}$$

If the latter expressions for u_i are then inserted in (2.2) and we subsequently assume the reduced version for isotropic solids (2.3), the stresses in the plate can be expressed as:

$$\tau_{22} = \lambda\Big(\frac{\partial^2\phi}{\partial x_2^2} + \frac{\partial^2\phi}{\partial x_3^2}\Big) + 2\mu\Big(\frac{\partial^2\phi}{\partial x_2^2} + \frac{\partial^2\psi_1}{\partial x_3\partial x_2}\Big) \tag{2.45}$$

$$\tau_{33} = \lambda\Big(\frac{\partial^2\phi}{\partial x_2^2} + \frac{\partial^2\phi}{\partial x_3^2}\Big) + 2\mu\Big(\frac{\partial^2\phi}{\partial x_3^2} - \frac{\partial^2\psi_1}{\partial x_2\partial x_3}\Big) \tag{2.46}$$

$$\tau_{23} = \mu\Big(2\frac{\partial^2\phi}{\partial x_2\partial x_3} + \frac{\partial^2\psi_1}{\partial x_3^2} - \frac{\partial^2\psi_1}{\partial x_2^2}\Big) \tag{2.47}$$

Using the assumption of plain strain, (2.28) and (2.29) can be reduced to

$$\frac{\partial^2\phi}{\partial x_2^2} + \frac{\partial^2\phi}{\partial x_3^2} = \frac{1}{c_1^2}\ddot{\phi}, \tag{2.48}$$

$$\frac{\partial^2\psi_1}{\partial x_2^2} + \frac{\partial^2\psi_1}{\partial x_3^2} = \frac{1}{c_2^2}\ddot{\psi}_1. \tag{2.49}$$

In order to solve (2.48) and (2.49), we assume a solution in form of

$$\phi = \Phi(x_3)\exp\left[i(kx_2 - \omega_t)\right], \tag{2.50}$$

$$\psi_1 = i\Psi(x_3)\exp\left[i(kx_2 - \omega_t)\right], \tag{2.51}$$

where k is the scalar wavenumber, ω the angular frequency and i is the imaginary unit [37]. The expected solution represents a standing wave pattern in x_3 direction and a propagating wave in x_2 direction. Therefore, the displacement and stress profiles throughout the thickness of the plate are governed only by

$\Phi(x_3)$ and $\Psi(x_3)$. The partial differential equations (2.48) and (2.49) are then reduced to the following ordinary differential equations

$$\frac{\partial^2 \Phi}{\partial x_3^2} + \alpha^2 \Phi = 0, \tag{2.52}$$

$$\frac{\partial^2 \Psi}{\partial x_3^2} + \beta^2 \Psi = 0, \tag{2.53}$$

where

$$\alpha^2 = \frac{\omega^2}{c_1^2} - k^2, \qquad \beta^2 = \frac{\omega^2}{c_2^2} - k^2. \tag{2.54}$$

The above introduced parameters are given in terms of wavenumber k, angular frequency ω and specific wave velocities. Since equations (2.52) and (2.53) are both Ordinary Differential Equation (ODE), the solution is readily known and can be written as

$$\Phi(x_3) = A \sin \alpha x_3 + B \cos \alpha x_3, \tag{2.55}$$

$$\Psi(x_3) = C \sin \beta x_3 + D \cos \beta x_3. \tag{2.56}$$

The solution for the corresponding displacements can be obtained in a general form by inserting $\Phi(x_3)$ and $\Psi(x_3)$ into (2.50) and (2.51) and further into (2.44).

$$u_2 = i[k(A \sin \alpha x_3 + B \cos \alpha x_3) + \beta(C \cos \beta x_3 - D \sin \beta x_3)] \exp i(kx_2 - \omega t) \tag{2.57}$$

$$u_3 = [\alpha(A \cos \alpha x_3 - B \sin \alpha x_3) + k(C \sin \beta x_3 + D \cos \beta x_3)] \exp i(kx_2 - \omega t) \tag{2.58}$$

As can be seen from (2.57) the displacement component u_2 can be split into symmetric and antisymmetric parts with respect to the center of the plate $x_3 = 0$. The symmetric part contains cosine terms only and the antisymmetric part consists exclusively of sine terms. On the contrary, u_3 is symmetric (antisymmetric) if it contains only sine (cosine) functions. Therefore, the solution can be divided into symmetric and antisymmetric parts to ease the derivation of the frequency-wavenumber dispersion relations.

Let us start with the antisymmetric modes.

Antisymmetric modes

The antisymmetric part of the displacement component reads

$$u_2 = i[kA \sin \alpha x_3 - \beta D \sin \beta x_3] \exp [i(kx_2 - \omega t)]. \tag{2.59}$$

Using the previous result and the expressions for potentials (2.44), we can complete the set of equations necessary for solving the case of antisymmetric modes:

$$\phi = A \sin \alpha x_3, \tag{2.60}$$

$$\psi_1 = iD \cos \beta x_3, \tag{2.61}$$

$$\tau_{23} = i\mu[2kA\alpha \cos \alpha x_3 + (k^2 - \beta^2) D \cos \beta x_3], \tag{2.62}$$

$$\tau_{33} = \mu[(k^2 - \beta^2) A \sin \alpha x_3 - 2k\beta D \sin \beta x_3] \tag{2.63}$$

$$u_2 = i[kA \sin \alpha x_3 - \beta D \sin \beta x_3] \tag{2.64}$$

$$u_3 = \alpha A \cos \alpha x_3 + kD \cos \beta x_3 \tag{2.65}$$

The exponential term $\exp[i(kx_2 - \omega t)]$ has been omitted in all equations for the sake of simplicity. It will vanish anyway in the next step of the derivation where the remaining boundary conditions are introduced. The identity

$$(\lambda k^2 + \lambda \alpha^2 + 2\mu \alpha^2) = \mu(\beta^2 - k^2) \tag{2.66}$$

was also used to further simplify the expression for τ_{33} [8]. The boundary conditions require that the upper and lower surface of the plate are free and therefore the traction and normal stress have to be zero for $x_3 = \pm h$

$$\tau_{23}(\pm h) \equiv 0, \qquad \tau_{33}(\pm h) \equiv 0. \tag{2.67}$$

After the substitution of the stresses into the boundary conditions, a two-by-two system of linear equations for the unknown coefficients A and D is formed. After a few basic operations it yields the form of

$$\begin{bmatrix} 2k\alpha \cos \alpha h & (k^2 - \beta^2) \cos \beta h \\ (k^2 - \beta^2) \sin \alpha h & -2k\beta \sin \beta h \end{bmatrix} \begin{bmatrix} A \\ D \end{bmatrix} = \begin{bmatrix} 0 \\ 0 \end{bmatrix}. \tag{2.68}$$

The derived homogeneous system yields a non-trivial solution only if the determinant of the matrix is zero. Using this fundamental theorem of linear algebra, we arrive at

$$\frac{\tan \beta h}{\tan \alpha h} = -\frac{(\beta^2 - k^2)^2}{4k^2 \alpha \beta}. \tag{2.69}$$

This transcendental equation links together the angular velocity ω and the wavenumber k. It yields an infinite number of solutions that form branches in the frequency-wavenumber $(f - k)$ space. Each of this branches represents one particular antisymmetric mode (see Fig. 2.6). By convention, the modes are usually named A_n, where $n = 0, 1, ...$ stands for the order of the mode. Despite

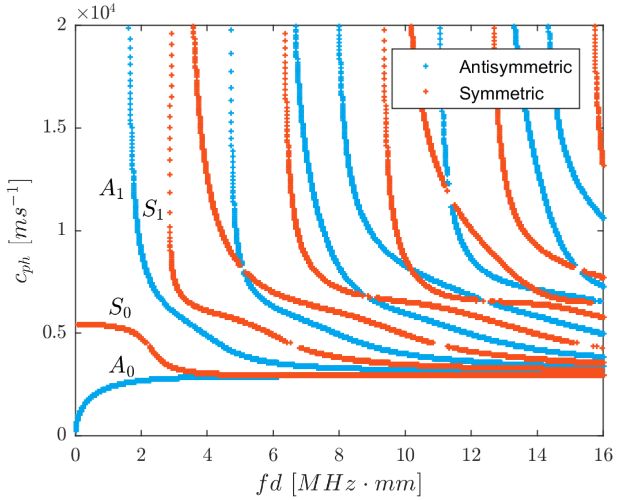

Figure 2.6: Antisymmetric (+) and symmetric (*) Lamb waves for an isotropic aluminum plate as calculated using the Lamb equations. Properties of the plate: $\rho = 2700\,\mathrm{kg\,m^{-3}}$, $E = 70.75\,\mathrm{GPa}$, $\nu = 0.34$.

the fact that it looks very elegant and rather simple, it is impossible to solve equation (2.69) analytically. Therefore, numerical methods have to be applied in order to find the corresponding solution for given angular frequency ω. The description of some of the most popular numerical algorithms is given in [38] and we will further expand on that in section 3.1.

Once the solutions, pairs $\omega - k$, have been found by numerically solving (2.69), the displacement profiles of the antisymmetric modes can be examined. Yet, coefficients A, D from (2.59) have to be first determined. Since the determinant of the matrix on the LHS of (2.68) is zero, the relation between A and D is determined from the second equation in (2.68), which yields the following ratio

$$\frac{A}{D} = \frac{2k\beta \sin \beta h}{(k^2 - \beta^2) \sin \alpha h}. \tag{2.70}$$

As a result, an infinite number of A, D pairs, scaled by a linear constant, satisfy the previous equation. To qualitatively visualize the displacements in a thin aluminum plate, we will use the following values:

$$A = 2k\beta \sin \beta h, \tag{2.71}$$

$$D = (k^2 - \beta^2) \sin \alpha h. \tag{2.72}$$

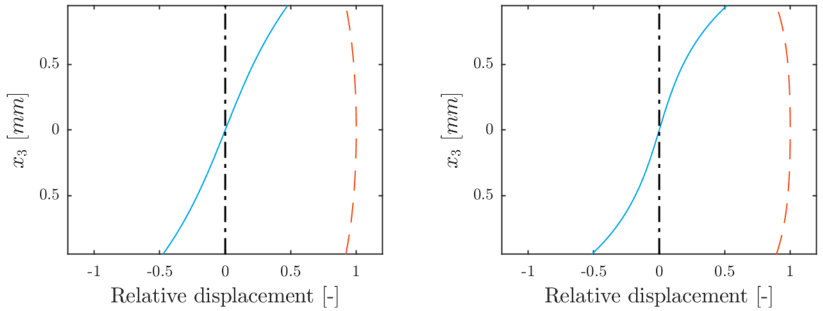

(a) $fd = 0.5\,\mathrm{MHz}\cdot\mathrm{mm}$ (b) $fd = 1\,\mathrm{MHz}\cdot\mathrm{mm}$

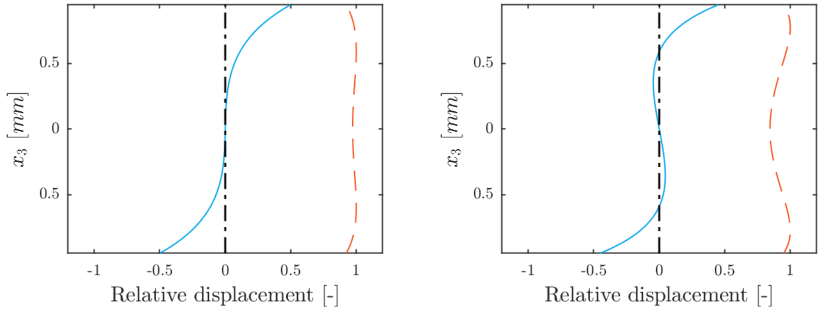

(c) $fd = 2\,\mathrm{MHz}\cdot\mathrm{mm}$ (d) $fd = 3\,\mathrm{MHz}\cdot\mathrm{mm}$

Figure 2.7: Displacement components, u_2 (–) and u_3 (–), for the first antisymmetric mode A_0 at different fd. Aluminum plate - $\rho = 2700\,\mathrm{kg}\,\mathrm{m}^{-3}$, $E = 70.75\,\mathrm{GPa}$, $\nu = 0.34$.

The typical displacement profiles for the fundamental antisymmetric mode A_0 in $2\,\mathrm{mm}$ thick aluminum plate are depicted in Fig. 2.7. It is apparent that the displacement profiles are strongly dependent on the fd product. The out-of-plane displacement u_3 has a constant sign and remains fairly constant throughout the thickness d of the plate. On the other hand, the in-plane displacement profile changes rather rapidly, reaching maximal values at the upper and lower surfaces of the sample. With increasing fd product, the in-plane displacement exhibits more direction changes and has generally a steeper profile.

Fig. 2.8 illustrates the behaviour of the A_1 mode. It is obvious that the behaviour has now become significantly more complex compared to a regular longitudinal

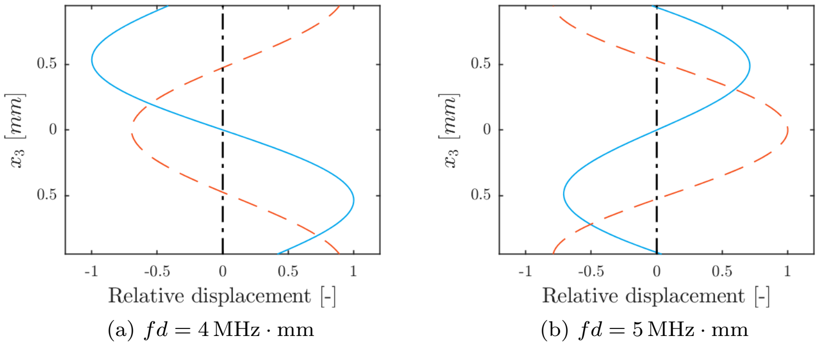

(a) $fd = 4\,\mathrm{MHz} \cdot \mathrm{mm}$ (b) $fd = 5\,\mathrm{MHz} \cdot \mathrm{mm}$

Figure 2.8: Displacement components, u_2 (—) and u_3 (—), for the second antisymmetric mode A_1 at different fd. Aluminum plate - $\rho = 2700\,\mathrm{kg\,m^{-3}}$, $E = 70.75\,\mathrm{GPa}$, $\nu = 0.34$.

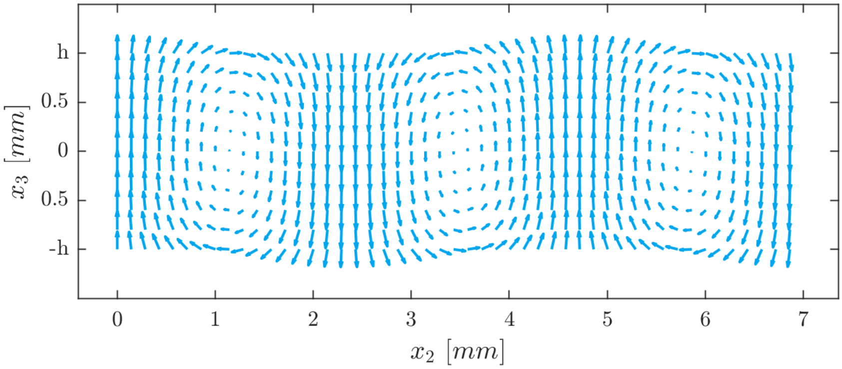

Figure 2.9: Particle displacement field for A_0 mode at $1\,\mathrm{MHz} \cdot \mathrm{mm}$.

or shear wave.

Since the full solution for the fundamental antisymmetric A_0 mode is known, the particle motion throughout the cross section of the sample can be easily visualized using a *quiver* plot (see Fig. 2.9). As can be seen in the figure, the particle displacement is an intriguing combination of time harmonic in-plane and out-of-plane motion.

Symmetric modes

The dispersion equation for the symmetric modes can be derived in exactly the same way as for the antisymmetric case. The only difference is that the symmetric part of (2.57) (containing only cosines) is now considered. Repeating exactly the same steps as for the antisymmetric case, the general solutions for the field variables are given by:

$$\phi = B\cos\alpha x_3, \tag{2.73}$$

$$\psi_1 = C\sin\beta x_3, \tag{2.74}$$

$$\tau_{23} = i\mu[-2kB\alpha\sin\alpha x_3 + (k^2-\beta^2)C\sin\beta x_3], \tag{2.75}$$

$$\tau_{33} = \mu[(k^2-\beta^2)B\cos\alpha x_3 + 2k\beta C\cos\beta x_3] \tag{2.76}$$

$$u_2 = i[kB\cos\alpha x_3 + \beta C\cos\beta x_3] \tag{2.77}$$

$$u_3 = -\alpha B\sin\alpha x_3 + kC\sin\beta x_3 \tag{2.78}$$

Next, we apply the similar (free) boundary conditions at the top and bottom of the plate and we arrive at the characteristic system

$$\begin{bmatrix} -2k\alpha\sin\alpha h & (k^2-\beta^2)\sin\beta h \\ (k^2-\beta^2)\cos\alpha h & 2k\beta\sin\beta h \end{bmatrix}\begin{bmatrix} B \\ C \end{bmatrix} = \begin{bmatrix} 0 \\ 0 \end{bmatrix}. \tag{2.79}$$

Hence, the dispersion relation for the symmetric modes can be established as

$$\frac{\tan\beta h}{\tan\alpha h} = -\frac{4k^2\alpha\beta}{(k^2-\beta^2)^2}. \tag{2.80}$$

Furthermore, the parameters B, C are given by the ratio

$$\frac{B}{C} = \frac{-2k\beta\cos\beta h}{(k^2-\beta^2)\cos\alpha h}. \tag{2.81}$$

Symmetric modes are usually denoted by S_n, where $n = 0, 1, ..,$ defines the order of the mode counting from the lowest one (S_0) (see Fig. 2.6). If we look at the shape of a typical first symmetric mode for thin aluminum plate, we see that due to the antisymmetric shape u_3, the upper and lower faces move in the opposite direction. The thickness of the plate is virtually increasing and decreasing due to the antisymmetric shape of u_3.

The particle motion for the fundamental symmetric mode can be again easily visualized using a *quiver* plot (see Fig. 2.12). The resulting particle motion is very much different from its antisymmetric counterpart.

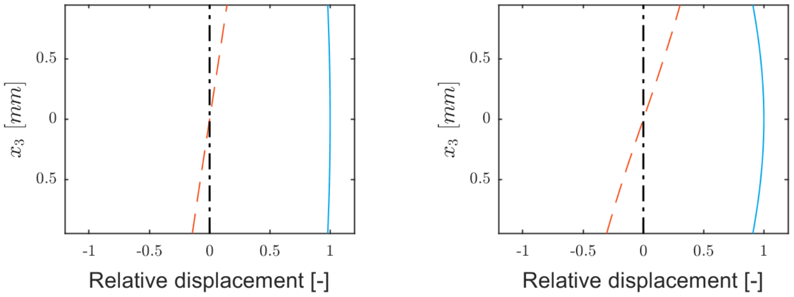

(a) $fd = 0.5\,\mathrm{MHz} \cdot \mathrm{mm}$ (b) $fd = 1\,\mathrm{MHz} \cdot \mathrm{mm}$

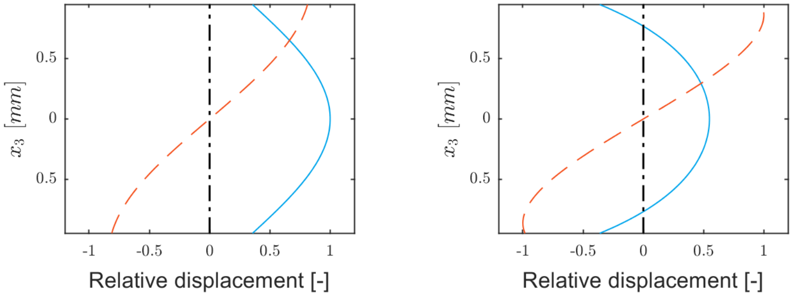

(c) $fd = 2\,\mathrm{MHz} \cdot \mathrm{mm}$ (d) $fd = 3\,\mathrm{MHz} \cdot \mathrm{mm}$

Figure 2.10: Displacement components, u_2 (—) and u_3 (—), for first symmetric mode S_0 at different fd.

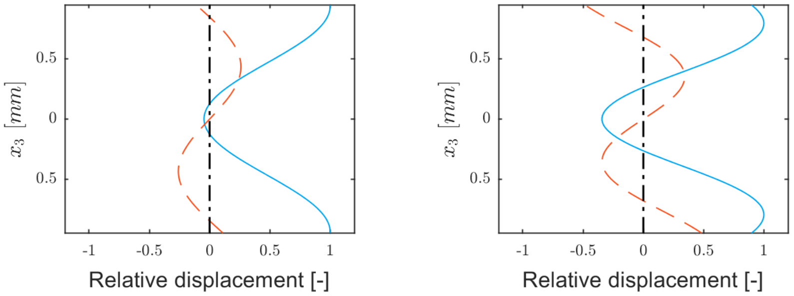

(a) $fd = 4\,\mathrm{MHz} \cdot \mathrm{mm}$ (b) $fd = 5\,\mathrm{MHz} \cdot \mathrm{mm}$

Figure 2.11: Displacement components, u_2 (—) and u_3 (—), for the second symmetric mode S_1 at different fd.

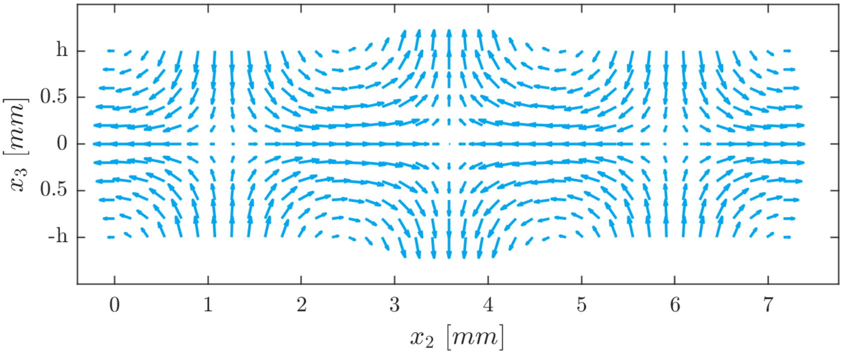

Figure 2.12: Displacement field for S_0 mode at $2\,\mathrm{MHz} \cdot \mathrm{mm}$.

It is apparent, especially from Fig. 2.8 and Fig. 2.11, why so little research has been done using higher order Lamb modes ($n > 1$), both antisymmetric and symmetric. At higher frequencies, the displacement profiles are becoming increasingly complex and what is even more complicated, they change suddenly with the varying fd product. Hence, the interaction of the propagating higher order modes with defects is difficult to predict. Moreover, it is very likely that in higher fd range, additional modes will be excited together with A_1 and S_1. The incoming signals can be then extremely difficult to analyze.

2.3.2 Shear horizontal waves in isotropic free plates

Another type of guided waves that can propagate in a free plate, and complement the traditional Lamb waves, is the SH wave. The SH waves are also a solution of the same set of equations defined in (2.25), but with a different set of constraints. Again, the solution for SH waves can be obtained using the method of potentials or the theory of partial waves or directly from the equation of motion [8, 26]. This time we start from the latter.

In order to derive the SH waves as a solution of the free plate problem governed by (2.25), we assume that the particle motion is in-plane only. We will suppose that the displacement is localized purely in the $x_1 - x_2$ plane and the resulting wave propagates in the direction of axis x_2. Hence, the two remaining displacement components are zero

$$u_2 = 0, \qquad u_3 = 0. \tag{2.82}$$

In case of SH, we do not need to assume the plane strain conditions and the problem can be solved generally. In the next step we assume a solution for the only remaining nonzero displacement component in the form of

$$u_1(x_2, x_3, t) = f(x_3) \exp\left[i(kx_2 - \omega t)\right], \tag{2.83}$$

where $f(x_3)$ is the through-thickness displacement profile. It is obvious that the particle motion is perpendicular to the propagation direction (shear) and to the axis x_3 (horizontal). The reduced form of (2.25) for the case of SH consequently reads

$$\frac{\partial^2 u_1}{\partial x_2^2} + \frac{\partial^2 u_1}{\partial x_3^2} = \frac{1}{c_2^2}\frac{\partial^2 u_1}{\partial t^2} \tag{2.84}$$

Since the equation contains only u_1, we can easily substitute it with (2.83) to obtain the ODE

$$\frac{d^2 f}{dx_3^2} + \beta^2 f = 0, \tag{2.85}$$

where

$$\beta^2 = \left(\frac{\omega^2}{c_2^2} - k^2\right). \tag{2.86}$$

The solution to this ODE is well-known. Since it is completely similar to the solution for Lamb waves, we can directly note down its final form

$$u_1(x_2, x_3, t) = \left[A \sin \beta x_3 + B \cos \beta x_3\right] \exp\left[i(kx_2 - \omega t)\right]. \tag{2.87}$$

In analogy with previous derivations, the displacement u_1 can again be separated in symmetric and antisymmetric parts with respect to the plane $x_3 = 0$ as follows:

$$u_1^S = B \cos \beta x_3 \exp\left[i(kx_2 - \omega t)\right], \tag{2.88}$$

$$u_1^A = A \sin \beta x_3 \exp\left[i(kx_2 - \omega t)\right], \tag{2.89}$$

where u_1^S and u_1^A stands for the symmetric and antisymmetric displacement components, respectively. The stress field of the SH waves has to satisfy the free boundary conditions as defined in (2.67). However, the problem can be simplified by the fact that τ_{23} and τ_{33} are both identically zero

$$\tau_{33} = \lambda\Big(\frac{\partial u_1}{\partial x_1} + \frac{\partial u_2}{\partial x_2} + \frac{\partial u_3}{\partial x_3}\Big) + 2\mu\frac{\partial u_3}{\partial x_3} \equiv 0, \tag{2.90}$$

$$\tau_{23} = \mu\Big(\frac{\partial u_2}{\partial x_3} + \frac{\partial u_3}{\partial x_2}\Big) \equiv 0. \tag{2.91}$$

Therefore, the only nonzero stress field component is

$$\tau_{13} = 2\mu\varepsilon_{13} = \mu\Big(\frac{\partial u_1}{\partial x_3} + \frac{\partial u_3}{\partial x_1}\Big) = \mu\frac{\partial u_1}{\partial x_3}. \tag{2.92}$$

Hence, only one single BC remains to be fulfilled

$$\tau_{13}(\pm h) = \mu\frac{\partial u_1}{\partial x_3}(\pm h) = 0 \tag{2.93}$$

which leads to

$$-\mu B\beta \sin\beta h \exp\left[i(kx_2 - \omega t)\right] = 0, \tag{2.94}$$

$$\mu A\beta \cos\beta h \exp\left[i(kx_2 - \omega t)\right] = 0, \tag{2.95}$$

for symmetric and antisymmetric modes, respectively. Dropping the exponential term and constants in (2.94) and (2.95) results in two fundamental dispersion relation

$$\sin\beta h = 0, \tag{2.96}$$

$$\cos\beta h = 0, \tag{2.97}$$

for symmetric and antisymmetric SH waves, respectively. These are simple transcendental equations with an infinite number of solutions. In contrast to Lamb waves, the SH dispersion curves can be easily solved analytically. Moreover, a common expression

$$\beta h = \frac{n\pi}{2} \tag{2.98}$$

satisfies both equations depending on the value of n. If n is even ($n \in \{0, 2, 4, \dots\}$), then the solution corresponds to the symmetric SH modes. Similarly, if n is odd ($n \in \{1, 3, 5, \dots\}$) the solution represents antisymmetric SH modes. The resulting dispersion curves are plotted in Fig. 2.13. The closed

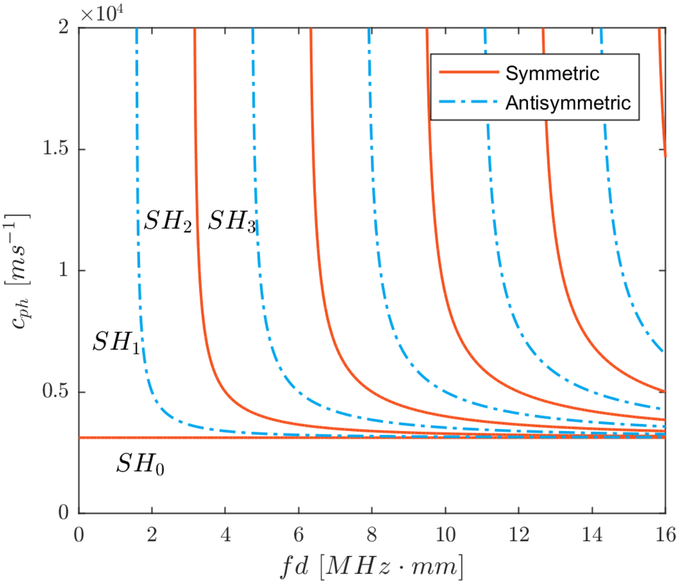

Figure 2.13: Dispersion curves for SH waves in a thin isotropic aluminum plate - $\rho = 2700\,\mathrm{kg\,m^{-3}}$, $E = 70.75\,\mathrm{GPa}$, $\nu = 0.34$.

form solution relating the phase velocity c_{ph} and fd can be derived from (2.86) as

$$\frac{\omega^2}{c_2^2} - \frac{\omega^2}{c_{ph}^2} = \left(\frac{n\pi}{d}\right)^2, \tag{2.99}$$

$$c_{ph}(fd) = 2c_2\left(\frac{fd}{\sqrt{4(fd)^2 - n^2c_2^2)}}\right). \tag{2.100}$$

It follows that the fundamental SH_0 mode ($n = 0$) is a special case that represents a nondispersive mode. However, all other modes are behaving dispersively.

Substituting (2.98) in (2.94) and (2.95) yields the final expressions for u_1

$$u_1^S(x_2, x_3, t) = B\cos\left(n\pi\frac{x_3}{d}\right)\exp\left[i(kx_2 - \omega t)\right] \tag{2.101}$$

$$u_1^A(x_2, x_3, t) = A\sin\left(n\pi\frac{x_3}{d}\right)\exp\left[i(kx_2 - \omega t)\right]. \tag{2.102}$$

As can be easily seen, the displacement profiles are independent of k and ω. Hence, the displacement profile remains constant for a specified SH mode for all

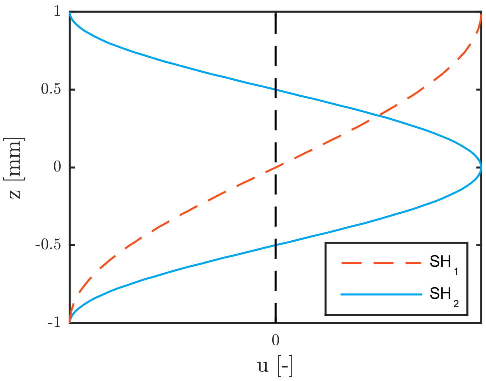

Figure 2.14: Displacement profiles for the SH_1 (antisymmetric) and SH_2 (symmetric) modes.

values of fd which is a fundamental difference between the SH waves and Lamb waves. Moreover, the displacement profiles are simple harmonic functions (see Fig. 2.14).

2.3.3 Lamb waves in anisotropic free plates

The problem of wave propagation in a free isotropic plate was discussed in section 2.3.1. A solution using the Helmholtz potentials was presented and applied in order to separate the problem in two independent parts - longitudinal and shear waves. However, the approach fails to solve the same problem for anisotropic solids, because the decomposition will not separate (2.33) in two parts [8]. Therefore, we have to follow a different solution method that will be more suitable for this problem. Nowadays, the most universally accepted solution is the *partial wave technique* described for anisotropic plate-like medium, for example by Rose [8], Nayfeh [27], Auld [36], Solie and Auld [39].

Let us first assume an anisotropic free plate as depicted in Fig. 2.15. The fundamental idea of the partial wave technique states that a guided wave mode that propagates in the plate can be constructed using upward and downward going partial waves [40]. Each of the partial waves has the following form

$$u_i = \alpha_i \exp\left[ik_1(x_1 + l_3 x_3)\right] \exp\left[-i\omega t\right], \tag{2.103}$$

where

$$k_1 = k = \frac{\omega}{c_{ph}} \tag{2.104}$$

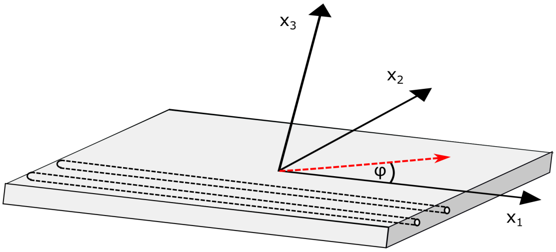

Figure 2.15: Anisotropic free plate with the coordinate axis.

is the x-component of the wave vector

$$\vec{k} = k \begin{bmatrix} 1 \\ 0 \\ l_3 \end{bmatrix} = k\vec{n} \tag{2.105}$$

and $l_3 = \frac{k_3}{k}$ defines the ratio between the wave vector components k_1 and k_3. It is further assumed that the wavevector is localized in the $x_1 - x_3$ plane and, therefore, $k_2 = 0$. Each of the partial waves has the same k, which is a requirement induced by the Snell's law for anisotropic media. It also means, that all partial waves move in the x_1-direction with the same phase velocity c_{ph} forming one particular guided wave mode. In order to calculate the polarization vectors $\vec{\alpha}$ of the partial waves and the wavenumber ratio l_3 for each partial wave, the assumed form of the solution (2.103) has to be substituted in the Christoffel equation (2.38). This results in

$$(C_{ijkl}k_jk_k - \rho\omega^2\delta_{il})\alpha_l = 0, \tag{2.106}$$

which represents a system of three linear equations for three components of polarization vector $\vec{\alpha}$. The unknown components in the system are the ratios l_3 and the polarization vectors. In contrast, the angular frequency ω and k are assumed to be known. As a matter of fact, the common factor k is often eliminated and ω is then simply replaced by $c_{ph} = \frac{\omega}{k}$. Since we assume that c_{ph} is known, the fundamental theorem of linear algebra requires the determinant of the system to vanish

$$\det[C_{ijkl}n_jn_k - \rho c_{ph}^2\delta_{il}] = 0 \tag{2.107}$$

in order to get a non-trivial solution for $\vec{\alpha}$. If we assume the case of general anisotropy, the determinant of the system results in a sixth order polynomial in l_3

$$p_6l_3^6 + p_5l_3^5 + p_4l_3^4 + p_3l_3^3 + p_2l_3^2 + p_1l_3^1 + p_0 = 0. \tag{2.108}$$

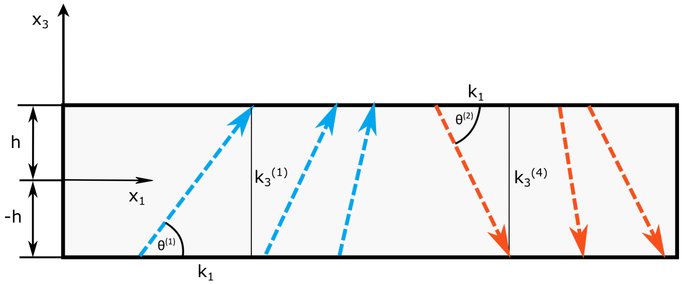

Figure 2.16: Partial wave technique - three upward going waves (-) and down going waves (- -). $k_3^{(i)}$ and k_1 denote the x_3 and x_1 component of the wave vector, respectively.

The polynomial has generally six roots representing a total of six different partial waves. However, if the material belongs to a symmetry class higher than *monoclinic*, the even powers of l_3 are zero ($p_1 = p_3 = p_5 = 0$) and the polynomial is reduced to

$$p_6 l_3^6 + p_4 l_3^4 + p_2 l_3^2 + p_0 = 0. \tag{2.109}$$

This simplification is valid for orthotropic materials as well as for transversely isotropic media. Moreover, for transversely isotropic symmetry, the polynomial can be further factorized into two independent parts, being the SH wave and a combination of pressure and SV waves described by a bi-quadratic polynomial. In this case, the analytical solution of the polynomial equation can be found. For orthotropic materials, it is clear that (2.109) has generally six roots ($l_3^{(i)}$, $i = 1, 2, \ldots, 6$) grouped in three pairs that are related to each other as follows:

$$l_3^{(4)} = -l_3^{(1)}, \quad l_3^{(5)} = -l_3^{(2)}, \quad l_3^{(6)} = -l_3^{(3)}. \tag{2.110}$$

Hence, the partial waves with negative l_3 represent the three upward going partial waves. The three downward going ones have positive l_3 (see Fig. 2.16). The grouped pairs of partial waves have the same k_3 facing in opposite directions.

The six polarization vectors $\vec{\alpha}^{(i)}$ can be subsequently calculated after substituting $l_3^{(i)}$ one-by-one into (2.106). Now that the six partial waves are determined, they are ready to be combined in order to satisfy the boundary conditions on the upper and lower interface of the plate. For the sake of simplicity, the time harmonic term from (2.103) will be omitted further in the derivation. It will vanish anyway thanks to the form of the zero boundary conditions the solution has to satisfy. A weighted sum of the partial waves is defined as

$$u_i = \sum_{j=1}^{6} A_j \alpha_i^{(j)} \exp[(ik(x_1 + l_3^{(j)} x_3)], \tag{2.111}$$

where the weights A_j represent the amplitudes of the particular partial waves. The assumed solution has to satisfy the free BC for the upper ($x_3 = h$) and lower ($x_3 = -h$) interfaces. The traction-free BC require the stress components to be zero

$$\tau_{13} = 0, \quad \tau_{23} = 0, \quad \tau_{33} = 0. \tag{2.112}$$

for $x_3 = \pm h = \frac{d}{2}$. These conditions can be expressed using the constitutive relation and the definition of linearized strain as

$$\tau_{33} = C_{33kl} u_{k,l} = 0 \tag{2.113}$$

$$\tau_{23} = C_{23kl} u_{k,l} = 0 \tag{2.114}$$

$$\tau_{13} = C_{13kl} u_{k,l} = 0, \tag{2.115}$$

where the sum of partial waves as in equation (2.111) should be substituted for u_i. This results in a homogeneous system of six equations, three for $x_3 = h$ and three for $x_3 = -h$, with unknown amplitudes $\vec{A}$.

$$\mathbf{B}\vec{A} = 0, \tag{2.116}$$

where

$$\vec{A} = [A_1, A_2, A_3, A_4, A_5, A_6]^T. \tag{2.117}$$

The system has a non-trivial solution, when its determinant is equal to zero. Having denoted the matrix of the system (2.113) as $\mathbf{B}$, this can be expressed as

$$\det[\mathbf{B}] = 0, \tag{2.118}$$

where the determinant of $\mathbf{B}(\rho, kd, \omega, C_{ijkl})$ is in fact an implicit function that relates together k and ω. The dispersion curves $k = k(\omega)$ can be constructed by finding k for different values of the input angular frequency ω.

Unfortunately, the above described partial wave technique can only be used to solve the problem analytically in a few special cases, such as for isotropic or transversely isotropic material aligned with the principal material axis. In all other cases, a root finding method or another numerical approach have to be used in order to solve (2.118) [41]. Moreover, special attention has to be paid if the propagation direction φ is not aligned with the principal material axis. An effective way to solve this case is to rotate the stiffness matrix accordingly using the Bond rotation matrix. Doing so, the demonstrated approach can be applied without loss of generality and without the need to redefine the wave vector $\vec{k}$. It is, however, important to keep in mind that the rotated stiffness matrix can have a complicated structure with an increased number of non-zero off-diagonal elements.

2.4 Conclusion

In this chapter, the fundamental theory of elastodynamics was presented. Special attention was paid to the theory of bulk and guided wave propagation in isotropic as well as anisotropic media because of their importance for ultrasonic NDT. Moreover, the typical dispersion behaviour of GW was described and the basic solution strategies, such as Helmholtz decomposition and partial wave technique, were demonstrated on simple isotropic and orthotropic samples. The next section will expand on this topic and discuss the dispersion analysis of layered anisotropic plates.

Chapter 3

Guided Waves in Anisotropic and Multilayered Materials

In the previous section, we have discussed the theory of guided wave propagation in homogeneous isotropic and anisotropic plates. However, the constantly growing usage of composite and functionally graded materials requires also a detailed knowledge and understanding of the guided wave propagation in anisotropic layered media. To properly assess the associated complexity, we look first at a geometry of the CFRP plate, which is a typical example of an anisotropic layered composite. As shown in Fig. 3.1, a composite plate consists of several layers with different main fibre orientations. Therefore, the mechanical behaviour of each layer is different and it depends on the mechanical properties of the fibres and the matrix as well as on the orientation of the fibres with respect to the direction of loading or wave propagation. As a bulk medium, however, the composite exhibits mechanical properties that are driven by a homogenized stiffness matrix [42].

It is clear that the problem of GW propagation becomes increasingly more complex due to the inherent anisotropy of composites. A simple analytical approach, such as the *Helmholtz potential decomposition*, cannot be simply used anymore. Fortunately, other solution strategies are at hand and were already successfully applied to solve the problem of wave propagation in a thin layered anisotropic plate (layer). Among these, the most popular and widespread methods are the partial wave *matrix techniques*, *state vector methods* based on a polynomial approximation and the Semi-Analytical Finite Elements (SAFE) method.

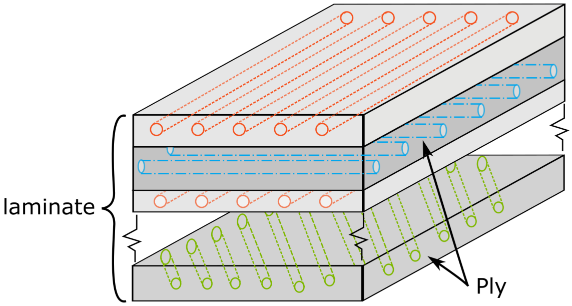

Figure 3.1: Example of a layered composite plate.

Although all the above mentioned methods can be used to analyze the propagation of the guided waves for most general cases, this section will focus solely on using them to obtain the dispersion curves of layered materials.

Dispersion curves provide the necessary tool for proper analysis and determination of the most suitable ultrasonic excitation frequency range in a view of successful imaging of defects. Using dispersion curves, one can easily identify the number and the type of the propagating GW modes and assess their properties, such as phase velocity c_{ph} and group velocity c_g. Moreover, displacement and stress profiles in the thickness direction of the plate can be calculated for each propagating mode identified in the dispersion curves. Hence, the information from the dispersion curves and the associated mode shapes can be beneficially used to fine-tune the excitation in order to provide the best possible detection/imaging results.

The aforementioned numerical methods will be shortly described in the first section of this chapter. Their application to the dispersion analysis of the actual test samples will be demonstrated and the calculated dispersion curves will be presented and discussed. Moreover, signal processing techniques that can be used to extract dispersion curves from experimental data will be carefully described in the second part of the section. Experimentally obtained dispersion curves will be presented and subsequently compared to the predictions that were obtained using the numerical solution methods.

3.1 Numerical methods

3.1.1 Matrix techniques

Matrix methods have dominated the numerical modelling of layered structures in last few decades thanks to their intuitiveness and straightforward numerical implementation. The matrix methods are formulated using the same partial wave technique as was described in section 2.3.3 ([18, 26]). They combine the fundamental solution for an anisotropic plate/layer with the appropriate boundary conditions at the inner interfaces between subsequent layers and at the outer surfaces of the sample.

The first pioneering works, which made use of the partial wave technique to calculate the wave propagation in layered flat plates, were carried out in 1950s by Thomson [43] and Haskell [44]. They introduced and used the Transfer Matrix Technique (TMT) or, as it is sometimes referred to, the *propagator matrix* technique. The transfer matrix relates the displacements and stresses on one interface of the layer to the corresponding values on the other (opposite) interface. Hence, the displacement and stress components can be propagated through the plate, layer-by-layer using the matrix multiplication of the transfer matrices [45]. The work of Thomson and Haskell was soon adopted by other researchers and the TMT became very frequented, especially in the field of geophysics [46]. However, several drawbacks were identified soon after. The most critical one was the *large fd problem* that caused numerical instability of the solution for the case of thick plates and high excitation frequencies. Several improvements were introduced and implemented to address the stability issues, e.g. the Delta operator [47] and the stiffness matrix method [48].

An alternative method for the problem, the Global Matrix Technique (GMT), was proposed in 1964 by Knopoff [49]. In this method, a large sparse *global* matrix is assembled and solved instead of the transfer matrix multiplication. The matrix contains a block of four equations for every interface of the sample [50]. Although the *global matrix* can be quite large and its solution computationally expensive, the GMT does not suffer from inherent numerical instability. Application of the matrix techniques to a layered anisotropic medium was further studied by Nayfeh [27, 51], Hosten [52] and Rokhlin and Wang [53]. Finally, an in-depth historical review of matrix methods was published in 1995 by Lowe [38], who also co-developed *Disperse*, a general simulation tool for guided wave analysis [54]. It is also worth noticing that, in case of dispersion curves analysis, both the TMT and the GMT techniques lead to a general root-finding problem. This last step of the solution proved to be numerically quite cumbersome [55].

Matrix methods for analysis of the guided wave propagation in layered media consist of three main steps. First, the wave propagation in a particular layer of the system is described using the partial wave approach as presented in section 2.3.3. The fundamental idea is that the fields (τ_{ij}, u_i) can be expressed as a superposition of six elastic bulk waves (three upward and three downward) propagating in a particular layer. The procedure of obtaining these six partial waves has already been described in detail in section 2.3.3. Since the subsequent layers in the medium can have significantly different elastic properties, the assembly procedure has to be repeated layer-per-layer.

As a second step, the continuity of displacement and traction is enforced on the interface between two adjacent layers. In our case, we assume that the layers are solid and that the plate is free and surrounded by vacuum. Therefore, the upper and lower interfaces can be considered traction-free.

Third, a *transfer* or a *global* matrix describing the propagation of guided waves is constructed using the previously defined BC and partial waves. In order to obtain the dispersion curves of the system, the determinant of the matrix is set to zero and numerical methods are applied to extract the roots of the resulting equation [56].

There are several general assumptions that have to be obeyed when calculating the dispersion curves:

- The assumed wavelengths of the propagating waves have to be sufficiently long to consider each ply as a homogeneous anisotropic/orthotropic medium [57].
- The layered plate is assumed to be unbounded (infinite) in the plane parallel to the plies.
- Body forces are negligible: $f_i = 0$.

Transfer Matrix technique

Transfer matrix is the most illustrative solution of a problem posed by the partial wave technique. In general, it connects displacements and stresses at the top surface of the plate to the corresponding displacements and stresses at the bottom surface via a transfer matrix. The transfer matrix is constructed layer-per-layer and uses the continuity of the displacement and stress at the interface between two adjacent layers.

Let us assume a flat layered plate with n_l layers and a total thickness of $h_{tot} = \sum_{i=1}^{n_l} h_i$ (see Fig. 3.2). Let us further assume that the layers are all orthotropic and that there is a guided wave propagating through the layer i in the x_1 direction. It has been shown in section 2.3.3 that a guided wave can be generally described as the sum of six partial waves, three upward going and three downward going ones. Additionally, the stress tensor components can be expressed in the same way. The displacement components as well as the stress components can then be gathered in a single vector

$$\vec{T} = [u_1, u_2, u_3, \tau_{13}, \tau_{23}, \tau_{33}]^T \tag{3.1}$$

and expressed using the *field matrix* $\mathbf{D}$ as

$$\vec{T} = \mathbf{D}\vec{A}, \tag{3.2}$$

where $\vec{A}$, as defined in (2.117), stores the amplitudes of the partial waves [58]. The elements of $\mathbf{D}$ are dependent on the position x_3, angular frequency ω, propagation direction φ and elastic properties of the given layer [38]. Nonetheless, equation (3.2) holds true for every point in the layer. Therefore, the partial wave amplitudes in layer i can be obtained from (3.2) if the displacements and stresses at the upper interface of layer i are known. This can be done by simple matrix inversion

$$\vec{A} = \mathbf{D}_{iu}^{-1}\vec{T}_u^i, \tag{3.3}$$

where the index i denotes the number of the layer, and index u stands for the upper interface. The displacement and stress fields can now be described using the newly obtained vector $\vec{A}$. The displacements and stresses at the lower interface of layer i (denoted with a subscript l) are given by

$$\vec{T}_l^i = \mathbf{D}_{il}\vec{A} = \mathbf{D}_{il}\mathbf{D}_{iu}^{-1}\vec{T}_u^i. \tag{3.4}$$

The previous equation relates the displacement and stress on the upper interface to the corresponding values on the lower interface of the ith layer. Hence, the vector of partial wave amplitudes $\vec{A}$ has been eliminated and the upper and lower interfaces of the ith layer are connected via the *transfer (propagator) matrix*

$$\mathbf{L_i} = \mathbf{D}_{il}\mathbf{D}_{iu}^{-1}, \tag{3.5}$$

where $\mathbf{L_i}$ depends also on the plate thickness. This procedure can be repeated for all remaining layers in the medium yielding

$$\vec{T}_l^{n_l} = \mathbf{L}\vec{T}_u^1, \tag{3.6}$$

where the total transfer matrix $\mathbf{L}$ is given by the matrix multiplication of the particular layer transfer matrices

$$\mathbf{L} = \mathbf{L_1}\mathbf{L_2}\ldots\mathbf{L_{n_l}}. \tag{3.7}$$

If the halfspaces surrounding the layered plate are considered to be vacuum, all traction on both interfaces has to vanish ($\tau_{13} = \tau_{23} = \tau_{33} = 0$). This reduces a 6x6 matrix in (3.6) to a 3x3 submatrix that only contains the lower-left elements from $\mathbf{L}$.

$$\begin{bmatrix} 0 \\ 0 \\ 0 \end{bmatrix} = \begin{bmatrix} L_{41} & L_{42} & L_{43} \\ L_{51} & L_{52} & L_{53} \\ L_{61} & L_{62} & L_{63} \end{bmatrix} \begin{bmatrix} u_1 \\ u_2 \\ u_3 \end{bmatrix} \tag{3.8}$$

In order to get a non-trivial solution of (3.8), the determinant of the submatrix has to be zero. This leads to an implicit characteristic equation that is dependent both on ω as well as on k. The common solution strategy for this problem includes fixing one of the parameters and invoking a robust root finding algorithm to locate the roots of the characteristic equation. The roots of the equation represent points in (ω,k) space that eventually form the different dispersion curves. This root finding procedure has to be repeated multiple times to construct a section of the dispersion curves with reasonable precision in the (ω,k) space.

Lowe [38] gave an excellent overview of the numerical challenges and pitfalls of the TMT as well as the optimal solution approach. One inherent and very significant drawback of the TMT, as was mentioned in the introduction, is the *large fd problem* that causes numerical instability of the solution at high frequency-thickness products. To address this issue, another solution approach was adopted, the GMT.

Global Matrix technique

The *global matrix technique* adopts a different approach to the same problem as TMT. Instead of propagating the solution from layer to layer via the continuity expressed by the BC and reducing the problem to a system of six equations, GMT assembles one large matrix with all equations that are provided by the boundary conditions of each interface. Thus, if there are n_l layers, the global matrix consists of $6(n_l - 1)$ equations.

Firstly, the starting point is similar to the TMT. The wave field in layer i is described using the field matrix $\mathbf{D}$, and the components of $\vec{T}$ are continuous over the interface between the ith and $(i + 1)$th layer. Therefore, the difference between the two vectors has to be $\vec{0}$ for each of the internal interfaces

$$\vec{T}_u^{i+1} - \vec{T}_l^{i} = \mathbf{D}_{i+1u}\vec{A}_{i+1} - \mathbf{D}_{il}\vec{A}_i = \vec{0}, \tag{3.9}$$

where the substitution for $\vec{T}$ was made using (3.2). Equation (3.9) can be rewritten in a more convenient form as

$$\begin{bmatrix} \mathbf{D}_{i+1u} & -\mathbf{D}_{il} \end{bmatrix} \begin{bmatrix} \vec{A}_{i+1} \\ \vec{A}_i \end{bmatrix} = \vec{0}, \tag{3.10}$$

where both field matrices are of dimension 6x6 and the partial wave amplitudes are 6x1 vectors.

Secondly, a similar construction can be applied to all internal interfaces of the media. The uppermost ($i = 1$) and the lowermost interfaces ($i = n_l$) pose the only exception to the rule, because they require traction to vanish and do not put any constraints on displacement. Therefore, the first and the last blocks of the GMT have to be altered to contain only three equations for three stress components [58]. As an example, the typical *global matrix* for a plate with three layers would take the form of

$$\underbrace{\begin{bmatrix} \mathbf{D}_{1u} & \mathbf{0} & \mathbf{0} \\ \mathbf{D}_{1l} & \mathbf{D}_{2u} & \mathbf{0} \\ \mathbf{0} & \mathbf{D}_{2l} & \mathbf{D}_{3u} \\ \mathbf{0} & \mathbf{0} & \mathbf{D}_{3l} \end{bmatrix}}_{global\ matrix\ \mathbf{G}} \begin{bmatrix} \vec{A}_1 \\ \vec{A}_2 \\ \vec{A}_3 \end{bmatrix} = \vec{0}, \tag{3.11}$$

where the matrices in the first and last row are 3x6 and the rest of the elements in the global matrix are 6x6 matrices. This explains the total of $6(n_l - 1)$ equations of the system.

Finally, the determinant of the global matrix $\mathbf{G}$ has to be zero for a non-trivial solution of (3.11) to exist. This leads again to a characteristic equation and a root finding problem. Since the particular elements of $\mathbf{G}$ depend both on ω as well as on k the same procedure as in TMT to find the roots of the characteristic equation can be applied. An excellent account on the root finding approaches suitable for this task in given by Lowe [38] and Pavlakovic et al. [54]. The team around Lowe and Pavlakovic also wrote a widely adopted and appreciated commercial simulation tool for guided wave analysis, which is called *Disperse* [54].

The great advantage of GMT is its unconditional numerical stability even for the large *fd* values. It is also considerably straightforward to assemble the global matrix $\mathbf{G}$. Although it may become very large for media with a large number of layers, it is not of a significant concern thanks to the highly efficient numerical packages for linear algebra (LAPACK, MKL).

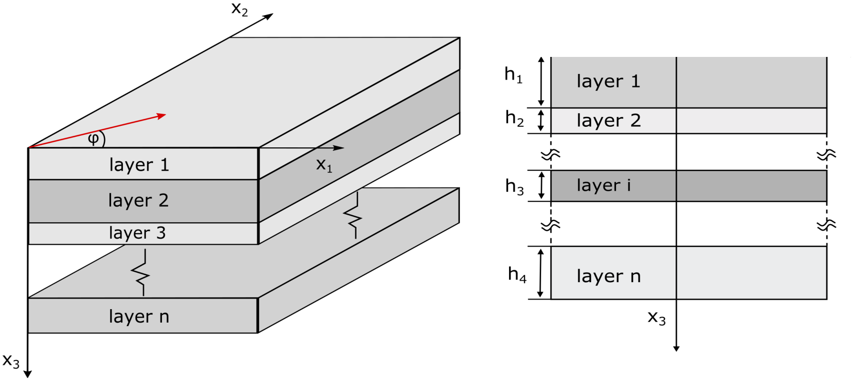

(a) Layer stacking and propagation direction (b) Cross-section of the layered plate

Figure 3.2: Geometry of the layered plate, state vector approach.

3.1.2 State vector and Legendre polynomial approximation

Another approach that can be used to calculate dispersion curves and the corresponding displacement profiles of guided waves in layered anisotropic plates is based on the *state vector* (Stroh's) formalism and polynomial expansion [59]. This approach is very attractive, because it replaces the rather cumbersome root-finding algorithms used in the matrix techniques with a generalized eigenvalue problem [60, 61]. As a result, both dispersion curves as well as the displacement profiles can be obtained at the same time as eigenvalues and eigenvectors of the system [62, 63]. Moreover, the solution for the Lamb waves and for the SH waves are obtained simultaneously without the need to reformulate the problem. The method also performs well for large fd compared to the matrix techniques [64]. Lefebvre et al. [65], Wang et al. [66] and Chen [67] adopted the approach to solve the complex problem of guided wave propagation in piezo-electro-elastic plates and functionally graded materials. More recently, Bou Matar et al. [68] and Quintanilla et al. [69] demonstrated the applicability of a Legendre polynomial approximation to state vector analysis for the layered anisotropic plates.

Similarly to the partial wave technique, we want to solve a system defined by the constitutive relation and the equation of motion

$$\tau_{ij} = C_{ijkl}\varepsilon_{kl}, \qquad \frac{\partial \tau_{ij}}{\partial x_j} = \rho \frac{\partial^2 u_i}{\partial t^2}, \tag{3.12}$$

and appropriate boundary conditions. The geometry of the layered plate is similar to the one introduced in Fig. 3.2. However, the present solution differs significantly from the partial wave technique presented in previous section which assumes the solution to be a linear combination of partial waves propagating in the layer. The Stroh's formalism makes use of the state vector $\vec{T}$, in which it gathers the field components that are continuous over the interfaces of the elastic layered system. In our case, the state vector is defined as

$$\vec{T} = [u_1, u_2, u_3, \tau_{13}, \tau_{23}, \tau_{33}]^T \tag{3.13}$$

and the governing equation it has to satisfy is given by

$$\frac{\partial \vec{T}}{\partial x_3} = \mathbf{A}\vec{T}, \tag{3.14}$$

where $\mathbf{A}$ is the *state (Stroh) matrix* given for elasto-piezoelectric medium by Fahmy and Adler [70]. Since the inspected system is purely linear elastic, the original matrix $\mathbf{A}$ can be further simplified by omitting the piezoelectric variables. The matrix can then be written as

$$\mathbf{A} = k^2 \begin{bmatrix} 0 & 0 \\ \mathbf{A}_1' & 0 \end{bmatrix} + jk \begin{bmatrix} \mathbf{A}_1' & 0 \\ & \mathbf{A}_2'' \end{bmatrix} + \begin{bmatrix} 0 & \mathbf{\Gamma}_{33}^{-1} \\ -\rho\omega^2 \mathbf{I_p} & 0 \end{bmatrix}, \tag{3.15}$$

where k is the wavenumber, j the imaginary unit, ω the angular frequency and ρ the density of the material. Matrix $\mathbf{I_p}$ is the 3x3 diagonal unit matrix. Matrices $\mathbf{A}_1'$, $\mathbf{A}_2'$, $\mathbf{A}_2''$ and $\mathbf{\Gamma}_{ij}$ are somewhat more complicated and are further defined in Appendix C. Details about the derivation of $\mathbf{A}$ can be found, for example in [59].

For an anisotropic layer, the matrices are functions of material properties as well as the propagation angle φ (see Fig. 3.2). If the principal directions of layers are not aligned with the global coordinate system (as depicted in Fig. 3.2), then the stiffness matrix $\mathbf{C}$ has to be rotated using the Bond formalism (see Appendix B and [70]).

The displacement vector $\boldsymbol{u}$ and the generalized stress vector $\vec{\tau} = [\tau_{13}, \tau_{23}, \tau_{33}]^T$ are linked together via

$$\vec{\tau} = \mathbf{\Gamma_{33}} \frac{\partial \vec{u}}{\partial x_3} - jk\mathbf{A_{BC}}, \tag{3.16}$$

where $\mathbf{A}_{BC} = \mathbf{\Gamma}_{33}\mathbf{A}_2' = \mathbf{\Gamma}_{31}\cos\varphi + \mathbf{\Gamma}_{32}\sin\varphi$. The generalized stress vector can be replaced in (3.14) using (3.16) which in turn leads to a quadratic equation in k^2 for the displacement vector

$$(k^2\mathbf{A}_1 + \mathbf{A}_2)\vec{u} + jk\mathbf{B}\frac{\partial \vec{u}}{\partial z} + \mathbf{C}\frac{\partial^2 \vec{u}}{\partial z^2} = 0, \tag{3.17}$$

where $\mathbf{A}_1 = \mathbf{A}_1' + \mathbf{A}_2''$, $\mathbf{B} = \mathbf{\Gamma}_{33}\mathbf{A}_2' + \mathbf{A}_2''\mathbf{\Gamma}_{33}$, $\mathbf{A}_2 = -\rho\omega^2\mathbf{I_p}$ and $\mathbf{C} = -\mathbf{\Gamma_{33}}$ [65]. This equation has to be solved to obtain the dispersion curves and displacement profiles for the inspected multilayered system. Additional normalization of the coefficients (density ρ and stiffness matrix $\mathbf{C}$) in the equation was proposed to improve the numerical stability of the solution [68]. The equation (3.17) can be solved using a polynomial approximation of $\boldsymbol{u}$.

Legendre polynomial approximation

An elegant way to numerically solve the system of equations given by (3.17) is to use a spectral method with polynomial basis. If we assume that the displacement is a continuous 'well-behaved' function, it can be projected on a set of orthogonal polynomials [71, 72]. There are several suitable types of polynomials to choose from. For example, Quintanilla et al. [69] selected the Chebyschev polynomials to calculate the dispersion curves in elastic anisotropic multilayered plate. Alternatively, Lefébvre et al. [65] and Bou Matar et al. [68] selected Legendre polynomials as an orthogonal basis. Both approaches are highly comparable without any significant advantages or disadvantages over each other. For the current study and analysis, we will work with Legendre polynomials as an orthogonal base.

The polynomial approximation of $\boldsymbol{u}$ is done per layer. Since the Legendre polynomials are defined on the interval $\langle -1, 1\rangle$, the local coordinates of the ith layer have to be transformed using

$$r = \frac{2}{h_i}(z - z_m^i), \tag{3.18}$$

where h_i is the thickness and z_m^i the absolute z-coordinate of the center of the ith layer. Hence, the coordinates for each layer are linearly rescaled to $\langle -1, 1\rangle$. This per-layer transformation ($\langle -1, 1\rangle$) provides significant benefits over the global one ($\langle 0, \sum h_i\rangle$) as will be demonstrated further in the section.

Using the transformed coordinate r, the Legendre polynomial approximation of order N_i in the ith layer can be written as

$$\vec{u}^i = \sum_{l=0}^{N_i - 1} \vec{U}_l^i P_l(r), \tag{3.19}$$

where $P_l(r)$ is the Legendre polynomial of degree l evaluated at r and $\vec{U}_l^i$ is a vector of scalar coefficients for a given polynomial order l and layer i. The displacement in (3.17) is then replaced with its approximation (3.19) forming a system of algebraic equations. Details of the derivation and resulting formulas can be found in Appendix C.

The transformed boundary conditions have to be added to complete the system. First, the displacement has to be continuous over the inner interfaces (layer-to-layer). Second, the stress components normal to the interface between the ith and the $(i + 1)$th layer have to be continuous. Third, the normal stress components have to be zero on the lower and upper outer interfaces of the plate. All equations and boundary conditions are given in detail in [68].

After the introduction of the necessary BC, the system yields the form of a generalized eigenvalue problem

$$\begin{bmatrix} \overline{\mathbf{F}}_1 & -\mathbf{I} \\ -\overline{\mathbf{H}}_1 & \mathbf{0} \end{bmatrix} Z = \frac{j}{\beta} \begin{bmatrix} \overline{\mathbf{G}}_1 & 0 \\ 0 & 1 \end{bmatrix} Z, \tag{3.20}$$

where $Z = \begin{bmatrix} X & j\beta\overline{\mathbf{H}}_1 X \end{bmatrix}$, $X = \begin{bmatrix} \overline{u}^1, & \dots & ,\overline{u}^{N_c} \end{bmatrix}$ and $\overline{u}^k$ is further defined as $\overline{u}^k = \begin{bmatrix} \overline{U}_0^k & ,\dots & ,\overline{U}_{N_i-1}^k \end{bmatrix}$. Eigenvalues of this problem represent the dispersion curves of the different modes, whereas the eigenvectors provide the coefficients $\vec{U}_l^i$ for the polynomial approximation. Next, the eigenvectors can be used to obtain the displacement and stress profiles in the cross section of the layered plate. Solving the system for a particular frequency results in the points on the dispersion curves for that frequency. Subsequently, a desired frequency band can be scanned and the procedure has to be repeated multiple times.

The solution obtained from the generalized eigenvalue problem yields at the same time the dispersion curves for the Lamb waves as well as for the SH waves. Bou Matar et al. [68] and Lancellotti and Orta [73] investigated the convergence of the method. As expected, there is a trade-off between speed and degree of polynomial approximation, and the frequency and order of the guided wave mode (see Fig. 3.3). The higher the Lamb/SH mode order, the higher has to be the degree of Legendre polynomial approximation. The approximation converges rapidly to the desired mode shape if the number of polynomials is at least equal to $N_i = P\pi$, where P is the number of complete oscillations of the mode in the through-thickness direction [74].

3.1.3 Semi-analytical finite element method

Lastly, the SAFE will be shortly discussed and demonstrated. The method was first introduced by Lagasse [75] to calculate the eigenmodes in acoustic waveguides of arbitrary cross section. It is a finite element method that restricts the analysis of the three-dimensional problem to two spatial dimensions only. The displacement and particle motion along the direction of wave propagation is described purely analytically using harmonic functions. Therefore, the finite element discretization is carried out only on a two-dimensional cross section which results in significant reduction in complexity and solution time [57, 76, 77].

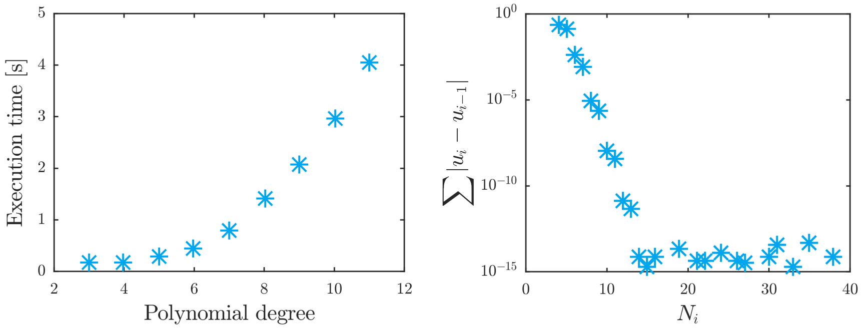

(a) (b)

Figure 3.3: a) Execution time and b) convergence of the state vector method as a function of the polynomial degree approximation for the Legendre based state vector method. Dispersion curves for a CFRP plate, 0-150 kHz, mean values of 8 repetitions.

SAFE is highly valued for its versatility, virtually any shape of the waveguide can be analyzed, and straightforward approach, where all the necessary output values, such group velocity c_g, phase velocity c_{ph} and mode shapes (displacement profile) can be calculated simultaneously. Moreover, the method is inherently designed to account for viscoelastic material and damped waveguides. Therefore, it can be used to analyze not only the attenuation of the propagating guided waves, but also the leaky Lamb modes [78]. Since the derivation of the SAFE method is rather lengthy and out-of-scope of the present thesis, it will not be presented here. Basically, it follows a standard Finite Element Method (FEM) construction via the variation of the Hamiltonian of the system. Details about the method can be found in [77].

Bocchini et al. have developed a versatile, MATLAB©-based implementation of the SAFE method called Graphical User Interface for Guided Ultrasonic Waves (GUIGUW) [79]. It uses quadratic one-dimensional finite elements to calculate the dispersion curves for plate-like structures. The discretization of the cross-section is done automatically to ensure a proper convergence of the method, and is based on a criterium suggested by Galan and Abascal in [80]. However, it can also be manually overridden to further improve accuracy of the displacement profiles. If the dispersion curves in the present thesis are marked as being calculated using SAFE, the GUIGUW was used to calculate them.

3.1.4 Numerical results

The analysis of the dispersion curves is crucial to understand the guided wave propagation in complicated layered systems. Therefore, we will demonstrate the previously introduced numerical algorithms on layered CFRP samples that were part of the ALAMSA and SARISTU EU funded projects. Subsequently, we will use this insight to select the most suitable modes and excitation frequency ranges to be used for damage detection and imaging.

Two different methods, Legendre polynomial approach and SAFE, were used to calculate the dispersion curves and displacement profiles for the aforementioned samples. The basic implementation of the former method was provided by prof. Bou Matar in the framework of the ALAMSA project and adjusted by the author. The program can calculate also the geometric dispersion and can be used to create the angular profiles. The SAFE calculations were carried out using the GUIGUW program. The results, performance and execution times of both methods will be compared.

SARISTU CFRP plate

The first sample to be investigated is a 400 x 400 mm CFRP plate consisting of 11 separate layers/plies. The stacking sequence of the laminate as well as the ply type is given in Tab. 3.1. The laminated composite can be concisely described using the standard stacking sequence notation as $[(0,45)_2,90,-45,0,-45,90,0]_T$ [81]. The elastic properties of the plies are collected in Tab. 3.2. The total thickness of the plate is approximately $h_{tot} = 4.3\,\text{mm}$. Due to the (non-symmetric) stacking sequence, the global (homogenized) in-plane elastic properties of the plate cannot be assumed simply quasi-isotropic. Isotropy can only be assumed for the lowest antisymmetric mode A_0 as can be seen in Fig. 3.4.

The angular profile of c_{ph} is nearly circular. The phase velocities of the other modes, such as S_0 and SH_0, are strongly dependent on the direction of propagation. This is a fact that has to be kept in mind during the damage location or beam-forming imaging of laminated plates with non-symmetric lay-ups.

The numerically calculated predictions of the dispersion curves for the plate are depicted in Fig. 3.5 and Fig. 3.6. The complementary group velocity dispersion curves are displayed in Fig. 3.7. The interesting features that can be inferred from the figures and that are relevant for NDT applications are:

- The dispersion of the A_0 and S_0 modes is low between 50-200 kHz.

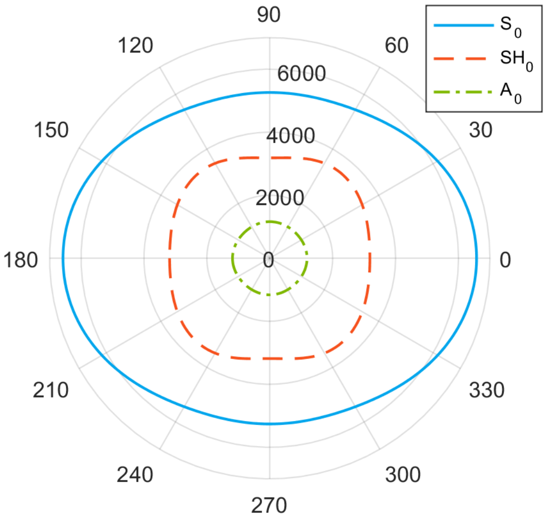

Figure 3.4: Angular dependence of the phase velocity at 50 kHz, SARISTU plate.

Ply #	**Type**	φ [°]	h_i [mm]	ρ [kg m^{-3}]
1	5 Harness	0	0.480	1770
2	NCF Biaxial	45	0.480	1790
3	Uniweave	0	0.480	1790
4	NCF Biaxial	45	0.480	1790
5	NCF Biaxial	0	0.480	1790
6	NCF Biaxial	90	0.480	1790
7	NCF Biaxial	-45	0.480	1790
8	Uniweave	0	0.480	1790
9	NCF Biaxial	-45	0.480	1790
10	5 Harness	90	0.480	1770
11	Glass Ply	0	0.127	2500

Table 3.1: Stacking sequence of the SARISTU CFRP plate. Angle φ defines the in-plane rotation of the ply with respect ot the global coordinate system (first Euler angle). The total thickness of the plate is 4.3 mm.

- The phase velocities c_{ph} and group velocities c_g of both modes are well separated.

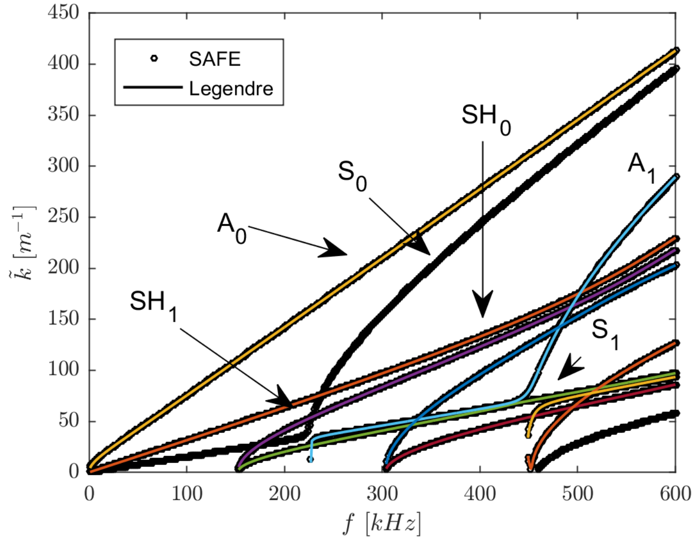

Figure 3.5: $\tilde{k} - f$ dispersion curves for the SARISTU plate. The angle of propagation is $\varphi = 0°$.

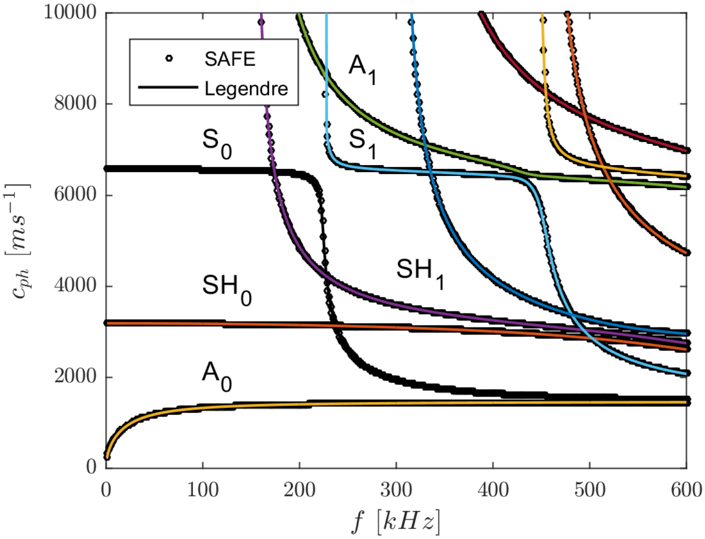

Figure 3.6: Phase velocity dispersion curves for the SARISTU plate. Angle of propagation $\varphi = 0°$.

Lamina	E_1	E_2	E_3	G_{12}	G_{23}	G_{13}	ν_{12}	ν_{13}	ν_{23}
		[GPa]			[GPa]			[-]	
5 Harness	65.0	65.0	8.8	3.6	3.6	3.6	0.041	0.041	0.041
NCF Biaxial	81.0	81.0	8.8	4.1	4.1	4.1	0.033	0.033	0.033
Uniweave	152.0	8.8	8.8	4.1	4.1	4.1	0.018	0.018	0.310
Glass ply	70.0	70.0	70.0	28.7	28.7	28.7	0.220	0.220	0.220

Table 3.2: Engineering elastic properties in the principal directions for the CFRP layered plate.

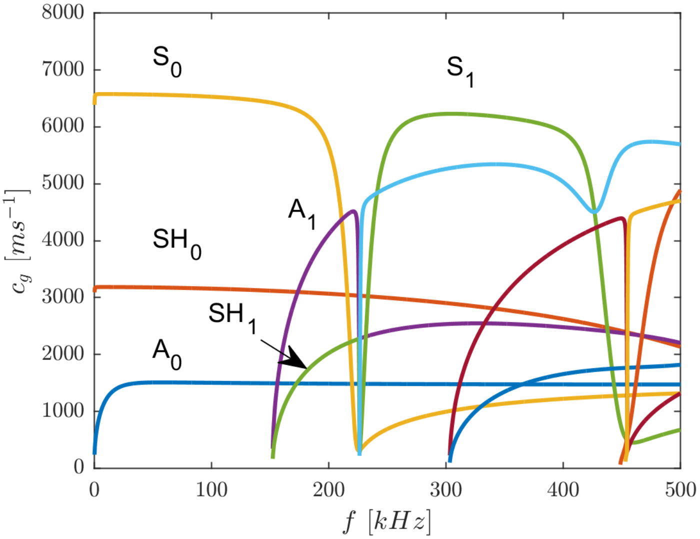

Figure 3.7: Group velocity dispersion curves for the SARISTU plate. Angle of propagation $\varphi = 0°$.

Moreover, as shown in Fig. 3.8, the displacement profiles in the low frequency range (≤ 200 kHz) do not change abruptly. Hence, the behaviour of the guided waves and their possible interaction with defects can be easily predicted. The complicated displacement profiles as well as the increasing number of propagating modes render frequencies above 300 kHz unsuitable for NDT applications.

Fig. 3.4 depicts the full angular profile of the first three modes at 50 kHz. Unlike the A_0, the other two modes exhibit a strong dependency on the angle of propagation. Therefore, this information has to be included in the potential imaging algorithm.

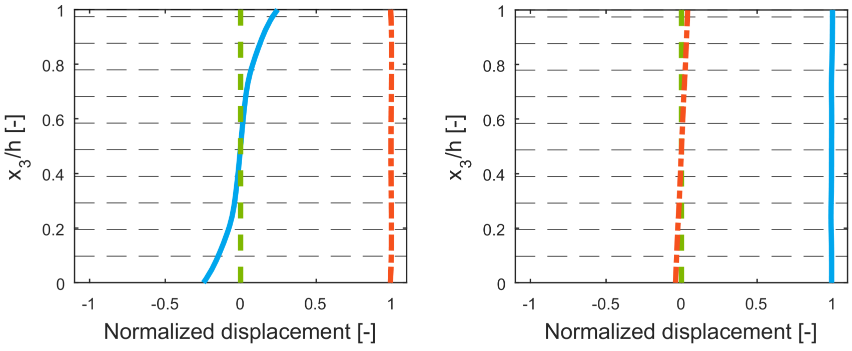

(a) A_0 (b) S_0

Figure 3.8: Mode shapes at 50 kHz. The separate layers are highlighted with the dashed line. Displacement components: u_1 (−), u_2 (−) and u_3 (−).

ALAMSA CFRP plate

A second demonstration sample is a strongly quasi-isotropic CFRP laminate (see Fig. 3.9) provided by the project partner Israel Aerospace Industries (IAI) in the framework of the ALAMSA project. The laminate consists of 12 similar layers with a total thickness of 4.3 mm. The lay-up of the sample is symmetric: $[(0/45)_3]_S$ as described using the standard stacking sequence notation [20]. The available elastic properties of the lamina are: $E_1 = E_2 = E_3 = 57\,\mathrm{GPa}$, $G_{12} = G_{23} = G_{13} = 3.9\,\mathrm{GPa}$, $\nu_{21} = \nu_{23} = \nu_{13} = 0.07$, $\rho = 1490\,\mathrm{kg\,m^{-3}}$.

Due to its symmetric lay-up, the laminate exhibits an in-plane isotropy. This fact can be easily seen in Fig. 3.10, where the angular profiles of the numerically calculated phase velocity c_{ph} clearly form nearly perfect circles. Hence, the laminate will mechanically behave in the same manner as an isotropic solid. The same then holds true for the guided wave propagation. If the wavelength of the propagating GW is larger than a typical thickness of the layer, a simple Rayleigh-Lamb solution for a homogeneous isotropic solid can be used to predict the displacement profiles and dispersion curves. Under these circumstances, the elastic properties are equal to the homogenized elastic properties of the laminate.

Furthermore, it is apparent from Fig. 3.11 and Fig. 3.12 that the quasi-nondispersive region is located in the frequency range between 25-400 kHz. In this frequency band, the A_0 and S_0 modes are well separated and their velocities are nearly constant. The calculated displacement profiles for both

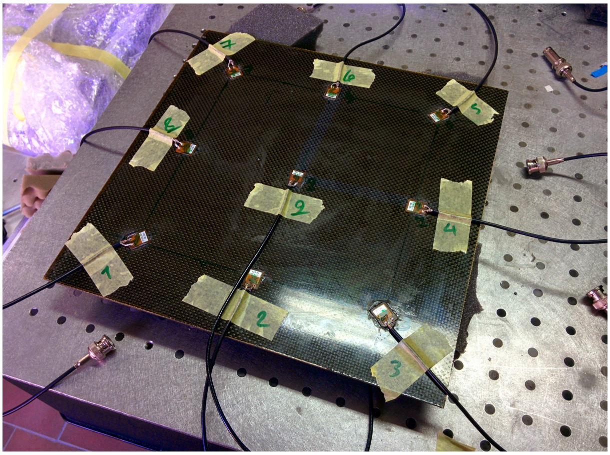

Figure 3.9: Image of the ALAMSA CFRP sample.

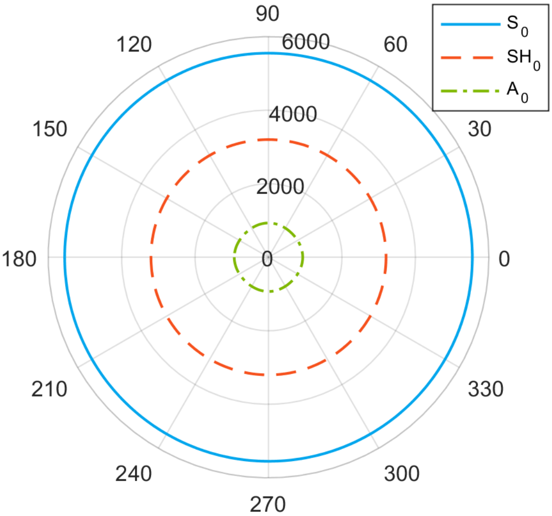

Figure 3.10: Angular dependence of the phase velocity for ALAMSA plate.

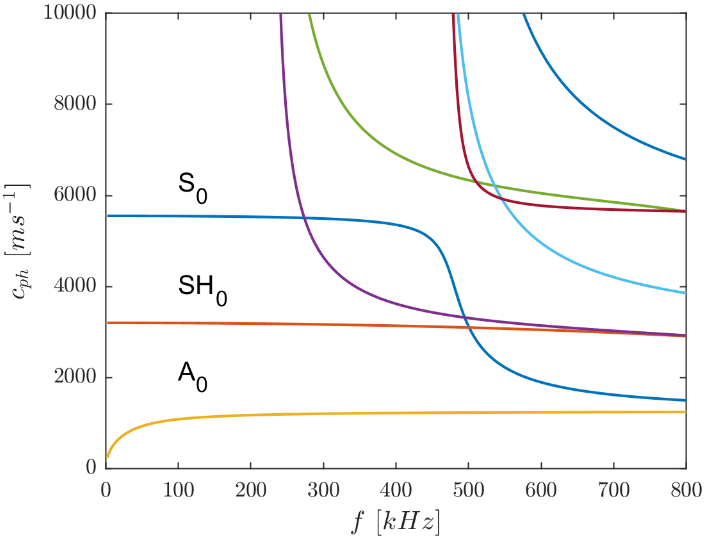

Figure 3.11: Phase velocity dispersion curves for the ALAMSA plate. Angle of propagation $\varphi = 0°$.

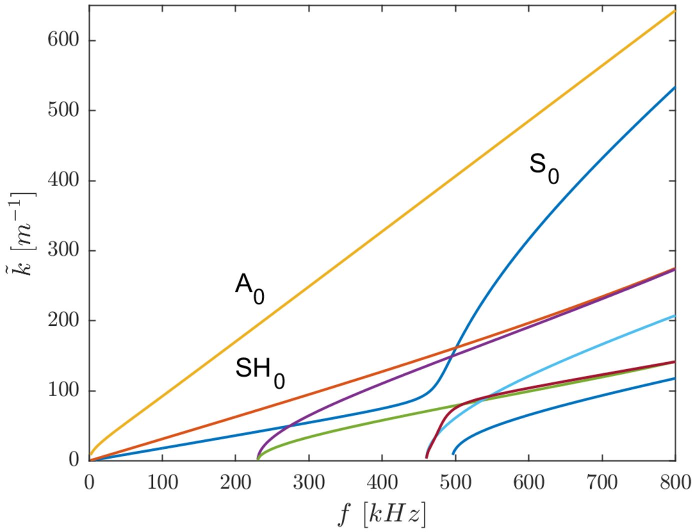

Figure 3.12: $\tilde{k}-f$ dispersion curves for the ALAMSA plate. Angle of propagation $\varphi = 0°$.

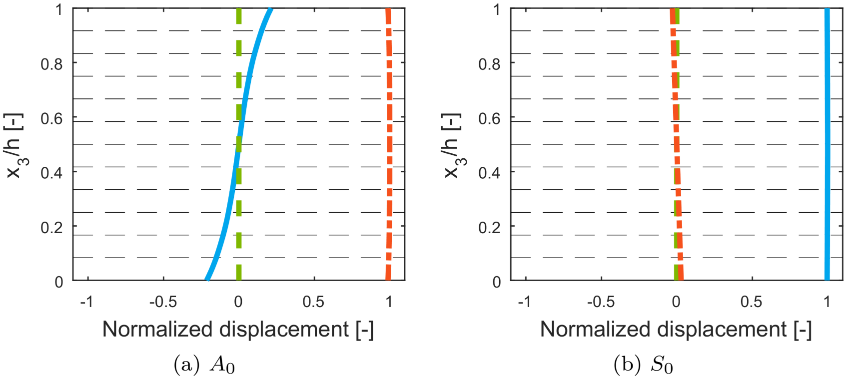

(a) A_0 (b) S_0

Figure 3.13: Mode shapes at 50 kHz. The individual layers are represented by the dashed line. Displacement components: u_1 (—), u_2 (—) and u_3 (—).

modes at 50 kHz are illustrated in Fig. 3.13. The displacement profiles of the sample for these two antisymmetric and symmetric modes are comparable to the SARISTU sample. The only differences are the group and phase velocities.

Comparison

The two previously presented methods provide quantitatively similar results. The difference between the two solutions is minimal as can be seen from Fig. 3.6. Significant differences, however, exist in the performance of implementation of the two methods. The SAFE method is significantly faster than the polynomial expansion method. The computation time necessary for solving the dispersion curves for frequency between 0 - 600 kHz was: 158 s for polynomial approximation and only 22 s for SAFE using the number of nodes recommended by the application (1 node per layer). The order of Legendre polynomial approximation was chosen to be $N_i = 4$ based on the criteria cited by Bou Matar in [68]. The number of approximation points/nodes in the thickness direction was similar for both methods.

The significant difference in the execution performance between the two methods can be partially caused by the implementation. The Legendre polynomial approximation is implemented in MATLAB© using the parallel computing toolbox. The source code of the algorithm is open and publicly available. However, it is not fully optimised and vectorized, and there is certainly room for speed optimization. On the other hand, the GUIGUW has been optimized by its author. It is also implemented in MATLAB$^{©}$, but the source code is not publicly available. A clear disadvantage of the GUIGUW is its lower flexibility. It is complicated to create plots with angular profiles of wave velocity or slowness due to the fact that the program is compiled as a standalone executable.

3.2 Experimental determination of dispersion curves

The most common simulation methods for calculating and predicting the dispersion curves in anisotropic layered system have been presented in the previous section, and illustrated on a typical layered composites. As a second step, experimental validation of the these algorithms has to be performed, because the available information about the inspected samples is often not complete.

Till a few decades ago, the experimental measurement of the actual dispersion curves posed a difficult challenge. It required either a large, equidistantly spaced, collinear array of transducers oriented normally to the propagating wavefront or a translational assembly that allowed for scanning of the receiving transducer [82]. Both approaches were cumbersome and rather difficult to implement, especially if the specimen under inspection was anisotropic and the dispersion characteristics had to be measured in several directions. Fortunately, the arrival of Laser Doppler Vibrometry (LDV) enabled an easy scanning and acquisition of signals in multiple points on a line under any given angle of propagation or on a grid.

In this section, the typical application of LDV to measure the dispersion in thin layered anisotropic plate will be discussed. In addition, two different processing algorithms will be described and their outputs will be compared. Since both algorithms use the same set of input signals, we will first describe the data acquisition procedure.

3.2.1 Data acquisition using laser vibrometer

Let us assume that the dispersion curves for a layered structure are to be determined experimentally. The following procedure is then usually observed. First, the propagation direction that is defined by the in-plane angle φ has to be selected. The angle φ is measured with reference to the positive part of the x_1 axis. If the orientation of principal axes x_1 and x_2 is not known beforehand, it can be selected arbitrarily and aligned afterwards using the simulated data. The second step depends on the reflective properties of the

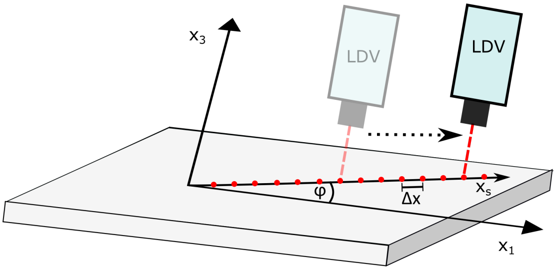

Figure 3.14: LDV data acquisition procedure for experimental dispersion analysis.

surface of the inspected sample. Since a single point-single beam LDV detects only the out-of-plane motion, the sample has to backscatter (reflect) enough light to successfully detect the propagating waves. If the reflection from the surface is poor, a retro-reflective tape or paint has to be applied on the line defined by the angle φ to improve the backscattering properties. The third and the last step of the measurement procedure is to scan the LDV[1] laser beam along the defined line with a selected spatial step Δx while sending out a signal from a source (DuraAct©) located along the considered line. The excitation signal was generated by a NI PXI-5142[2], routed via the Falco WMA-320[3] to the PZT, and digitized by a NI PXI-5122[4] digitizer.

The measurement procedure results in a spatially encoded set of signals $u_3(x,t)$ (equivalent to a B-scan), where x stands for the axial spatial coordinate in the direction of angle φ (see Fig. 3.15). The acquired signals can be arranged into a $n_s \times m$ matrix, where m stands for the number of signals (measurement points) and n_s denotes the number of samples in each signal. It is assumed that n_s remains constant during the acquisition.

It is obvious that a single point-single beam LDV can only be used to measure dispersion curves of modes with non-zero normal displacement component u_3 at the scanned surface. Hence, SH modes cannot be captured reliably by this technique. On the other hand, the vast majority of the antisymmetric and symmetric modes has a non-zero u_3 and, therefore, can be readily detected using a single point-single beam LDV.

---

[1] Polytec OFV-3001 LDV coupled OF-303 sensor head with velocity and displacement decoders

[2] AWG, 1-channel, 100 Ms/s, 14-bit

[3] Power amplifier, gain 25x

[4] Digitizer, 2-channels, 100 MHz, 14-bit

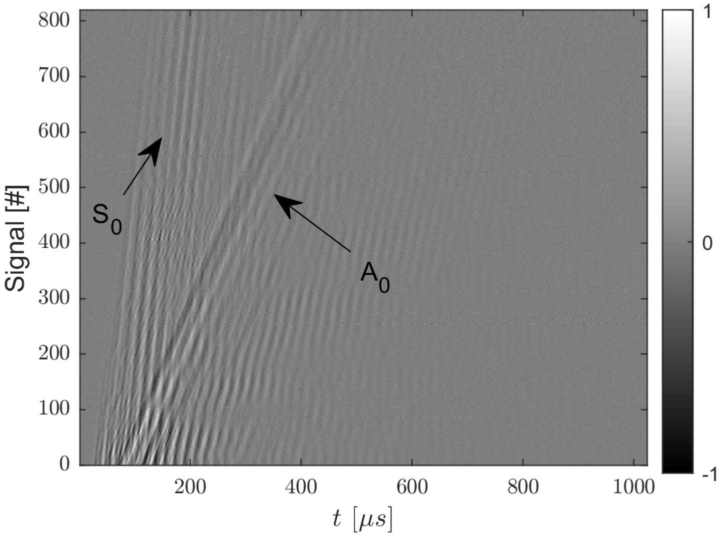

Figure 3.15: Typical time profiles (B-scan) as recorded by the LDV for a dispersion analysis.

3.2.2 2D Fourier Transform

Once the measurement is completed, the acquired data can be further processed. The method of analysis is based on two dimensional (2D) Fourier transform and was first proposed in 1990 by Alleyne and Cawley [83]. Since then, it has been constantly applied for numerical as well as experimental dispersion data analysis [84, 85]. Fourier transform applications are not restricted to 1D spatial dispersion analysis only. For example, the 2D Fast Fourier Transform (FFT) method also forms the backbone of the local wavenumber imaging technique that identifies the presence of damage using localized changes in the magnitude of the wave vector $\vec{k}$ [86]. For the analysis, the wave vector is calculated by 2D FFT extended to two spatial dimensions/plane ($\vec{k} = [k_x, k_y]$) [87]. In order to appreciate its value, it is important to introduce the method itself and describe its strong and weak spots.

Let us assume that a set of m signals $u_3(x,t)$ each consisting of n_s samples was acquired using the procedure described in the previous section. The spacing between the two measurement points is Δx and the scan line constitutes an angle φ with respect to the principal axis of the plate (denoted x_1). The dispersion

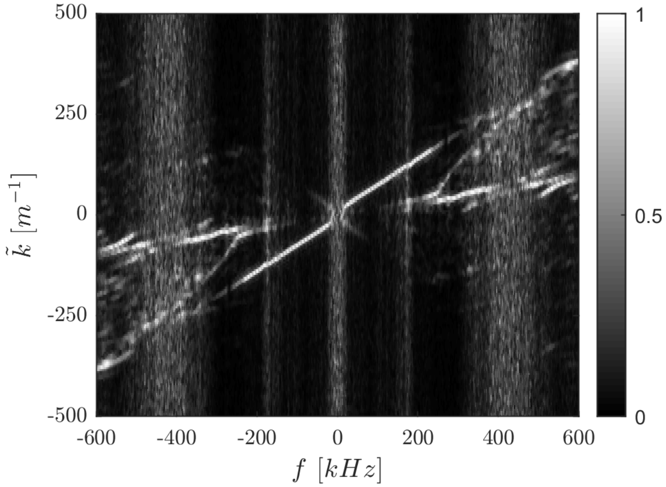

Figure 3.16: Intensity image converted to $\tilde{k} - f$ space using the 2D FFT (SARISTU plate).

curves can then be obtained using the two-dimensional Fourier transform

$$U_3(k,f) = \int_{-\infty}^{+\infty}\int_{-\infty}^{+\infty} u_3(x,t)e^{-i(kx+\omega t)}dxdt. \tag{3.21}$$

As a result of this transformation, the acquired signals are projected from the space-time $(x-t)$ domain to the wavenumber-angular frequency $(k-\omega)$ domain. Subsequently, the angular quantities are then often converted to the spatial and temporal frequencies $(\tilde{k},\ f)$. These values are generally easier to understand and interpret.

As can be seen from Fig. 3.16, the full two-dimensional Fourier transform results in both positive and negative wavenumbers as well as positive and negative frequencies . Unlike the negative frequencies, negative wavenumbers actually have a physical meaning. They represent the waves propagating in the opposite direction to the scanning direction. Since we are only interested in plain dispersion curves and not the direction of propagation, the analysis can be restricted to the first (positive) quadrant of the $\tilde{k} - f$ plane. The magnitude of the transformed data $U_3(\tilde{k}, f)$ form an intensity image (see Fig. 3.17).

In the next step, the dispersion curves that exhibit themselves as ridges in the $U_3(\tilde{k}, f)$ landscape have to be extracted. First, the image represented as a matrix containing intensity values has to be rescaled column per column to the

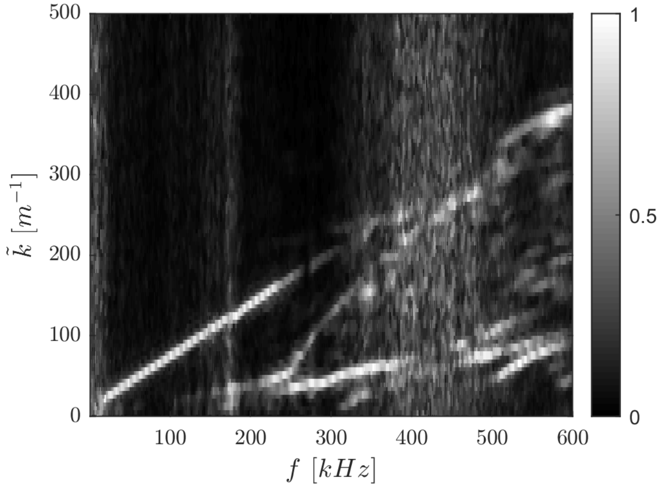

Figure 3.17: Intensity image converted to $\tilde{k} - f$ space using the 2D FFT. Dataset obtained from the SARISTU sample using the following parameters: $\Delta x = 0.1\,\mathrm{mm}$, $f_s = 10\,\mathrm{MHz}$, $m = 1024$, $n_s = 8192$.

interval $\langle 0, 1\rangle$. Second, a selected threshold is applied to convert the intensity matrix to a logical one. In the ideal case, all the logical ones would represent the points belonging to the dispersion curves (ridges). However, the logical matrix is contaminated with a certain amount of noise that makes the direct extraction of the dispersion curves complicated. Therefore, image processing techniques, such as median filtering, have to be used before thresholding to remove the noise and improve the performance of the extraction. In a third step, the coordinates $[f_i, \tilde{k}_i]$ of the logical ones, that form the dispersion curves, are found, sorted and visualized (see Fig. 3.18).

The 2D FFT method is very robust and can successfully be used to extract the dispersion curves from signals with very low SNR values. Moreover, it is computationally cheap, because it uses the very efficient FFT algorithm. An average time to process an $n_s \times m$ measurement matrix is 6.6 s using a regular PC (MATLAB© 2016a 64-bit, Intel Core i5-3570, 3.40 GHz, 8 GB). It can be easily speeded up when implemented Graphical Processing Unit (GPU) or parallelized. On the other hand, the main disadvantage of the method is the generally higher amount of noise on the output (see Fig. 3.18). It is also important to keep in mind that the input signals are sampled not only in the time domain, but also in the spatial domain. Therefore, the same rules and limitations regarding the maximum detectable frequency (Nyquist theorem)

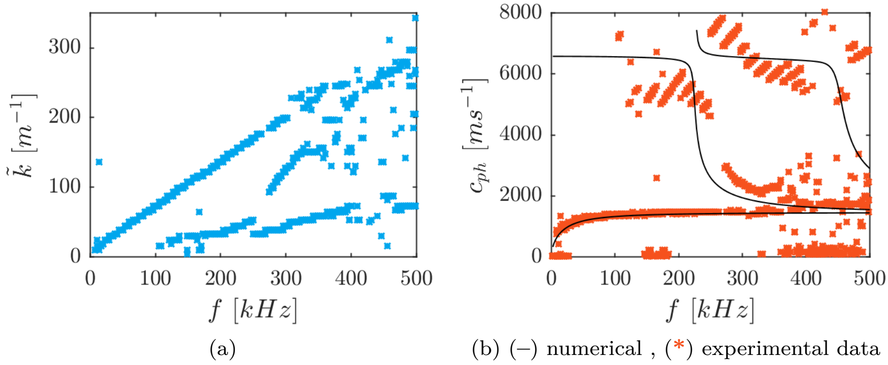

(a)

(b) (–) numerical , (*) experimental data

Figure 3.18: Dispersion curves extracted from LDV measurement using the 2D FFT method on the SARISTU sample. a) Dispersion curves in $\tilde{k} - f$ space. b) Phase velocity dispersion curves.

and wavenumber resolution $\left(\frac{1}{m\Delta x}\right)$ apply.

3.2.3 Matrix Pencil Method

Another method for extracting the dispersion curves from the experimental data is the Matrix Pencil Method (MPM) elaborated by Hua and Sarkar in [88]. MPM was initially employed in vibration analysis to identify the structural eigenmodes [89]. Later, it found a widespread use in geophysics and earth exploration to extract the dispersion curves and to analyze data from borehole acoustic arrays [90]. The applicability of the MPM for the guided wave dispersion analysis was recently demonstrated by Schöpfer et al. [91] and Mazzotti et al. [92].

Let us assume that we have a set of signals $u_3(x,t)$ obtained using the measurement technique described in section 3.2.1. Furthermore, it is assumed that the recorded set contains q independent guided wave modes. Although the signals were not acquired at the same time instant, they are in fact equivalent to a single shot array measurement with the number of scanning points m being equal to the number of array elements [90]. Therefore, we can use a similar approach to extract the dispersion relations from the LDV measurements.

First, each signal from the set is Fourier transformed from the time domain to the frequency domain

$$U(x,f) = \int u(x,t)e^{i2\pi f t}dt. \tag{3.22}$$

At a particular frequency f_0, $U(x, f_0)$ forms a complex-valued sequence of length m. In fact, $U(x, f_0)$ is a slice through the Fourier-transformed data at a particular frequency f_0. Moreover, it can be approximated by a sum of p complex exponentials

$$U(x, f_0) = \sum_{j=1}^{p} a_j e^{-ik_j x}, \tag{3.23}$$

where p defines the model order (matrix pencil parameter), k_j is the wavenumber and a_j is the amplitude coefficient. It is apparent that both a_j and k_j are functions of frequency and therefore unique for each fixed frequency f_0. The model order p is chosen to be higher than the expected number of propagating modes $q \leq p \leq m - q$. The reason for this is the better estimation of $k(f)$ in presence of noise. Details about the SNR performance can be found in [88, 90].

Second, a Hankel matrix

$$\mathbf{X} = \begin{bmatrix} U(x_1, f_0) & U(x_2, f_0) & \cdot & U(x_{p+1}, f_0) \\ U(x_2, f_0) & U(x_3, f_0) & \cdot & U(x_{p+2}, f_0) \\ \cdot & \cdot & \cdot & \cdot \\ U(x_{m-p}, f_0) & U(x_{m-p+1}, f_0) & \cdot & U(x_m, f_0) \end{bmatrix}, \tag{3.24}$$

is formed using the values of (3.23) evaluated at the measurement points $x_i, i = 1, 2, \ldots, m$. In order to reduce the computational complexity, $\mathbf{X}$ is decomposed in two unitary matrices $\mathbf{U}$, $\mathbf{V}$ and one diagonal matrix $\mathbf{\Sigma}$ using the Singular Value Decomposition (SVD)

$$\mathbf{X} = \mathbf{U\Sigma V}^*. \tag{3.25}$$

The (*) sign represents the hermitian (conjugate) transposition. Only the first q dominant singular values of $\mathbf{\Sigma} = diag(\sigma_1, \sigma_2, ...)$ are kept for further calculations and the rest is discarded. This results in a rank-reduced matrix $\mathbf{\Sigma}_0 = diag(\sigma_1, \sigma_2, ..., \sigma_p)$.

The third and the last step starts with the assembly of the modified matrices $\mathbf{X_0}$ and $\mathbf{X_1}$ using the rank-reduced $\mathbf{\Sigma}_0$

$$\mathbf{X}_0 = \mathbf{U\Sigma}_0\mathbf{V}_0^* \qquad \mathbf{X}_1 = \mathbf{U\Sigma}_0\mathbf{V}_1^*, \tag{3.26}$$

where the two matrices $\mathbf{V}_0$ and $\mathbf{V}_1$ are being defined as $\mathbf{V}_0 = V(2 : p + 1, 1 : \mu)$, $\mathbf{V}_1 = V(1 : p, 1 : \mu)$. The sets of backward ($\lambda_k^-$) and forward ($\lambda_k^+$) estimates of the complex exponential terms in (3.23) are then calculated as solutions of the eigenvalue problems

$$(\mathbf{X}_1^+\mathbf{X}_0 - \lambda_k^-\mathbf{I_p})\vec{e}_k = \vec{0}, \tag{3.27}$$

$$(\mathbf{X}_0^+\mathbf{X}_1 - \lambda_k^+\mathbf{I_p})\vec{e}_k = \vec{0}, \tag{3.28}$$

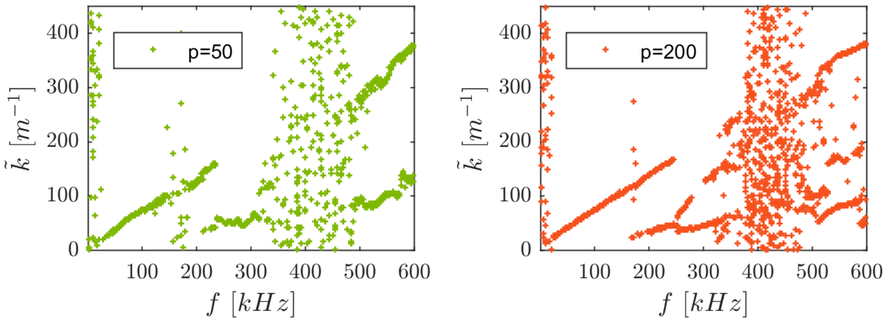

(a) $p = 50$ (b) $p = 200$

Figure 3.19: Experimental dispersion curves calculated using the MPM for the SARISTU sample.

where $\mathbf{I_p}$ denotes the identity matrix and $(^+)$ stands for the generalized inversion (Moore-Penrose). The backward and forward wavenumbers are extracted from complex exponentials as

$$k_j^-(f_0) = -\frac{\ln \lambda_j^-}{ix_j} \tag{3.29}$$

$$k_j^+(f_0) = \frac{\ln \lambda_j^+}{ix_j} \tag{3.30}$$

and averaged together to reduce the noise using the procedure described in [92]. The result is then a set of dispersion curves for a given material and frequency range (see 3.22).

The quality of the wavenumber estimation depends on p with higher values of p generally giving more accurate results (see 3.19). However, the processing time grows significantly with rising value of p too (see Fig. 3.20). Hence, the balance between these two counteracting parts has to be found. For example, the optimal value for the experimental LDV data for the SARISTU CFRP sample was $p = 200$. The accuracy of the wavenumber estimation did not grow significantly for p above this value and the processing time on a regular laptop was still acceptable. Moreover, as can be seen from Fig. 3.20, the execution grows steeply above $p = 200$.

As can be seen from Fig. 3.21b, the resulting dispersion curves still contain a significant amount of noise in particular frequency bands. At these frequencies, the transmitter does not inject enough power to the sample. Therefore, the

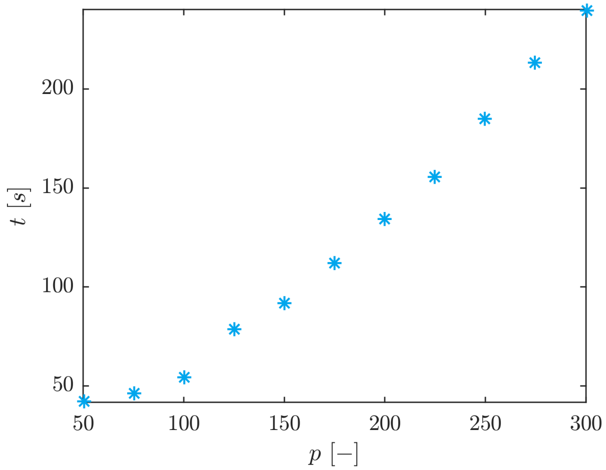

Figure 3.20: MPM execution time as a function of pencil parameter p. Calculated using a regular PC (MATLAB 2016a 64-bit, Intel Core i7-3520M, 2.90 GHz, 8 GB) for a dataset consisting of $m = 1024$ signals each with 8192 samples. Points represent the mean value of 8 runs.

guided wave modes appropriate for these frequency bands are excited weakly or not at all. Nonetheless, the noise in the weakly excited bands can be easily filtered out using two datasets $\tilde{k}_p(f)$ and $\tilde{k}_{p+1}(f)$ for two subsequent pencil parameters. Unlike the true points belonging to the dispersion curves, the noise is highly uncorrelated and strongly depends on the pencil parameter p (see Fig. 3.21b). It follows that using a simple formula

$$\tilde{k}(f) = \begin{cases} \tilde{k}_p(f) & \text{if } |\tilde{k}_p(f) - \tilde{k}_{p+1}(f)| \leq \varepsilon \\ NaN & \text{if } |\tilde{k}_p(f) - \tilde{k}_{p+1}(f)| > \varepsilon \end{cases}, \tag{3.31}$$

the invalid points can be removed. In contrast, the detected points that belong to the true dispersion curves $\tilde{k}(f)$ are preserved because they are nearly identical for two subsequent values of p. This is a very simple, but effective way to reduce the amount of noise in the weakly excited frequency region.

3.2.4 Comparison of 2D FFT and MPM

Building on the experimental results and a theoretical comparative study of the 2D FFT and MPM methods by del Rio and Sarkar [93], we can make the following conclusions. Compared to the 2D FFT, the MPM is computationally

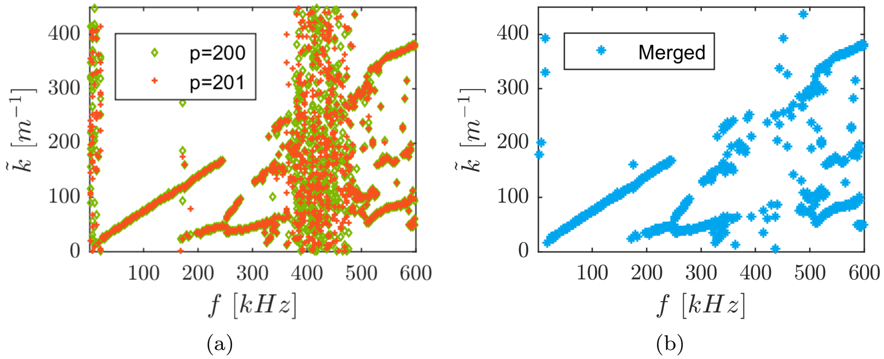

Figure 3.21: Experimental dispersion curves calculated using the MPM for SARISTU plate: a) datasets for two different pencil parameters p, b) merged dispersion curves.

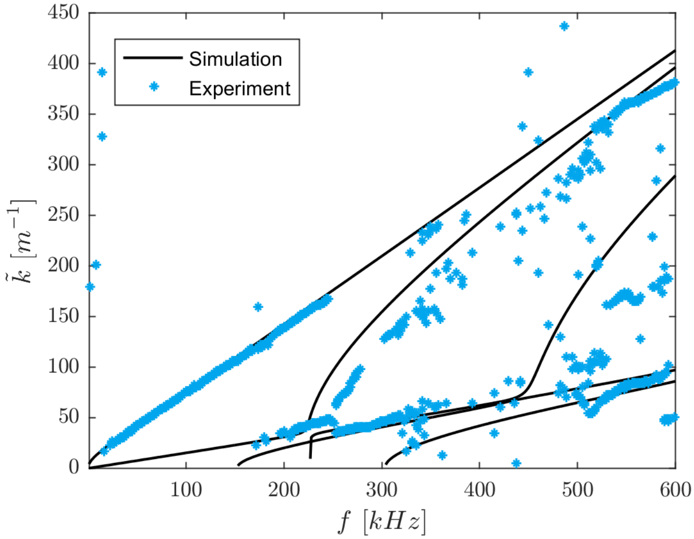

Figure 3.22: Comparison of the experimental MPM dispersion curves and the theoretical values for the SARISTU sample.

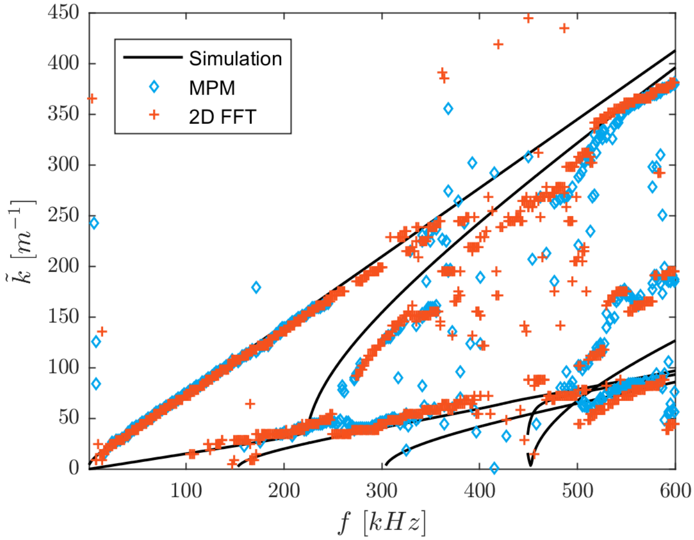

Figure 3.23: Merged experimental data from MPM and 2D FFT in $\tilde{k} - f$ space for SARISTU sample.

more straightforward because it avoids landscape searching and line following steps. The points of the dispersion curves are calculated as the eigenvalues of a generalized eigenvector problem [91] for a specified frequency. Moreover, the SVD can be easily applied to automatically determine the number of dominant modes propagating in the structure as well as their attenuation. On the other hand, the MPM is computationally demanding even if the size of the problem is reduced by SVD.

In contrast, the 2D FFT is significantly faster and provides very robust results. However, the extraction of the dispersion curves from the 2D FFT intensity image poses a tough challenge and determines the quality of the estimation as well as the amount of noise in the final result. Nonetheless, both methods are complementary and can be used together to improve the experimental analysis of the dispersion curves for ultrasonic guided waves (see Fig. 3.23). The blank spaces that are not fully covered by one method can be often filled by the data from the other method. This combination can facilitate a better analysis of the experimental dispersion data that can be further used to improve the results of GW imaging or elastic properties inversion.

It is clear that none of the methods can completely fill the frequency gaps at which the sample is not properly excited by the PZT transducers. These transducers have their own fixed frequency response that cannot be easily changed and cannot be considered as fully broadband devices. In order to cover the full frequency band, a truly broadband excitation, such as a laser-pulse, has to be used [91, 94, 95]

3.3 Conclusion

In this section, three standard numerical methods for dispersion analysis were presented. The output of the second (Legendre/state matrix) and the third method (SAFE) will be used in the forthcoming sections to improve the GW imaging algorithm. Therefore, it was crucial to introduce them, discuss their performance and identify their weak spots. SAFE is very fast and accurate, but it provides less flexibility for geometric dispersion analysis due to its closed-source nature. On the contrary, the method based on the Legendre polynomial approximation provides great flexibility due to the open access to the source code. However, it suffers from computational complexity and cost, especially with higher order of approximation. The precision of the two methods is comparable for the purposes of GW imaging.

A combination of the 2D FFT and MPM methods was proposed and its synergetic performance, superior to both individual methods, was demonstrated. The experimental dispersion analysis was used to confirm the validity of the mechanical properties of two samples provided by different project partners. Moreover, the procedure can be used to invert material properties from the LDV measurement data.

Chapter 4

Nonlinear Elastic Wave Spectroscopy

In this chapter, the basic nonlinear elastic models that are being used in the field of NEWS are described. Special attention is paid to models and approaches that proved to be successful in describing the behaviour of (micro)damaged materials. Originally, nonlinear elastic models were proposed to explain the anomalous behaviour of certain solids that deviated from the simply linear Hooke's law. The first authors, who dealt with the topic, were Landau and Lifschitz with their famous textbook on elasticity [96]. Later on, the research on the topic of nonlinear elasticity and finite deformations gained momentum and several important publications followed, e.g. [97, 98, 99, 100, 101].

In the last 30 years, the focus has shifted from theoretical and experimental analysis of the higher order elastic theories to the direct application of nonlinear elasticity in damage analysis [101]. The first inspected samples were mostly rocks and stones that exhibit a large nonlinear response due to the inherent microcracking in their structure [102, 103]. Subsequently, it was only a small step to study the application of nonlinear elasticity and NEWS to the assess the presence of damage in various types of media, such as plexiglas, concrete [104], aluminum [105] or sandwich composites [106].

The nonlinear effects in guided and especially Lamb waves are a rather new topic. Some pioneering work on metallic structures was done by Ryles et al. [107] and Pruell et al. [108], Shkerdin and Glorieux [109], but there is still lot of potential.

Nowadays, the main issue with NEWS techniques is their firm establishment and standardization. It is very challenging to transfer the techniques from the laboratory scale to industrial applications, because the values that are measured are several orders of magnitude smaller than what is evaluated using current conventional NDT methods, and therefore, require a precise instrumentation [110]. It is also problematic to directly quantify the size and the location of the damage based on nonlinearity measurements.

In the next two sections, the basic concepts of NEWS and the most important techniques will be introduced.

4.1 Nonlinear material models

Nonlinear elastic material models can be generally divided in two branches: classical and nonclassical theories.

4.1.1 Classical nonlinear elasticity

One of the first analytical descriptions of the so called finite deformation and nonlinear phenomena was given by Murnaghan [99] and Landau and Lifshitz [96]. They both used a power expansion of the *elastic strain energy* W to derive the fundamental governing equations. The basic assumption for this approach is the fact that W can be written as an analytical function. Using this assumption and Hooke's law (2.3), the W can be expressed as [111, 112]

$$W = W_0 + C_{ij}\varepsilon_{ij} + \frac{1}{2!}C_{ijkl}\varepsilon_{ij}\varepsilon_{kl} + \frac{1}{3!}C_{ijklmn}\varepsilon_{ij}\varepsilon_{kl}\varepsilon_{mn} + \dots \quad . \tag{4.1}$$

According to De Lima and Hamilton [113], the elastic strain energy for the case of isotropic solids can be expressed using the invariants of strain tensor ε_{ij}

$$I_1 = \varepsilon_{ii} \qquad I_2 = \varepsilon_{ij}\varepsilon_{ij} \qquad I_3 = \varepsilon_{ij}\varepsilon_{jk}\varepsilon_{ki} \tag{4.2}$$

as

$$W = \frac{1}{2}\lambda I_1^2 + \mu I_2 + \frac{1}{3}CI_1^3 + BI_1I_2 + \frac{1}{3}AI_3 + \mathcal{O}(\varepsilon_{ij}^4), \tag{4.3}$$

where λ, μ stand for Lamé constants and A, B, C are the *Landau moduli* [114]. If we assume that the initial elastic strain energy is zero and the volumetric deformation of the elastic body is also zero, the first two terms in (4.1) can be neglected which, according to Hearmon [115] leads to

$$W = \frac{1}{2}C_{ijkl}\varepsilon_{ij}\varepsilon_{kl} + \frac{1}{6}C_{ijklmn}\varepsilon_{ij}\varepsilon_{kl}\varepsilon_{mn}. \tag{4.4}$$

Keeping only the third and fourth term of expansion (4.1), we can formulate a relevant physical meaning for each of these. Employing the definition of stress as the first derivative of the elastic strain energy with respect to strain, i.e.,

$$\tau_{ij} = \frac{\partial W}{\partial \varepsilon_{ij}}, \tag{4.5}$$

the *classical weakly nonlinear* stress-strain relation is obtained

$$\tau_{ij} = C_{ijkl}\varepsilon_{kl} + \frac{1}{2}C_{ijklmn}\varepsilon_{kl}\varepsilon_{mn}, \tag{4.6}$$

where C_{ijkl} and C_{ijklmn} are the 2nd order and 3rd order elastic (stiffness) constant tensors. The first tensor is the classical one that describes the linear elasticity and the latter is responsible for the nonlinear effects. The tensor C_{ijklmn} contains 56 constants in the case of generally anisotropic media, but this is reduces to three independent elements for an isotropic symmetry class. According to De Pascalis et al. [112], equation (4.4) can be consequently further simplified to

$$W = \frac{1}{2}\lambda I_1^2 + \mu I_2 + \frac{1}{3}CI_1^3 + BI_1I_2 + \frac{1}{3}AI_3 \tag{4.7}$$

using the invariants. The procedure to experimentally measure the Landau moduli is described for example in [116].

The stress tensor τ_{ij} can then be obtained by substituting (4.7) in (4.5). If the loading is restricted to a simple uni-axial tension (stress σ, strain ε), one can write

$$\sigma = \big[E_0(1-\beta\varepsilon)\big]\varepsilon, \tag{4.8}$$

using the notation that is common in ultrasonic nonlinear testing. E_0 is a constant Young's modulus, and the parameter β is generally a function of 2nd and 3rd order elastic constants (elements of C_{ijkl} and C_{ijklmn}). According to Ostrovsky and Johnson [117] and Naugolnykh [118], β can be expressed using λ, μ, A, B, C as

$$\beta = \frac{3}{2} + \frac{A+3B+C}{\lambda+2\mu}. \tag{4.9}$$

The 4th order elastic constants have been used for the purpose of NEWS. To do this, equation (4.8) should be augmented with an extra parameter δ. Following the works of Meurer and Qu [119] and Van Den Abeele et al. [120], (4.8) can then be rewritten as

$$\sigma = E_0(1-\beta\varepsilon-\delta\varepsilon^2)\varepsilon, \tag{4.10}$$

where $\beta\varepsilon$ and $\delta\varepsilon^2$ are usually much smaller than one and are determined by the type of nonlinearity (symmetric or asymmetric stress-strain contributions). From the physical point of view, the constants β and δ determine whether the

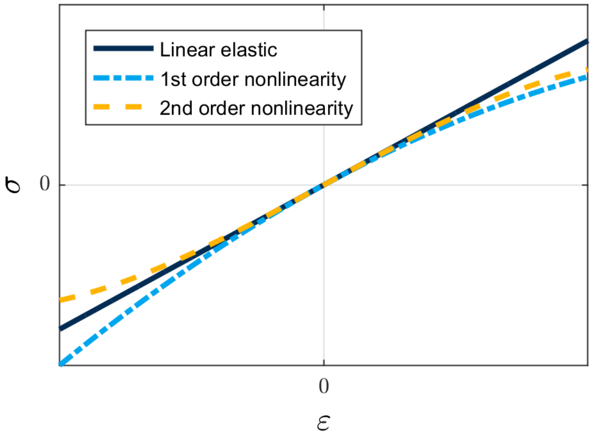

Figure 4.1: $\sigma - \varepsilon$ for linear and two types of weakly nonlinear behaviour.

sample material or a part of it is softening or hardening. The illustration of this behaviour can be seen in Fig. 4.1 [121].

The elasticity modulus can be expressed from (4.10) as

$$E = E_0(1 - \beta\varepsilon - \delta\varepsilon^2). \tag{4.11}$$

If $\delta = 0$ and $\beta \neq 0$, one speaks about *1st order nonlinearity*. Conversely, if $\beta = 0$ and $\delta \neq 0$, the term *2nd order nonlinearity* is used. The different shapes of stress-strain curves in the case of classical nonlinearity are depicted in column 2 and 3 of Fig. 4.2.

The above introduced classical nonlinearity thus originates from the anharmonicity of the inter-atomic potentials [105]. Johnson [117] calls this type of nonlinearity *atomic elasticity*. Many materials exhibit this type of behaviour. However, the values of nonlinear parameters are often very low and therefore, extremely hard to measure. On the other hand, the geomaterials, such as rocks that contain an intricate system of micro-cracks and soft bonds in an otherwise hard matrix, exhibit this type of nonlinear behaviour even at low strain amplitudes.

It is apparent from Fig. 4.2 that the classical nonlinear model explains the generation of higher harmonics nf in the spectrum. The 2nd order nonlinearity gives rise to odd harmonics ($3f$, $5f$) only, while the 1st order nonlinearity produces both, even and odd higher harmonics ($2f$, $3f$).

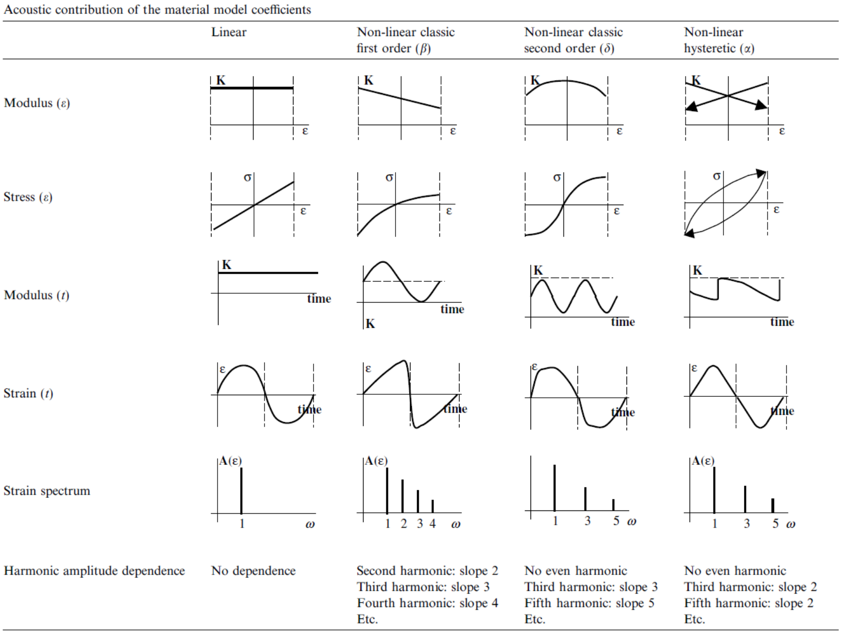

Acoustic contribution of the material model coefficients

	Linear	Non-linear classic first order (β)	Non-linear classic second order (δ)	Non-linear hysteretic (α)
Modulus (ε)				
Stress (ε)				
Modulus (t)				
Strain (t)				
Strain spectrum				
Harmonic amplitude dependence	No dependence	Second harmonic: slope 2 Third harmonic: slope 3 Fourth harmonic: slope 4 Etc.	No even harmonic Third harmonic: slope 3 Fifth harmonic: slope 5 Etc.	No even harmonic Third harmonic: slope 2 Fifth harmonic: slope 2 Etc.

Figure 4.2: Schematic overview of different types of nonlinear behaviour [104].

4.1.2 Nonclassical nonlinear elasticity

A new advancement in the description of nonlinear elastic behaviour of the solids was the introduction of so-called nonclassical theories. These theories were developed mainly in order to describe the peculiar behaviour of rocks and complex sediments that exhibit an asymmetric behaviour of their stress-strain curve in compression and tension loading. Such effects are mostly related to the asymmetric opening and closing of clusters of micro-cracks (e.g. mechanical hysteresis) as well as to the presence of grains with different stiffness in the bulk medium of the studied sample (discontinuous stress-strain behaviour).

From a mathematical point of view, nonclassical theories dropped the requirement of W being an analytical function. The constitutive equation is thus no longer derived directly from W. Instead, nonanalytical terms are added. Most of these terms were added based on the empirical experience and therefore, lack the proper physical basis. Several authors tried to relate the underlying physics to these terms, e.g. [114, 122, 123].

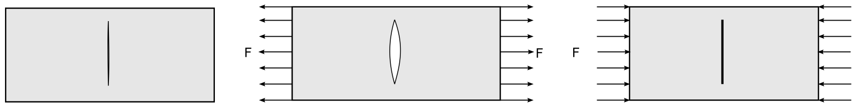

(a) Initial (unloaded state)

(b) Tensile loading $\varepsilon > \varepsilon_c$

(c) Compression $\varepsilon < \varepsilon_c$

Figure 4.3: Schematic representation of the bimodular model with $\varepsilon_c = 0$.

Bimodular model

A first model that can be used to describe the nonclassical nonlinearity is the *bimodular model*, sometimes also called Contact Acoustic Nonlinearity (CAN) or *crack clapping*. Although it is one of the simplest models, it provides useful insight in the generation of higher harmonics during a harmonic monofrequency excitation [124].

The original model assumes a linearly elastic body with a central crack. If the crack is stressed in mode I by propagating elastic waves, it "breathes" (opens and closes). If the displacement amplitude at the crack surface is sufficiently large, an asymmetry between its response to tension and compression, caused by the contact between the two crack surfaces, starts to appear. As a result, the material seemingly becomes stiffer after crossing a certain deformation threshold. This virtual change of the elastic moduli can be described as

$$E = E_0\Big[1 - H(\varepsilon - \varepsilon_c)\Big(\frac{\Delta E}{E_0}\Big)\Big], \tag{4.12}$$

where E_0 is the Young's modulus, ΔE its change caused due to the contact of the crack surfaces and $H(\varepsilon)$ Heaviside function. ε_c is the contact strain threshold at which the crack surfaces touch each other. An illustration of such a behaviour is depicted in Fig. 4.3. If the crack is initially closed, the previous equation can be written as

$$E = \begin{cases} E^+ & \text{for } \varepsilon > 0 \\ E^- & \text{for } \varepsilon < 0 \end{cases}, \tag{4.13}$$

where E^+ and E^- are tension and compression moduli, respectively. The graphical representation of this formula is illustrated in Fig. 4.4. This model was experimentally tested by several authors, for example in references [125] and [126].

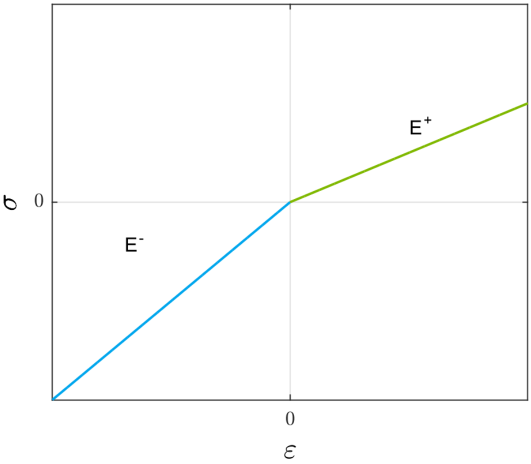

Figure 4.4: σ-ε curve for the bimodular model with $\varepsilon_c = 0$.

The CAN model results in a rectification of a monofrequency excitation waveform $\varepsilon(t) = \varepsilon_a \cos(2\pi f t)$ (see Fig. 4.5), which can be described analytically as

$$\sigma(t) = E(t)\varepsilon(t) = E_0\Big[1 - H(\varepsilon(t) - \varepsilon_c)\Big(\frac{\Delta E}{E_0}\Big)\Big]\varepsilon(t). \tag{4.14}$$

This equation actually describes a plain pulse modulation (see Fig. 4.6). It follows that such a modulation results in the creation of higher harmonic content in the propagating signal (see Fig. 4.7). The development of higher harmonics with increasing excitation amplitude, as illustrated in Fig. 4.8, can be calculated using a Fourier transform of (4.14)

$$F(mf) = \frac{\Delta E}{E_0}\frac{\tau}{T}\varepsilon_a \cdot \sum_{n=1}^{\infty} \mathrm{sinc}\Big[\frac{n\tau}{T}\Big]\delta[(m \pm 1) - n)], \tag{4.15}$$

where τ is the pulse width, m the order of the higher harmonic and T the period of the signal as illustrated in Fig. 4.6 [124, 127].

There is ongoing research that builds on the basic ideas of CAN and tries to accurately take into account the whole complexity of the contact between the crack faces, such as friction, slip and geometry of asperities [128].

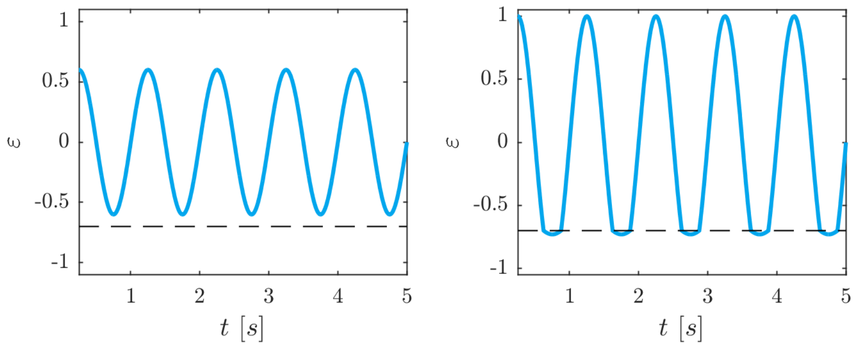

(a) Harmonic signal $\varepsilon(t)$ for $\varepsilon < \varepsilon_c$ (b) Deformed signal $\varepsilon(t)$ for $\varepsilon > \varepsilon_c$

Figure 4.5: Signal deformation due to CAN.

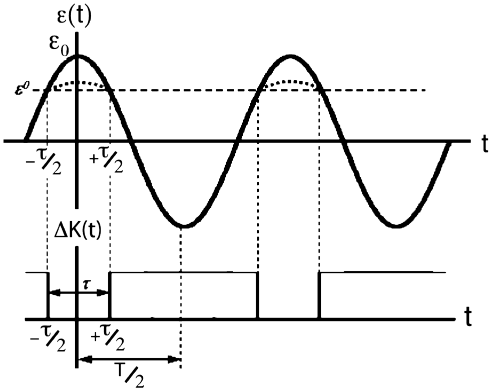

Figure 4.6: Pulse modulation as a function of time [127]. Compression part of a cycle is oriented in the positive part of y-axis.

Hysteretic model

The classical nonlinear theory and the bimodular model are useful as first order approximations of the nonlinear behaviour of solids. However, they cannot fully describe the dynamic nonlinear response of the majority of samples with inherently high nonlinearity such as rocks, and damaged samples which contain a sizeable distribution of micro-cracks. Characteristic for these type of materials is that another set of nonclassical effects, such as slow dynamics, hysteresis and end-point-memory, comes into the spotlight. It is not at all the goal of the

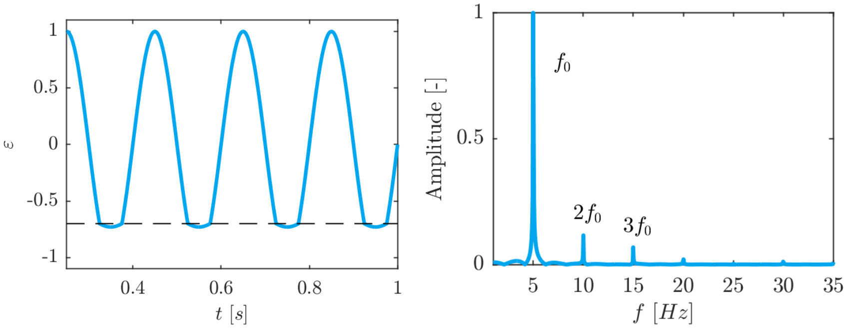

(a) Distorted signal (b) Spectrum of the signal

Figure 4.7: Signal distortion and higher harmonic content - bimodular model, $f = 5$ Hz

.

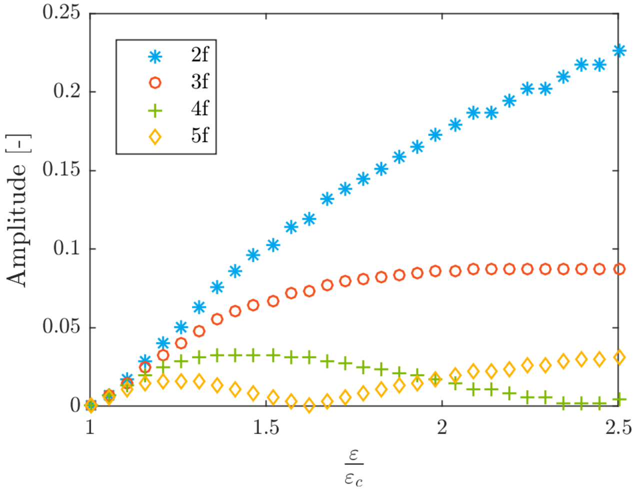

Figure 4.8: Numerically calculated amplitudes of higher harmonics that were normalized with respect to the amplitude of fundamental frequency $f = 5\,\mathrm{Hz}$ with $\frac{\Delta E}{E} = 1$, $\varepsilon_c = 0.1$.

present work to fully describe all these effects. Nevertheless, it will be briefly shown, how they can be accounted for and what their effect is on ultrasonic testing.

First, it is necessary to use more complicated and sophisticated relations to describe hysteretic nonlinear behaviour. A typical feature in this description is the dependency on the strain rate $\dot{\varepsilon}$ and the strain direction $\mathrm{sgn}(\dot{\varepsilon})$. Therefore, it is necessary to account not only for the current state of the elastic body, but also for its history. If the problem is restricted to one dimension, the general formula can be written as

$$\sigma = \int E(\varepsilon, \dot{\varepsilon}) d\varepsilon, \tag{4.16}$$

where $E(\varepsilon, \dot{\varepsilon})$ is the strain and strain rate dependent elastic modulus. In the most general case, $E(\varepsilon, \dot{\varepsilon})$ consists of the classical nonlinear part (as described before) and the terms that describe hysteresis and other nonclassical effects. This nonclassical part on top of the classical nonlinear terms is often denoted as $f(\varepsilon, \dot{\varepsilon})$ and there are several theories that describe its structure and implementation. Let us start with the purely hysteretic model for the sake of simplicity. Hence, all nonlinear terms except of $f(\varepsilon, \dot{\varepsilon})$ are neglected and (4.16) is reduced to

$$\sigma = E[\varepsilon - f(\varepsilon, \dot{\varepsilon})], \tag{4.17}$$

where $|f(\varepsilon, \dot{\varepsilon}) \ll 1|$. A first model that describes $f(\varepsilon, \dot{\varepsilon})$, was proposed by Davidenkov [129] and is often called the *inelastic model*. According to Nazarov [130] the hysteretic term $f(\varepsilon, \dot{\varepsilon})$ has the form of

$$f(\varepsilon, \dot{\varepsilon}) = \alpha \varepsilon_m \varepsilon + \begin{cases} \frac{\beta_1}{2}\varepsilon^2 - \frac{\beta_1+\beta_2}{4}\varepsilon_m^2 & \dot{\varepsilon} > 0 \\ \\ -\frac{\beta_2}{2}\varepsilon^2 + \frac{\beta_1+\beta_2}{4}\varepsilon_m^2 & \dot{\varepsilon} < 0, \end{cases} \tag{4.18}$$

where $|\alpha|\varepsilon_m \ll 1$, $|\beta_{1,2}|\varepsilon_m \ll 1$ and $|\beta_{1,2} \gg 1|$. ε_m stands for the local strain amplitude and α, β_1 and β_2 are independent parameters that characterize the hysteretic behaviour of the body. Certain cases of (4.18) are very interesting with respect to the previously introduced classical nonlinear models and the later discussed non-classical models. If $\alpha = 0$ and $\beta_1 + \beta_2 = 0$ and (4.18) is substituted in (4.17), the latter is reduced to the case of pure quadratic nonlinearity. On the other hand, if $\beta_1 + \beta_2 \neq 0$ then the hysteretic behaviour is preserved and the shape of the hysteretic curve is displayed in Fig. 4.9a. It is worth noticing that the hysteretic loop does not pass through the origin. Therefore, zero strain corresponds to a nonzero stress and vice versa. This type of hysteresis was typically observed in crystals of LiF and NaCl [131].

The second widespread hysteretic model is based on the Granato-Lücke model of amplitude dependent attenuation (internal friction). It is often called the *elastic* or *ratchet* type of hysteresis thanks to the shape of the hysteretic curve.

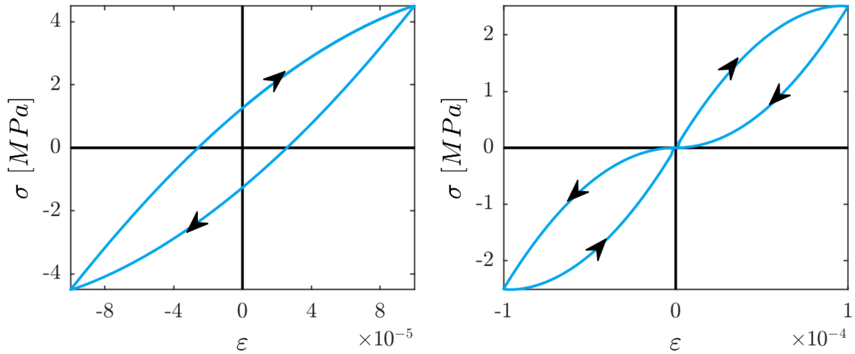

(a) Hysteretic loop - *slider* type (b) Hysteretic loop - typ *ratchet* type

Figure 4.9: Comparison of two basic hysteretic models - *inelastic* and *elastic*.

According to Nazarov et al. [130], it can be described as

$$f(\varepsilon, \dot{\varepsilon}) = \begin{cases} \frac{\gamma_1}{2}\varepsilon^2 & \dot{\varepsilon} > 0 \wedge \varepsilon > 0 \\ -\frac{\gamma_2}{2}\varepsilon^2 + \frac{\gamma_1+\gamma_2}{2}\varepsilon_m^+\varepsilon & \dot{\varepsilon} < 0 \wedge \varepsilon > 0 \\ \frac{\gamma_3}{2}\varepsilon^2 & \dot{\varepsilon} < 0 \wedge \varepsilon < 0 \\ -\frac{\gamma_4}{2}\varepsilon^2 + \frac{\gamma_3+\gamma_4}{4}\varepsilon_m^-\varepsilon & \dot{\varepsilon} > 0 \wedge \varepsilon < 0, \end{cases} \tag{4.19}$$

where γ_1, γ_2, γ_3, γ_4 are constants and ε_m^+, ε_m^- represent the local strain amplitudes of the positive and the negative part of the loading cycle respectively. These two parameters are equal in most cases, however, they can be different in the most general case. The shape of the curve is depicted in Fig. 4.9b. In contrast to the *inelastic* model, zero strain always corresponds to zero stress - $[\varepsilon, \sigma] = [0, 0]$ [132].

A complete model of nonlinearity will combine hysteretic effects with classical nonlinear phenomena. It is apparent from (4.11) that the classical contributions do not depend on the strain rate. In combination with the hysteretic contribution, $E(\varepsilon, \dot{\varepsilon})$ can be expressed in the following way:

$$E(\varepsilon, \dot{\varepsilon}) = E_0(1 - \beta\varepsilon - \delta\varepsilon^2) + f(\varepsilon, \dot{\varepsilon}), \tag{4.20}$$

where $f(\varepsilon, \dot{\varepsilon})$ describes the selected hysteretic model. In case of nonlinear ultrasound, the widespread version is

$$E(\varepsilon, \dot{\varepsilon}) = E_0(1 - \beta\varepsilon - \delta\varepsilon^2 - \alpha[\varepsilon_m + \varepsilon\,\mathrm{sgn}(\dot{\varepsilon}) + \ldots]), \tag{4.21}$$

where ε_m stands for the local strain amplitude in the last cycle and α is the *first order hysteretic nonlinear constant* [133]. The underlying phenomenology for this model is the Preisach-Mayergoyz space (PM) space. In fact, this is the first order approximation for PM space with a uniform distribution of hysteretic units.

The other ways to describe the combination of hysteresis and nonlinear elasticity using the PM space are described, for example in [134, 135, 136, 128]. Nevertheless, this topic is already out of scope of the present work. The intent of this section was simply to introduce the basic description of the nonlinear behaviour and to provide some insight into its origins.

4.2 Nonlinear Wave Modulation Spectroscopy

Nonlinear Wave Modulation Spectroscopy (NWMS) is one of the most popular NEWS methods at the moment. The technique is based on tracking the amplitude dependent product of nonlinear frequency mixing. It has been tested and verified by several research teams on many different materials with different types of damage, e.g. aerospace grade aluminum alloys [137, 138] and composite plates [106]. This technique is mostly suitable for qualitative NDT to discern the difference between an intact and a damage state. One of its major advantages is that it can be used to investigate samples with arbitrarily complex shapes.

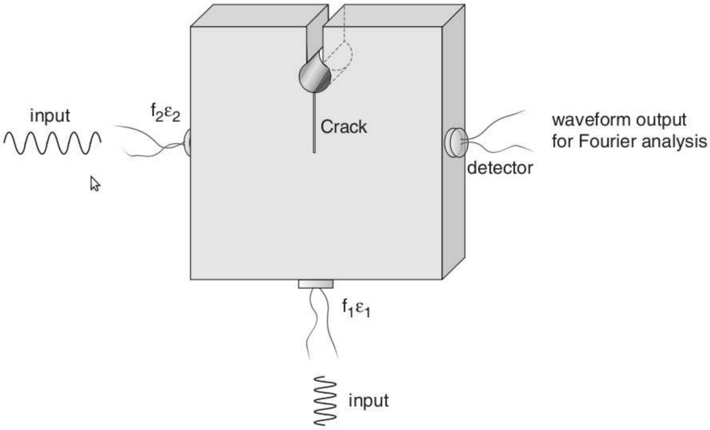

Figure 4.10: Scheme of basic NWMS experiment [127].

Let us image two ultrasonic sources that generate harmonic signals with two different frequencies f_1 and f_2, where $f_1 < f_2$ and $f_2 \neq kf_1, k \in N$. These two sources generate elastic waves that interact with each other in the material. If the material behaves nonlinearly due to the presence of damage, a so-called *mixing frequencies* starts to appear in the frequency spectrum. The mixing or intermodulation frequencies are specific combinations of the two input frequencies, such as $f_2 \pm f_1$ or more generally $f_2 \pm kf_1$, where k stands for the order of the sideband (intermodulation) frequency. The sidebands can be generated also around the higher harmonics of f_2, for example $2f_2 \pm kf_1$.

The true physical origins of the nonlinear mixing are still to be fully described and depend on the type of nonlinearity. For certain cases, several empirical models were developed that describe these effects as in [127]. For example, the combined classical and non-classical model (4.20) can be satisfactorily used to phenomenologically describe the various spectral effects produced during a nonlinear modulation.

For practical applications, it is crucial to identify the suitable parameter of the model that is correlated with the degree of damage in the sample. Let us assume that the amplitude of the excitation with frequency f_1 and f_2 are a_1 and a_2 respectively. If the sample is intact there is no occasion for the generation of intermodulation frequencies. However, if the sample is damaged combination frequencies start to appear. If the amplitude dependence of the intermodulation frequency $(f_2 \pm 2f_1)$ is plotted, in a medium for which the nonlinear modulus can be described by (4.20), it will be linear in both amplitudes, i.e. $\alpha \cdot A_1 \cdot A_2$ in case of hysteretic nonlinearity or quadratic in A_1 and linear in A_2, i.e. $C_{\beta\delta} \cdot (A_1)^2 \cdot A_2$ for the case of classic nonlinearity. $C_{\beta\delta}$ is a combination of β^2 a δ. Similar relations can be inferred for other intermodulation products, for example $C_\beta \cdot A_1 \cdot A_2$ for $(f_2 \pm f_1)$ [139]. Using a regression analysis of the measured data, these nonlinear parameters, for example $C_{\beta\delta}$ or C_β, can be calculated and related to the severity of the damage in the sample.

The advantage of NWMS over the higher harmonic analysis is mainly technical. The sidebands are relatively close to the frequency f_1 which means they are still in the operational bandwidth of the transducer. Hence, it is easier to measure them compared to the higher harmonics that are often out of the transducer's bandwidth.

4.3 Scaling Subtraction Method

Scaling Subtraction Method (SSM) is a rather new method that does not actually belong to the NEWS category, because it evaluates the changes in the signal in the time domain instead of the frequency domain [140]. However, it is a very interesting and promising nonlinear NDT technique, and it forms the backbone of the baseline-free GW imaging method that will be proposed in the next part of the thesis.

The basic idea of the SSM is to analyze the scalability of the input-output response of a damage sample. First, the sample is stimulated using a signal at a reference amplitude A_{lin}. This signal is denoted v_{lin}. It is assumed that the amplitude A_{lin} is low enough not to provoke any nonlinear response in the sample [141]. Second, the excitation amplitude is scaled up and the subsequent responses at different amplitudes are recorded. The nonlinear part of the response at a given excitation amplitude A is then extracted using a simple scaling and subtraction formula. To do this, the reference signal v_{ref} is first linearly up-scaled

$$v_{ref}(t) = k_s v_{lin}(t) \qquad k \gg 1 \ , \tag{4.22}$$

creating a reference linear signal v_{ref} for the considered excitation amplitude A. The scaling coefficient k_s is defined as $k_s = \frac{A}{A_{lin}}$ and thus, equation (4.22) yields [142]

$$v_{ref}(t) = k_s v_{lin}(t) = \frac{A}{A_{lin}} v_{lin}(t) \ . \tag{4.23}$$

Next, this reference signal is subtracted from the measured signal

$$w_A(t) = v_A(t) - v_{ref}(t) = v_A(t) - \frac{A}{A_{lin}} v_{lin}(t). \tag{4.24}$$

The resulting signal $w_A(t)$ is called the SSM signal and contains all of the nonlinear contributions of the sample's response. To evaluate the nonlinearity and indirectly the severity of the damage, a scalar measure θ is defined as the energy of the $w_A(t)$ signal [143]

$$\theta(A) = \frac{1}{T} \int_0^T w_A^2(t) dt \ , \tag{4.25}$$

where T is the length (duration) of the signal. The nonlinear output parameter $\theta(A)$ can be related to the input using similarly calculated energy value for input signal $v_A(t)$

$$\eta(A) = \frac{1}{T} \int_0^T v_A^2(t) dt \ . \tag{4.26}$$

The benefits of the SSM method are obvious: it is fast and computationally inexpensive, because it is carried out in the time domain rather than in the frequency domain. Moreover, as illustrated in Bruno et al. [144], it can be used for damage localization in idealized structures. The next chapter will demonstrate that it can also be used in conjunction with GW to detect the nonlinear damage in composite structures.

4.4 Conclusion

In this chapter, we presented a short overview of several NEWS phenomena. These features were recapitulated in order to illustrate the nonlinear effects that can occur during elastic wave propagation in nonlinear or damaged materials. They highlight the most important nonlinear indicators that can be used for defect localization and imaging. Apart from the popular NWMS technique, special attention was given to the SSM method which will turn out to be vital to the novel imaging method that will be proposed in the following chapter.

Chapter 5

Ultrasonic Guided Wave Imaging

5.1 Introduction

Nowadays, conventional NDT methods, such as visual inspection, ultrasonic C-scan, thermography or shearography, are well established and frequently used in the field of quality control and defect inspection. Unfortunately, as one can imagine from an example such as an ultrasonic C-scan of a composite aircraft wing, these methods are quite bulky and time consuming and they require a team of skilled personnel to complete the set-up and interpret the analysis. Even though automation can decrease the inspection time significantly, there is still a great potential for improvement. Unlike point-by-point inspection techniques, GW techniques in these fields are driven by their ability to inspect large areas using only a limited amount of ultrasonic transducers. Therefore, the use of GW based NDT could significantly decrease the inspection time and costs compared to conventional NDT methods. Moreover, the transducers can be kept in place during the operational lifetime of the component, because they are small enough not to influence the mechanical performance of the component and they are durable. Therefore, GW based methods represent a perfect choice for SHM and defect imaging.

Lamb waves are one type of guided waves usually associated with elastic wave propagation in thin plates. Worlton [145, 146] was perhaps the first author who recognized the potential of Lamb waves for NDT. Shortly after, Grigsby [147] described and highlighted the most important properties of Lamb waves with respect to the inspection of thin plates. However, the modern era of Lamb wave research and practical applications dates back to the influential book written by Viktorov in 1967 [148]. In his publication, Viktorov described not only the underlining theoretical principles, but he also proposed a very practical way to generate Lamb waves in solid structures. Since then, Lamb waves found their way into many different fields. In NDT only, they have been used for inspection of plates [149, 150, 151], pipelines [152, 153], rails [10], steel wire ropes [154, 155, 156] and other complex structures, such as aircraft wings and fuselage panels [7, 157, 158, 159]. In the framework of our studies, we will focus solely on the application of the Lamb waves for the defect imaging in the plate-like structures.

One of the first attempts to visualize defects, in a form of a through thickness hole or a step change in thickness, in a thin aluminum isotropic plate was carried out in 1990 by Jansen and Hutchins [160]. They used immersion coupled transducers and the well-known *filtered back-projection* tomographic algorithm to reconstruct velocity and attenuation map of the inspected area. Wright and Hutchins [161] applied the same approach using the Air-coupled Ultrasound (ACU) to detect Flat Bottom Hole (FBH) and through thickness holes in perspex and CFRP plates. Hinders [162] and McKeon and Hinders [163] conducted very similar experiments replacing the ACU transducers with contact transducers. Several other studies followed soon after, e.g. [164, 165, 166], and suggestions were made to improve the performance of the tomographic method [167]. Nonetheless, the repeatability of the tomographic data acquisition procedure as well as the sensitivity to measurement noise proved to be very problematic [84, 168]. In addition, it turns out to be very difficult and cumbersome to extract proper Time of Flight (TOF) and amplitude values from a mixture of modes that interfere in the recorded GW signal. As a result, the attention has shifted to different concepts of inspection methods.

The most popular alternative methods are the *sum-and-delay* methods and the *probability based algorithms.* Both approaches rely on information obtained from a *sparse array* or network of ultrasonic transducers that are in most cases permanently attached to the inspected sample (see Fig. 5.1). The sparse array usually consists of variable number of small but efficient PZT *patches* [169].

The *sum-and-delay* methods are based on a signal processing tools that are known from ultrasonic phased arrays, the so called *beamforming.* Introduced to the field of ultrasonic GW testing by Giurgiutiu [170], these methods rapidly gained popularity. A thorough account on this topic has been written and compiled by Michaels et al. [171, 172, 173, 174].

The second group of methods employ probability based algorithms, and are based on the Signal Difference Coefficient (SDC) which quantifies the difference

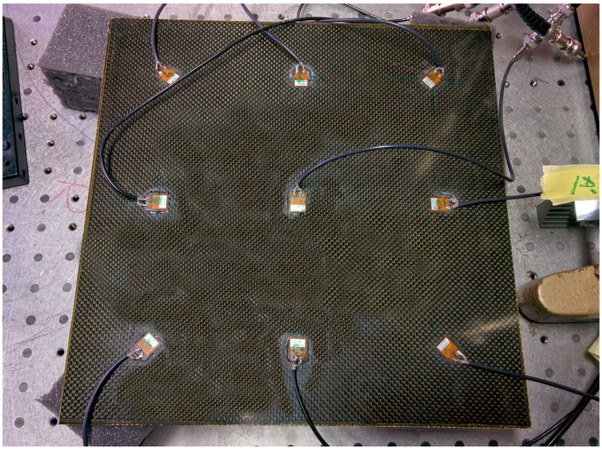

Figure 5.1: Ultrasonic sparse array attached to a composite sample.

between a signal acquired in the intact state and a signal acquired after damage was introduced to the sample [175]. Next, the SDC of each Transmitter-Receiver Pair (T-R) is projected on the corresponding path between the transmitting and receiving elements of the sparse array and all contributions are summed to provide a map of the damage indicator (damage index). This way, the damage is visualized and localized within the area defined by the sparse array network. The typical example of probabilistic SDC-based algorithm is Reconstruction Algorithm for Probabilistic Inspection of Damage (RAPID), which has been introduced by Hay et al. [176]. Since RAPID is a very flexible and versatile, it has been selected as the backbone of the proposed baseline-free nonlinear imaging algorithm that will be further developed in this chapter.

Since the main topic of this chapter deals with ultrasonic NDT of composite plates, we first have to understand the interaction of elastic waves with typical flaws in composite plates. Therefore, the first section of this chapter is dedicated to the guided wave interaction with damage. In the second section, we describe the conventional RAPID. The third section presents the novel baseline-free version of RAPID, taking into account features of nonlinear wave propagation. The capabilities and performance of the proposed method are demonstrated in the fourth section. The chapter is then summarized and conclusions are made in the last section.

5.2 Typical defects of layered composites

The typical defects found in layered composite materials can be divided in two major groups. The first group contains defects that were potentially introduced to the sample during the manufacturing process. Therefore, they should be rejected by the manufacturer's quality control. The second group contains defects that occur while the component is *in-service*. These are usually caused by external forces and excessive mechanical and/or thermal loading, such as foreign object impact, lighting strike or thermal damage. A great advantage of the non-metallic composites is their resistance to chemical degradation [177].

Since components leaving the manufacturing facilities are assumed to be defect-free, the development of inspection tools for in-service defects are of greater importance for SHM and NDT. Nonetheless, certain types of manufacturing defects can successfully serve as model for real in-service defects.

5.2.1 Manufacturing defects

Manufacturing defects usually occur during the lay-up or curing of the composite part. Since the fabrication and stacking of the plies is still mostly done manually without a significant degree of automation, human errors may occur. According to [178] and [179], the main types of manufacturing defects can be summarized by Tab. 5.1. Most of these defects can be detected during the final quality check of the manufactured component using standard NDT methods such as UT, VT or thermography [180].

Defect	Description
Disbond	An area in which two layers (plies) failed to bond together. Usually caused by lack of adhesive.
Delamination	An area where previously connected (bonded) layers of laminated material have been separated.
Porosity	The entrapment of bubbles in the laminate.
Inclusion	Foreign object inclusion.
Ply waviness	Deviation of the plies from straight alignment.

Table 5.1: Typical manufacturing defects that occur in layered composites. Adapted from [177].

5.2.2 In-service defects

SHM and NDT of in-service defects pose a greater challenge than in the case of manufacturing defects, even though the monitoring and inspection basically deal with very similar types of damage (see Tab. 5.2). In-service damage may occur due to the unforeseen environmental effects (hail, lightning) and excessive mechanical or thermal loading (turbulence, impact, tool drop, lightning strike) [181].

Defect	**Description**
Cracking	Cracking of the fibres or matrix due to excessive loading.
Impact damage	Internal damage of composite caused by collision with an external body typically marked by delaminations, fiber breaking, and matrix cracking.
Delamination	An area where previously connected (bonded) layers of laminated material have been separated.
Disbond	An area in which two layers do not adhere to each other anymore (zero volume).
Lightning burns	An area of the composite that has been subjected to high temperatures causing decomposition and degradation in properties of the matrix.

Table 5.2: Typical in-service defects that occur in layered fibrous composites. Adapted from [177].

The main reason why it is more difficult to detect in-service damage is the actual physical accessibility of the inspected part. It may concern a part with only one-sided access, or a stringer, or even a part that is not accessible at all with a conventional ultrasonic NDT system. The three most relevant defects - disbond, delamination and impact damage - will be further described.

Disbond, as described in Tab. 5.1, is usually introduced during the manufacturing process of the composite laminates. Typically, the main cause is a lack of adhesive (tape, paste) at a certain location that leads to poor bonding of the adjacent layers. Disbonds occur less frequently in plain laminated composite, but they are quite common in composite sandwich structures. In these structures, a ply or a laminate has to be bonded to a Nomex$^{©}$ core that is formed by a network of interconnected hollow hexagonal pillars. This may result in a poor quality bond thanks to a low bonding area between the skin and the core.

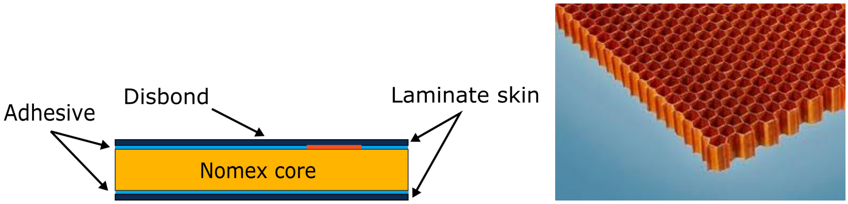

(a) (b) Nomex© core[1].

Figure 5.2: Disbond between a laminate skin and a Nomex© core.

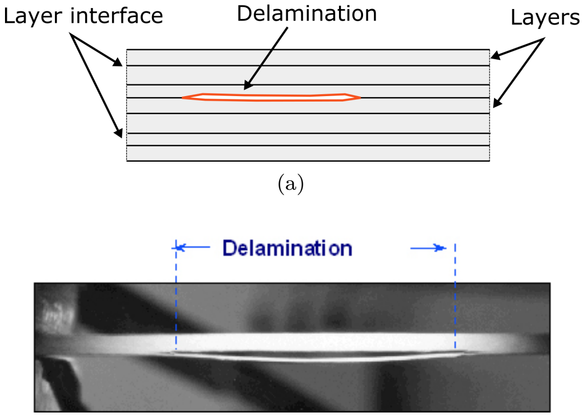

(a)

(b)

Figure 5.3: Delamination in a laminated composite[2].

Delamination is created when two previously bonded layers in the structure disconnect from each other. The layer faces are not connected anymore and a void can be created, as illustrated in Fig. 5.3. Delaminations typically run along the bond line (interlayer) and sometimes jump to another layer (intralayer). It locally weakens the structure and it can easily increase its area when subjected to additional stress. It also serves as a initiation point for crack propagation.

In layered composites, delaminations are usually caused by excessive out-of-plane loading. They are also often formed as a side effect of impact damage in which case they can initiate in more than one layer simultaneously.

---

[1] `http://www.nauticexpo.com/prod/plascore-gmbh-cokg/product-26310-172874.html`, 20/06/2016

[2] Adapted from `http://rutgersscholar.rutgers.edu/volume01/pelestra/pelestra.htm`, 22/06/2016

On the other hand, creating a sample that contains only a single artificial delamination is very challenging. Nonetheless, such type of samples with controlled artificial delamination is critical for the purpose of laboratory testing. The most widely adopted way to achieve this is to include a Teflon© or Kapton© insert in between the selected layers during the lay-up, creating a discontinuity between the layers. However, due to the curing at elevated pressure and temperature, the intended air void is usually tightly filled. Therefore, an insert can only serve as a first approximation of a real-world delamination.

Impact damage is a mixed type of defect that is created by an impact of a foreign object on to the surface of the laminate. It is often composed of a surface breaking crack, fibre and matrix cracking and several delaminations [182]. It represents perhaps the most severe defect that can affect a layered composite structure. The shape and severity of the fibre/matrix cracking is highly dependent on the size, velocity and energy of the impact [183, 184]. If the impact energy is high enough, the defect can be easily detected with simple visual inspection (see Fig. 5.4). On contrary, if the energy is sufficiently low, there may not be any visible indication of the impact on the surface of the laminate and the impact is termed Barely Visible Impact Damage (BVID). However, even BVIDs typically cause significant internal damage to the structure [185].

Microfocus computed tomography (μCT) provides an excellent tool to visualize and understand the damage made by an impactor in a plate. Several studies employing μCT reveal the extent and multi-scale structure of the internal damage [186, 187]. Currently, the golden standard in the ultrasonic detection of impact damage is the phased array or single transducer C-scan. If the appropriate frequency is applied and the measurements are combined with TOF analysis, the position of a horizontal stratification of the delamination can be determined [188]. Conversely, it is merely impossible to detect overlapping defects using the C-scan technique due to the specific nature of the pulse-echo testing in combination with the high acoustic impedance mismatch created by the delamination. In other words, the delamination closest to the transmitter will reflect most of the energy and block the wave propagation to the lower layers.

5.3 Optimal mode selection

There is a significant difference between bulk wave based and guided wave based NDT. For the inspection of plates, guided wave based techniques using

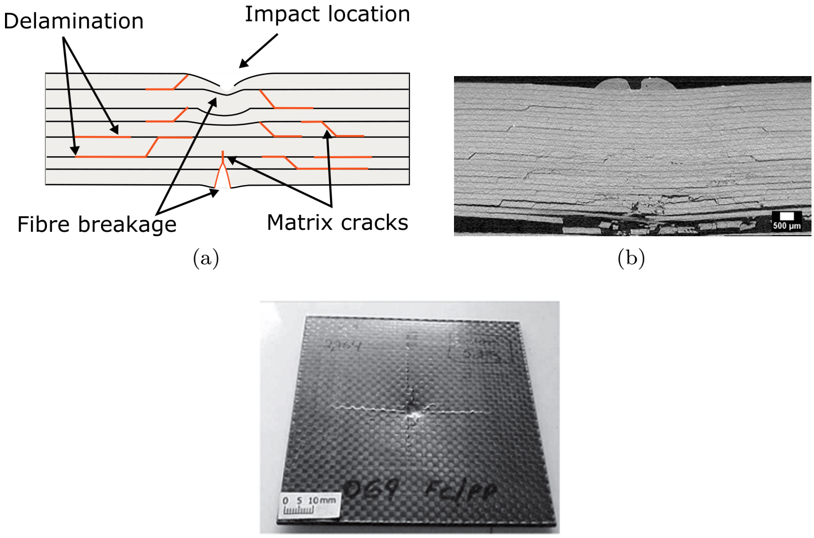

(a) (b)

(c)

Figure 5.4: Typical impact damage in a CFRP laminate: a) Illustration of the damage b) cross section as obtained using Microfocus Computed Tomography (μCT) [186] c) typical surface trace following a high energy[3].

symmetric and anti-symmetric Lamb modes are preferable. Successful detection and localization of damage depends heavily on the selected mode. It has been shown in chapter 3 that different modes have particular displacement profiles in the thickness direction of the plate. For example, it is desirable and more effective to detect surface and close-to-surface defects with GW modes that exhibit high stress and displacement components at the outer interfaces of the plate (A-modes). In contrast, defects in the center of a plate might be more easily detected using symmetric modes, since they have large in-plane displacements in the center plane of the plate. However, there are multiple parameters that have to be taken into account and an optimal mode selection is often very complicated. In order to make the right choice, we have to further investigate the interaction of guided elastic waves with the typical defects, introduced earlier.

GW mode selection plays an extremely significant role in the NDT research. The Probability of Detection (POD) can be greatly improved if the most appropriate mode is used. However, there are no straightforward guidelines for optimal

---

[3] Adapted from `http://www.scielo.br/scielo.php?script=sci_arttext&pid=S1516-14392005000100015`, 22/06/2016

mode selection, and discovering the best candidate mode remains a rather empirical procedure [189]. The following aspects have to be taken into account when searching for the optimal mode:

- excitability, generation and reception,
- dispersion and attenuation,
- interaction with defects,
- resolution,
- presence of surrounding liquid,
- shape of the sample.

5.3.1 Generation and reception of GW

Finding the most optimal means for GW excitation is the first problem that has to be solved before any NDT procedure can be started. There are generally five major ways to launch waves into thin plate-like structures:

- PZT transducer,
- wedge (angle beam) transducer,
- comb transducer,
- Electromagnetic Acoustic Transducer (EMAT),
- laser excitation.

PZT transducers

The first and perhaps the most popular way to launch and sense a GW in solid materials is the use of a simple PZT element (wafer) [170]. A typical PZT wafer, as depicted in Fig. 5.5 and Fig. 5.6, is cheap, light and small. Although not exactly suitable for single mode excitation, it is frequently chosen for its inherent simplicity [190, 170]. It is usually permanently attached to the structure using Polymethyl methacrylate (PMMA), epoxy-glue or other adhesives. Of course, the quality of the coupling significantly influences the performance of the transducer [191].

Figure 5.5: Typical PZT element (wafer)[4].

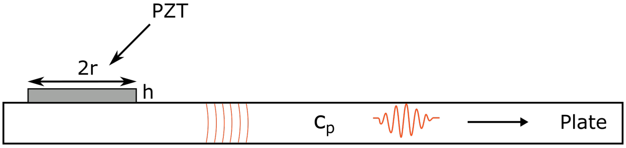

Figure 5.6: PZT transducer attached to the plate.

A typical PZT has a thin disk-shaped or rectangular-shaped element with high radius-to-thickness $\left(\frac{r}{h}\right)$ ratio. The mode selectivity of the transducer depends on this ratio as well as on the excitation waveform. A general rule of thumb for circular transducers is as follows: the thinner the transducer, the better it generates symmetric modes [192]. Su et al. [84] suggested that the dimensions of the element can be optimized for improved single-mode generation by applying the following rule:

$$2r = \frac{c_{ph}}{f}\left(n + \frac{1}{2}\right), \quad (n = 0, 1, 2, ..), \tag{5.1}$$

where c_{ph} is the phase velocity of the desired mode and r is the radius of the PZT. According to Nieuwenhuis et al. [193], this is mostly valid for generating the S_0 mode and suppressing the antisymmetric contribution. However, a more intricate design involving two coupled transducers on opposite faces of the sample can be used to effectively excite the antisymmetric modes [84, 194].

Another way to optimize mode selectivity and to suppress dispersion effects is to alter the shape of the excitation bandwidth. The goal is to excite the structure using a signal with as low bandwidth as possible in order to avoid other higher order parasitic modes. Therefore, sine-based waveforms are clearly more favourable than the pulse-shaped ones. However, the price to be paid is

---

[4] Adapted from `http://www.annon-piezo.com/pzt-4.asp`, 07/08/2016

that, if a windowed sine function is supposed to have a low bandwidth, it has to contain a larger number of cycles. This in turn increases the duration which is a strongly undesired effect due to the potential overlap of reflected signals with a direct emission response. Hence, a simple expression in the form of

$$f_{min} = f_0\Big(1 - \frac{k}{n_c}\Big) \tag{5.2}$$

$$f_{max} = f_0\Big(1 + \frac{k}{n_c}\Big) \tag{5.3}$$

where n_c stands for the number of cycles, k is a constant determined by the definition of the bandwidth being used (e.g. $k = 0.44$ for $-3\,\mathrm{dB}$ bandwidth) and f_0 is the excitation frequency, can be used to determine the bandwidth of the excitation [84, 189, 195]. Using the knowledge of the sample's geometry, n_c can be adjusted to minimize the bandwidth and preserve the separation of a direct transmission and reflection.

Wedge (angle beam) transducer

The wedge transducer is the oldest and most often employed method of generation and reception. It was first introduced and described by Viktorov in his pioneering work on Lamb waves [148]. The idea behind the method is in fact very simple. Imagine that a regular ultrasonic transducer is attached to a perspex solid wedge with longitudinal wave velocity c_1 under an incident angle θ (see Fig. 5.7). The wedge-transducer assembly can then be used to excite a GW with frequency f in a thin plate with longitudinal phase velocity c_{ph} if the projection of the wavelength of the incident wave λ onto the plate is given by [196]

$$\lambda_p = \frac{\lambda}{\sin\theta}, \tag{5.4}$$

where $c_{ph} = f\lambda$. In terms of longitudinal velocities, the previous equation yields

$$c_{ph} = \frac{c}{\sin\theta}. \tag{5.5}$$

This equation can be interpreted as Snell's law for a critical angle of refraction $\theta_2 = \frac{\pi}{2}$. In other words, it tells us what the incident angle θ if we want to launch a GW along the surface of the plate with a given phase velocity c_{ph}. Since the velocity of the guided wave can be precisely matched, the wedge technique is useful in narrowband generation and reception of a predefined mode. Moreover, a liquid wedge or even air-coupled transmission can be used

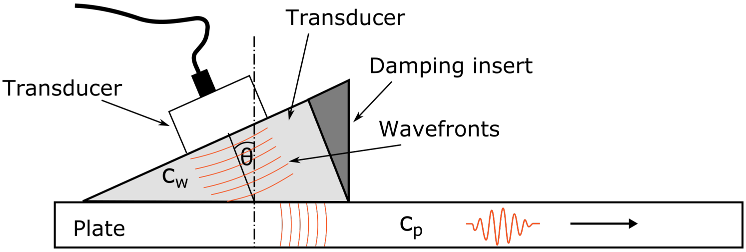

Figure 5.7: Wedge transducer.

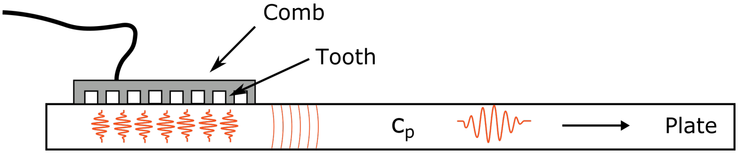

Figure 5.8: Comb transducer.

to excite specific Lamb modes in the plate, enabling non-contact GW NDT [12] and thus faster inspection times. On the down-side, since wedges and regular ultrasonic transducers are usually too bulky and too heavy to be permanently attached to an inspected structure, their application to SHM is extremely limited. A thorough mathematical study of wedge transducer operation was conducted by Jia in [197].

Comb transducer

Comb transducers (or interdigital transducers) are mainly utilized in the field of surface acoustic waves. However, they can be easily used to generate guided waves too. A mathematical model of the comb transducer is given for example by Rose et al. [198]. Typically, a comb transducer consists of a group of equally spaced parallel teeth bonded to a supporting layer, as depicted in Fig. 5.8. The whole comb is then attached to the sample and the teeth are forced to vibrate simultaneously, generating guided waves in the supporting plate [11].

EMAT

EMAT transducers are often used to excite and sense GWs in thin metal plates. They use the Lorentz principle in which a magnetic field is created underneath the transducer using a permanent magnet or an electromagnet. Elastic waves

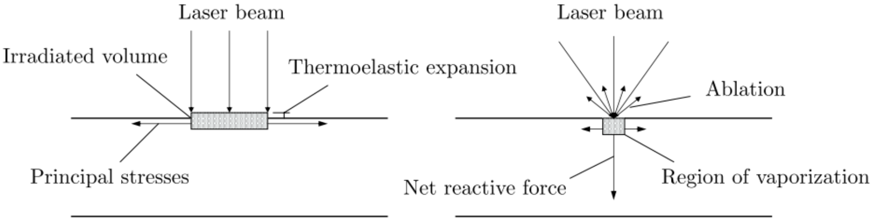

Figure 5.9: Different types of GW generation by laser irradiation [203].

are subsequently generated due to the interaction of eddy currents produced by the coil in the EMAT [11]. Their center frequency, bandwidth and output power depends predominantly on the geometry and the properties of the coil [199]. The most important advantage of EMATs is the non-contact excitation that excludes any type of liquid or solid couplant. On the other hand, EMATs operate only on electrically conducting materials, and they are also rather large.

Laser excitation

Laser excitation generates guided waves in materials via the thermoelastic effect. A short laser pulse (several ns) heats up a small region of the sample's surface leading to a rapid thermal expansion (adiabatic) [200]. Hence, an elastic wave is launched from the laser focus spot in all directions. The emitted wave is broadband due to the step-like nature of the excitation [15]. This feature is very useful in dispersion analysis and material characterization, because it enables probing large parts of the spectra. The advantages of laser generation are: non-contact, flexibility and speed. On the other hand, the broadband nature of the laser excitation is an obvious problem for guided wave based SHM, because it is very difficult to tune a specific mode. This can be partially overcome by sophisticated use of beam splitters and other optical elements to mimic a phased array transducer [17, 201]. Another concern includes safety and thermal ablation of the sample. As for the thermal absorption, the ablation also effectively launches GWs, but also destroys the surface of the sample [202]. The two different mechanisms, thermal expansion and ablation, are depicted in Fig. 5.9.

5.3.2 Dispersion and attenuation

Dispersion

Typically only the two lowest antisymmetric and symmetric modes are employed in NDT applications in order to decrease the complexity of the recorded signals and to enable an easier understanding. As can be seen from Fig. 5.10, the A_0 and S_0 modes are both nearly non-dispersive in the low frequency region. Moreover, their phase and group velocities are far different which makes them easy to separate. Another advantage of this low-frequency region is that higher order modes simply do not exist here, because it is below their cut-off frequency. The preference to work with the lowest order modes is very straightforward in this case as they enable easier interpretation due to their lower dispersion, difference in speed and limited mode conversion potential.

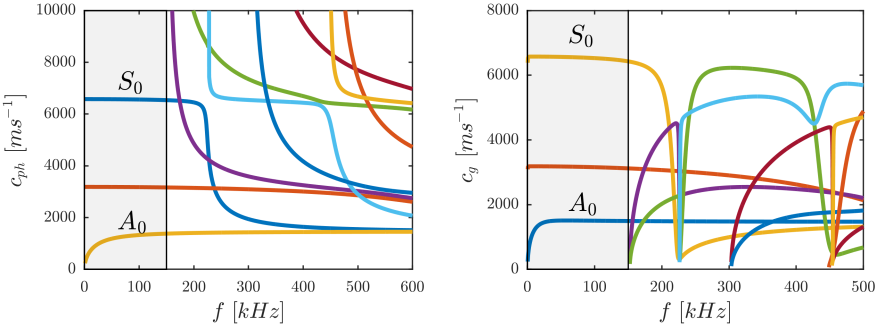

(a) Phase velocity (b) Group velocity

Figure 5.10: Example of GW dispersion.

In cases where higher order modes cannot be avoided, it is beneficial to apply dispersion compensation methods. Some of the appropriate algorithms to deal with dispersion compensation can be found in [204, 205, 206, 207, 208]. However, it is still better for array imaging to avoid frequency regions with significant dispersion if possible.

Attenuation

The amplitude of propagating Lamb waves in laminated composites decreases partially due to the geometric spreading effect which is proportional to the inverse square root of distance $\left(\frac{1}{\sqrt{r}}\right)$ and partially because of attenuation [209].

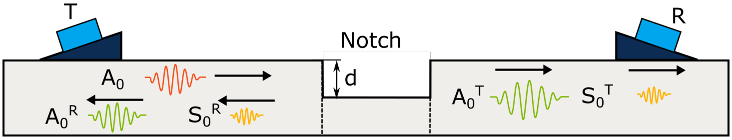

Figure 5.11: Guided wave mode conversion in a plate with notch. A_0 is launched from transmitter.

In fact, two main factors play a role in Lamb wave attenuation. The first one is the *material absorption* and the second is *leakage*. In our case, leakage effects do not have to be considered, because the GW testing in the present work always takes place in air. On the other hand, energy leakage is very important for attenuation of Lamb waves in fluid loaded samples [203]. The material absorption has a significant effect on the propagation in the laminated composites. For example, in a CFRP with a $[0, 45, 45, 0]_{2s}$ lay-up the attenuation due to material absorption can be as high as $1.45\,\mathrm{Np\,m^{-1}}$ and $10.60\,\mathrm{Np\,m^{-1}}$ for the S_0 and the A_0 modes, respectively, at 250-300 kHz range [209, 210]. Attenuation, alike most of the GW properties in anisotropic samples, is again direction dependent. Moreover, the direction dependency is generally different for different modes, according to Ono and Callego [210].

5.3.3 Guided wave interaction with defects

The first research studies that dealt with guided wave interaction with defects investigated predominantly the effects of a notch embedded in a plate-like structure [211]. The archetype of a notch was selected, because it can be used to approximate commonly encountered surface breaking defects, such as impact, corrosion (in metal plates) or cracks. Moreover, a notch in a plate in fact represents a step change in the plate thickness which is a typical design feature in many common aircraft structures, e.g. stringers [212]. The step in a skin-stringer assembly influences the GW propagation in a similar fashion as a notch in a plate [213].

In order to assess the effect of a notch on GW propagation, let us assume a simple homogeneous isotropic plate with a simple notch as depicted in Fig. 5.11. If a pure A_0 mode is launched from point T towards point R, it is partially reflected and partially transmitted towards the receiver R. Moreover, the A_0 mode is not only reflected, but also mode converted. Part of the fundamental antisymmetric mode's energy is converted to the first symmetric mode S_0 and vice-verse, if the emission would have been initiated using a symmetric mode [214]. Similarly, the transmitted signals contain the converted modes too [215].

As reported in [211], the sensitivity of different modes to the notch depends on the fd product as well as on the notch depth. In the same work, Alleyne and Cawley demonstrated that the reflection and transmission coefficients are relatively insensitive to the notch width if it is smaller than the wavelength of the propagating mode.

Leckey et al. expanded the analysis to rounded rectangle FBH in an isotropic aluminum sample and employed the 3D Elastodynamic Finite Integration Technique (EFIT) technique to study the GW interaction at higher fd values [216]. The authors concluded that a specific combination of shape and depth of the FBH (notch) results in the disappearance of certain modes and that the position of the transmitter with respect to the receiver plays a significant role in the scattering. Moreover, they pointed out that 2D simulations of GW interaction with damage is largely insufficient, even for a quite simple notch, because it does not take into account the full wavefield and geometry of the interaction.

Delamination

Studies addressing the interaction of guided waves with delaminations started to emerge two decades ago. Pioneering work was done by Guo and Cawley, who studied the interaction of the first symmetric mode S_0 with a delamination in CFRP laminate both analytically and experimentally [217]. Using a pulse-echo setup with a wedge transducer, they concluded that the interaction results in a back-scattered S_0 mode as well as a mode converted A_0. Moreover, they reported that the amplitude of the reflected wave depends predominantly on the depth (x_3-position) of the delamination and on the shear stress distribution of the incident mode. The reflected amplitude is largest, when the through-thickness position of the delamination corresponds to a maximum of the shear stress. If the delamination is placed in a plane where the shear stress approaches zero, the amplitude of reflection decreases. This was further confirmed by Hayashi and Kawashima [218], who numerically simulated the GW interaction with delaminations in cross-ply CFRP laminates using the Strip Element Method (SEM). In addition to the results of Guo and Cawley, they pointed out that no significant mode conversion takes place at the delamination site when considering an excitation using the anti-symmetric A_0 mode. Instead, the antisymmetric mode undergoes multiple forward and backward reflections in the layer above and below the delamination, causing the wave to be virtually *trapped* in the sections above and underneath the delamination. Another conclusion of their study was the fact that the A_0 mode is sensitive to delamination regardless of its through-thickness position.

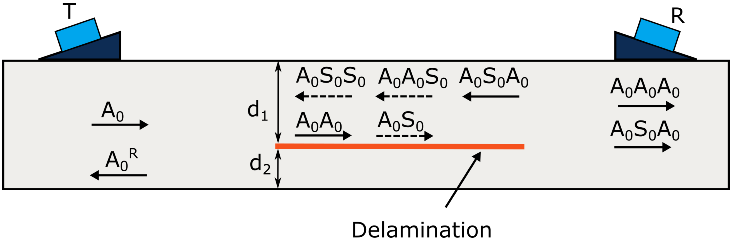

Figure 5.12: Guided wave mode conversion in a plate with delamination. The sequences in names define the chain of mode conversions that occurred due to the discontinuities.

Ramadas et al. [219] confirmed the trapped wave hypothesis presented in [218] and corrected the results of Hayashi and Kawashima fact by claiming that a symmetric S_0 mode is also created and is propagating through the sub-laminate, when an A_0 mode impinges on the edge of the delamination. However, the thus generated S_0 mode is confined to the delaminated region. The same conclusion is valid for symmetrically and asymmetrically located delaminations [220]. In support of this, Okabe and Fujibayashi [221] demonstrated numerically as well as experimentally that the mode conversion at the delamination is caused by the step change in thickness due to the delamination. The laminates separated by the delamination can be treated as two independent sub-laminates with different thickness d_1 and d_2 (see Fig. 5.12). Consequently, the two sub-laminates act as two plates with specific frequency-thickness products fd_1 and fd_2. Since these are different from the fd of the intact plate, they may generally support a different set of GW modes or the same modes with different velocities.

Ng et al. used FEM simulations to study the scattering of the fundamental A_0 mode by a delamination in 3D [222, 223]. They concluded that the scattered amplitude and its directivity depend on the wavelength-to-delamination-size ratio as well as the through-thickness position. Finally, Ricci et al. [224] confirmed that the previous observations in experiments are valid and stated that these conclusions can be easily applied even to more complex structures, such a stiffened CFRP panels. Additional numerical simulations and experimental measurements were done by Leckey et al., who demonstrated that the 3D EFIT simulation code can be applied to study the interaction of GWs with delaminations in anisotropic composites [225].

Disbond

From the interaction-with-GW point of view, disbonds generally behave similarly to delaminations. However, as they do not occur in plate-like CFRP laminates, they have not seen such a great share of attention up to now. Nevertheless, they are a common type of defect in sandwich composites, especially in cases where Nomex© cores are used. Disbonds are usually created during the manufacturing stage where the skin and core are bonded using a layer of adhesive paste. Any irregularity in its distribution can lead to the formation of a disbond.

Several pioneering studies were recently published trying to describe and analyze GW interaction with defects in sandwich structures [226, 227, 228]. Until recently, there has been little progress in the experimental detection of disbonds in sandwich structures. To date, most of the NDT on honeycomb and foam-core sandwich structures is done using acoustic-impedance-based bondtesters. Nonetheless, GW waves are slowly finding their way in this field too [229, 230, 231, 232].

Impact damage

As can be seen from Fig. 5.4, an impact results in a cluster of distinct defects with the most significant being delaminations and cracking (matrix, fibre). Moreover, the delaminations can be localized in multiple layers and they can be interconnected via an intricate network of fibre cracks [184]. Therefore, it is generally not a trivial task to simulate and predict the effect of impact damage on a propagating GW. Nonetheless, Leckey et al. performed such a numerical simulation using the EFIT method in which they implemented the actual impact damage geometry obtained using μCT [225]. They were able to numerically study the interaction and to compare it with experimental data. However, their results cannot be easily generalized since every impact creates a spectrum of complex internal damage. In addition, there is a huge computational cost in carrying out these 3D simulations.

Recently, several authors have demonstrated the method of *local wavenumber analysis* of propagating GWs to localize impacts, analyze the through-thickness distribution and the in-plane extent of delaminations [233, 87, 234]. The latest results also show that the local wavenumber method is very versatile when it comes to imaging different types of damage, such as cracks and delaminations [235, 236]. Even though definite progress has been made [236], the measurement time (up to 3 hours for an area 80x80 mm) and the employment of expensive LDV equipment that is necessary to capture the full wavefield propagation, currently prohibits its wider adoption.

5.3.4 Resolution

The resolution that can be achieved by carrying out experiments using specific GW modes depends on the wavelength of the applied mode which in turn directly relates to the phase velocity c_{ph} and the frequency f. Clearly, imaging using the antisymmetric A_0 mode generally provides a better resolution at the same frequency than symmetric modes due to the shorter wavelength.

5.4 Conventional baseline-dependent RAPID

Conventional RAPID, as described by Gao et al. [175], utilizes data from an ultrasonic sparse array consisting of n_e permanently attached PZT transducers. The direct line-of-sight coverage of such an array is visualized in Fig. 5.13. The SDC for each transmitter-receiver pair in the array is calculated. The SDC value thus represents a measure of the dissimilarity between each two signals obtained in two different states. Typically for the conventional RAPID, the two different states are: *baseline* (intact, without damage) and *damaged* (after the damage has been introduced). Most commonly, the SDC values are calculated based on the correlation coefficient or on the mean square error [176].

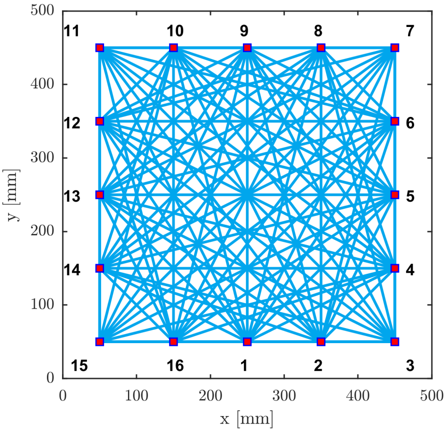

Figure 5.13: Array coverage with 16 PZTs.

Let the signal transmitted from the sparse array element i to element j be denoted B_{ij} and D_{ij} for the baseline and damage state, respectively. If the sparse array consists of n_e elements, then the total number of acquired signals is $n_e(n_e-1)$. The total number of signals can be reduced down to $\frac{n_e}{2}(n_e-1)$, if

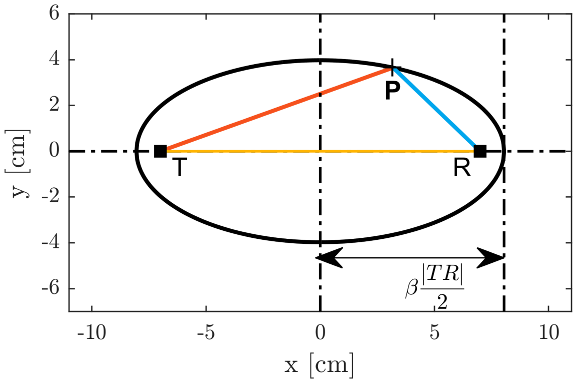

Figure 5.14: Geometrical interpretation of $R_{ij}(x,y)$ function.

reciprocity of the system ($B_{ij} = B_{ji}$) is assumed [158, 168]. From computational point, it is beneficial to recast the sparse array signals in a rank 3 tensor with time being the third dimension. All arithmetic operations can be then effectively implemented in MATLAB©.

5.4.1 RAPID algorithm

Fundamentally, the algorithm can be broken down into two major parts: the SDC calculation and the imaging. Even though being the second step in the algorithm, the imaging part will be described first, since it is general and common for both the baseline-dependent (linear) and baseline-free (nonlinear) version of the algorithm. Let us first thus assume that the SDC_{ij} coefficients are known for all T-R pairs. We start by dividing the inspected area of the sample in a rectangular equidistant mesh. Next, we define *a priory* probability distribution $s_{ij}(x,y)$ for each T-R and every point $[x,y]$ of the mesh as follows:

$$s_{ij}(x,y) = \begin{cases} \frac{\beta - R_{ij}(x,y)}{\beta - 1}, & \text{if } \beta > R_{ij}(x,y) \\ 0, & \text{if } \beta \leq R_{ij}(x,y) \end{cases}, \tag{5.6}$$

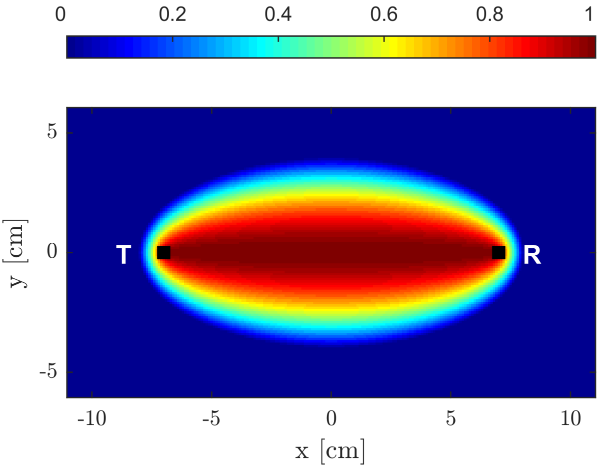

Figure 5.15: Values of the $s_{ij}(x, y)$ function for the shapes parameter $\beta = 1.15$.

where β stands for a free-to-choose shape factor that defines the area influenced by one T-R pair [237]. $R_{ij}(x, y)$ is a geometrical function defined as

$$R_{ij}(x, y) = \frac{\sqrt{(x_i - x)^2 + (y_i - y)^2} + \sqrt{(x_j - x)^2 + (y_j - y)^2}}{\sqrt{(x_j - x_i)^2 + (y_j - y_i)^2}}. \tag{5.7}$$

which is representing the ratio of the distances $|TP| + |PR|$ and the $|TR|$. As a result, the term $\beta - R_{ij}(x, y)$ from (5.6) actually describes an ellipse with focal points located in T, R and a major axis length $\beta\frac{|TR|}{2}$, as illustrated in Fig. 5.14. This ellipse forms the borderline of the region influenced by a particular T-R pair. If a selected point P lies within the area defined by the borderline, its $s_{ij}(x, y)$ decreases with the distance from the straight line that connects points T and R, as illustrated in Fig. 5.15. In other words, the further the point P from the direct path between the transmitter and the receiver, the lower its $s_{ij}(x, y)$ value will be.

The $s_{ij}(x, y)$ is evaluated for all T-R pairs and at all points of the rectangular grid. Once combined with the individual SDC_{ij} values, the final damage index heatmap is calculated as

$$P(x, y) = \sum_{i=1}^{n_e} \sum_{j=1, i\neq j}^{n_e} SDC_{ij} s_{ij}(x, y), \tag{5.8}$$

where contributions from all T-R pairs are summed up at a particular grid point with the SDC_{ij} values serving as geometrical weights. A cluster of points with a high damage index $P(x, y)$ then indicates the potential location of a flaw in the sample.

To illustrate the outcome, the conventional version of the algorithm will be described first. In case of the conventional implementation of RAPID, the SDC_{ij} is calculated using the standard *correlation coefficient* defined as

$$\rho_{ij} = \frac{\mathrm{Cov}(B_{ij}, D_{ij})}{\sigma(B_{ij})\sigma(D_{ij})}, \tag{5.9}$$

where

$$\sigma(B_{ij}) = \sqrt{\sum_{k=1}^{n_s}(B_{ij}[k] - \mu_{ij}^B)^2}, \qquad i, j = 1, 2, \ldots, n_e, \quad i \neq j, \tag{5.10}$$

$$\sigma(D_{ij}) = \sqrt{\sum_{k=1}^{n_s}(D_{ij}[k] - \mu_{ij}^D)^2}, \qquad i, j = 1, 2, \ldots, n_e, \quad i \neq j \tag{5.11}$$

are the variances and

$$\mathrm{Cov}(B_{ij}, D_{ij}) = \sum_{k=1}^{n_s}(B_{ij}[k] - \mu_{ij}^B)(D_{ij}[k] - \mu_{ij}^D), \quad i, j = 1, 2, \ldots, n_e, i \neq j \tag{5.12}$$

defines the covariance of the baseline and the damaged signals. Values μ_{ij} denote the mean value of the corresponding signal between transmitter i and receiver j, and the index $[k]$ simply indicates that all signals are discretely sampled at a sampling rate of $f_s = \frac{1}{\Delta_t}$ (Δt is the sampling interval). The SDC_{ij} value that quantifies the difference in signals can then be calculated using ρ_{ij} as

$$SDC_{ij} = 1 - \rho_{ij}, \qquad i, j = 1, ..., n_e, \quad i \neq j. \tag{5.13}$$

The lower the correlation between the baseline and damaged signals, the higher the SDC coefficient will be and more profound dissimilarity between the two signals.

The basic idea behind the use of SDC values for imaging purposes can be illustrated with the following example. Imagine that a damage has been introduced to a sample after the acquisition of baseline signals. The presence of the damage triggers changes in the wave propagation through the sample, and if the damage lies close to a direct path between a selected T-R pair of the network, the wave propagation will be altered significantly, resulting in a rise of the corresponding SDC_{ij} (correlation decreases). However, if the damage is sufficiently far from the sensor pair, its influence on the wave propagation will

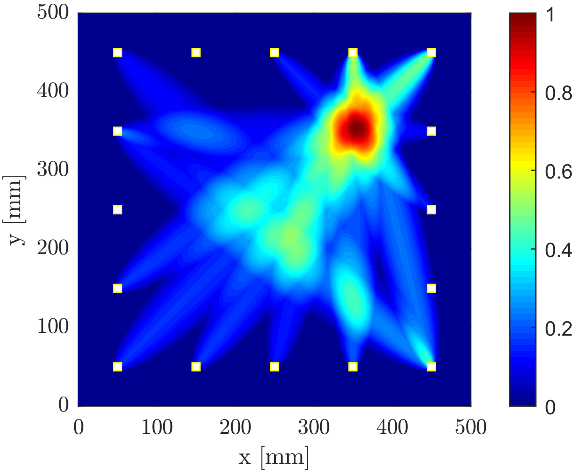

Figure 5.16: Example of a baseline-dependent RAPID imaging on a SARISTU plate. The red zone indicates the location of the defect.

be negligible and the corresponding SDC_{ij} value is low. Thus, by combining the input from all T-R pairs, the damage index $P(x, y)$ map can be constructed and the damage can be visualized. A typical result of the baseline-dependent RAPID is depicted in Fig. 5.16.

5.4.2 Experimental setup

For the experimental validation of RAPID, an experimental setup for GW imaging was developed, consisting of a single channel Arbitrary Waveform Generator (AWG) NI PXI-5412 that was routed to a multiplexing unit via a Falco WMA-320 amplifier or AR150A100B[5]. The signal from the switch board was connected to the individual PZTs of the sparse array network using a 50 Ω shielded coaxial cable (see Fig. 5.17). The input from the amplifier is connected to the transmitting element while the other elements are connected to the receiving digitizers - NI PXI-5122. Since the digitizer is a high-speed model, it only has two inputs. Therefore, multiple similar digitizers were used to acquire the signal from the sparse array. All transmitting and receiving cards were hosted in a single chassis NI PXI-1022. The transmitting element is disconnected from the receiving stage during the excitation to avoid leakage and crosstalk of this signal to other channels.

---

[5] Power amplifier, selectable gain up to 52 dB

(a) PXI instruments (b) Multiplexing unit

Figure 5.17: Experimental setup and measurement devices.

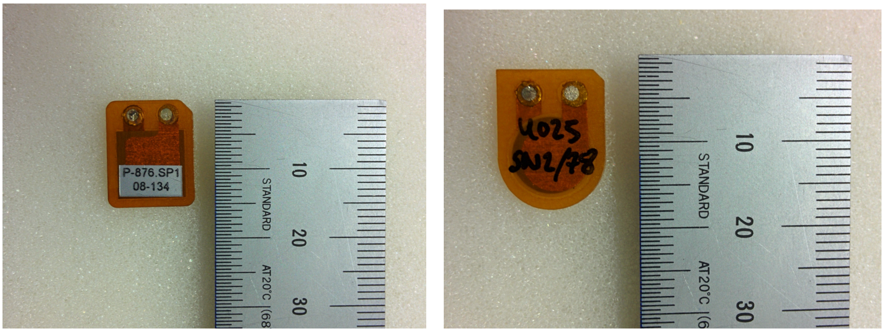

(a) Rectangular (b) Circular

Figure 5.18: DuraAct© P-876 PZT transducer.

The PZT transducers typically used as sparse array elements are depicted in Fig. 5.18. It concerns DuraAct© P-876 flexible PZT emitters/sensors, in either rectangular of circular shape, covered in a protective polymeric layer. The transducer specifications can be found in the datasheet[6] that is provided by the manufacturing company. It has been selected, because it has a safety approval for aerospace applications. Moreover, it is small and durable and it provides sufficient excitation amplitude. A typical annular sparse array can be seen in Fig. 5.19.

The entire measurement was controlled using a virtual instrument (VI) program written in LabVIEW©. The acquired raw waveforms were stored in the form

---

[6] `https://www.piceramic.com/en/products/piezoceramic-actuators/patch-transducers/p-876-duraact-patch-transducer-101790/`

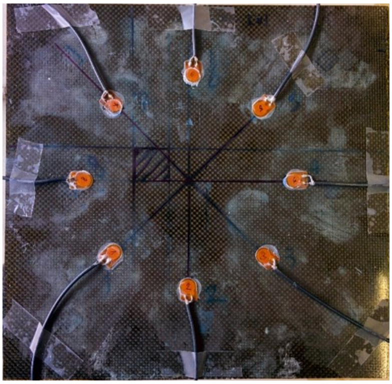

Figure 5.19: Sparse array of PZT transducers connected via coaxial cables.

of *.tdms* files. This datafile is a native ordered LabVIEW© equivalent of the *.hdf* (HDF5) file format that can be easily read and processed in MATLAB©. It also provides a built-in attribute and labelling option that help with tagging the waveform using the corresponding T-R. This makes it very easy to load any desired portion of the signal or even a single waveform specifically.

5.4.3 Experimental demonstration of RAPID

In order to illustrate the conventional baseline dependent RAPID, a test was conducted on a CFRP plate. The testing sample was the SARISTU plate that was previously described in section 3.1.4. It was equipped with 16 rectangular DuraAct© transducers that were coupled using Hysol© epoxy adhesive. The baseline signal was recorded at standard room temperature in laboratory conditions using the experimental setup described in section 5.4.2. It was then shipped to the University of Naples for impact testing, and it returned back with an 21 J impact in the upper right corner (see Fig. 5.20b).

Before and after the impact, the sample was excited using a 5-cycle sine burst at 50 kHz with Hanning window. According to the discussion of the dispersion curves in section 3.1.4, only the A_0 and S_0 modes are excited at this frequency range. Moreover, using the experimental dispersion analysis, it was found that the A_0 mode is the most dominant mode at this excitation frequency. The received signals were sampled at 10 MHz and $n_s = 16384$ samples were acquired. The input amplitude to the amplifier was 0.1 V. The "current" set of signals D_{ij} were acquired using the same test stand at ambient room temperature without any precise temperature adjustments.

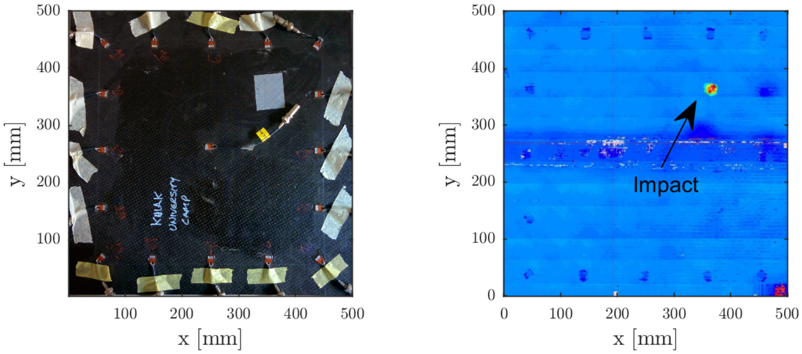

(a) (b)

Figure 5.20: SARISTU sample: a) a photo of the sample with the employed PZT array, b) ultrasonic C-scan of the sample after the 21 J impact. In addition to the red zone representing the impact location, the transducers are clearly visible as dark blue spots around the perimeter of the plate.

For the subsequent analysis, the length of the signal between every T-R pair was restricted to include only the direct propagation of the A_0 mode [238]. This was easily done based on the angular dispersion data, and the phase and group velocities from section 3.1.4. Hence, knowing the propagation distance, direction and velocity, the signal can be properly time-windowed.

The resulting heatmap of $P(x, y)$ for the SARISTU plate is displayed in Fig. 5.21. it clearly highlights the damaged area of the plate. There are several ways to improve the results of the conventional RAPID imaging method. First, the shape factor β can be decreased in order to narrow down the area influenced by each individual T-R pair. The effect of this adjustment is illustrated in Fig. 5.22. Recently, Sheen and Cho [239] propose the shape factor β optimization that applies changeable values for different T-R pairs. Unfortunately, the shape factor optimization algorithm is only applicable to isotropic samples.

Secondly, the SDC value can be thresholded prior to being used in the imaging step. The SDC values are first rescaled to $\langle 0, 1\rangle$. Next, the values below a specified threshold are set to 0 and the remaining ones are left intact. The subfigures a) and b) in Fig. 5.23 depict the matrices of SDC values for all T-R pairs before thresholding and after thresholding using a cut-off at 0.5. Clearly, the number of contributing T-R pairs significantly dropped after applying the threshold value of 0.5. In a more advanced manner, the value of the threshold t_{SDC} can be determined empirically or linked to the mean value and standard

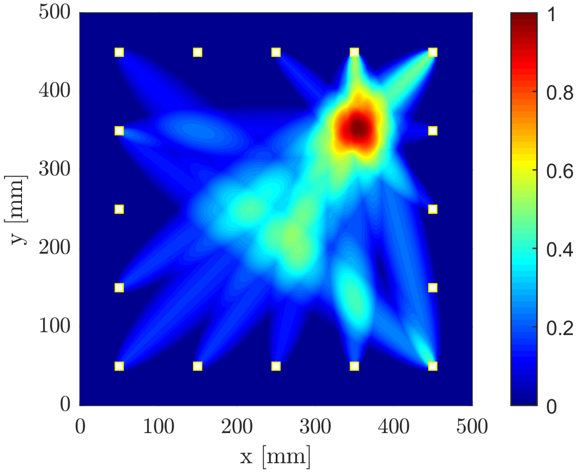

Figure 5.21: Baseline-dependent RAPID imaging on the SARISTU plate, excitation frequency $f = 50\,\text{kHz}$, $\beta = 1.015$, thresholded SDC values. The red zone indicates the location of the defect.

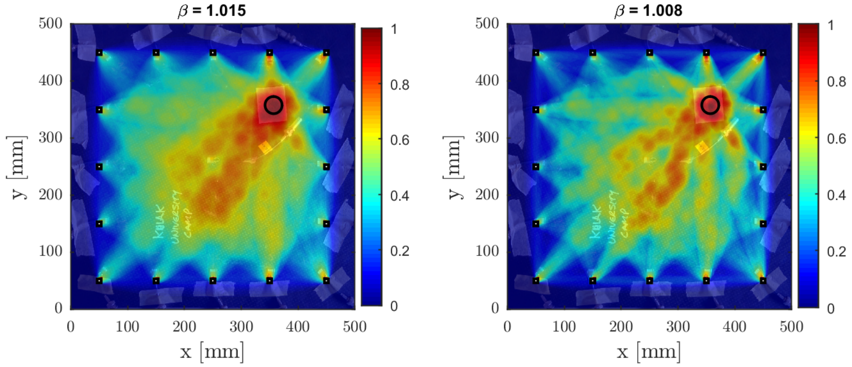

(a) $\beta = 1.015$

(b) $\beta = 1.008$

Figure 5.22: Final image using different values of shape factor β and no SDC threshold.

deviation of the initial SDC values. The general description of this thresholding operation is

$$SDC_{ij} = \begin{cases} 0 & \text{if } SDC_{ij} < t_{SDC} \quad i,j = 1,2,..,n_e, i \neq j \\ SDC_{ij} & \text{if } SDC_{ij} \geq t_{SDC} \quad i,j = 1,2,...,n_e, i \neq j \end{cases} . \tag{5.14}$$

The values in Fig. 5.23a represent only a half-populated SDC matrix, because reciprocity was assumed during the signal acquisition. The non-symmetric distribution of the values in the matrix is caused by the fact that elements 14-16 were used (out-of-order) as receivers instead of transmitters due to the lack of acquisition channels. Using this switching scheme, a significant time gain was achieved. The effect of this thresholding on the quality of the RAPID image is clearly illustrated in Fig. 5.23c and Fig. 5.23d. A third way to improve the obtained image is to simply threshold the probability distribution at a fixed level, thereby creating a binary image which immediately pinpoints the areas with the highest damage index $P(x, y)$ (see Fig. 5.24). If a fixed threshold is applied to the result, the size and location of the suspected defect(s) can be easily estimated.

Although the procedure looks very simple and effective, an important problem in conventional RAPID is the baseline selection. If the coupling of the transducers and the measurement conditions remain constant during both acquisitions, the result is accurate, as was described in this section. However, problems may arise when the measurement conditions change before and after damage. Several means to counteract these effects are summarized in the next section.

5.4.4 Baseline selection

As can be understood from (5.9), the SDC values strongly depend on the quality of the baseline. Note that the set of baseline signals has to be acquired prior to the damage introduction, i.e. in an intact state. This usually implies that the data are acquired under rather controlled environmental conditions. However, that is not necessarily the case for the damaged state which is assumed to be performed during operation (SHM) or during maintenance checks (NDT). Therefore, the measurement conditions can be very different and may considerably influence the guided wave propagation characteristics, and subsequently the imaging result.

Temperature, humidity, loading conditions and deterioration of the transducer coupling can be considered as the most significant environmental influences affecting the quality of the baseline-dependent RAPID [240]. Their effect on the acquired signals and the imaging procedure can be basically compensated using the following approaches:

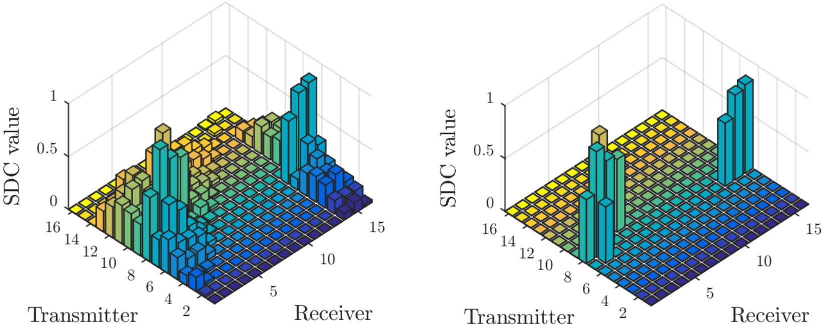

(a) Without SDC threshold

(b) SDC threshold at $\frac{\max\{SDC_{ij}\}}{2}$

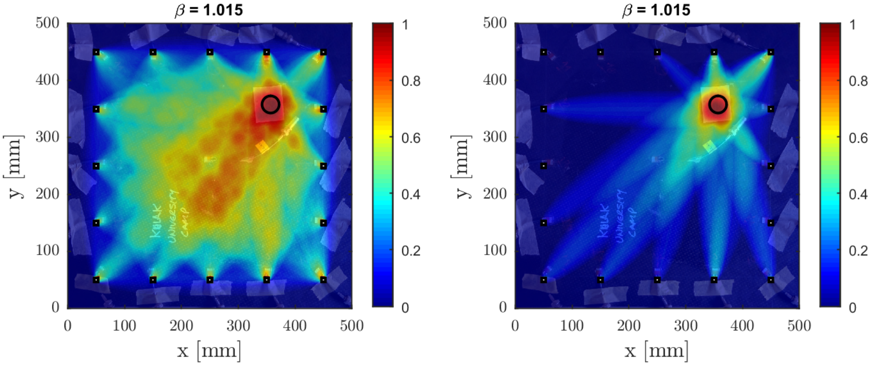

(c) Without SDC threshold

(d) SDC threshold at $\frac{\max\{SDC_{ij}\}}{2}$

Figure 5.23: Influence of the t_{SDC} threshold on the imaging algorithm. a) and b) show the SDC values before and after thresholding for different T-R pairs while c) and d) display the corresponding imaging result. Excitation waveform: 5-cycle sine burst 50 kHz with Hanning window.

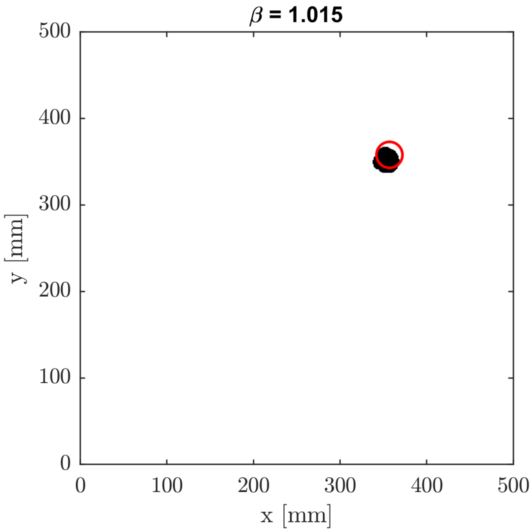

Figure 5.24: Thresholded binary RAPID image using a threshold level at $T_P = 0.9\max\{P(x,y)\}$. Excitation waveform: 5-cycle sine burst 50 kHz with Hanning window. Red circle indicates the real damage location.

.

- Optimal Baseline Selection (OBS)
- Baseline Signal Stretch (BSS)
- Combination of OBS and BSS.

Optimal Baseline Selection

The OBS approach utilizes a database of baseline signals that were acquired under varying conditions of temperature, loading, etc.. The database is created using the anticipated conditions that the structural part can be exposed to during its lifetime [174, 240]. After acquiring the signals in damaged state, the database of sparse array baselines is searched for the optimal signals that minimize the residuum of subtraction from the damaged signals. This algorithm is then called the optimal baseline and is further used as input for the imaging algorithm. The two most typical residuum measures are the mean square deviation

$$m_{opt} = \arg\min_{m} \Big\{ \int_0^N (D_{ij}(t) - B_{ij}^m(t))^2 dt \Big\}, \tag{5.15}$$

and the maximum residual amplitude [241]

$$m_{opt} = \arg\min_{m} \Big\{ \max |D_{ij}(t) - B_{ij}^{m}(t)| \Big\}, \tag{5.16}$$

where m runs over all possible sets of baseline signals in the database, and m_{opt} denotes the index of the optimal baseline in the baseline dataset. It is better to carry out this search for each T-R pair. However, it can be done using a single selected pair if environmental conditions are assumed to be constant along the inspected sample. The OBS approach suffers from one major problem: the database of baselines has to be large and dense in order to provide a reasonable subtraction performance. For example, Clarke et al. [242] advised to consider a temperature step of approximately 0.1 °C between two subsequent baselines in order to achieve sufficient imaging quality in a steel plate. Yet, this is only one to account for one varying parameter. One can imagine that the size of the database becomes extremely large and excessive if one wants to anticipate complex changes in measurement conditions.

Baseline Signal Stretch

Another approach for baseline selection is the BSS. Unlike the OBS, it only requires a single set of sparse array baseline signals to compensate temperature and other parasitic effects [241]. The original baseline signals $B_{ij}(t)$ are stretched (compressed or dilated) by a stretch factor $\hat{\beta}$ in order to best match the current (damaged) signal.

$$\hat{B}_{ij}(t)|_{T=T_0} = B_{ij}(t/\hat{\beta})|_{T=T_0}, \tag{5.17}$$

where T_0 stands for the temperature at which the baseline was acquired. The effects introduced by temperature drift can be compensated by the signal stretching. Typically the stretching is performed in the frequency domain as a stretch in time domain corresponds to a change in the position of the frequency peaks. The best match is then obtained iteratively using the residuum metrics defined in (5.15) and (5.16). Details of the numerical implementation and the pitfalls of the approach are thoroughly described by Croxford et al. in [241].

According to Croxford [241], the best result can be achieved by employing a combination of OBS and BSS. However, problems with the applicability to real-world conditions remain, e.g. keeping the size of the baseline database practicable. In order to circumvent these problems, it is worth the effort to try to develop a baseline-free imaging method.

5.5 Baseline-free nonlinear RAPID

5.5.1 Algorithm

The conventional RAPID methodology was outlined in the previous section together with its main advantages and disadvantages. It is clear that the weakest spot is the baseline selection process. In this section, we propose a method that transforms the conventional RAPID into a baseline-free method by introduction of an SSM-based SDC parameter. This eliminates the requirement for an intact baseline signal which should improve the real-world applicability of RAPID.

First, some major assumptions have to be presented before the method itself is described. It is assumed that

- the defect behaves nonlinearly with increasing excitation amplitude,
- the nonlinearity of the equipment is low.

These assumptions have to made, otherwise the new localization concept would make no sense. If the nonlinearity of the transmitter and receiver is higher than the nonlinearity of the defect, the imaging would simply fail.

The details of the baseline-free RAPID method are as follows. First, a low amplitude excitation signal is applied to the sparse array transducers and the corresponding response signals B_{ij} are obtained. The response signals B_{ij} will act as reference (defect-free) signals. Next, a high amplitude excitation is applied and the response signals D_{ij} are acquired under the same measurement conditions. Both sets of measurements can be obtained at the same time (a matter of seconds difference). The only difference is that the excitation amplitude has been up-scaled by a scaling factor

$$k_s = \frac{A_D}{A_B}, \tag{5.18}$$

where A_B, A_D are the amplitudes of the excitation signals for low and high amplitude, respectively. The new, nonlinearity based, SDC coefficient, as defined in section 4.3, is obtained by calculating the mean square difference between the high amplitude response signals and the up-scaled low amplitude response

$$SDC_{ij} = \frac{1}{n_s} \sum_{k=1}^{n_s} (k_s B_{ij}(t_k) - D_{ij}(t_k))^2. \tag{5.19}$$

As can be seen from (4.25), this definition of the new SDC values is based on the SSM parameter $\theta(A)$. If the inspected system is purely linear, the response signals scale up perfectly and are simply equal to $k * B_{ij}$. Hence, the value of the SDC will be equal zero in this case. The imaging will result in a blurred unfocused image without any defect indication. However, if a nonlinear defect is present in the interrogated sample, the SDC value attains a non-zero value for some of the T-R paths. Based on this principle, the SDC in (5.8) can be simply replaced by equation (5.19) and the new RAPID method basically becomes baseline-independent, because it does not need an input from a state measured before the damage took place.

There are currently no fixed guidelines to select the appropriate values of A_B and A_D. Hence, a simple rule of thumb can be used. The value of A_B has to be as low as possible and, at the same time, it has to preserve a useful SNR. This ensures that the low amplitude response is not dominated by noise. The high amplitude value A_D has to be as high as possible without provoking a significant nonlinear response of the transducer and the measuring circuitry.

5.5.2 Correction for direct path propagation

The original RAPID algorithm brings about one obvious problem. For the imaging to be successful, the SDC value for each T-R pair should be calculated only for a direct propagation path (extended by parameter β) between the transducers. In this case, it is clear then that the damage (current) signal only alters inside the imaging area (i.e. the area inside the sparse array). Otherwise the SDC might have been spoiled by changes in reflection that occur outside of the imaging area.

In order to restrict the useful signal and include only the direct propagation, a simple manipulation can be suggested for the received signal. Let us assume that the distance between the transmitter and receiver is x and the angle of propagation with respect to the coordinate system of the plate is θ, as illustrated in Fig. 5.25. Furthermore, we assume that the entire recorded signal contains n_s samples. To assure that only the direct propagation is taken into account, a reduced amount of samples n_r can be considered. Here, n_r $(n_r < n_s)$ can be easily calculated from an estimate of the TOF between transmitter i and receiver j as follows

$$n_r = \lfloor TOF_{ij} f_s \rfloor + \frac{n_c}{2}\frac{f_s}{f}, \tag{5.20}$$

where f_s is the sampling frequency, n_c is the number of cycles in the excitation waveform at a frequency f. TOF_{ij} is a time of flight defined as

$$TOF_{ij} = \frac{x}{c_{ph}(\theta)}, \tag{5.21}$$

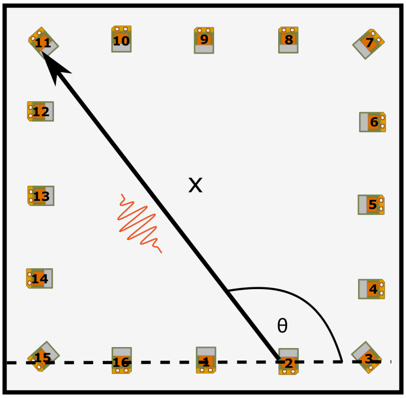

Figure 5.25: Adaptive signal length correction.

where x is the distance between T-R and $c_{ph}(\theta)$ is the phase velocity in the direction given by the angle of propagation θ. As can be seen from (5.20), a number of cycles n_c that is equal to the arrival time of the center of the wave packet is taken into account. The velocity can be determined from numerical dispersion data, as can be seen in Fig. 3.4, provided most of the elastic constants of the sample are known. This approach is called Adaptive Signal Length Correction (ASLC) and is used to ensure a proper imaging strategy in anisotropic materials. The phase velocity can be replaced by group velocity depending on the type of excitation (continuous sine or pulsed). Generally, if the excitation is narrowband, the use of phase velocity is sufficiently accurate.

Respecting the above described basic concepts, the following section demonstrates the performance of the algorithm with the numerical simulation data.

5.5.3 Numerical simulation

Numerical model

Numerical simulations were carried out in order to verify the proposed baseline-free RAPID methodology. The test sample was simulated as a simple bulk square CFRP T300/924C plate with orthotropic symmetry and dimensions of 288 x 296 x 2.7 mm. The density of the material is $\rho = 1548\,\mathrm{kg/m^3}$ and its elastic properties are summarized in Tab. 5.3. The simulation model also includes damping that was implemented using a Rayleigh damping model, which is standard included in COMSOL Multiphysics©. The model is described by

Young's modulus [GPa]	Shear modulus [GPa]	Poisson's ratio
$E_{xx} = 127.10$	$G_{xy} = 5.0$	$\nu_{xy} = 0.320$
$E_{yy} = 8.34$	$G_{yz} = 2.7$	$\nu_{yz} = 0.461$
$E_{zz} = 8.85$	$G_{zx} = 4.8$	$\nu_{zx} = 0.461$

Table 5.3: Material properties of the T300/924C composite.

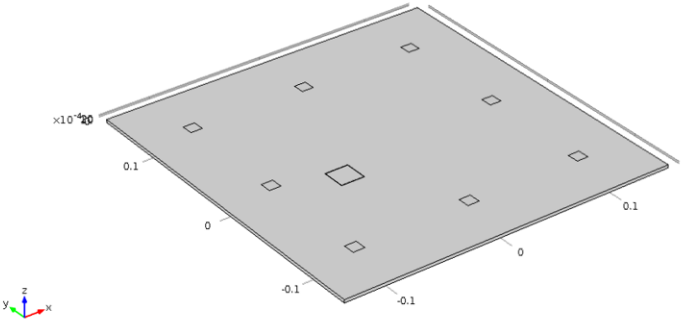

Figure 5.26: Simulated plate.

equation

$$c = \alpha_{dM} m + \beta_{dK} k, \tag{5.22}$$

where α_{dM} and β_{dK} are mass and stiffness damping coefficients, respectively. m stands for a mass and k denotes stiffness of the system. The parameter α_{dM} controls the damping in a low frequency region while β_{dK} governs high frequency regions. Details of the implementation of the damping model can be found in the COMSOL Multiphysics© manual[7]. In our case, the mass damping parameter α_{dM} was set to zero and the stiffness damping parameter

$$\beta_{dK} = \frac{1}{2\pi f Q} \tag{5.23}$$

was defined based on the quality factor Q. The quality factor was chosen to be constant ($Q = 20$) for all simulations.

Fig. 5.27 shows the dispersion curves of the simulated plate that were calculated using the Legendre approximation approach. The dependency of the phase velocity on the angle of propagation for the fundamental modes at a fixed

---

[7] `http://plato.fab.hs-rm.de/web-mathematik/mathematik/semester8/mechanik/StructuralMechanicsModuleUsersGuide.pdf`

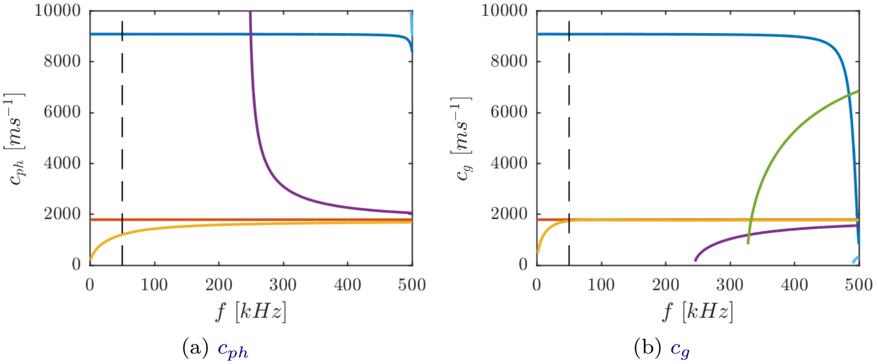

(a) c_{ph} (b) c_g

Figure 5.27: Dispersion curves for the simulated plate (T300/924C).

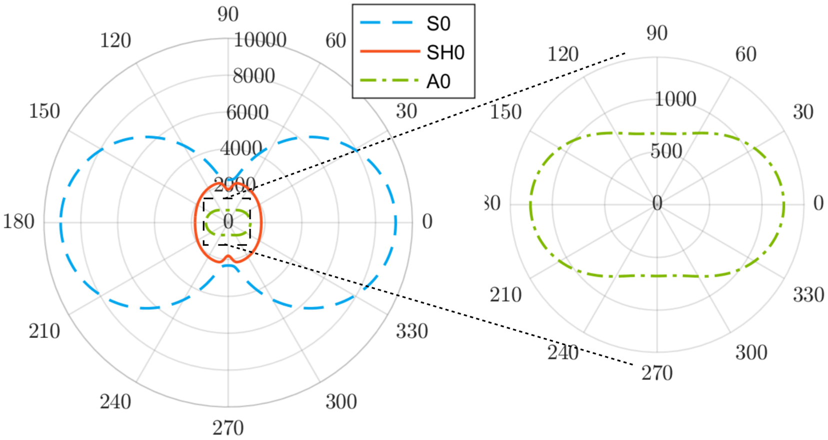

Figure 5.28: Angular profile of c_{ph} at 50 kHz for simulated plate (T300/924C).

frequency of 50 kHz is illustrated in Fig. 5.28. These data will be used to carry out the direct propagation correction.

For the simulations, the sample contained either one or two (depending on the configuration) 20 x 20 mm nonlinear delaminations located at 1/4th of the plate's thickness (see Fig. 5.26). Each defect was simulated as a clapping system (kissing bond) based on the nonlinear stress-strain model developed by Delrue and Van Den Abeele [243]. The graphical representation of this model is illustrated in Fig. 5.29. The nonlinear dynamic behaviour of the delamination is controlled by a set of virtual spring and damper forces at both sides of the delamination, as illustrated in Fig. 5.29. These forces can be expressed as functions of the gap distance Δz. Above a certain separation threshold, the two sides are completely separated (stress free surfaces), below the threshold particular formulations of the Vanderwaals forces are implemented. When the surfaces are close to each other, they will be attracted to each other. However, when they tend to be too close, the attraction force will turn into a repulsive force, trying to separate the surfaces again. The piecewise behaviour of these additionally introduced elastic contact forces for a kissing bond is illustrated in Fig. 5.30.

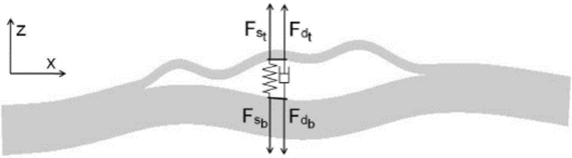

Figure 5.29: Spring-damper model of a nonlinear delamination [244].

Apart from the elastic contact force, damping forces were also implemented which are acting against the velocity of separation. These forces make sure that the surfaces of the delamination are not opening too abruptly, avoiding a destruction of the material. At the same time, they assure that the surfaces are not closing too fast so that the two surfaces cannot overlap. These forces are shown in Fig. 5.31. The nonlinear viscoelastic behaviour at the delamination level mimics the clapping behaviour of a delamination. Depending on the displacement amplitude of the wave passing by the defect, this nonlinearity will be activated or not, creating a distortion in the wave propagation which can be measured in the received signal after appropriate signal processing. Amplitudes must reach a certain threshold for the clapping nonlinearity to be activated. If the wave amplitudes are too low to separate the surface in case of a closed defect, or too low to bring together the surface in case of an open crack, there will be no influence in terms of waveform distortion or spectral broadening on the wave propagation.

The implementation of the nonlinear spring-damper forces is performed by introducing dynamic boundary conditions in COMSOL Multiphysics$^{©}$, at those nodes that correspond to the delamination surface. At these positions, the nodes are split in pairs and the following analytical formulae are implemented for the spring and damper forces [243]:

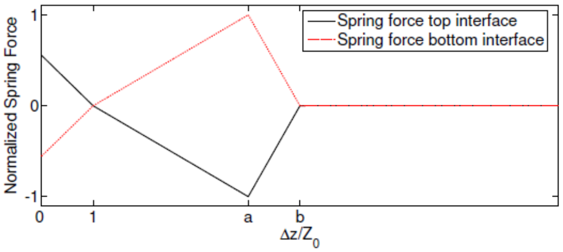

Figure 5.30: Spring forces F_{s_t} and F_{s_b} at the simulated delamination interfaces as a function of the gap distance Δz [244].

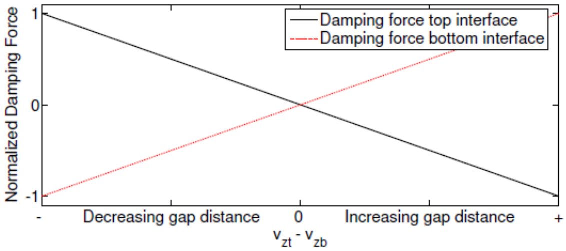

Figure 5.31: Damping forces F_{d_t} and F_{d_b} at the simulated delamination as a function of the gap distance Δz [244].

$$F_{s_t} = -F_{s_b} = \begin{cases} k_1(Z_0 - \Delta z) & \text{if} \quad \Delta z < Z_0 \\ k_2(Z_0 - \Delta z) & \text{if} \quad Z_0 \leq \Delta z < aZ_0 \\ k_3(bZ_0 - \Delta z) & \text{if} \quad aZ_0 \leq \Delta z < bZ_0 \\ 0 & \text{if} \quad bZ_0 \leq \Delta z \end{cases}, \tag{5.24}$$

$$F_{d_t} = -F_{d_b} = \begin{cases} -\gamma(v_{z_t} - v_{z_b}) & \text{if} \quad \leq \Delta z < bZ_0 \\ 0 & \text{if} \quad \Delta z \geq bZ_0 \end{cases}, \tag{5.25}$$

where Z_0 is a small characteristic distance between the faces of the delamination, a, b are free parameters defining the separation conditions ($1 < a < b$), γ is a damping coefficient, and v_{z_t} and v_{z_b} stand for the normal velocities of the top and bottom interfaces. k_1, k_2, k_3 are the virtual spring constants that are connected by

$$k_3 = \frac{1-a}{b-a} k_2. \tag{5.26}$$

Parameter name	Value	Unit
Z_0	0.1	mm
a	4	
b	5	
k_1	$5 \cdot 10^{13}$	Nm^{-3}
k_2	$5 \cdot 10^{12}$	Nm^{-3}
γ	10^7	Nsm^{-3}

Table 5.4: Model parameters of the nonlinear delamination.

Details on the parameter values for the nonlinear delamination model that was used in the numerical simulation are summarized in Tab. 5.4. The baseline excitation amplitude was $A = 10^{-8}$m and the waveform consisted of 20 cycle Hanning windowed sine burst at 50 kHz. The SSM scaling factor was set to $k_s = 100$. The excitation was implemented as a prescribed normal displacement at the area of the transmitting virtual element. The received signal was sampled with a sampling frequency of $f_s = 10\,\mathrm{MHz}$.

Results

Figures 5.32 to 5.36 show the results for a CFRP plate containing of the baseline-free RAPID detection of a single or two nonlinear delaminations with the properties described in previous section. The imaging was carried out using a sparse network of 8 virtual transducers placed in a rectangular array. The locations of the transducers are depicted in Fig. 5.26.

Test case 1

The first test case included a single nonlinear delamination that was placed in the lower left corner of the plate. The center of the delamination is located at [-50,-20]. The adaptive signal length correction was applied using the dispersion data from Fig. 5.28, the shape factor was fixed to $\beta = 1.015$ and the SDC threshold was set to $t_{SDC} = 0.25$. Fig. 5.32 depicts the imaging result using the prescribed scaling coefficient $k_s = 100$, without and with binary thresholding. The delamination is clearly indicated on both figures. Using the binarized image with the threshold set to $P(x, y) = 0.8$, the precise location of the delamination can be obtained (see Fig. 5.32b). The predicted location is in very good agreement with the actual position of the delamination in the plate. Moreover, the size of the delamination is well estimated at this given threshold level. A small parasitic indication that is caused by the array shape appears next to the central-left transducer. However, it is negligible in size compared to the defect indication.

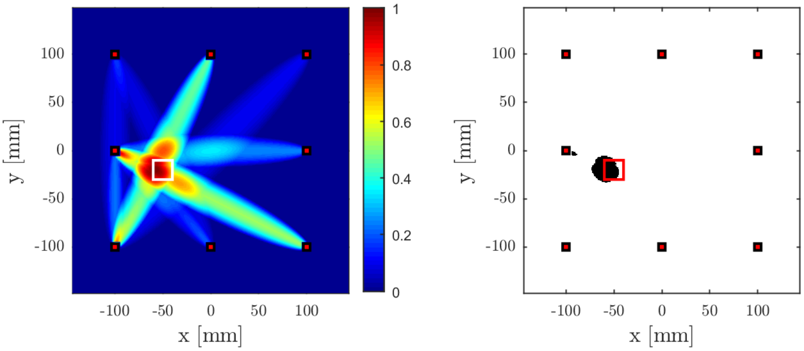

(a) $P(x, y)$ (b) Binarized image

Figure 5.32: Result of nonlinear RAPID imaging on a simulated anisotropic plate, without binarization (left) and with binary thresholding (right). The excitation waveform was a 20-cycle sine burst, at 50 kHz with Hanning window. The center of the delamination is located at [-50,-20]. Threshold for binarization was set to $P(x, y) = 0.8$. The actual location of the delamination is marked with white and red squares, respectively.

Test case 2

In the second test case, the same delamination was moved to a different sector on the plate (location [30,70]). The output of the baseline-free RAPID is displayed in Fig. 5.33a. The imaging parameters were similar to the test case 1. As can be seen from Fig. 5.33b, the size and location of the delamination was detected very precisely.

The imaging algorithm performs very well in the single-defect scenario, the next step in the evaluation of the imaging performance is a test case with multiple delaminations.

Test case 3

The third test case consisted of a plate with two identical (in size and in nonlinear parameters) delaminations located in different positions: delamination 1 (DEL1)

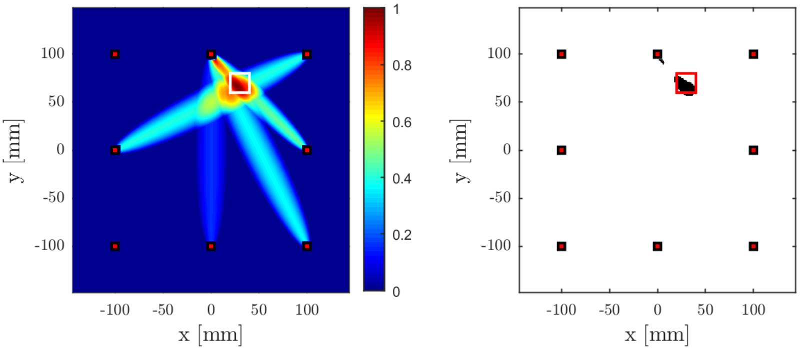

(a) $P(x,y)$ (b) Binarized image

Figure 5.33: Result of nonlinear RAPID imaging on a simulated anisotropic plate, without binarization (left) and with binary thresholding (right). The excitation waveform was a 20-cycle sine burst, at 50 kHz with Hanning window. The center of the delamination is located at [30,70]. For the picture on the right hand side, the threshold for binarization was set to $P(x,y) = 0.8$. The actual location of the delamination is marked with white and red squares, respectively.

at [-50,-20] and delamination 2 (DEL2) [30,70]. The parameters of the imaging algorithm were kept identical to both previous test cases. The result of the imaging is depicted in Fig. 5.34. Interestingly, the first delamination (DEL1) cannot be adequately reconstructed. It has approximately the same damage index values as the phantom region with coordinates [-30,30]. The failure to image the DEL1 feature is mainly caused by the shape of the array as well as by the mutual position of DEL1 and DEL2. Clearly, the phantom region at [-30,30] corresponds to a high probability of damage due to the fact that both defects modify the signals on the T-R paths crossing this zone. As a result, the zone is illuminated without actual damage being present. This is a common problem with rectangular arrays. However, other mutual array-defects positions, even when the defects are nearly collinear (see Fig. 5.35a), do not affect the imaging performance. On the binary image, we also notice a small false indication in the vicinity of the upper-central array element, next to DEL2.

Test case 4

The fourth test case also contained two identical delaminations located in different positions, namely DEL1 at [-50,-20] and DEL2 at [40,-60]. The imaging

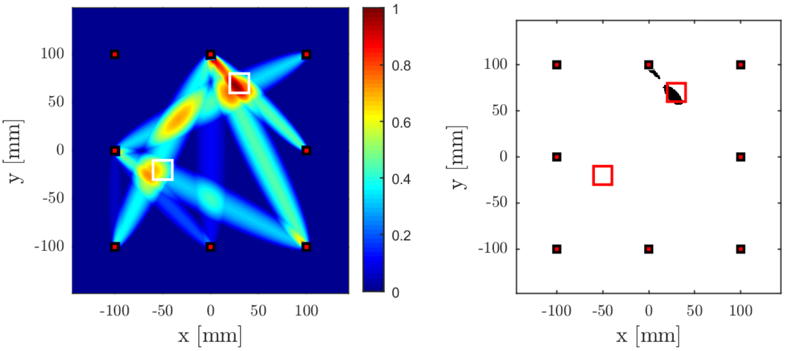

(a) $P(x, y)$ (b) Binarized image

Figure 5.34: Result of nonlinear RAPID imaging on a simulated anisotropic plate, without binarization (left) and with binary thresholding (right). The excitation waveform was a 20-cycle sine burst, at 50 kHz with Hanning window. The center of the delaminations are located at [30,70] and [-50,-20]. Threshold for binarization was set to $t_P = 0.8$. The actual locations of the delaminations are marked with white and red squares respectively.

result employing the original imaging parameters is depicted in Fig. 5.35. The output of the imaging algorithm is better than in the previous test case, and the two defect zones can be distinguished. However, the binarized image with $t_P = 0.8$ displays only one defect: DEL2. Its position is slightly shifted to the left and its centroid is approximately 12 mm away from the actual center of the simulated delamination. Unlike in the previous test case, the defects are easy to discern in Fig. 5.35a. Upon reducing the threshold t_P by just 5 %, both delaminations become visible in the binary image (see Fig. 5.36).

Test case 5

The fifth and last test case demonstrates the effect of signal duration (number of sine cycles) on the imaging performance. The test case is similar to the first test case with one exception. The number of cycles in the excitation signal was decreased from $n_c = 20$ to $n_c = 3$. The effect of this change can be observed in Fig. 5.37. It is obvious from Fig. 5.37a and Fig. 5.32a that the imaging output is different for different values of n_c. A higher number of cycles clearly improves the performance of the baseline-free imaging algorithm.

The main reason for the inferior imaging performance is the fact that a shorter

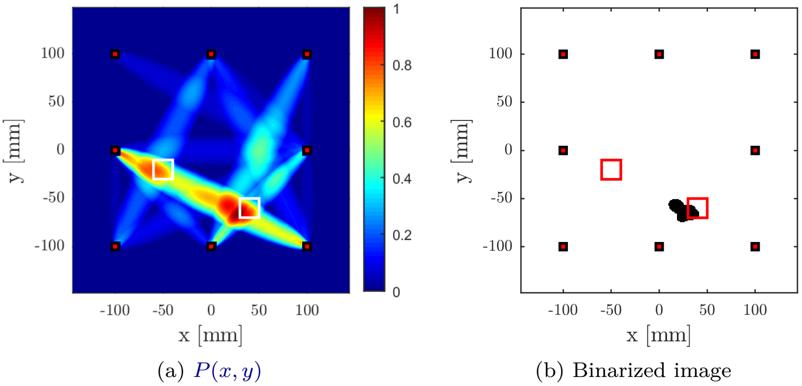

(a) $P(x, y)$ (b) Binarized image

Figure 5.35: Result of nonlinear RAPID imaging on a simulated anisotropic plate, without binarization (left) and with binary thresholding (right). The excitation waveform was a 20-cycle sine burst, at 50 kHz with Hanning window. The center of the delaminations are located at [-50,-20] and [40,-60]. Threshold for binarization was set to $t_P = 0.8$. The actual locations of the delaminations are marked with white and red squares, respectively.

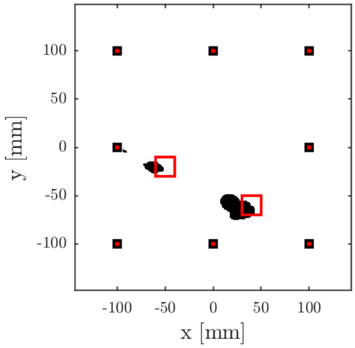

Figure 5.36: Binarized image for test case 4 with the lower threshold - $t_P = 0.75$. The actual locations of the delaminations are marked with white and red squares, respectively.

signal is inherently more broadband (see (5.2)), and the more broadband the signal is, the higher the dispersion will be. Obvious consequences to this are: a less precise estimation of the TOF and a poorer adaptive signal length correction. On the other hand, a larger n_c instigates the unavoidable problems with reflections coming back from the edges of the plate. Therefore, an optimal n_c that avoids reflections and provides narrowband excitation has to be found for every application, based on the sample geometry and the sample's dispersion characteristics.

Another reason may be linked to the nonlinear delamination model and related SDC value. Only a very small portion of the signal is distorted due to the nonlinear delamination, because the faces of the delamination undergo just 3 cycles instead of 20. Therefore, the nonlinear effects influence the result only slightly. According to Delrue and Van Den Abeele [243], the combination of SSM and the nonlinear delamination model performs very well for larger $n_c \approx 40$. The rigorous study of the mode behaviour for the small n_c has not been published yet.

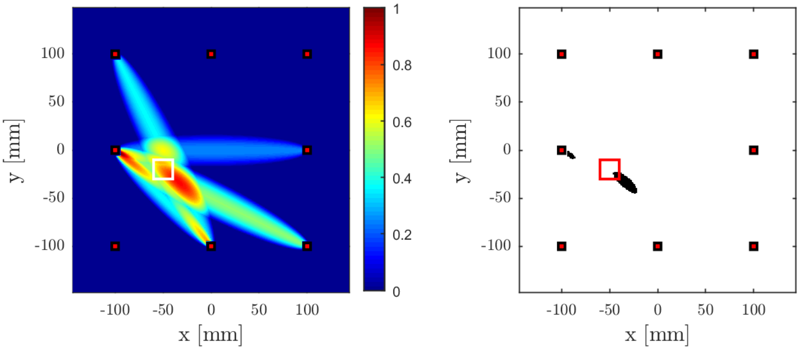

(a) $P(x, y)$ (b) Binarized image

Figure 5.37: Result of nonlinear RAPID imaging on a simulated anisotropic plate, without binarization (left) and with binary thresholding (right). The excitation waveform was a 3-cycle sine burst, at 50 kHz with Hanning window. The center of the delamination is located at [-50,-20] . Threshold for binarization was set to $t_P = 0.8$.

The numerical simulations have shown that the proposed nonlinear baseline-free algorithm is a viable tool for detection of nonlinear delaminations. By analyzing several test cases, certain pitfalls could be identified in the imaging, in particular regarding the mutual position of the sparse array elements and the defects. A circular sparse array is generally more preferable than a rectangular one, but at the same time, this option also has its limitations due to the poor coverage of the edge zones of the inspected samples. When the inspection of edge zones is important, a rectangular array should be used, however, it should be noted that this arrangement requires more elements in order to avoid imaging failures such as observed in the test case 3.

5.5.4 Experimental results

The results obtained in the previous section suggests that the proposed nonlinear baseline-free alternative of the RAPID algorithm can be used to detect nonlinear damage in anisotropic plates. In order to experimentally verify these findings, two different CFRP samples, each with different type of damage, were tested.

SARISTU plate with impact damage

The first tested sample is the SARISTU plate that was first introduced in section 3.1.4. The dispersion curves and the other important mechanical properties can be found in the same section. The sample contains a single impact damage (impact energy 21 J) that was introduced after the transducers were bonded to the structure. Details on the coupling agent and the type of transducers that were used for the inspection have been reported in section 5.4.3. It was demonstrated in the same section that the conventional RAPID is able to successfully detect the impact damage. This fact is not surprising, because as discussed in section 5.2.2, the impact damage results in a combination of different damage types, ranging from fibre-cracking to delaminations. Hence, one can expect that the impact will affect the wave propagation in a linear way as well as in a nonlinear manner. The conventional RAPID merely focuses on the linear part of the response for the detection of damage: scattered waves, mode converted waves and attenuation changes. Conversely, the newly introduced nonlinear version of the algorithm only senses the nonlinear features (distortion, lack of scalability) and it does not need to rely on a damage free baseline.

The experimental setup was the same as was described in section 5.4.2. An AR150A100B power amplifier with 52 dB gain was used to amplify the input signal that is transmitted to the individual PZT elements. The lower input amplitude to the amplifier was set to $A_{lin} = 0.01\,\mathrm{V}$ and the SSM scaling coefficient was $k_s = 10$. The actual voltage input to the PZT was approximately 8 V and 80 V for the lower and higher amplitude excitation, respectively. The excitation frequency was $f = 50\,\mathrm{kHz}$ and the waveform was a 3-cycle Hanning windowed tone burst. Such a low cycle count was selected due to the position of the defect and due to the shape of the sparse array. Longer duration of excitation would result in a mixing of directly propagating signals and signals that are reflected from the edges of the sample. Hence, the short excitation is unavoidable in this case. The signals were sampled with a sampling frequency

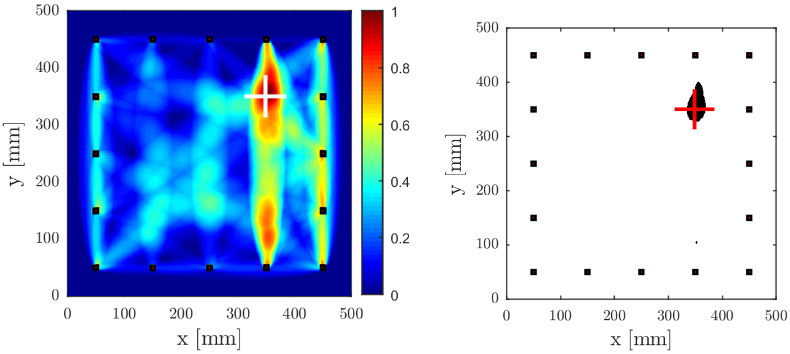

(a) $P(x, y)$ (b) Binarized image

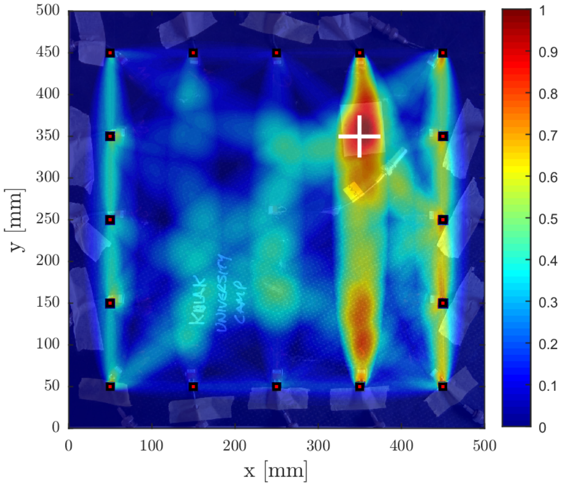

(c) Image overlay

Figure 5.38: Result of nonlinear RAPID imaging on SARISTU anisotropic plate, a) without binarization, b) with binary thresholding and c) superimposed on a visual picture of the plate. The excitation waveform was a 3-cycle sine burst at 50 kHz with Hanning window. Threshold for binarization was set to $t_P = 0.8$. The actual location of the impact damage is marked with white and red cross, respectively.

$f_s = 10\,\mathrm{MHz}$ and each signal was average 512 times to get a good SNR for the low amplitude excitation.

Fig. 5.38 shows the result of the nonlinear RAPID imaging of the impact damage, applying the following imaging parameters: $t_{SDC} = 0.15$, $\beta = 1.015$, $t_P = 0.8$. The defect was satisfactorily highlighted in the damage index map and subsequently segmented using a fixed threshold. The predicted location of the damage corresponds with the ultrasonic C-scan data depicted in Fig. 5.20b. On the other hand, the size of the defect is somewhat overestimated. There is also a phantom area with considerably high damage index values in the lower right corner of the image. It lies on the same T-R path as the defect region and it is probably caused by a higher inherent nonlinearity of the transducers that are placed along the right edge of the sample. The cross-section of diagonal T-R paths that originate from these transducers and the defect T-R path results in a creation of the phantom area. The elevated level of nonlinearity is clear when the left and right group of elements are compared and it can be caused by a slightly different quality of coupling.

Fig. 5.38a suggests that most of the nonlinear effects are generated when waves propagate through the damaged region in the y-direction. This can be attributed to the distribution of the partial damage caused by the impact along the dominant material symmetry axes (0°, 90°). However, the shape of the damage distribution inferred by the nonlinear RAPID method is not entirely conform with the result from the ultrasonic C-scan. Therefore, another technique with higher spatial resolution for instance μCT should be used to confirm whether the micro-cracking is indeed present in a wider area than predicted by the C-scan.

ALAMSA plate with delamination

The second testing sample is a quasi-isotropic CFRP plate, which is one of the testing objects in the ALAMSA project. The plate is equipped with 8 circular DuraAct© transducers that form an annular array (see Fig. 5.39). The annular shape of the array was selected to overcome the imaging issues related to rectangular shaped arrays that became apparent during the simulation part. The delamination is relatively centrally localized inside the plate which means that the annular array does not have to cover the edge zones. The array elements were coupled to the structure with the Salol© in order to allow for easier reconfiguration of the array, which was not the case for the permanent Hysol© coupling on the SARISTU plate.

The plate contains a single 20 x 20 mm delamination in the form of a Teflon© layer that was inserted at a depth of 1/4 of the plate thickness, closest to the instrumented surface. The location of the delamination is highlighted in Fig. 5.39 by the red rectangle. The elastic properties of the plate are similar

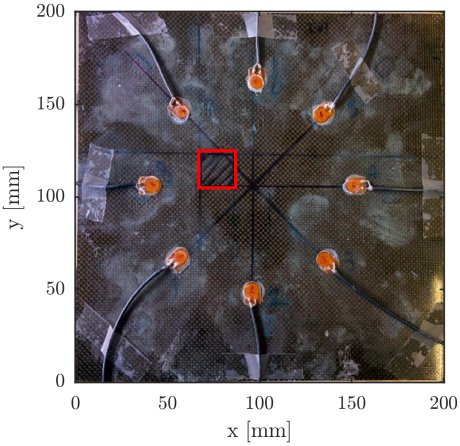

Figure 5.39: Annular array of circular DuraAct© transducers attached to the ALAMSA plate.

to the intact plate described in section 3.1.4. Hence, the numerical simulation results of dispersion properties can be used for nonlinear imaging.

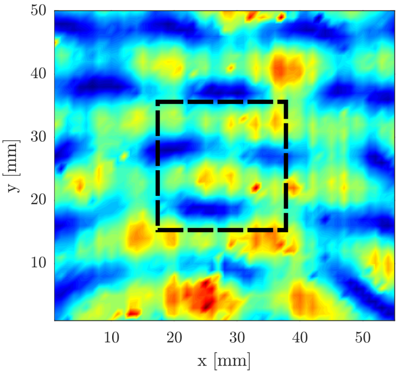

Figure 5.40: Root mean square of the LDV C-scan data at 50 kHz (5-cycle sine burst with Tukey window). No significant interaction of GW with the delamination (marked by black box) can be observed.

The acquisition parameters were identical to the ones used for the SARISTU sample with one exception: the AR150A100B power amplifier was replaced by a Falco WMA-320. A total of $n_s = 16384$ samples per signal were collected and

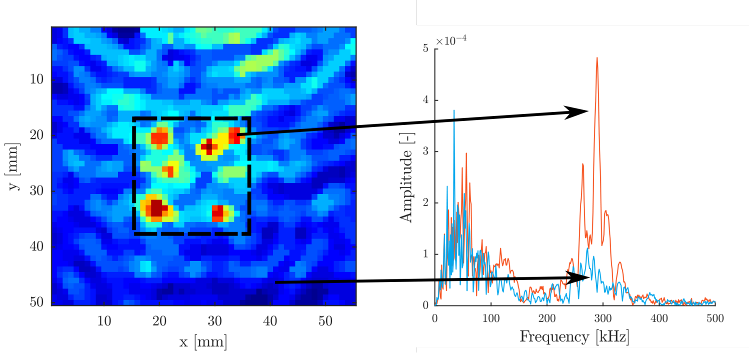

Figure 5.41: Interaction of GW with a delamination in the ALAMSA plate. Root mean square of signals from an LDV C-scan that was carried out using an excitation waveform that consisted of a 5-cycle sine burst (with Tukey window) at 282 kHz. The black box marks the position of the delamination.

stored. The excitation input amplitude to the power amplifier was $A_{lin} = 0.1\,\mathrm{V}$ and $A = 1.6\,\mathrm{V}$ for the low and high excitation signals, respectively. Other imaging parameters that were used are: $t_{SDC} = 0.3$, $\beta = 1.015$, $t_P = 0.8$. The scaling coefficient is $k_s = 16$.

The excitation waveform is a 5-cycle sine burst at 283 kHz with a Tukey (apodized cosine) window. Such a high frequency was selected, because the imaging at 50 kHz was not successful due to the mechanical nature of the delamination. In order to understand the reason behind this, an LDV scan of the damage zone was carried out to assess the interaction between the propagating waves and the delamination. It was concluded that no significant interaction (mode conversion, scattering) takes place at the low frequencies (see Fig. 5.40). However, a significant wave trapping, as described by Leckey et al. [225] and Tian et al. [245], occcurs at frequencies between 250-300 kHz (see Fig. 5.41). The two spectra were selected to represent the damaged zone (delamination) and the intact part of the sample. A striking difference of the amplitudes of spectral components in the previously mentioned frequency band is clear. Therefore, this frequency, although in the highly dispersive region, was selected.

As can be seen from Fig. 5.42, the performance of the imaging algorithm is sufficient to discern the indication of the delamination from the background. However, the damage index heatmap, as shown in Fig. 5.42a, is visually fairly noisy. A lot of smaller indications tend to appear in the lower half of the interrogated area. Nonetheless, as observed from the binary image shown in Fig. 5.42b, none of the zones crosses the critical threshold value $t_P = 0.8$. An

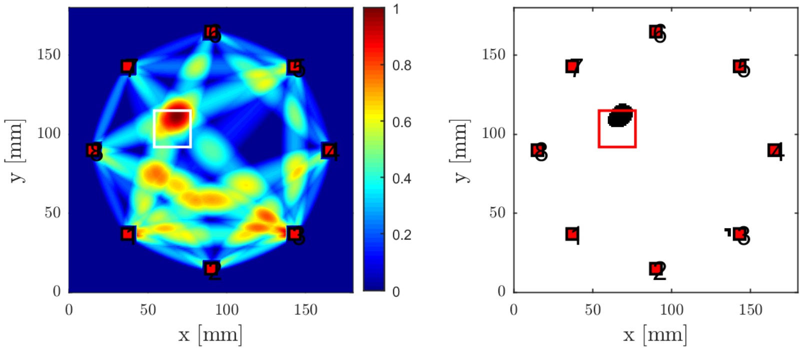

(a) $P(x, y)$

(b) Binarized image

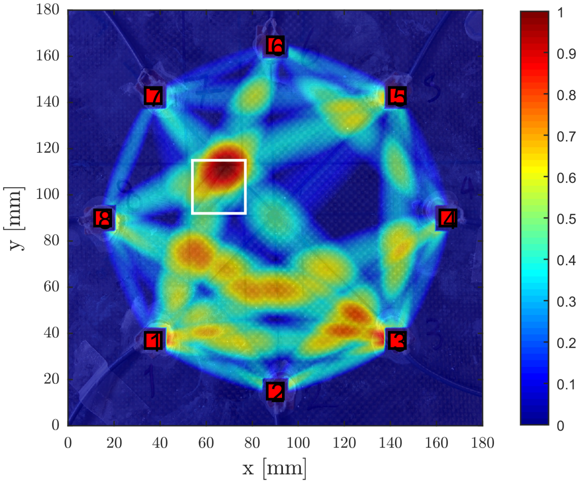

(c) Image overlay

Figure 5.42: Result of nonlinear RAPID imaging on ALAMSA quasi-isotropic plate, a) without binarization, b) with binary thresholding and c) superimposed on a visual picture of the plate. The excitation waveform was 5-cycle sine burst at 283 kHz with Tukey window. Threshold for binarization was set to $t_P = 0.8$.

overlay of the nonlinear RAPID imaging result with a photo of the delaminated area is displayed in Fig. 5.42c.

5.6 Conclusion

In this chapter, a nonlinear baseline-free GW imaging method based on RAPID was proposed and described in detail. The proposed method was first tested on numerically simulated data and then verified experimentally on two layered anisotropic CFRP samples. Two corrective measures, both based on the dispersion data numerically calculated in the previous chapter, were proposed to improve the performance of the basic imaging algorithm. The novel nonlinear algorithm provides slightly inferior results compared to its linear counterpart. However, the reduced imaging quality is an expected trade-off that is compensated by the baseline-free nature of the proposed method.

Chapter 6

Local Defect Resonance

6.1 Introduction

Exploiting the features of Local Defect Resonance (LDR) for the detection of various types of damage represents one of the latest additions to the family of ultrasonic methods. LDR, as first described by Solodov in [246, 247], is an interesting effect that strongly resembles the typical resonance behaviour of solid structures [248, 249]. In the same way as for traditional resonance analysis, the vibration amplitude of a defect increases significantly when the excitation frequency matches the defect's LDR frequency [246]. However, in case of LDR, this increase is strongly localized in the defect region providing an excellent contrast between the damaged and intact parts of the tested specimen (see Fig. 6.1) [250, 251]. Experimentally, the increase of the vibration amplitude can be easily measured by means of a LDV.

LDR behaviour has been illustrated for different types of damage, such as Flat Bottom Holes (FBH), delaminations, cracks and disbonds, and it can be observed in various materials, e.g. PMMA, Glass-Fiber-Reinforced plastic (GFRP), CFRP and others [252, 253]. Once the LDR frequency of a defect is known, one can estimate the position of this defect within the sample, the size of the defect, and, to a certain extent, its shape by exciting the sample at that particular frequency [254, 255]. Moreover, LDR frequencies can be used to provoke nonlinear elastic wave effects by activating the defect into the finite amplitude nonlinear regime [104, 127, 256, 257]. These nonlinear effects could then be used to enhance the conventional defect detection and sizing capabilities, as described by Solodov et al. [254].

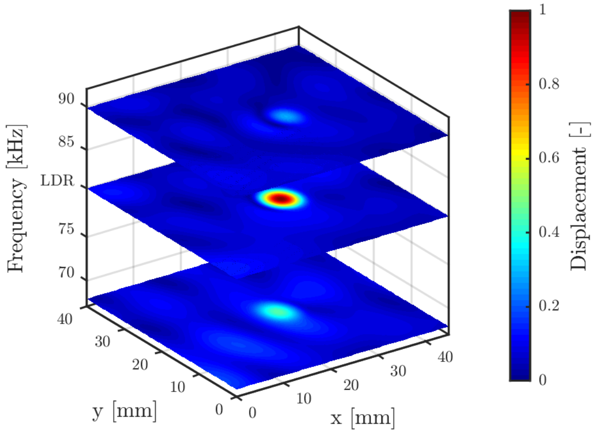

Figure 6.1: Typical evolution of the spatial 'eigen'vibration pattern of a defect in frequency domain. The second slice corresponds to the LDR frequency. Data from a numerical simulation of an aluminum plate (80 mm × 60 mm × 5 mm) with low reflecting boundaries Low Reflecting Boundaries (LRB) containing a single FBH with radius $r = 10\,\text{mm}$ and depth $d = 4\,\text{mm}$.

An interesting side effect linked to LDR is the heat generation induced by the strongly vibrating defect [258]. Renshaw et al. [259, 260] linked the heat generation to three main physical sources: friction, plasticity and viscoelastic losses. Viscoelasticity plays the most significant role in the case of FBH, while the key mechanism for heat generation in delaminations is a combination of viscoelasticity and friction between the opposite faces of the delamination [261]. Irrespective of the actual mechanism, the effect of the local vibration at the defect location eventually results in an elevated temperature at the defect zone, that can be easily picked up by means of an Infrared (IR) camera [254, 262]. This coupling effect between ultrasonic and thermographic phenomena presents an interesting opportunity for Nondestructive Evaluation (NDE) data fusion and enhanced NDT inspection results. Inspite of this, the LDR research field is still quite young and not yet fully explored.

The first section in this chapter deals with the analytical description of the LDR. Next, an automatic algorithm for LDR frequency detection will be presented for different defects in various materials. The proposed algorithm will be further tested using both numerical simulations and experimental measurements. Finally, the capabilities of LDR and the automatic detection algorithm for defect localization and defect size estimation will be demonstrated.

6.2 Theory of Local Defect Resonance

Analytical approaches describing and predicting LDR frequencies are not common. Theoretical formulas, mainly based on the classical plate theory, have been proposed by Solodov for a square-shaped FBH and for the case of a circular FBH [246, 255]. In [263] Solodov derived the LDR frequency f_t using the following approach. A solid sample of simple geometry containing one single FBH is assumed. The LDR can then be seen as a natural frequency of the defect with a effective stiffness E_{eff} and mass M_{eff}. In order to determine these parameters, several additional assumptions have to be made. Firstly, the depth of the defect d has to be comparable with the full thickness of the plate h ($d \approx h$). This means that the remaining thickness $h - d$ is low and that the edges of the FBH can be considered as clamped (displacement and first spatial derivative are zero at the boundary). Secondly, the FBH has to be thin, which means the radius r has to be much greater than the residual thickness of the plate ($h - d \ll r$). Under these assumptions, the FBH can be approximated by a circular membrane with radius r (see [264]) and we can use the approach suggested by Solodov in [263]. The theoretical LDR frequency can then be calculated as

$$f_t = \frac{1}{2\pi}\sqrt{\frac{E_{eff}}{M_{eff}}} \approx \frac{1.6(h-d)}{r^2}\sqrt{\frac{E}{12\rho(1-\nu^2)}}, \tag{6.1}$$

where r and $h - d$ are the radius and the residual thickness of the plate at the position of the FBH, E is the Young's modulus, ρ the material density and ν the Poisson's ratio. Note that this formula is only valid for thin FBHs ($h - d \ll r$) [263]. As a practical extension, the same formula has also been used for a simple delamination, in which case $h - d$ stands for the remaining thickness of the layer above the delamination [246].

As obviously seen from (6.1), f_t is independent of the boundary conditions of the parental sample, as well as of the position of the excitation. The LDR should therefore not be affected by changing the global boundary conditions, unlike the specimen's eigenmodes. This will be further verified by numerical simulation and experimental measurements.

As can be expected, the analytical formula faces serious difficulties in case of defects with a lower $\frac{r}{h-d}$ ratio embedded in stiffer materials such as aluminum. Moreover, it has been derived using two partially conflicting theories - membrane and plate theory - which makes its area of application extremely narrow. Except for FBHs and delaminations, there are unfortunately no analytical models that can predict the LDR frequency of a disbond or an impact in an anisotropic laminated structure. Therefore, an alternative and more practical way to identify LDR of defects is necessary.

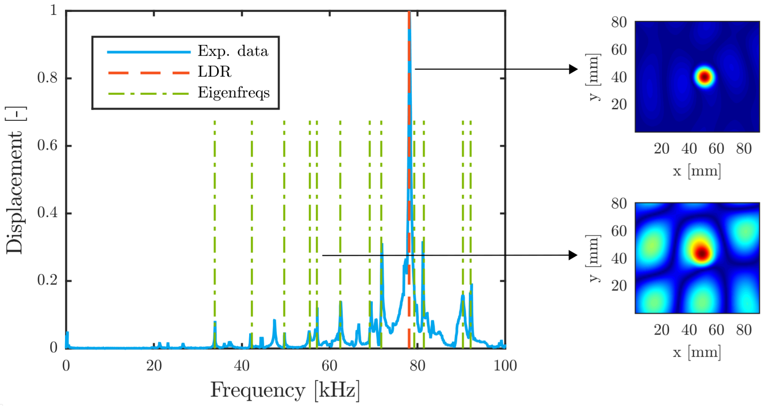

Figure 6.2: Normalized amplitude of the out-of-plane particle velocity as function of frequency at the center of the defect (experimental data), showing that the precise LDR is contained in a narrow frequency band.

6.3 Automated detection of Local Defect Resonance

Instead of relying on analytical formula, another approach to identify and quantify the LDR frequency of heterogeneous features is based on the vibrational behaviour of the sample under LDR circumstances. From previous studies by the group of Solodov [246, 263], it is apparent that LDR manifests itself as a vibrational "eigenmode" with a strongly localized ("isolated"), high-amplitude peak of quasi-circular shape, occurring at the location of the defect (see Fig. 6.1 and Fig. 6.2). Due to the significant difference between the peak amplitude and the average amplitude of the remaining intact part of the sample at the same frequency of excitation, the background energy is strongly suppressed. Under the assumption of a single defect, the LDR frequency can then automatically be detected by distinguishing and exploiting this typical behaviour in the out-of-plane response, measured at the surface by means of a LDV.

The detection procedure requires a number of pre- and post-processing steps which will be illustrated in the next section (6.4) by means of a simulation study. To illustrate the concept and the experimental requirements, let us consider a rectangular plate with length l, width w and thickness h and assume that the plate contains a single FBH with depth d and radius r. A piezoelectric transducer, attached to the sample surface, is excited using a broadband chirp signal with frequency bandwidth B, start frequency f_s and duration T, and

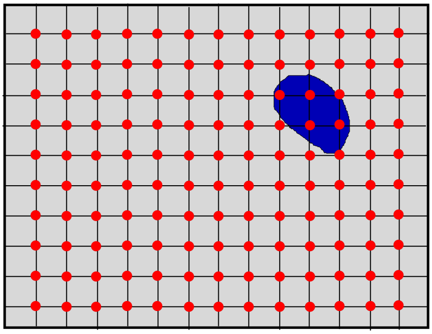

Figure 6.3: Illustration of the surface scanning procedure. The defect is highlighted with blue color. Red dots represent the measurement points.

forces the sample to vibrate accordingly. The bandwidth is chosen such that it contains the theoretical LDR frequency f_t, estimated using equation (6.1).

The out-of-plane component u_z ($u_z = u_z(x, y, t)$) of the time domain response of the sample is measured in a rectangular grid on the top surface of the sample by means of a LDV (see Fig. 6.3). The recorded signals are then transformed to the frequency domain using the FFT

$$U_z(x, y, f) = \mathcal{F}[u_z(x, y, t)], \tag{6.2}$$

where $\mathcal{F}$ denotes the FFT operation. All post-processing operations can be easily performed in MATLAB©.

At the LDR frequency, the contrast between the vibration amplitude of the defect zone and the average amplitude in the rest of the plate reaches its maximum (see Fig. 6.1). A function $g(f)$ that describes this contrast can be defined as the ratio between the maximum amplitude within the presumed defect zone and the average value of the background

$$g(f) = \frac{\max\limits_{(x_d,y_d)\in\Omega_d} U_z(x_d, y_d, f)}{\operatorname*{mean}\limits_{(x_i,y_i)\in\Omega\setminus\Omega_d} U_z(x_i, y_i, f)}, \quad f_s \leq f \leq (f_s + B), \tag{6.3}$$

where the frequency f is restricted to the frequency band of the excitation chirp, Ω denotes the entire 2D scan area and Ω_d marks the presumed defect area. As the true defect zone is not known beforehand, Ω has to be segmented in variable Ω_d regions using the MATLAB© implementation of Otsu's algorithm (*graythresh*) and further processed using the *bwboundaries* function [265, 266]. An example of this thresholding process and its effect on the analyzed frames is depicted in Fig. 6.4 where the white zones mark the presumed defect areas

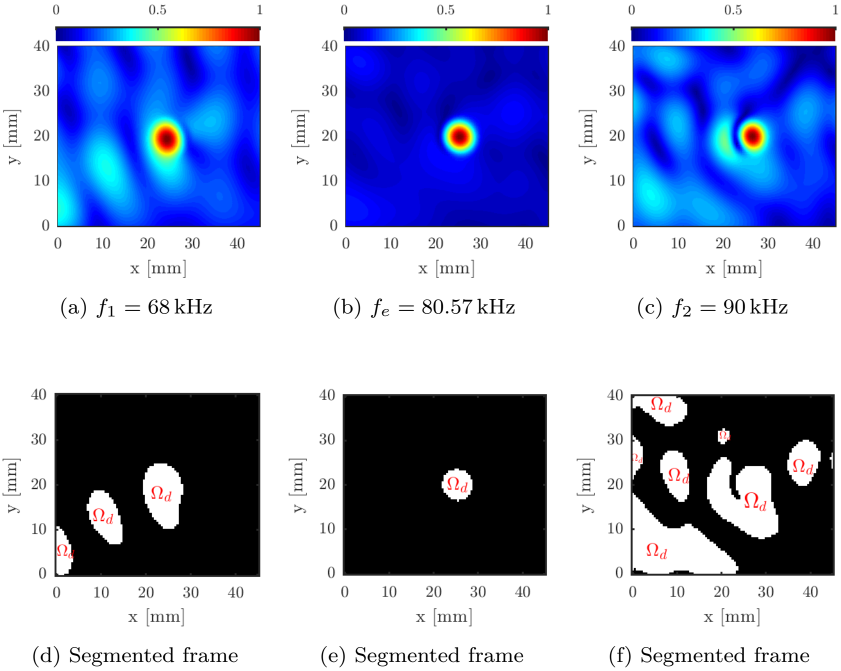

(a) $f_1 = 68\,\text{kHz}$ (b) $f_e = 80.57\,\text{kHz}$ (c) $f_2 = 90\,\text{kHz}$

(d) Segmented frame (e) Segmented frame (f) Segmented frame

Figure 6.4: The example of the frame segmentation using Otsu's algorithm. Only the second frame could represent LDR and is further processed by the algorithm.

Ω_d as output of the analysis procedure for the corresponding frequency. The dataset used in this example is obtained from a numerical simulation of an aluminum plate ($80\,\text{mm} \times 60\,\text{mm} \times 5\,\text{mm}$) with LRB containing a single FBH with radius $r = 10\,\text{mm}$ and depth $d = 4\,\text{mm}$. It will be further used throughout this section to demonstrate different steps in the detection algorithm. All figures presented in 6.3 were obtained using this dataset if not mentioned otherwise.

To ease the detection of valid frames that identify the LDR, we make use of its typical properties. Commonly, only those frames $U_z(x, y, f = const.)$ that contain one *quasi-circular* compact area Ω_d with

- eccentricity $e \leq 0.65$,
- and equivalent diameter $1\,\text{mm} \leq r_e \leq 30\,\text{mm}$,

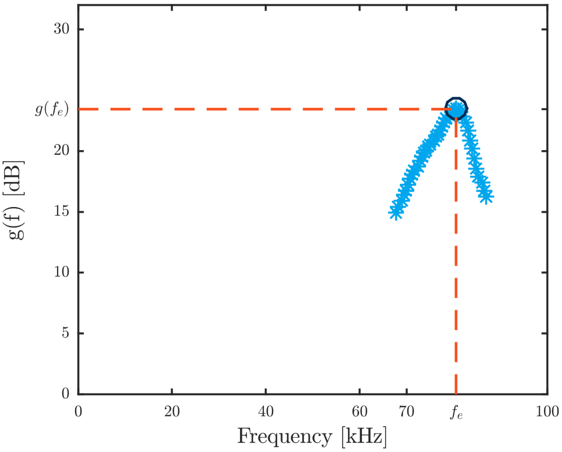

Figure 6.5: Shape of the $g(f)$ curve as obtained for the simulated aluminum plate.

can represent a true LDR (see Fig. 6.1 and 6.4). Only these frames are selected for further evaluation and the rest of the frames is neglected. The lower limit of r_e is given by the scan resolution and the upper limit has been selected to cover the typical sizes of the defects involved in practical studies (FBH, delamination). Otsu's nonparametric unsupervised segmentation algorithm secures that always in the end the same Ω_d is segmented from a given frame. Consequently, we can assume $g(f)$ to be only a function of the frequency f. The value of the eccentricity guaranties that the area Ω_d is compact and continuous. Non-compact areas generally correspond to the conventional sample eigenmodes. Once all the frames that can possibly represent the LDR are selected, the segmented images, such as the one in Fig. 6.4e, are used as binary masks to separate each original frame into defect area Ω_d and the intact rest of the sample $\Omega \setminus \Omega_d$. Eq. (6.3) can then be readily applied and each frame is assigned its corresponding contrast (gain) value. The typical shape of $g(f)$ slightly resembles the form of standard resonance curve (see Fig. 6.5).

After the geometrical constraints have been applied and $g(f)$ has been calculated, the argument of the maximum contrast

$$f_e = \arg\max_f [g(f)], \tag{6.4}$$

is defined as the predicted to the true LDR frequency f_e. The maximum value $g(f_e)$ is called the LDR gain and the corresponding 2D vibration pattern on $U_z(x, y, f_e)$ is called the LDR mode. Moreover, the above proposed procedure

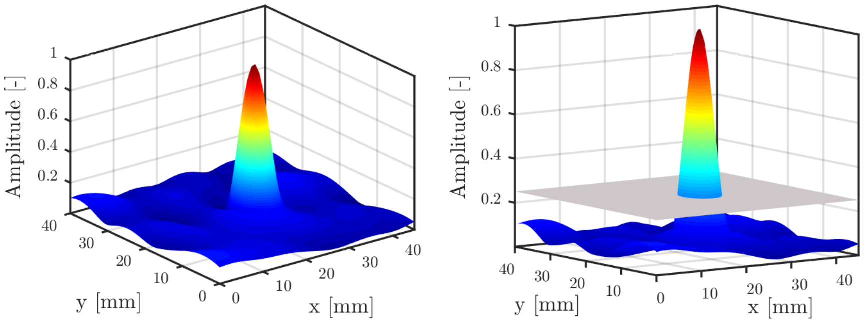

(a) Mode shape at f_e (b) $-12\,\text{dB}$ threshold applied

Figure 6.6: Estimation of the size using a specified ($-12\,\text{dB}$) threshold.

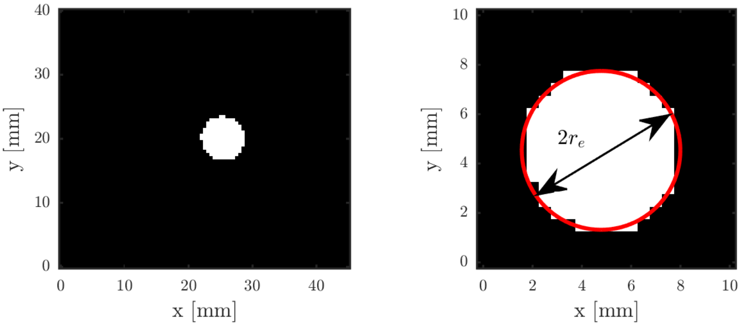

(a) Thresholded LDR mode (b) Detail of Ω_d

Figure 6.7: Estimation of the equivalent radius r_e from the thresholded mode shape depicted in Fig. 6.6. The red circle is generated using the *bwboundaries* function and is used to estimate the equivalent radius.

can be used to localize the defect and estimate its size using the position and the equivalent radius r_e of the area Ω_d at a given threshold (see example in Fig. 6.6 and Fig. 6.7) [267]. However, generally, the defect size estimation can be rather rough when applying such a basic approach. The main reason for this is the *ad hoc* selection of the threshold value. Since there are no guidelines on how to select an appropriate threshold value beforehand, one has to resort either to numerical simulation that can be used to calibrate the threshold or to an iterative sizing algorithm as proposed and described in the following section.

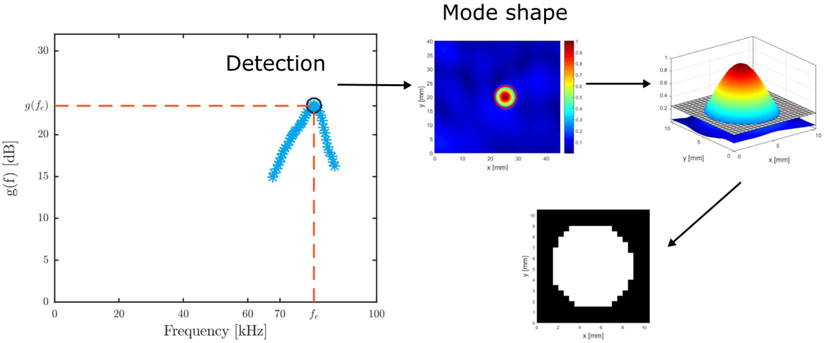

Figure 6.8: Illustration of the automatic detection and sizing technique.

The graphical illustration of the different steps in the LDR detection algorithm is depicted in Fig. 6.8.

6.3.1 Iterative sizing

Since the original sizing approach only allows a rough size estimation, we propose a more advanced iterative sizing algorithm. Let us assume that the LDR frequency and its corresponding 2D vibration pattern, i.e, the LDR mode or frame, is known. In order to size the LDR, first, a conservative starting threshold value c_s is defined, typically $c_s = -3\,\text{dB}$. Next, the LDR frame is segmented using this threshold and the segmented image is analyzed. If the following criteria are met:

1. Ω_d is a single, compact area,
2. Ω_d is quasi-circular with eccentricity $e \leq 0.65$,
3. The center of Ω_d has not shifted for more than 1 mm in any direction with respect to the original position calculated for c_s,

then the equivalent radius of the defect is stored in memory and the threshold is decreased by a given decrement Δc. These steps are repeated until one of the condition is not fulfilled, and at that point the iteration is stopped. The last stored value of the equivalent radius r_e is then considered to be the new estimate of the defect size. The iteration process is graphically depicted in Fig. 6.9.

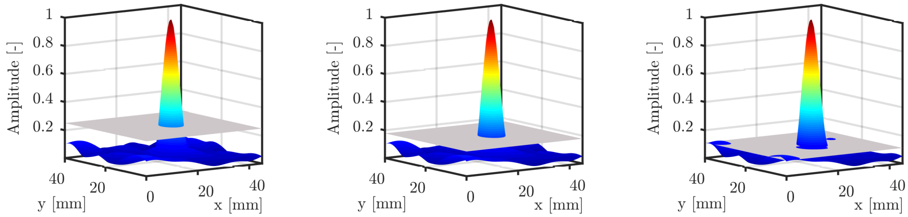

(a) Threshold @ $-12\,\mathrm{dB}$ (b) Threshold @ $-15\,\mathrm{dB}$ (c) Threshold @ $-19\,\mathrm{dB}$

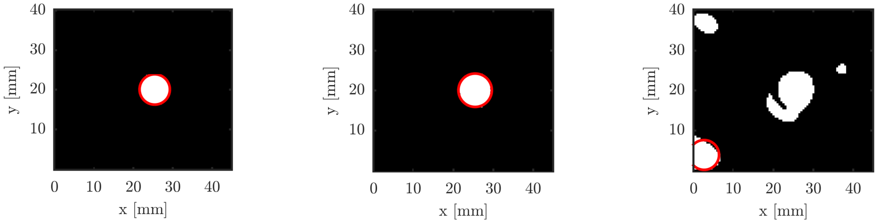

(d) $r_e = 3.85\,\mathrm{mm}$ (e) $r_e = 4.19\,\mathrm{mm}$ (f) Stop iteration

Figure 6.9: Iterative process of lowering of the threshold for automatic sizing of defects.

The proposed iterative sizing approach yields a more accurate estimation of the true defect size than a plain thresholding at an arbitrarily selected threshold, as will be further demonstrated in the section 6.4. Another advantage of this approach is its robustness. Except for starting threshold c_s, which can be easily set as low as $-1\,\mathrm{dB}$, no other inputs are necessary to start the iterative search. Therefore, the algorithm does not have to be readjusted again for different samples under inspection. The general flowchart of the detection algorithm is depicted in Fig. 6.10.

6.4 Numerical simulations

The performance of the LDR detection and sizing algorithm described in section 6.3 was tested by means of a numerical study applied to a circular FBH in an aluminum sample. The numerical implementation is based on a time-dependent finite element simulation using the structural mechanics module of COMSOL Multiphysics$^{©}$.

The aluminum sample considered in the simulations is a rectangular plate with

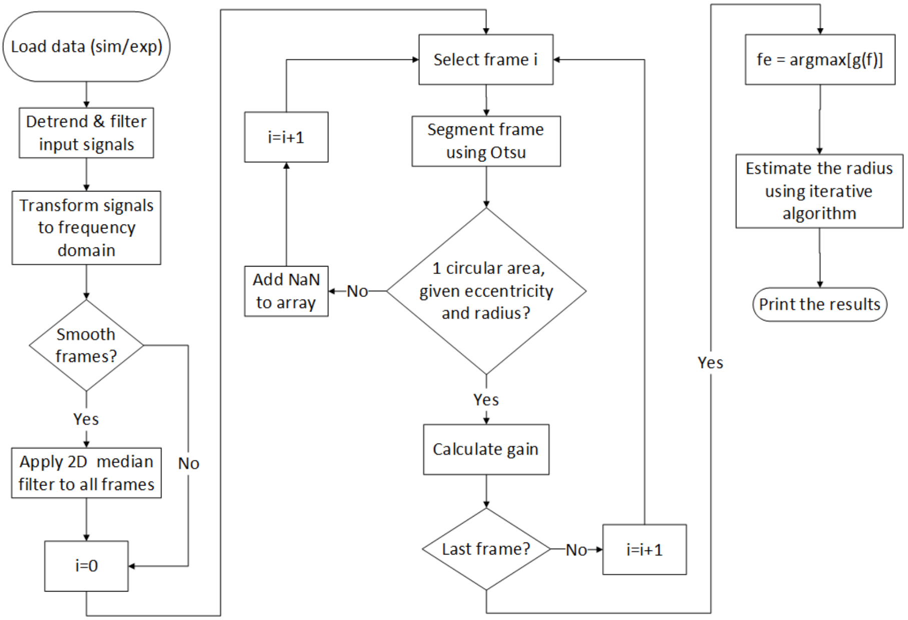

Figure 6.10: General flowchart of the automatic LDR detection and sizing algorithm.

dimensions 80 mm × 60 mm × 5 mm (see schematic in Fig. 6.11). It contains a FBH that has a radius $r = 5\,\mathrm{mm}$ and a depth $d = 4\,\mathrm{mm}$. The relevant material properties are listed in Tab. 6.1. The analytical LDR frequency of the FBH with the above given parameters, as calculated using (6.1), is $f_t = 100.56\,\mathrm{kHz}$. However, as was pointed out in the comments regarding this equation, this can only be used as a rough estimation.

ρ $[\mathrm{kg\,m^{-3}}]$	E [GPa]	ν	v_L $[\mathrm{m\,s^{-1}}]$	v_S $[\mathrm{m\,s^{-1}}]$
2700	70.75	0.34	6320	3130

Table 6.1: Material properties of the aluminum sample used in the simulation.

The action of an external ultrasonic circular source with a diameter of 10 mm is implemented in the model by applying an out-of-plane (normal) displacement boundary condition within a circular region at the lower surface of the sample, representing the active surface of the transmitter. The applied displacement corresponds to a linear sweep excitation that extends from 50 kHz to 100 kHz in 1 ms. All other boundaries of the sample are assumed to be free. Simulations

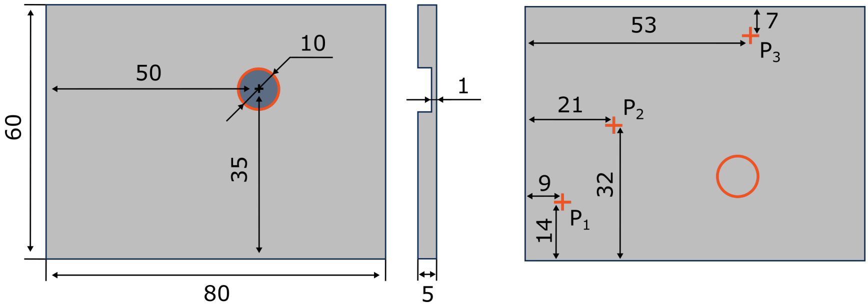

(a) Upper surface

(b) Lower (scan) surface

Figure 6.11: Drawing of the aluminum sample with a FBH as being used in the simulations and in the experiments. The positions of the transducer contact points, virtual or real, are marked by red crosses. Transducers are attached to the lower surface of the sample.

were performed for a position of the source varying between locations P_1, P_2 and P_3 as shown on Fig. 6.11b.

During and following the excitation, the normal displacement time signals at the lower surface of the sample (i.e. the surface containing the PZT from where the FBH is invisible, as illustrated in Fig. 6.11) are calculated within a square area of 45 mm × 40 mm, encompassing the defect position. The spatial steps in x and y direction are constant and equal to $\Delta x = \Delta y = 0.5\,\text{mm}$. The time signals were calculated for a total duration of 2 ms with a fixed time step of 0.5 μs. The numerical simulation for one scenario took 4h 55 min to complete on a workstation with 2 quad-core CPUs (Intel Xeon E5-2623 v3, 3.0 GHz, 64 GB RAM). The complete mesh consists of 76913 domain elements, 10458 boundary elements, and 460 edge elements. The total number of degrees of freedom solved for is 340143. The calculated time signals are stored in data files for further analysis using the automatic LDR detection algorithm.

After executing the various steps outlined in the above described detection algorithm (FFT, contrast, selection) for three different source positions, an average LDR frequency with Standard Deviation (SD) $f_e = (78.8 \pm 0.3)\,\text{kHz}$ was found for the FBH in case we consider the sample to have free boundary conditions (see Tab. 6.2). As an example, the corresponding LDR mode for source the positions P_2 is depicted in Fig. 6.12.

For the defect sizing, firstly, a threshold value of $-12\,\text{dB}$ on the amplitude distribution was used to estimate the radius of the defect. Alternatively, the radius was also calculated using the iterative sizing algorithm applied to the

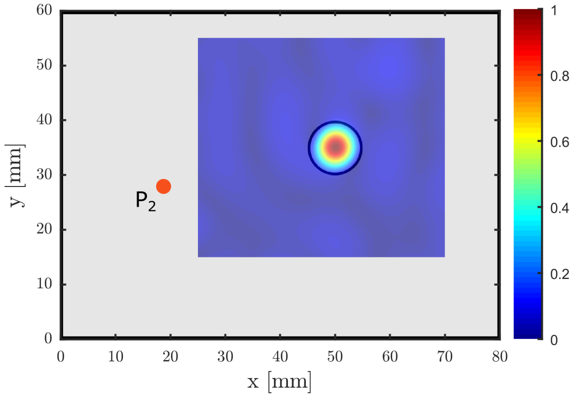

(a) LDR mode plotted over the virtual sample, black circle indicates position of the defect

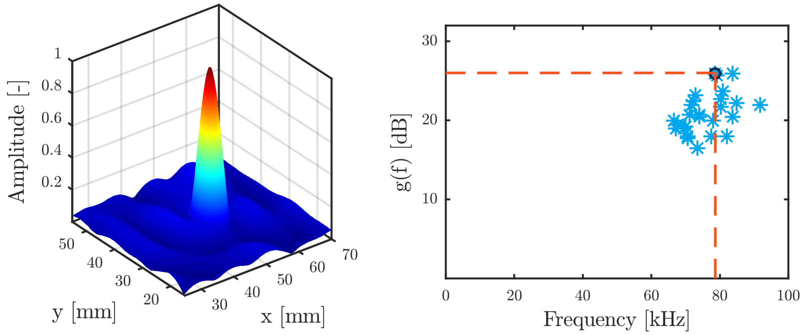

(b) 3D view, detail of the LDR mode

(c) LDR value highlighted in red

Figure 6.12: Simulation results for excitation position P_2 - LDR mode shape for the aluminum sample with FBH, assuming free boundaries, $f_e = 78.61\,\text{kHz}$, $g(f_e) = 26.01\,\text{dB}$.

Position	BC	f_e [kHz]	gain [dB]	$r_e^{-12\,\mathrm{dB}}$ [mm]	r_e [mm]
P_1	Free	78.61	30.58	3.85	4.76
P_2	Free	78.61	26.01	3.87	4.69
P_3	Free	79.10	29.03	3.85	4.88
Average ± SD		78.8 ± 0.3	29 ± 2	3.86 ± 0.01	4.8 ± 0.1

Table 6.2: Test scenarios and results of the simulation study with free edges. The equivalent diameter r_e of the defect was estimated at $-12\,\mathrm{dB}$ with respect to the maximum response and using the iterative algorithm.

same datasets. Therefore, we can easily compare both approaches. The average value (± SD) of the radius at $-12\,\mathrm{dB}$ was $r_e = (3.86 \pm 0.01)\,\mathrm{mm}$ which is an underestimation of 23% with respect to the real size. This error is mainly due to the fact that the selected threshold is rather conservative for lightly damped material such as aluminum. If a more aggressive threshold of $-20\,\mathrm{dB}$ would have been applied, the radius would have reached an average value of $r_e = (4.7 \pm 0.1)\,\mathrm{mm}$, resulting in only 6% mismatch with respect to the actual value. On the other hand, the iterative algorithm resulted in an average value of $r_e = (4.8 \pm 0.1)\,\mathrm{mm}$, approximately 6% lower than the real value and comparable with a threshold at $-20\,\mathrm{dB}$. However, no *ad-hoc* threshold guess was necessary to reach this degree of precision. This clearly demonstrates the benefit of using the iterative sizing approach over the constant threshold.

Position	BC	f_e [kHz]	$g(f_e)$ [dB]	$r_e^{-12\,\mathrm{dB}}$ [mm]	r_e [mm]
P_1	LRB	80.57	23.45	3.85	4.54
P_2	LRB	81.05	24.87	3.81	4.62
P_3	LRB	81.05	26.72	3.78	4.88
Average ± SD		80.9 ± 0.3	25 ± 2	3.81 ± 0.04	4.7 ± 0.2

Table 6.3: Test scenarios and results of the simulation study with low-reflecting boundaries.

The postulation that a LDR frequency should be independent of the material boundaries can be easily verified by repeating the numerical simulation and the post-processing procedure on a bigger sample with the same thickness and containing the same flat bottom hole. Even in the extreme case of an infinite plate with the same FBH, one should expect to get the same LDR. To illustrate this, we simulate such an infinite aluminum plate by changing the free boundaries of the plate (except for the top and bottom side) to low-reflecting boundaries (LRB). Doing so, it is assured that the propagating ultrasonic waves in the sample can not (or only slightly) be reflected back from the edges, and therefore, the modelled plate should be a good representation of an infinite aluminum plate. Applying the above proposed algorithm to the database of out-of-plane displacement signals taken at the lower surface of this infinite plate, the LDR frequency in this case was found to be $f_e = (80.9 \pm 0.3)\,\text{kHz}$ (see Tab. 6.3), which is close to the value found earlier and therefore demonstrates the robustness of the algorithm. The estimated radius was $r_e = (4.7 \pm 0.2)\,\text{mm}$. The resulting mode for excitation position P_2 is depicted in Fig. 6.13a and 6.13b and shows the exact same position of the defect with a slightly changed vibration pattern of the background caused by the different boundary conditions.

Fig. 6.12a and Fig. 6.13a also show overlays of the simulation results in a 45 mm x 40 mm window on top of the virtual FBH containing aluminum sample that was simulated in the model. The overlay illustrates the match between the predicted LDR indication and the real position of the defect. The simulation results were both calculated using the datasets with excitation from P_2 assuming free boundary conditions and LRB, but in fact, any other source location or boundary condition could have equally been used. The results of the simulations confirm that the choice of boundary conditions as well as position of the excitation or shape of the maternal sample do not significantly influence the LDR frequency. This will be validated by experimental studies in section 6.5.

Remark also the difference between the shape of $g(f)$ for different boundary conditions (see Fig. 6.12c and Fig. 6.13c). It is obvious that the smaller the sample size, the more difficult it is to identify the LDR frequency correctly. This complication arises from the multitude of standing wave patterns created due to the edge reflections. If an 'infinite' sample is simulated using LRB, the $g(f)$ resembles a more or less isolated resonance peak with reasonably smooth in its vicinity.

6.5 LDR as an independent damage controlled parameter

In this section, we will experimentally investigate the influence of sample shape and source excitation position on the repeatability of the LDR values. The experimental study will allow us to demonstrate that LDR indeed is a defect related parameter and to estimate amount of variance that can be expected in a typical measurement.

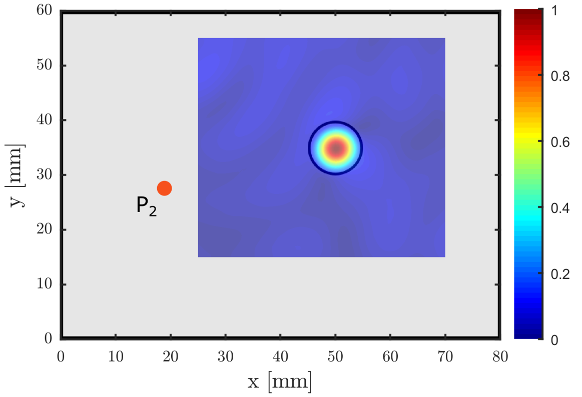

(a) LDR mode plotted over the virtual sample, black circle indicates position of the defect

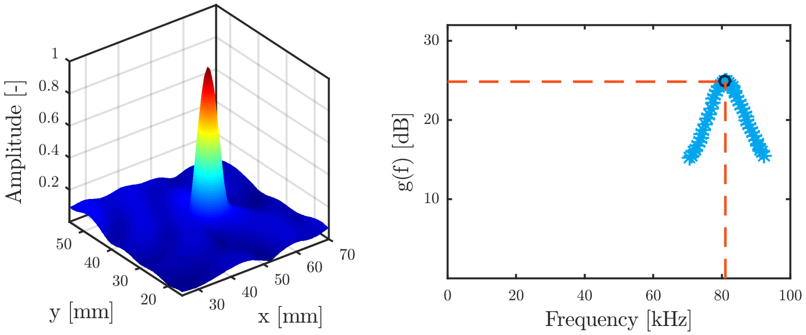

(b) 3D view, LDR mode

(c) $g(f)$, LDR value highlighted in red

Figure 6.13: Simulation results - LDR mode shape for the aluminum sample with FBH, assuming low-reflecting boundaries and excitation at P_2, $f_e = 81.05\,\text{kHz}$, $g(f_e) = 24.87\,\text{dB}$.

6.5.1 Experimental setup

In order to verify our assumption that LDR is only a function of the material properties and geometry of the defect, we prepared the following experiment. A large aluminum plate with dimensions of 300 x 210 x 5 mm that contains a circular FBH with radius $r = 5\,\mathrm{mm}$ and depth $d = 4\,\mathrm{mm}$ was divided into six sections (labelled from 0 to 5, see Fig. 6.15). Four different excitation points were defined and labelled P_1-P_4 and four DuraAct© transducers were attached onto the structure at these designated locations. Salol© was used to couple the transducers to the plate. The plate was supported on small patches of soft foam. Therefore, all boundary conditions (both faces and edges) are assumed to be free.

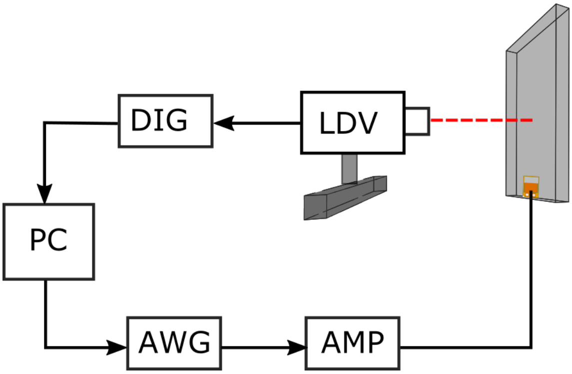

Figure 6.14: Scheme of the experimental setup.

The response of the plate when subjected to a sine sweep excitation was measured in a rectangular grid 45 x 45 mm with step $\Delta x = \Delta y = 1\,\mathrm{mm}$ using the Polytec OFV-3001 LDV with the OF-303 sensor head (single point measurement). The sweep signal was generated by a NI PXI-5142 AWG, routed via the Falco WMA-320 power amplifier, and the output of the LDV was digitized using the NI PXI-5122 digitizer. The sweep waveform used for the excitation throughout the experimental study had following parameters:

- Starting frequency $f_0 = 1\,\mathrm{kHz}$,
- Bandwidth $B = 99\,\mathrm{kHz}$,
- Duration $t = 2\,\mathrm{ms}$,
- Amplitude $A = 50\,\mathrm{V}_{\mathrm{pp}}$ after amplification.

Each signal contains $n_s = 16384$ samples that were digitized at a sampling rate of $f_s = 2\,\text{MHz}$. After the signals were transformed to the frequency domain, a 2D median filter with 3 x 3 core was applied to all frames $U_z(x, y, f = const.)$. This pre-processing step smooths the experimental data and removes the 'salt and pepper' image noise that is inherently present in vibrometric data. In contrast, the simulation data does not require this pre-processing step since it does not contain noise that is introduced by the data acquisition instrumentation.

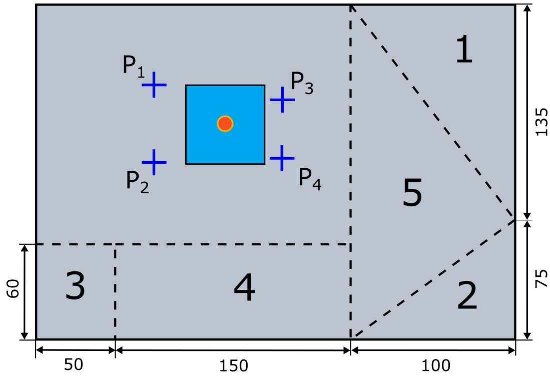

Figure 6.15: Aluminum plate dimensions and layout of the sections. The position of the defect (a FBH) is marked by a red dot and its center is located at [135,119]. The transducer locations correspond to the dark blue crosses. The locations of the transducers (in mm) referenced from the lower left corner are: $P_1 = [75, 158]$, $P_2 = [75, 110]$, $P_3 = [156, 150]$, $P_4 = [156, 112]$. The scan area is highlighted in light blue.

The experimental procedure was as follows: A database of response signals of the tested sample was measured using subsequent excitation from locations P_1 to P_4. Then the plate segment with label 1 was cut off (see Fig. 6.15 and Fig. 6.16) and a 'new' sample with different eigenmodes and eigenfrequencies was created. A new database of response signals of this setup was again measured using all available transducers and the procedure was repeated in the same manner for the remaining segments that were marked on the plate: segment 2, 3, 4 and 5. The experimental study thus resulted in six datasets, each containing four measurements. The first dataset, denoted as 0, was obtained on the intact sample. If the hypothesis of a constant LDR frequency is valid, the measured value should be similar for all tested setups and transducer locations.

---

[1] Sample provided by Geert Calu, Katholieke Hogeschool VIVES, Kortrijk.

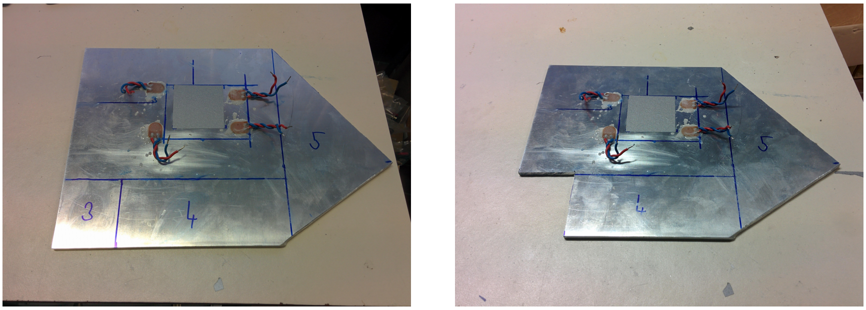

(a) Setup 2

(b) Setup 3

Figure 6.16: Photos of the aluminum sample[1].

6.5.2 Results

The experimental results, as output of the automatic LDR frequency detection algorithm, are summarized in Tab. 6.4. The iterative algorithm was used to estimate the defect radius r_e. The mean LDR frequency calculated using all the measurements was $f_e = (85 \pm 3)\,\mathrm{kHz}$ and the estimated FBH radius $r_e = (4.5 \pm 0.3)\,\mathrm{mm}$. Fig. 6.17 represents the mean value and standard deviation of f_e and r_e averaged over the four transducer positions for each setup.

As can be easily seen, the values differ only slightly from setup to setup. The difference between the lowest and highest values of f_e is only 2.8 kHz which is approximately twice the resolution in the frequency domain ($\Delta f = f_s/N_s = 1.22\,\mathrm{kHz}$). The standard deviation differs slightly between the setups. However, again, there is no great discrepancy or significant difference between the setups. The values of r_e are roughly constant with exception of setup 4 where the value dropped down to 4.33 mm. The relative variance of r_e is generally higher than the variance of f_e. The results grouped per transducer location does not reveal any irregularity. The mean values of both - f_e and r_e - are nearly constant. However, the r_e results generally have a higher variance (see Fig. 6.18).

Considering the results in Tab. 6.4 and the per group/per transducer position analysis presented in Fig. 6.17 and Fig. 6.18, it can be concluded that the LDR frequency is constant (up to ±3 %) for a given defect (FBH). The position of the excitation as well as the overall shape of the sample does not play a significant role in the detection procedure. The same conclusion applies to the radius (defect size) estimation. However, it is plausible that there exists a critical sample size, under which the detection and the iterative sizing algorithm will start to fail due to the internal reflections and dominant standing wave patterns.

Setup	Position	f_e [kHz]	gain [dB]	r_e [mm]
0	P_1	86.67	26.57	4.37
	P_2	85.45	26.16	4.33
	P_3	85.08	26.94	4.72
	P_4	86.06	25.26	4.51
1	P_1	86.79	24.26	4.30
	P_2	82.76	25.33	4.62
	P_3	82.76	26.27	4.72
	P_4	86.18	26.33	4.37
2	P_1	86.79	23.41	4.22
	P_2	88.13	24.74	4.15
	P_3	78.74	24.81	5.20
	P_4	85.57	25.84	4.58
3	P_1	85.69	23.06	4.15
	P_2	81.79	25.96	4.82
	P_3	80.69	25.20	5.01
	P_4	88.38	26.40	4.11
4	P_1	84.96	26.65	4.48
	P_2	84.96	26.41	4.62
	P_3	89.60	26.47	4.11
	P_4	88.26	24.37	4.11
5	P_1	79.83	26.69	5.01
	P_2	85.94	29.65	4.58
	P_3	85.94	28.03	4.33
	P_4	86.79	24.54	4.33
Average ± SD		85 ± 3	25.8 ± 1.4	4.5 ± 0.3

Table 6.4: Test scenarios and results of the experiment to confirm the stability of the LDR frequency. All measurements were with the free boundary conditions.

However, this would only be the case for very lightly damped materials, such as metal alloys. As will be further demonstrated in Sec. 6.6, this critical sample size lies well below the dimensions of usually inspected specimens. Therefore, it is not of a great concern for ultrasonic NDT applications in practice.

The localization of the FBH defect using the experimental data is demonstrated in Fig. 6.19. The dataset from setup 2 (after cutting off two segments) and for the transducer position P_3 was used to create this figure. The LDR mode shape is drawn over the photo of the sample and aligned with the Region of Interest

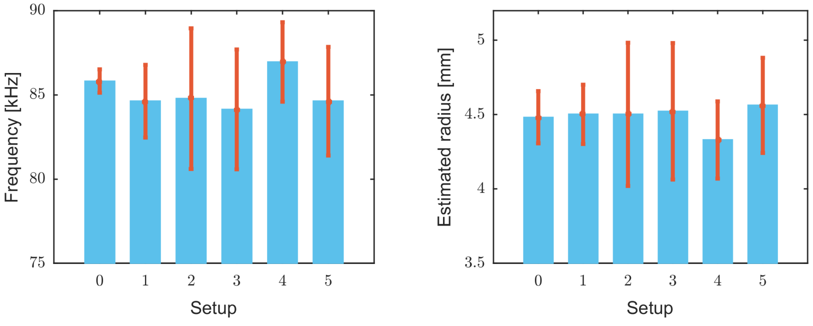

(a) (b)

Figure 6.17: Mean values of a) LDR frequency f_e and b) estimated radius r_e as a function of setup (sample geometry).

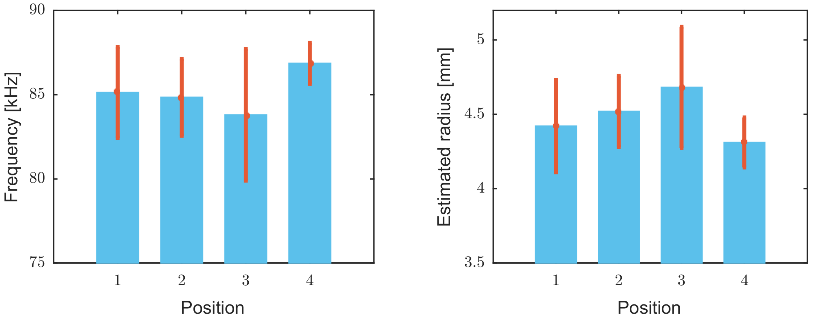

(a) (b)

Figure 6.18: Mean values of a) LDR frequency f_e and b) estimated radius r_e as a function of transducer position.

(ROI). The position of the peak in the mode shape accurately matches the real position of the FBH.

The relative error of the radius estimation, taking into account all datasets, was less the 10 %.

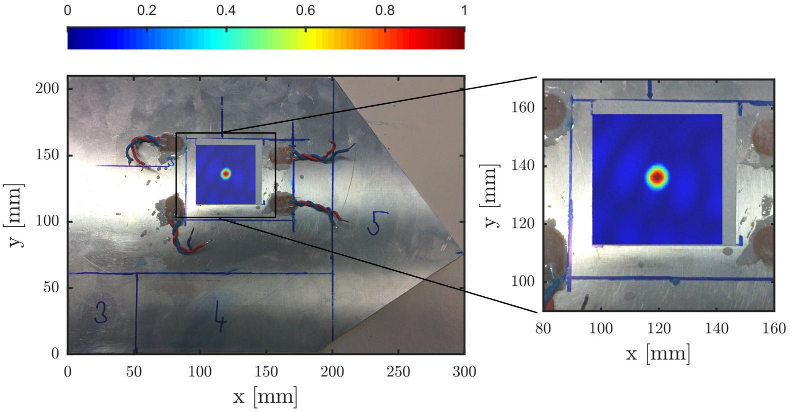

Figure 6.19: Localization of the FBH - after setup 2, for transducer position P_3.

6.6 Damage detection using LDR

In addition to the experimental robustness study of the FBH detection in aluminum, experimental measurements using a LDV were conducted in order to validate the LDR frequency detection algorithm in various other cases. Four different samples were prepared, with defects that represent the common type of damage features found in plate-like structures: an aluminum alloy plate with a FBH, which served as the model for the simulations discussed in the previous section 6.5.1, a GFRP plate with a circular delamination, an A-sandwich with a Rohacell© core and CFRP skin containing a disbond between the core and the laminate and a ionomer composite with delaminations located in different layers.

The experimental setup for the vibrometric measurements is depicted in Fig. 6.14 and it is identical as the one used in section 6.5. The only difference is that the output of the power amplifier ($\approx 50\,\mathrm{V_{pp}}$) was connected to either a DuraAct© circular PZT or to a DAKEL IDK-9. This was specifically meant to test the influence of different excitation elements on the f_e value. Both transducers were attached to the sample using either cyanoacrylate glue or Salol©. Reflective tape (Polytec - 91060 A-RET-T050) was used on the surface of the GFRP sample to increase the power of the reflected laser beam. The signal generation and acquisition was controlled using LabVIEW©.

Using a linear 2D motion stage, the laser beam scans a rectangular grid on the surface of the sample, covering a predefined region of interest (ROI). The spatial steps in Δx and Δy direction are kept constant and equal $\Delta x = \Delta y = 1\,\text{mm}$ for all the performed measurements. The typical size of the scanned area Ω is $45\,\text{mm} \times 40\,\text{mm}$. At each grid point $p(x, y)$, a signal containing 16384 samples is acquired at a sampling rate of $f_s = 2\,\text{MHz}$. The signal is averaged 128 times to increase its SNR. After the completion of the scan, the full data matrix $u(x, y, t)$ is formed and ready for further processing.

6.6.1 Aluminum with FBH

The first sample under study is an aluminum plate ($h = 5\,\text{mm}$) containing a single FBH with radius $r = 5\,\text{mm}$ and depth $d = 4\,\text{mm}$, similar to the plate modelled in the simulations (see Sec. 6.4 for details) and Tab. 6.1 for the material parameters). As mentioned in section 6.4, the theoretical LDR frequency for this sample is (as calculated using (6.1)) $f_t = 100.56\,\text{kHz}$.

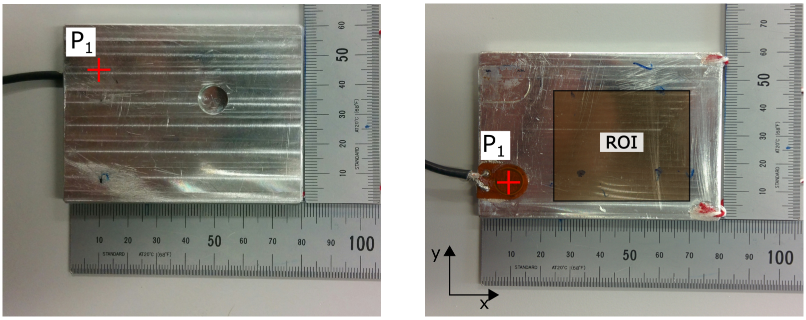

(a) Upper side

(b) Lower side

Figure 6.20: Aluminum sample with FBH and attached DuraAct© transducer (its position is indicated by a red cross on the bottom side picture). The scanning area on the front side is highlighted by a light yellow box[2].

An initial measurement was conducted using a single DuraAct© transducer at position P_1 (see Fig. 6.11 and Fig. 6.20). The excitation waveform comprised of a chirp with starting frequency $f_0 = 10\,\text{kHz}$, bandwidth $B = 90\,\text{kHz}$ and duration $T = 2\,\text{ms}$. The sample was suspended on two strings with negligible weight and can therefore be considered as having free boundary conditions.

The LDR frequency, obtained after postprocessing the experimental vibrometric signals by way of the proposed algorithm, was found to be $f_e = 78.00\,\text{kHz}$ with a gain $g(f_e) = 30.06\,\text{dB}$ (see Fig. 6.21). Several other test scenarios were

---

[2] Sample provided by Geert Calu, Katholieke Hogeschool VIVES, Kortrijk.

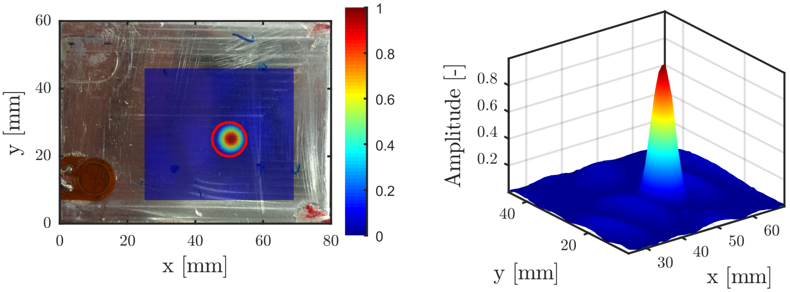

(a) Top view, image overlay (b) 3D view

Figure 6.21: Vibration pattern (normalized amplitude) of the FBH containing aluminum sample at LDR frequency - $f_e = 78.00\,\mathrm{kHz}$, gain $g(f_e) = 30.06\,\mathrm{dB}$, excitation - DuraAct© transducer at position P_1.

conducted in order to verify the postulation that the LDR frequency is constant for a given defect and to substantiate the robustness of the detection algorithm. The boundary conditions as well as the position and type of transducer were altered in different scenarios to asses the influence of the plate modes on the accuracy of the detection. The list of all test scenarios, together with a short description and the detected LDR frequency, is given in Tab. 6.5. The transducer locations P_1, P_2 and P_3 are the same as marked in Fig. 6.11.

As can be seen from Tab. 6.5, the LDR frequency is definitely a defect-related constant, independent of the position of excitation or boundary conditions. The mean value of the LDR frequency is $f_e = (78.0 \pm 0.4)\,\mathrm{kHz}$, which is lower than the analytically predicted value by approximately 22.4 %, but it in excellent agreement with the numerical simulation found in Section 6.4 (relative error $< 2\%$). The average LDR gain of the tested FBH is $g(f_e) = (31.4 \pm 1.8)\,\mathrm{dB}$ and the estimated radius of the defect (using iterative method) is $r_e = (4.4 \pm 0.2)\,\mathrm{mm}$. The true defect size is underestimated by 1.20 mm (12.5 %).

This confirms our hypothesis that a transient numerical FEM analysis provides the best prediction of the LDR and that it is far superior to the analytical formulae or the FEM eigenfrequency solution for this given sample. It is apparent from Tab. 6.5 that the selection of the transducer does not play a significant role in the detection. The only requirement for the transducer is to deliver the sufficient power output in the inspected frequency range.

Transducer	Position	BC	Coupl.	f_e [kHz]	gain [dB]	r_e [mm]
DuraAct©	P_1	Free	Glue	78.00	30.06	4.44
DuraAct©	P_1	1 edge cl.	Glue	78.25	30.21	4.30
DuraAct©	P_1	2 edges cl.	Glue	77.21	28.66	3.91
DuraAct©	P_1	Added mass	Salol©	78.37	30.81	4.41
IDK-9	P_1	Free	Glue	78.13	32.56	4.44
IDK-9	Opposite side	Free	Glue	78.49	32.33	4.48
IDK-9	P_2	Free	Glue	77.76	31.81	4.51
IDK-9	P_3	Free	Glue	77.94	34.76	4.51
Average ± SD				78.0 ± 0.4	31.4 ± 1.8	4.4 ± 0.2

Table 6.5: Test scenarios and results of the LDR detection for the FBH containing aluminum sample.

ρ [kg m^{-3}]	E_{xx} [GPa]	G_{xy} [GPa]	μ_{xy}
1800	2.70	0.6	0.14

Table 6.6: Material properties of the GFRP sample.

6.6.2 GFRP with delamination

The second sample is a GFRP plate ($h = 4\,\text{mm}$) containing an artificial delamination with a radius $r = 6\,\text{mm}$ (see Fig. 6.22). The GFRP is manufactured from plain weave (0°/90°) plies and its global elastic properties are summarized in Tab. 6.6. The delamination was introduced into the sample during the manufacturing process and represents a realistic delamination without an insert of any kind (Teflon©, Kapton©). The excitation signal in this experiment is a chirp with $f_0 = 1\,\text{kHz}$, bandwidth $B = 90\,\text{kHz}$ and duration $T = 2\,\text{ms}$. As in the case of the FBH in the aluminum sample, different source positions and boundary conditions have been investigated. The results of the LDR detection algorithm, as well as a short description of the test scenarios are summarized in Tab. 6.7.

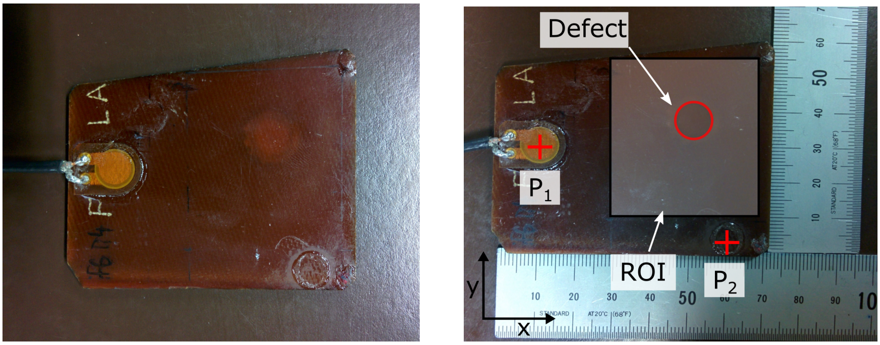

(a) Image of the GFRP sample (b) Sample with the the highlighted ROI

Figure 6.22: GFRP sample with the DuraAct© transducer in place. The scanned area (ROI) with the delamination (red circle) is highlighted. Transducer positions P_1 and P_2 are marked with red crosses.

The average value of the LDR frequency obtained after analyzing the data for all test scenarios is found to be $f_e = (58.4 \pm 0.8)\,\text{kHz}$. The corresponding value of the gain is $g(f_e) = (17.8 \pm 0.2)\,\text{dB}$ and the estimated defect radius using the iterative algorithm is $r_e = (4.6 \pm 0.1)\,\text{mm}$. The corresponding mode shape is depicted in Fig. 6.23a and Fig. 6.23b. It is apparent that the LDR gain is

Transducer	Position	BC	f_e [kHz]	gain [dB]	r_e [mm]
DuraAct©	P_1	Free	57.62	17.94	4.62
IDK-9	P_2	Free	58.47	17.58	4.75
IDK-9	P_2	1 edge cl.	59.20	17.84	4.55
	Average ± SD		58.4 ± 0.8	17.8 ± 0.2	4.6 ± 0.1

Table 6.7: Test scenarios and results of the LDR detection for the GFRP sample. The transducer was coupled to the sample with cyanoacrylate superglue.

approximately half of the gain measured in aluminum. This is caused mainly due to the higher attenuation of the tested GFRP specimen. Part of the lower gain can also be attributed to the smaller size of the sample which leads to a denser spectrum of eigenmodes close to the LDR.

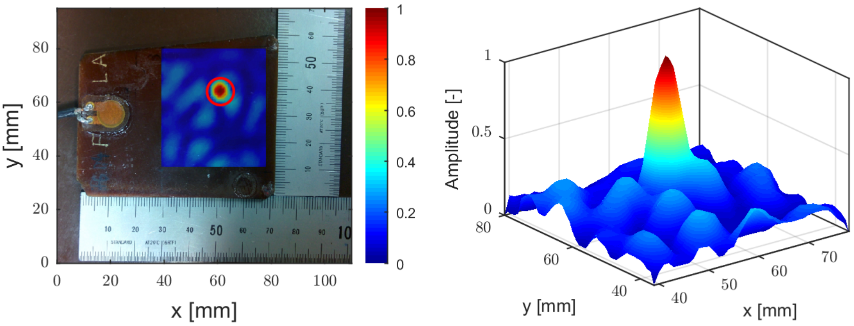

(a) Localization

(b) 3D LDR mode shape

Figure 6.23: Vibration pattern of the GFRP sample at $f_e = 58.47\,\text{kHz}$, gain $g(f_e) = 17.58\,\text{dB}$. The results correspond to the sample response for an excitation at position P_2.

6.6.3 Composite A-sandwich with disbond

The third sample is an A-sandwich consisting of a 10 mm thick Rohacell© core surrounded by two thin CFRP skins which is glued to a CFRP laminate of 5.5 mm. The lay-up of the sample is depicted in Fig. 6.24. The sample under consideration contains a 20 x 20 mm disbond between the adhesive layer and the inner CFRP skin. A DuraAct© transducer is attached to the lower outer surface of the CFRP laminate. In this case, the experiment was performed for two chirp excitations with different bandwidths. For the first experiment, the starting frequency was $f_0 = 1\,\text{kHz}$, the bandwidth $B_1 = 199\,\text{kHz}$, and the duration $T = 2\,\text{ms}$. In the second experiment, the same starting frequency and duration were used, however, the bandwidth was reduced to $B_2 = 99\,\text{kHz}$. A rectangular zone of 45 mm x 45 mm around the defect was scanned from the lower surface as indicated by the zone covered by a gray reflecting tape in Fig. 6.25b.

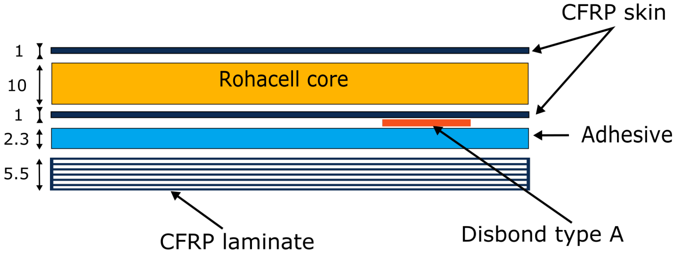

Figure 6.24: Lay-up of the A-sandwich sample. The core is enclosed between two thin CFRP skins and bonded to a thicker CFRP laminate using a layer of adhesive. The disbond is located in the upper part of the adhesive layer between the CFRP skinned core and the CFRP laminate.

The LDR of the disbond in the tested sample is found to be $f_e = 155.02\,\text{kHz}$ for an excitation with the largest bandwidth B_1 with a gain of $g(f_e) = 17.84\,\text{dB}$ and an estimated radius $r_e = 5.50\,\text{mm}$ (iterative sizing). The corresponding LDR mode is shown in Fig. 6.26a which clearly indicates the correct position of the disbond. The smallest rectangle (bounding box) that encloses the defect zone Ω_d has a size of 13 x 11 mm which is again an underestimation of the real size. Interestingly, for the smaller excitation bandwidth B_2 of 99 kHz (sweep from 1-100 kHz), we have found nearly the same LDR frequency of $f_e = 154.72\,\text{kHz}$, with gain of $g(f_e) = 17.40\,\text{dB}$ and estimated radius $r_e = 7.68\,\text{mm}$.

The fact that the LDR has been detected outside of the excitation bandwidth B_2 is not entirely surprising. Looking at the frequency spectrum of the received signals, one clearly observes components up to 200 kHz (see Fig. 6.27). This can be attributed to the broadband frequency response (1-300 kHz) of the transducer, in combination with the spectral broadening of the frequency spectrum as a result of nonlinear effects in the wave propagation causing harmonics to be generated due to a non-Hookian constitutive relation between stress and strain at the defect location. In light of the expected transfer of energy to higher frequencies, it is thus quite normal to find the LDR frequency outside the excitation bandwidth. Fig. 6.26b shows the LDR mode for this case, and confirms that its distribution is similar to the results shown in Fig. 6.26a. In both cases, the correct position of the disbond is revealed.

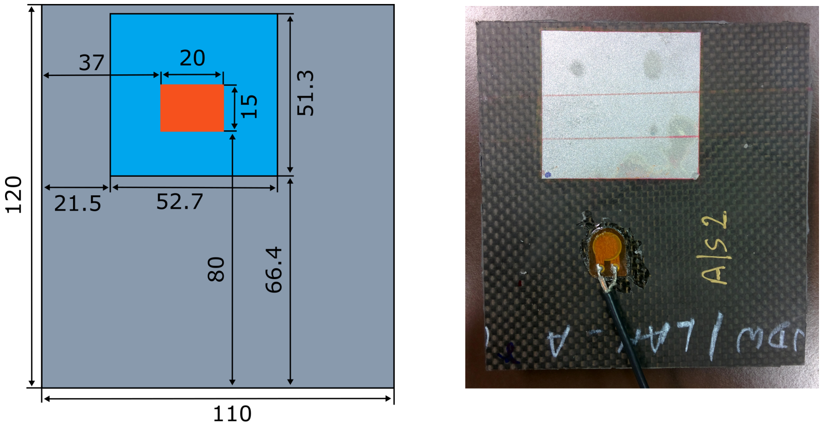

(a) Sketch of the sample (b) Image of the sample

Figure 6.25: Dimensions of the composite A-sandwich sample, the position of the disbond is highlighted in red and the scanned ROI is marked by a blue rectangle.

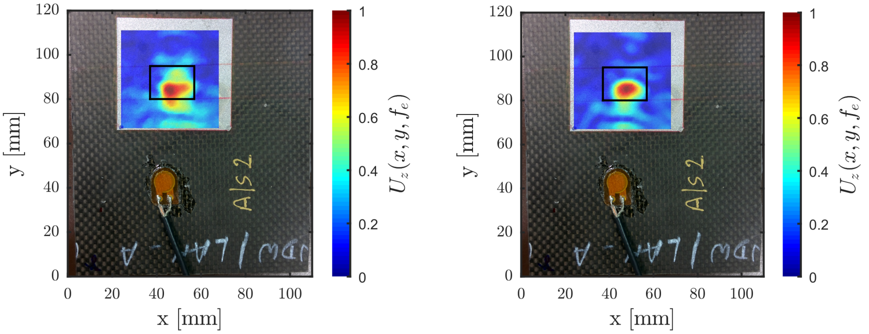

(a) $f_e = 154.72\,\mathrm{kHz}$ (b) $f_e = 155.02\,\mathrm{kHz}$

Figure 6.26: Vibration pattern and the location of the disbond in a composite A-sandwich at the LDR frequency a) bandwidth B_2 b) bandwidth B_1.

6.6.4 Ionomer samples

The final batch of samples that were tested using the proposed methodology was manufactured from a combination of CFRP and an ionomeric layer that acts in the system as a self-healing agent. The 1 mm thick layer of the ionomer/Fe_3O_4

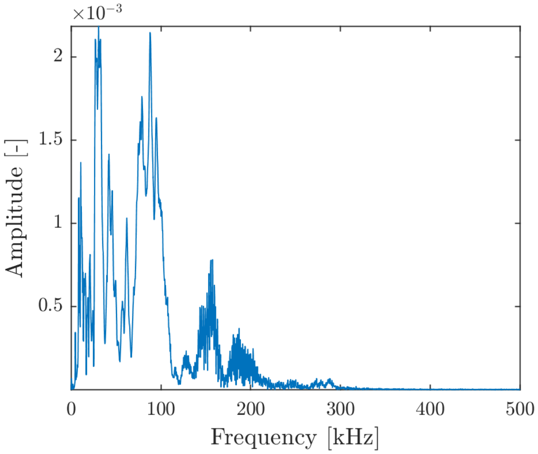

Figure 6.27: Spectrum of the response signal with the excitation bandwidth B_2. The spectral content reaches up to 200 kHz.

nanoparticle composite was squeezed between two outer CFRP skins. The general dimensions of the samples were 100 x 100 mm with a thickness of 3 mm. A circular delamination was formed in the central section of the sample. Two types of samples that differ in the through-thickness position of the delamination are considered for testing. For each batch of samples, the radii of the included delaminations were 10 mm and 25 mm. All test samples were developed and manufactured at TU Delft and kindly provided for testing in the framework of the ALAMSA project.

The ionomeric mid-thickness layer, doped with Fe_3O_4, provides a self-healing capability to the sample that is expected to restore the mechanical properties at the location of the delamination when heated. In other words, the ionomeric composite is a self-healing system that will heal a delamination when triggered by elevated temperatures [268, 269, 270]. This type of specimen is a very fine benchmark for LDR detection, because the delamination is easily detectable by a conventional pulse-echo or through transmission ultrasonic testing.

Rigid-soft delamination

In the first pair of samples, the delamination is located underneath the first CFRP cover layer (see Fig. 6.28). This setup was termed *rigid-soft* by the team at TU Delft, because the delamination separates the stiff CFRP from the soft ionomer layer.

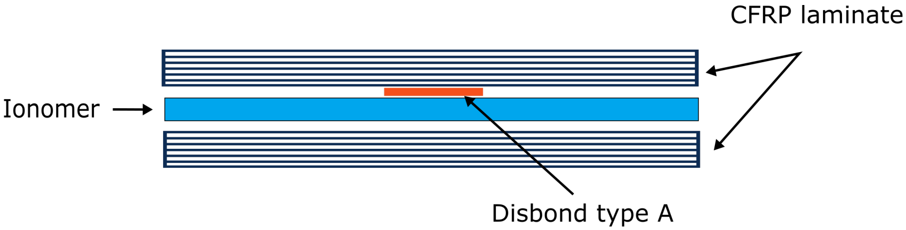

Figure 6.28: Location of the rigid-soft delamination.

A conventional ultrasonic C-scan of the samples revealed the actual sizes of the delaminations (see Fig. 6.29b and Fig. 6.31b). The C-scan measurements were carried out in the NDT laboratory of the University of Gent (UGent) and they serve as a control measurement. The C-scans were obtained using a 5 MHz unfocused immersion transducer (GE H5K) and a USIP40 acquisition unit. The system was operated in through-transmission mode.

Fig. 6.31b reveals that the real radius of the larger delamination is actually smaller than the declared 25 mm. The real size, according to the C-scan measurement, is 20.0 mm. The size of the smaller delamination is also slightly underestimated, the real value being 18.0 mm.

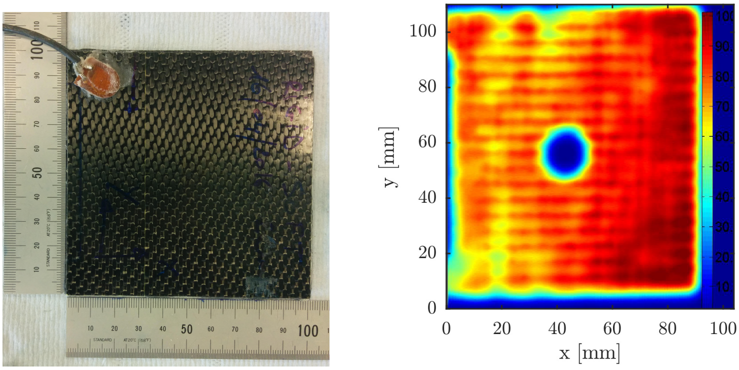

(a) Photo of the sample

(b) Ultrasonic transmission C-scan

Figure 6.29: The ionomer sample with a $r = 10\,\mathrm{mm}$ rigid-soft delamination.

The excitation waveform for LDR inspection was a sweep 1-50 kHz with duration of $T = 2\,\mathrm{ms}$. This signal was routed via Falco WMA-320 amplifier to a DuraAct© circular PZT that was coupled to the sample using Salol©.

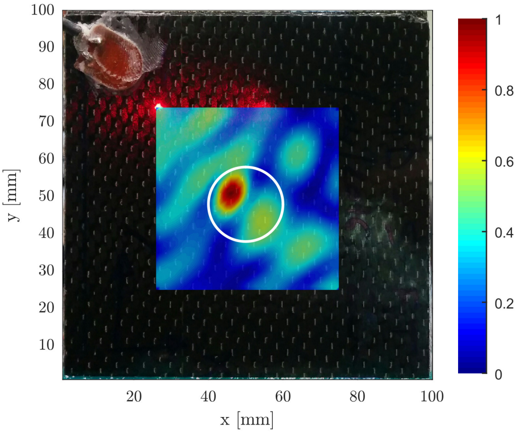

Figure 6.30: LDR of the ionomer sample with a $r = 10\,\mathrm{mm}$ rigid-soft delamination. LDR frequency $f_e = 20.6\,\mathrm{kHz}$.

Fig. 6.30 shows the LDR shape predicted from the acquired data. It is clear from the image that the LDR mode only highlights the upper left quadrant of the delamination. In this case, the automatic sizing does not provide a relevant estimation of the equivalent radius and the size of the defect is significantly underestimated. On the other hand, the position of the defect was successfully indicated and the indication stands out from the background eigenvalue pattern of the ionomeric sample. The detected LDR frequency of $f_e = 20.6\,\mathrm{kHz}$ is considerably high for the size of the delamination. This may be attributed to the stiff CFRP layer that typically leads to higher f_e values (see section 6.6.2).

The larger delamination, with designed $r = 25\,\mathrm{mm}$, was detected in a similar fashion as the smaller one using the same excitation signal. There is a clear indication properly located in the center of the delamination, but the size of the indication is again underestimated. Unlike the smaller delamination, it is not superposed on an eigenmode of the ionomeric sample. Hence, the indication is more apparent. The detected LDR frequency, $f_e = 3.96\,\mathrm{kHz}$, is significantly lower than the frequency of the smaller delamination.

All-in-all, it can be concluded that a rigid-soft delamination that is embedded in a ionomeric layer between two CFRP layers can be detected successfully. However, its size cannot be reliably determined.

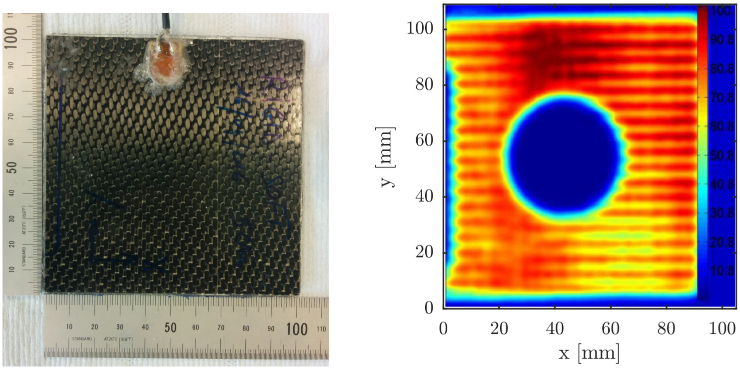

(a) Photo of the sample (b) Ultrasonic transmission C-scan

Figure 6.31: The ionomer sample with a $r = 25.0\,\mathrm{mm}$ rigid-soft delamination.

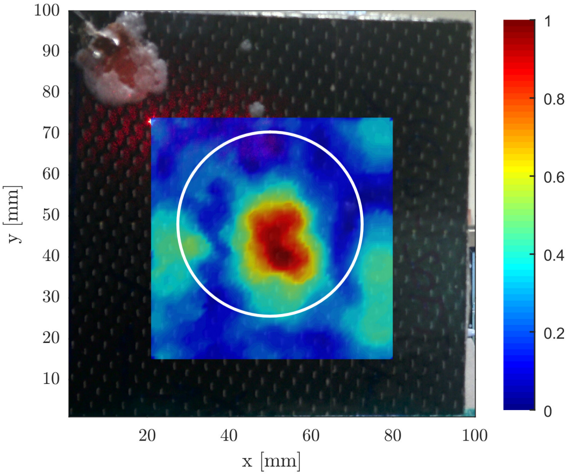

Figure 6.32: LDR of the ionomer sample with a $r = 25.0\,\mathrm{mm}$ rigid-soft delamination. The LDR frequency is $f_e = 3.96\,\mathrm{kHz}$.

Soft-soft delamination

The second batch of ionomeric composite samples contain a delamination that is located exactly in the middle of the ionomer layer (see Fig. 6.33), and is therefore called *soft-soft*. Fig. 6.34b and Fig. 6.36b show the C-scans of the samples provided by UGent for a 10 and 25 mm radius size soft-soft delamination. The measurement setup for the C-scans was identical to the rigid-soft delaminations. The sizes estimated from a Full Width Half Max (FWHM) analysis of the C-san data are 8.5 and 22.5 mm respectively.

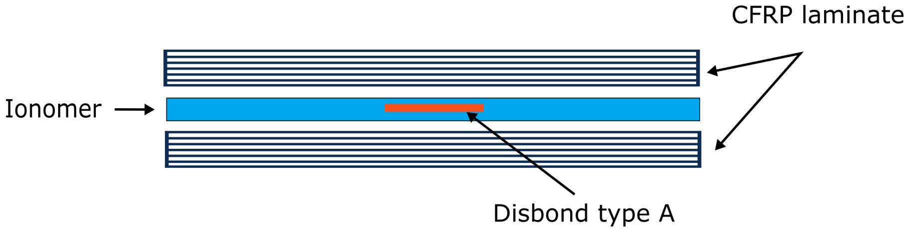

Figure 6.33: Location of the soft-soft delamination.

The first sample contained a single soft-soft delamination with a target radius $r = 10\,\mathrm{mm}$. However, the actual diameter, as determined from the ultrasonic C-scan data using a FWHM method, was 8.5 mm. The white circle in Fig. 6.35 indicates the actual size and location of the delamination, as determined from the C-scan data.

This composition proved to be significantly more difficult to inspect with the LDR method, particularly for the largest delamination. The experimentally determined LDR frequency for the first sample, containing a single soft-soft delamination with designed radius $r = 10\,\mathrm{mm}$, was found to be $f_e = 14.4\,\mathrm{kHz}$. The corresponding LDR mode shape, depicted in Fig. 6.35, matches very well the center of the delamination. The location is predicted with a high accuracy, however, the size of the delamination was again substantially underestimated. It is worth noticing that the LDR is clearly superimposed on an eigenmode of the plate. Hence, the level of background is generally high in comparison with other results.

The second sample in this batch contained a central soft-soft delamination with a theoretical radius $r = 25.0\,\mathrm{mm}$, whereas the C-scan analysis merely reveals 22.5 mm (see Fig. 6.36b). In this case, the LDR detection was not successful and no LDR frequency was detected. Neither the automated algorithm, nor a manual search revealed any sign of LDR in the recorded response of the sample. Consequently, the LDR technique failed to detect the damage in this case. The reason of this failure may be the fact that the LDR is very low ($\ll 1\,\mathrm{kHz}$) and the transducer cannot successfully excite it due to its limited frequency range.

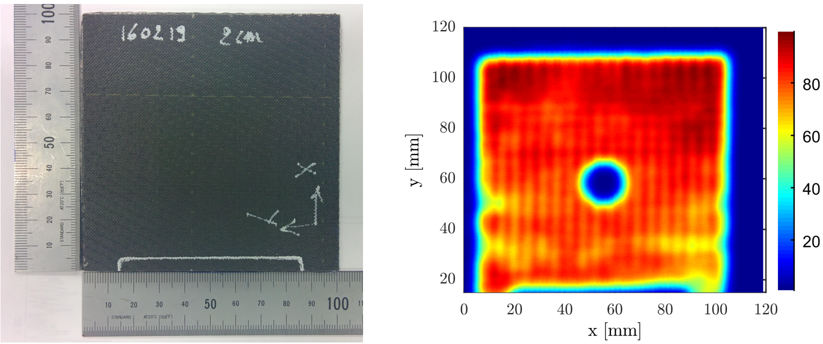

(a) Photo of the sample (b) Ultrasonic transmission C-scan

Figure 6.34: The ionomer sample with a $r = 10.0\,\mathrm{mm}$ soft-soft delamination.

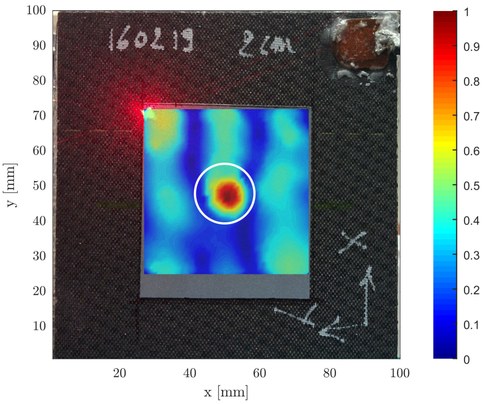

Figure 6.35: LDR of the ionomer sample with a $r = 10.0\,\mathrm{mm}$ soft-soft delamination, $f_e = 14.4\,\mathrm{kHz}$.

6.7 Conclusion

In this section of the manuscript, we have demonstrated an automatic LDR detection algorithm that is based on characteristic LDR mode shape patterns and image processing techniques. The algorithm is coupled to an iterative sizing routine that is capable of estimating the size of an equivalent circular defect. The equivalent circular defect is used as an idealization of a real defect shape and size based on the expected distribution of the fundamental LDR mode shape. The methodology is verified in numerical simulations as well as

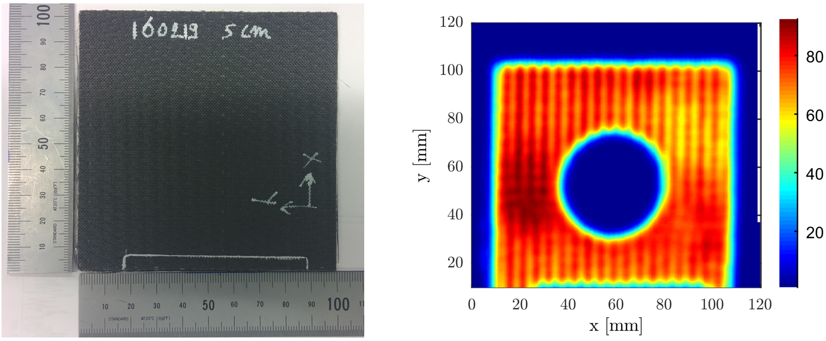

(a) Photo of the sample (b) Ultrasonic transmission C-scan

Figure 6.36: The ionomer sample with a $r = 25\,\mathrm{mm}$ soft-soft delamination.

in experiments. Several measurements were carried out on different samples, e.g. sandwich composite, GFRP, ionomer composite, that contain various type of damage, such as delaminations or disbonds. Moreover, it was demonstrated that the LDR mode frequency and shape is independent of the BC and the source location up to the measurement error.

The various scenarios in the experimental study confirm that the LDR characteristics are defined by the combination of its geometry and elastic properties of the maternal material and not by the BCs, which only play an insignificant role in the determination of the LDR frequency.

Chapter 7

Conclusion

7.1 Conclusion

This manuscript is divided in three major parts. In the first part, a theoretical background on GW ultrasonic testing of anisotropic plates was given, starting from the very basics of anisotropy to the numerical and experimental methods for dispersion analysis. Several observations and suggestions for improvement were made in the course of the first chapters, especially with regard to the analysis of the dispersion data using the MPM matrix and its combination with the well known 2D FFT method. Next, the fundamental parts of nonlinear elastic wave spectroscopy (NEWS) were introduced in order to better understand the underlying mechanisms of nonlinear elasticity and to select the most suitable method that can be combined with the GW propagation to provide new and better NDT techniques.

The knowledge from the first part of the manuscript is essential for the second part where a novel nonlinear GW imaging method has been proposed. The method is based on the nonlinear SSM method and on the well-known probabilistic imaging algorithm RAPID. The algorithm was tested in multiple simulated test cases, including for instance the case of two nonlinear delaminations inside a single anisotropic plate. The results of these test cases suggest that the proposed algorithm is performing well and that it is worthwhile to be tested experimentally. From subsequent experimental verification, it was concluded that the imaging algorithm can indeed detect a real impact damage and an artificial delamination in CFRP, even though with considerably decreased quality in latter case.

The third and last part of the manuscript was dedicated to the LDR method. Several improvements to the development of an automatic detection algorithm for the appropriate LDR frequency as well as to an iterative sizing approach were proposed and implemented. These new developments were first tested using numerical simulations and then further successfully verified on different samples, ranging from GFRP to composite sandwich. The fundamental question whether the LDR frequency is dependent on the sample geometry or on the boundary conditions was addressed. Using the numerical simulation and experimental measurements, it was concluded that the LDR frequency is independent on sample and boundary parameters, and thus only defined by the defect characteristics.

7.2 Future work

Future work in the field of SHM and NDT should continue to improve the proposed GW based nonlinear RAPID imaging method. A very challenging task is the maturation of this technique and its application outside of the laboratory environment. The crucial parts of this maturation process are the development of accessible measurement instrumentation with extremely low inherent nonlinearity, optimal array shape determination and a detailed analysis of the nonlinear GW-defect interaction. Although the new RAPID concept removes the cumbersome intact baseline dependency, it is very sensitive to any nonlinearity in the measurement equipment which makes it currently very demanding. Another interesting challenge is the application of nonlinear RAPID to more complex structures, such as T-stringers, reinforced CFRP panels or even sandwich composites.

In case of LDR, the fundamental questions are mostly answered and the functionality has been demonstrated thoroughly. However, the main challenge here is to find a way to detect the LDR frequency without having to use a laser vibrometer. LDV is an extremely expensive piece of equipment that requires a skilled operator. In this respect, we suggest to investigate the potential of alternative detection methods, such as for instance thermography or ultrasonic emission, that may allow an easier and faster detection of the LDR thanks to the consideration of coupled effects. This will greatly help the method to leave the laboratory and to become a standardized inspection technique.

First attempts to test the coupled thermographic-LDR detection approach have already been done. It was observed in the GFRP sample (described in section 6.6.2) that a low power ultrasonic excitation at the LDR leads to a localized heating of the defect area, as illustrated in Fig. 7.1. This effect is

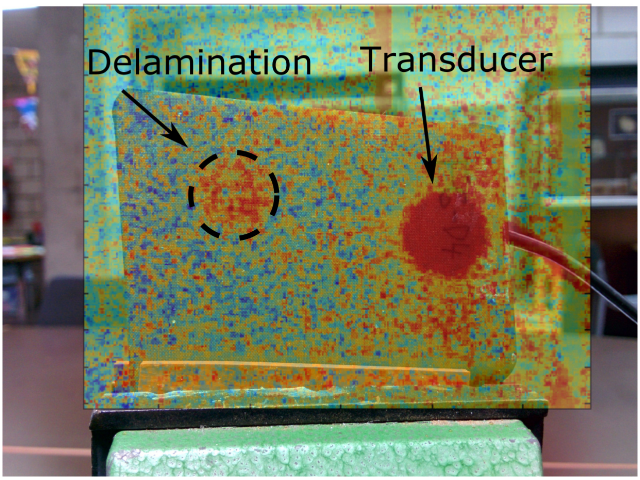

Figure 7.1: Phase image from a lock-in thermography on a GFRP sample from section 6.6.2 with delamination (image overlay). Thermograms were captured by a FLIR X6540sc IR camera with a frame rate of 80 Hz and integration time 2 ms. The sample was excited using a single DuraAct© transducer driven at the LDR frequency 57.62 kHz with a lock-in frequency of 1 Hz.

caused by a high amplitude of vibration at LDR frequency that is contained in the area of the defect and that results in more intensive friction, clapping and visco-elastic losses. Hence, it can provide a convenient detection tool for a future LDR-based IR detection method. Moreover, it can help to reduce the cost of such measurements by replacing a LDV with an IR camera.

Appendix A

Tensor and vector algebra

A.1 Vector and tensor algebra

Let us assume a vector field $\boldsymbol{u} = [u_1, u_2, u_3]$, then the gradient of $\boldsymbol{u}$ is a vector that is defined as

$$\operatorname{grad}(\boldsymbol{u}) = \nabla \boldsymbol{u} = \vec{e}_1 \frac{\partial u_1}{\partial x_1} + \vec{e}_2 \frac{\partial u_2}{\partial x_2} + \vec{e}_3 \frac{\partial u_3}{\partial x_3}, \tag{A.1}$$

where

$$\nabla = \vec{e_1} \frac{\partial}{\partial x_1} + \vec{e_2} \frac{\partial}{\partial x_2} + \vec{e_3} \frac{\partial}{\partial x_3}. \tag{A.2}$$

The divergence of $\vec{u}$ is a scalar that is defined as

$$\operatorname{div}(\boldsymbol{u}) = \nabla \cdot \boldsymbol{u} = \frac{\partial u_1}{\partial x_1} + \frac{\partial u_2}{\partial x_2} + \frac{\partial u_3}{\partial x_3}, \tag{A.3}$$

and lastly the curl of a vector field is a vector

$$\operatorname{curl}(\boldsymbol{u}) = \nabla \times \boldsymbol{u} = \Big(\frac{\partial u_3}{\partial x_2} - \frac{\partial u_2}{\partial x_3}\Big)\vec{e_1} + \Big(\frac{\partial u_1}{\partial x_3} - \frac{\partial u_3}{\partial x_1}\Big)\vec{e_2} + \Big(\frac{\partial u_2}{\partial x_1} - \frac{\partial u_1}{\partial x_2}\Big)\vec{e_3}. \tag{A.4}$$

The *Laplace (operator)* of a scalar field f is a scalar that is defined as

$$\Delta f = \nabla^2 f = \frac{\partial^2 f}{\partial^2 x_1} + \frac{\partial^2 f}{\partial^2 x_2} + \frac{\partial^2 f}{\partial^2 x_3}. \tag{A.5}$$

Tensors

The Einstein's summation rule is defined as

$$a_i b_i = \sum_{i=1}^{n} a_i b_i. \tag{A.6}$$

The derivation of the tensor with respect to the spatial coordinate x_j is indicated using the comma

$$u_{i,j} = \frac{\partial u_i}{\partial x_j}. \tag{A.7}$$

Appendix B

Elasticity

B.1 Traction

Traction (stress vector) is defined as

$$T_i = \tau_{ji} n_j \tag{B.1}$$

using the stress tensor τ_{ij} and $\vec{n}$ which is the normal to the surface at a given point of the elastic body. The stress-free or traction-free BC implicate that all the stress tensor components normal to the free surface of the elastic body are zero or equivalently, the traction on the surface is zero

$$T_i \equiv \tau_{ji} n_j = 0 \quad \Leftrightarrow \quad \tau_{ij} n_j = 0 \tag{B.2}$$

B.2 Voigt's notation

Voigt's notation recasts the equation of elasticity from the tensor to vector form. First, the indices are contracted

$$11 \to 1, \quad 22 \to 2, \quad 33 \to 3, \quad 23, 32 \to 4, \quad 31, 13 \to 5, \quad 12, 21 \to 6. \tag{B.3}$$

and second, the original shear strain components are replaced by $\epsilon_4 = 2\varepsilon_{23}$, $\epsilon_5 = 2\varepsilon_{13}$ and $\epsilon_6 = 2\varepsilon_{12}$. Hence, equation

$$\tau_{ij} = C_{ijkl} \varepsilon_{kl}, \tag{B.4}$$

can be rewritten element-wise as

$$\begin{bmatrix} \tau_1 \\ \tau_2 \\ \tau_3 \\ \tau_4 \\ \tau_5 \\ \tau_6 \end{bmatrix} = \begin{bmatrix} C_{11} & C_{12} & C_{13} & C_{14} & C_{15} & C_{16} \\ & C_{22} & C_{23} & C_{24} & C_{25} & C_{26} \\ & & C_{33} & C_{34} & C_{35} & C_{36} \\ & & & C_{44} & C_{45} & C_{46} \\ & & sym & & C_{55} & C_{56} \\ & & & & & C_{66} \end{bmatrix} \begin{bmatrix} \varepsilon_1 \\ \varepsilon_2 \\ \varepsilon_3 \\ \varepsilon_4 \\ \varepsilon_5 \\ \varepsilon_6 \end{bmatrix} \tag{B.5}$$

or in a more concise form as

$$\vec{\tau} = \mathbf{C}\vec{\varepsilon}. \tag{B.6}$$

B.3 Rotation of the stiffness tensor

Let us assume that the principle axes of an anisotropic sample are rotated by Euler angles φ, θ, ψ with respect to the principal material coordinates see Fig. B.1. The rotated stiffness tensor in the global coordinate system can be then expressed using the Bond transformation matrix $\mathbf{M}$ as

$$\mathbf{C} = \mathbf{M}\mathbf{C}\mathbf{M}^T, \tag{B.7}$$

where $\mathbf{C}$ is the stiffness tensor in the original coordinate system. The 6x6 transformation matrix has a form of

$$\mathbf{M} = \begin{bmatrix} M_1 & M_2 \\ M_3 & M_4 \end{bmatrix}, \tag{B.8}$$

where

$$\mathbf{M}_1 = \begin{bmatrix} A_{11}^2 & A_{12}^2 & A_{13}^2 \\ A_{21}^2 & A_{22}^2 & A_{23}^2 \\ A_{32}^2 & A_{32}^2 & A_{33}^2 \end{bmatrix} \tag{B.9}$$

$$\mathbf{M}_2 = \begin{bmatrix} 2A_{21}A_{13} & 2A_{13}A_{11} & 2A_{11}2A_{12} \\ 2A_{22}A_{23} & 2A_{23}A_{21} & 2A_{21}2A_{22} \\ 2A_{32}A_{33} & 2A_{33}A_{31} & 2A_{31}2A_{32} \end{bmatrix} \tag{B.10}$$

$$\mathbf{M}_3 = \begin{bmatrix} A_{21}A_{31} & A_{22}A_{32} & A_{23}A_{33} \\ A_{31}A_{11} & A_{32}A_{12} & A_{33}A_{13} \\ A_{11}A_{21} & A_{12}A_{22} & A_{13}A_{23} \end{bmatrix} \tag{B.11}$$

$$\mathbf{M}_4 = \begin{bmatrix} A_{22}A_{33} + A_{23}A_{32} & A_{21}A_{33} + A_{23}A_{31} & A_{22}A_{31} + A_{21}A_{32} \\ A_{12}A_{33} + A_{13}A_{32} & A_{13}A_{31} + A_{11}A_{33} & A_{11}A_{32} + A_{12}A_{31} \\ A_{12}A_{23} + A_{13}A_{22} & A_{13}A_{21} + A_{11}A_{23} & A_{11}A_{22} + A_{12}A_{21} \end{bmatrix}. \tag{B.12}$$

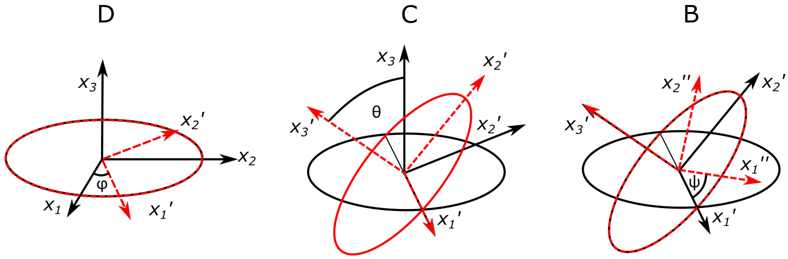

Figure B.1: Rotation of the coordinate system, Euler angles.

where the matrix $\mathbf{A}$ can be calculated from

$$\mathbf{A} = \mathbf{BCD}. \tag{B.13}$$

The matrices on the RHS represent the rotation around axis x_3 by angle φ

$$\mathbf{D} = \begin{bmatrix} \cos\varphi & \sin\varphi & 0 \\ -\sin\varphi & \cos\varphi & 0 \\ 0 & 0 & 1 \end{bmatrix}, \tag{B.14}$$

around the new axis x_1' by angle θ

$$\mathbf{C} = \begin{bmatrix} 1 & 0 & 0 \\ 0 & \cos\theta & \sin\theta \\ 0 & -\sin\theta & \cos\theta \end{bmatrix} \tag{B.15}$$

and around the new x_3' by angle ψ

$$\mathbf{B} = \begin{bmatrix} \cos\psi & \sin\psi & 0 \\ -\sin\psi & \cos\psi & 0 \\ 0 & 0 & 1 \end{bmatrix}. \tag{B.16}$$

Appendix C

State matrix formalism and Legendre polynomial approximation

C.1 Legendre Polynomials

The nth degree Legendre polynomial is given by

$$P_n(x) = \frac{1}{2^n n!} \frac{d^n}{dx^n} (x^2 - 1)^n \tag{C.1}$$

or recursively as

$$P'_{n+1}(x) - P'_{n-1}(x) = (2n + 1) P_n(x). \tag{C.2}$$

The shape of the Legendre polynomials on the closed interval <-1,1> are depicted in Fig. C.1

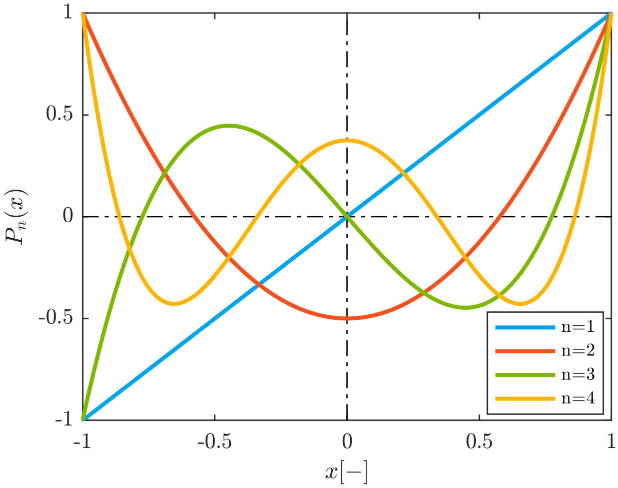

Figure C.1: Shape of the Legendre polynomials for different polynomial degrees.

C.2 Matrices

Matrices A_1', A_2', A_2'' that form the state matrix A are given as

$$\begin{aligned} A_1' &= (\Gamma_{11} - \Gamma_{13}\Gamma_{33}^{-1}\Gamma_{31})\cos^2\varphi + && \text{(C.3)} \\ &+ (\Gamma_{12} + \Gamma_{21} - \Gamma_{13}\Gamma_{33}^{-1}\Gamma_{32} - \Gamma_{23}\Gamma_{33}^{-1}\Gamma_{31})\cos\varphi\sin\varphi && \text{(C.4)} \\ &+ (\Gamma_{22} - \Gamma_{23}\Gamma_{33}^{-1}\Gamma_{32})\sin^2\varphi && \text{(C.5)} \\ A_2' &= \Gamma_{33}^{-1}(\Gamma_{31}\cos\varphi + \Gamma_{32}\sin\varphi) && \text{(C.6)} \\ A_2'' &= (\Gamma_{13}\cos\varphi + \Gamma_{23}\sin\varphi)\Gamma_{33}^{-1}, && \text{(C.7)} \end{aligned}$$

where

$$\Gamma_{il} = \begin{bmatrix} C_{i11l} & C_{i12l} & C_{i13l} \\ C_{i21l} & C_{i22l} & C_{i23l} \\ C_{i31l} & C_{i32l} & C_{i33l} \end{bmatrix}. \tag{C.8}$$

Bibliography

[1] I. G. Scott and C. M. Scala, "A review of non-destructive testing of composite materials," *NDT International*, vol. 15, no. 2, pp. 75–86, 1982.

[2] R. Adams and P. Cawley, "A review of defect types and nondestructive testing techniques for composites and bonded joints," *NDT International*, vol. 21, no. 4, pp. 208–222, 1988.

[3] H. Kaczmarek and S. Maison, "Comparative ultrasonic analysis of damage in CFRP under static indentation and low-velocity impact," *Composites Science and Technology*, vol. 51, pp. 11–26, jan 1994.

[4] U. Schnars and R. Henrich, "Applications of NDT Methods on Composite Structures in Aerospace Industry," in *Conference on Damage in Composite Materials*, 2006.

[5] C. J. Lissenden and J. L. Rose, "Structural Health Monitoring of Composite Laminates Through Ultrasonic Guided Wave Beam Forming," in *NATO Applied Vehicle Technology Symposium on Military Platform Ensured Availability*, pp. 1–14, 2008.

[6] P. Fromme, P. Wilcox, and P. Cawley, "Remote Monitoring of Plate-Like Structures Using Guided Wave Arrays," *Review of Quantitative Nondestructive Evaluation*, vol. 22, pp. 157–164, 2003.

[7] R. Unnþórsson, M. T. Jonsson, and T. P. Runarsson, "NDT Methods for Evaluating Carbon Fiber Composites," *Proceedings of Composites Testing and Model Identification*, pp. 1–17, 2004.

[8] J. L. Rose, *Ultrasonic Waves in Solid Media.* Cambridge University Press, 2004.

[9] J. L. Rose, *Ultrasonic Guided Waves in Solid Media.* Cambridge University Press, 1 ed., 20014.

[10] P. Cawley and M. J. S. Lowe, "Practical long range guided wave inspection-applications to pipes and rail," *Materials Evaluation*, pp. 66–74, 2003.

[11] P. D. Wilcox, *Lamb Wave Inspection of Large Structures Using Permanently Attached Transducers.* PhD thesis, Imperial College of Science, Technology and Medicine, 1998.

[12] M. Castaings and P. Cawley, "The generation, propagation, and detection of Lamb waves in plates using aircoupled ultrasonic transducers," *The Journal of the Acoustical Society of America*, vol. 100, no. 5, pp. 3070–3077, 1996.

[13] P.-M. Lam, K.-T. Lau, H.-Y. Ling, Z. Su, and H.-Y. Tam, "Acousto-ultrasonic sensing for delaminated GFRP composites using an embedded FBG sensor," *Optics and Lasers in Engineering*, vol. 47, no. 10, pp. 1049–1055, 2009.

[14] M. Mieloszyk, M. Krawczuk, L. Skarbek, and W. Ostachowicz, "An application of neural network for Structural Health Monitoring of an adaptive wing with an array of FBG sensors," *Journal of Physics: Conference Series*, vol. 305, pp. 012066–012076, jul 2011.

[15] J. L. Rose, D. D. Hongerholt, and D. J. Sames, "Laser based, guided wave experiments for tubing," *Experimental Mechanics*, vol. 37, no. 2, pp. 165–168, 1997.

[16] E. B. Flynn, J. LEE, G. Jarmer, and G. Park, "Frequency-wavenumber processing of laser-excited guided waves for imaging structural features and defects," *6th European Workshop on Structural Health Monitoring*, pp. 1–8, 2012.

[17] P. Huke, M. Schröder, S. Hellmers, M. Kalms, and R. B. Bergmann, "Efficient laser generation of Lamb waves.," *Optics letters*, vol. 39, no. 20, pp. 5795–5797, 2014.

[18] B. A. Auld, *Acoustic fields and waves in solids, Volume I.* John Wiley & Sons, Inc., 1972.

[19] S. W. Tsai, "Mechanics of Composite Materials, Part II - Theoretical aspects," tech. rep., Air Force Materials Laboratory, 1966.

[20] R. M. Jones, *Mechanics of Composite Materials.* CRC Press, 2 ed., 1998.

[21] M. Kersemans, "Nondestructive characterization of the elastic properties of orthotropic composites with ultrasound," in *Sampe Europe Technical Conference (SETEC-11): Advanced composites, the integrated system*, pp. 1–8, 2011.

[22] M. Kersemans, A. Martens, N. Lammens, K. Van Den Abeele, J. Degrieck, F. Zastavnik, L. Pyl, H. Sol, and W. Van Paepegem, "Identification of the Elastic Properties of Isotropic and Orthotropic Thin-Plate Materials with the Pulsed Ultrasonic Polar Scan," *Experimental Mechanics*, vol. 54, no. 6, pp. 1121–1132, 2014.

[23] G. Z. Voyiadjis and P. I. Kattan, *Mechanics of Composite Materials with MATLAB.* Berlin/Heidelberg: Springer-Verlag, 2005.

[24] P. D. Soden, M. J. Hinton, and A. S. Kaddour, "Lamina properties, lay-up configurations and loading conditions for a range of fibre reinforced composite laminates," *Composites Science and Technology*, vol. 58, pp. 1011–1022, 1998.

[25] R. D. Kriz and W. W. Stinchcomb, "Elastic moduli of transversely isotropic graphite fibers and their composites," 1979.

[26] J. D. Achenbach, *Wave Propagation in Elastic Solids.* Amsterdam: North-Holland, 2nd ed., 1976.

[27] A. H. Nayfeh and D. E. Chimenti, "Free Wave Propagation in Plates of General Anisotropic Media," *Journal of Applied Mechanics*, vol. 56, pp. 181–188, 1989.

[28] C. Lane, *The Development of a 2D Ultrasonic Array Inspection for Single Crystal Turbine Blades.* Springer Theses, Cham: Springer International Publishing, 2013.

[29] M. Rudolph, *Ultrasonic beam models in anisotropic media.* PhD thesis, Iowa State University, 1999.

[30] M. Kersemans, N. Lammens, J. Degrieck, K. Van Den Abeele, L. Pyl, F. Zastavnik, H. Sol, and W. Van Paepegem, "Extraction of bulk wave characteristics from a pulsed ultrasonic polar scan," *Wave Motion*, vol. 51, no. 7, pp. 1071–1081, 2014.

[31] J.-F. Chai and T.-T. Wu, "Determinations of anisotropic elastic constants using laser-generated surface waves," *The Journal of the Acoustical Society of America*, vol. 95, no. 6, pp. 3232–3241, 1994.

[32] D. W. Greve, I. J. Oppenheim, and P. Zheng, "Lamb waves and nearly-longitudinal waves in thick plates," *Proceedings of SPIE*, pp. 69321I–69321I–10, 2008.

[33] H. Lamb, "On Waves in an Elastic Plate," *Proceedings of the Royal Society A: Mathematical, Physical and Engineering Sciences*, vol. 93, pp. 114–128, mar 1917.

[34] J. W. Strutt, *Theory of Sound*. London: The Macmillan Company, 1 ed., 1877.

[35] R. Stoneley, "Elastic Waves at the Surface of Separation of Two Solids," *Proceedings of the Royal Society A: Mathematical, Physical and Engineering Sciences*, vol. 106, no. 738, pp. 416–428, 1924.

[36] B. A. Auld, *Acoustic fields and waves in solids, Volume II*. John Wiley & Sons, Inc., 1973.

[37] V. Giurgiutiu, *Structural health monitoring: with piezoelectric wafer active sensors*. Burlington: Academic Press, 2nd ed., 2008.

[38] M. J. S. Lowe, "Matrix Techniques for Modeling Ultrasonic-Waves in Multilayered Media," *IEEE Transactions on Ultrasonics, Ferroelectrics, and Frequency Control*, vol. 42, no. 4, pp. 525–542, 1995.

[39] L. P. Solie and B. A. Auld, "Elastic waves in free anisotropic plates," *The Journal of the Acoustical Society of America*, vol. 54, no. 1, pp. 50–65, 1973.

[40] Y. Li and R. B. Thompson, "Influence of anisotropy on the dispersion characteristics of guided ultrasonic plate modes," *The Journal of the Acoustical Society of America*, vol. 87, no. 5, pp. 1911–1931, 1990.

[41] H. Gravenkamp, *Numerical methods for the simulation of ultrasonic guided waves*. PhD thesis, Technische Universität Braunschweig, 2014.

[42] C.-T. Sun, J. D. Achenbach, and G. Herrmann, "Continuum Theory for a Laminated Medium," *Journal of Applied Mechanics*, vol. 35, no. 3, pp. 467–475, 1968.

[43] W. T. Thomson, "Transmission of Elastic Waves through a Stratified Solid Medium," *Journal of Applied Physics*, vol. 21, no. 2, pp. 89–93, 1950.

[44] N. A. Haskell, "The dispersion of surface waves on multilayered media," *Bulletin of the Seismological Society of America*, vol. 43, no. 1, pp. 17–34, 1953.

[45] E. Thrower, "The computation of the dispersion of elastic waves in layered media," *Journal of Sound and Vibration*, vol. 2, no. 3, pp. 210–226, 1965.

[46] D. Anderson, "Elastic wave propagation in layered anisotropic media," *Journal of Geophysical Research*, vol. 66, no. 9, pp. 2953–2963, 1961.

[47] M. Castaings and B. Hosten, “Delta operator technique to improve the Thomson-Haskell-method stability for propagation in multilayered anisotropic absorbing plates,” *The Journal of the Acoustical Society of America*, vol. 95, no. 4, pp. 1931–1941, 1994.

[48] L. Wang and S. I. Rokhlin, “Stable reformulation of transfer matrix method for wave propagation in layered anisotropic media,” *Ultrasonics*, vol. 39, no. 6, pp. 413–424, 2001.

[49] L. Knopoff, “A Matrix Method for Elastic Wave Problems,” *Bulletin of the Seismological Society of America*, vol. 54, no. 1, pp. 431–438, 1964.

[50] G. J. Tango, M. F. Werby, and H. Schmidt, “Global matrix formulation of wave phenomena in plane layered media,” *Mathematical Modelling*, vol. 8, pp. 450–456, 1987.

[51] A. H. Nayfeh, “The general problem of elastic wave propagation in multilayered anisotropic media,” *The Journal of the Acoustical Society of America*, vol. 89, no. 4, pp. 1521–1531, 1991.

[52] B. Hosten and M. Castaings, “Transfer matrix of multilayered absorbing and anisotropic media. Measurements and simulations of ultrasonic wave propagation through composite materials,” *The Journal of the Acoustical Society of America*, vol. 94, no. 3, pp. 1488–1495, 1993.

[53] S. I. Rokhlin and L. Wang, “Ultrasonic waves in layered anisotropic media: characterization of multidirectional composites,” *International Journal of Solids and Structures*, vol. 39, no. 21-22, pp. 5529–5545, 2002.

[54] B. Pavlakovic, M. Lowe, D. N. Alleyne, and P. Cawley, “Disperse: A General Purpose Program for Creating Dispersion Curves,” in *Review of Progress in Quantitative Nondestructive Evaluation*, vol. 16, pp. 185–192, Boston, MA: Springer US, 1997.

[55] M. J. S. Lowe, *Plate waves for the NDT of diffusion bonded titanium.* PhD thesis, University of London, 1992.

[56] S. Pant, J. Laliberte, M. Martinez, and B. Rocha, “Derivation and experimental validation of Lamb wave equations for an n-layered anisotropic composite laminate,” *Composite Structures*, vol. 111, no. 1, pp. 566–579, 2014.

[57] S. K. Datta, A. H. Shah, R. L. Bratton, and N. Chakraborty, “Wave propagation in laminated composite plates,” *The Journal of the Acoustical Society of America*, vol. 86, no. 6, pp. 2020–2026, 1988.

[58] S. Pant, *Lamb Wave Propagation and Material Characterization of Metallic and Composite Aerospace Structures for Improved Structural Health Monitoring (SHM).* PhD thesis, Carleton University, Ottawa, 2014.

[59] L. Y. Bahar, "A State Space Approach to Elasticity," *Journal of the Franklin Institute*, vol. 229, no. 1, pp. 33–41, 1975.

[60] K. Tanuma, "Stroh Formalism and Rayleigh Waves," *Journal of Elasticity*, vol. 89, no. 1, pp. 5–154, 2007.

[61] W.-L. Yin, "Deconstructing plane anisotropic elasticity Part II: Stroh's formalism sans frills," *International Journal of Solids and Structures*, vol. 37, no. 38, pp. 5277–5296, 2000.

[62] E. L. Adler, "Matrix methods applied to acoustic waves in multilayers," *IEEE Transactions on Ultrasonics, Ferroelectrics and Frequency Control*, vol. 37, no. 6, pp. 485–490, 1990.

[63] W. Karusena, A. H. Shah, and S. K. Datta, "Ultrasonic characterization of multilayered thick composite plates," *Review of Progress in Quantitative Nondestructive Evaluation*, vol. 10B, pp. 1631–1637, 1991.

[64] V. Pagneux and A. Maurel, "Determination of Lamb Mode Eigenvalues," *The Journal of the Acoustical Society of America*, vol. 110, no. 3, pp. 1307–1314, 2001.

[65] J. E. Lefebvre, V. Zhang, J. Gazalet, and T. Gryba, "Legendre polynomial approach for modeling free-ultrasonic waves in multilayered plates," *Journal of Applied Physics*, vol. 85, no. 7, pp. 3419–3427, 1999.

[66] J. Wang, L. Chen, and S. Fang, "State vector approach to analysis of multilayered magneto-electro-elastic plates," *International Journal of Solids and Structures*, vol. 40, no. 7, pp. 1669–1680, 2003.

[67] J. Chen, E. Pan, and H. Chen, "Wave propagation in magneto-electro-elastic multilayered plates," *International Journal of Solids and Structures*, vol. 44, no. 3-4, pp. 1073–1085, 2007.

[68] O. Bou Matar, N. Gasmi, H. Zhou, M. Goueygou, and A. Talbi, "Legendre and Laguerre polynomial approach for modeling of wave propagation in layered magneto-electro-elastic media.," *The Journal of the Acoustical Society of America*, vol. 133, no. 3, pp. 1415–24, 2013.

[69] F. H. Quintanilla, M. J. S. Lowe, and R. V. Craster, "Modeling guided elastic waves in generally anisotropic media using a spectral collocation

method," *The Journal of the Acoustical Society of America*, vol. 137, no. 3, pp. 1180–1194, 2015.

[70] A. H. Fahmy and E. L. Adler, "Propagation of acoustic surface waves in multilayers: A matrix description," *Applied Physics Letters*, vol. 22, no. 10, pp. 495–497, 1973.

[71] P. Grandclément, "Introduction to spectral methods," *EAS Publications Series*, vol. 21, pp. 153–180, 2006.

[72] L. N. Trefethen, *Spectral Methods in Matlab.* SIAM, 2000.

[73] V. Lancellotti and R. Orta, "Modes of open layered anisotropic waveguides: a numerical method with exponential convergence," *Optical and Quantum Electronics*, vol. 31, pp. 781–796, 1999.

[74] V. Lancellotti, "Guided waves in layered cubic media: Convergence study of a polynomial expansion approach," *The Journal of the Acoustical Society of America*, vol. 104, no. 5, pp. 2638–2644, 1998.

[75] P. E. Lagasse, "Higher-order finite-element analysis of topographic guides supporting elastic surface waves," *The Journal of the Acoustical Society of America*, vol. 53, no. 4, pp. 1116–1122, 1973.

[76] I. Bartoli, A. Marzani, F. Lanza di Scalea, and E. Viola, "Modeling wave propagation in damped waveguides of arbitrary cross-section," *Journal of Sound and Vibration*, vol. 295, no. 3-5, pp. 685–707, 2006.

[77] A. Marzani, E. Viola, I. Bartoli, F. Lanza di Scalea, and P. Rizzo, "A semi-analytical finite element formulation for modeling stress wave propagation in axisymmetric damped waveguides," *Journal of Sound and Vibration*, vol. 318, no. 3, pp. 488–505, 2008.

[78] F. Treyssède, K. L. Nguyen, A. S. Bonnet-BenDhia, and C. Hazard, "Finite element computation of trapped and leaky elastic waves in open stratified waveguides," *Wave Motion*, vol. 51, no. 7, pp. 1093–1107, 2014.

[79] P. Bocchini, M. Asce, A. Marzani, and E. Viola, "Graphical User Interface for Guided Acoustic Waves," *Journal of Computing in Civil Engineering*, vol. 25, no. 3, pp. 202–210, 2011.

[80] J. M. Galán and R. Abascal, "Numerical simulation of Lamb wave scattering in semi-infinite plates," *International Journal for Numerical Methods in Engineering*, vol. 53, no. 5, pp. 1145–1173, 2002.

[81] A. Nettles, "Basic mechanics of laminated composite plates," Tech. Rep. October, NASA, Marshall Space Flight Center, Alabama, 1994.

[82] L. R. Adkins and A. J. Hughes, "Elastic Surface Waves Guided by Thin Films: Gold on Fused Quartz," *IEEE Transactions on Microwave Theory and Techniques*, vol. MTT-17, no. 11, pp. 904–911, 1969.

[83] D. N. Alleyne and P. Cawley, "A two-dimensional Fourier transform method for the measurement of propagating multimode signals," *The Journal of the Acoustical Society of America*, vol. 89, no. 3, pp. 1159–1168, 1991.

[84] Z. Su, L. Ye, and Y. Lu, "Guided Lamb waves for identification of damage in composite structures: A review," *Journal of Sound and Vibration*, vol. 295, no. 3-5, pp. 753–780, 2006.

[85] Z. Tian and L. Yu, "Lamb wave frequency-wavenumber analysis and decomposition," *Journal of Intelligent Material Systems and Structures*, pp. 1–17, 2014.

[86] E. B. Flynn, G. S. Jarmer, S. Y. Chong, and J.-R. Lee, "Imaging and characterizing structural defects through the estimation of local dispersion curves," *Key Engineering Materials*, vol. 569-570, pp. 956–961, 2013.

[87] M. D. Rogge and C. A. C. Leckey, "Characterization of impact damage in composite laminates using guided wavefield imaging and local wavenumber domain analysis," *Ultrasonics*, vol. 53, no. 7, pp. 1217–1226, 2013.

[88] Y. Hua and T. K. Sarkar, "Matrix pencil method for estimating parameters of exponentially damped/undamped sinusoids in noise," *IEEE Transactions on Acoustics, Speech, and Signal Processing*, vol. 38, no. 5, pp. 814–824, 1990.

[89] K. Grosh and E. G. Williams, "Complex wave-number decomposition of structural vibrations," *The Journal of the Acoustical Society of America*, vol. 93, no. 2, pp. 836–848, 1993.

[90] M. Ekstrom, "Dispersion estimation from borehole acoustic arrays using a modified matrix pencil algorithm," in *Twenty-Ninth Asilomar Conference on Signals, Systems and Computers*, vol. 1, 1995.

[91] F. Schöpfer, F. Binder, A. Wöstehoff, T. Schuster, S. Ende, S. Föll, and R. Lammering, "Accurate determination of dispersion curves of guided waves in plates by applying the matrix pencil method to laser vibrometer measurement data," *CEAS Aeronautical Journal*, vol. 4, no. 1, pp. 61–68, 2013.

[92] M. Mazzotti, I. Bartoli, G. Castellazzi, and A. Marzani, "Computation of leaky guided waves dispersion spectrum using vibroacoustic analyses and

the Matrix Pencil Method: A validation study for immersed rectangular waveguides," *Ultrasonics*, vol. 54, no. 7, pp. 1895–1898, 2014.

[93] J. del Rio and T. K. Sarkar, "Comparison between the Matrix Pencil Method and the Fourier Transform Technique for High-Resolution Spectral Estimation," *Digital Signal Processing*, vol. 6, no. 6, pp. 108–125, 2004.

[94] T.-T. Wu and Y.-H. Liu, "On the measurement of anisotropic elastic constants of fiber-reinforced composite plate using ultrasonic bulk wave and laser generated Lamb wave," *Ultrasonics*, vol. 37, no. 6, pp. 405–412, 1999.

[95] C. Eisenhardt, L. J. Jacobs, and J. Qu, "Application of laser ultrasonics to develop dispersion curves for elastic plates," *Journal of Applied Mechanics*, vol. 36, no. 3, pp. 1043–1045, 1999.

[96] L. D. Landau and E. M. Lifshitz, *Course of Theoretical Physics Vol 7: Theory and Elasticity.* Pergamon Press, 1959.

[97] K. Brugger, "Thermodynamic definition of higher order elastic coefficients," *Physical Review*, vol. 133, no. 6A, pp. A1611–A1612, 1964.

[98] P. J. Westervelt, "Parametric Acoustic Array," *The Journal of the Acoustical Society of America*, vol. 35, no. 4, pp. 535–537, 1963.

[99] F. D. D. Murnaghan, *Finite deformation of an elastic solid.* Dover New York, 1951.

[100] B. Fornberg and G. B. Whitham, "A numerical and theoretical study of certain nonlinear wave phenomena," *Phil. Trans. R. Soc. A*, vol. 32, pp. 373–404, 1978.

[101] P. A. Johnson, T. J. Shankland, R. J. O'Connell, and J. N. Albright, "Nonlinear generation of elastic waves in crystalline rock," *Journal of Geophysical Research*, vol. 92, no. B5, pp. 3597–3602, 1987.

[102] P. A. Johnson and T. J. Shankland, "Nonlinear generation of elastic waves in granite and sandstone: Continuous wave and travel time observations," *Journal of Geophysical Research*, vol. 94, no. B12, pp. 17729–17733, 1989.

[103] P. A. Johnson, A. Migliori, and T. J. Shankland, "Continuous wave phase detection for probing nonlinear elastic wave interactions in rocks," *The Journal of the Acoustical Society of America*, vol. 89, no. 2, pp. 598–603, 1991.

[104] K. Van Den Abeele, P. A. Johnson, and A. Sutin, “Nonlinear elastic wave spectroscopy (NEWS) techniques to discern material damage, part I: nonlinear wave modulation spectroscopy (NWMS),” *Research in Nondestructive Evaluation*, vol. 12, no. 1, pp. 17–30, 2000.

[105] D. Stobbe, *Acoustoelasticity in 7075-T651 Aluminum and Dependence of Third Order Elastic Constants on Fatigue Damage.* PhD thesis, Georgia Institute of Technology, 2005.

[106] M. Meo and G. Zumpano, “Nonlinear elastic wave spectroscopy identification of impact damage on a sandwich plate,” *Composite Structures*, vol. 71, no. 3-4, pp. 469–474, 2005.

[107] M. Ryles, F. H. Ngau, I. Mcdonald, and W. J. Staszewski, “Comparative study of nonlinear acoustic and Lamb wave techniques for fatigue crack detection in metallic structures,” *Fatigue & Fracture of Engineering Materials & Structures*, vol. 31, no. 8, pp. 674–683, 2008.

[108] C. Pruell, J.-Y. Kim, J. Qu, and L. J. Jacobs, “Evaluation of fatigue damage using nonlinear guided waves,” *Smart Materials and Structures*, vol. 18, no. 3, pp. 1–7, 2009.

[109] G. Shkerdin and C. Glorieux, “Nonlinear clapping modulation of Lamb modes by normally closed delamination,” *IEEE Transactions on Ultrasonics, Ferroelectrics and Frequency Control*, vol. 57, no. 6, pp. 1426–1433, 2010.

[110] L. Haumesser, J. Fortineau, D. Parenthoine, T. Goursolle, and F. Vander Meulen, “Ultrasonic nonlinear parameter measurement: critical investigation of the instrumentation,” *Ultrasonic Wave Propagation in Non Homogeneous Media*, vol. 128, pp. 387–397, 2009.

[111] D. S. Hughes and J. L. Kelly, “Second-order elastic deformation of solids,” *Physical Review*, vol. 92, no. 5, pp. 1145–1149, 1953.

[112] R. De Pascalis, “The Semi-Inverse Method in solid mechanics: Theoretical underpinnings and novel applications,” *The Semi-Inverse Method in solid mechanics: Theoretical underpinnings and novel applications*, 2010.

[113] W. Delima and M. Hamilton, “Finite-amplitude waves in isotropic elastic plates,” *Journal of Sound and Vibration*, vol. 265, no. 4, pp. 819–839, 2003.

[114] Y. Hamiel, V. Lyakhovsky, and Y. Ben-Zion, “The Elastic Strain Energy of Damaged Solids with Applications to Non-Linear Deformation of Crystalline Rocks,” *Pure and Applied Geophysics*, vol. 168, no. 12, pp. 2199–2210, 2011.

[115] R. Hearmon, “Third-order elastic coefficients,” *Acta Crystallographica*, vol. 6, no. 4, pp. 331–340, 1953.

[116] S. Catheline, J.-L. Gennisson, and M. Fink, “Measurement of elastic nonlinearity of soft solid with transient elastography,” *The Journal of the Acoustical Society of America*, vol. 114, no. 6, pp. 3087–3091, 2003.

[117] L. A. Ostrovsky and P. A. Johnson, “Dynamic nonlinear elasticity in geomaterials,” *Rivista del Nuovo Cimento*, vol. 24, no. 7, pp. 1–46, 2001.

[118] K. A. Naugol’nykh and L. Ostrovsky, *Nonlinear Wave Processes in Acoustics.* Cambridge: Cambridge University Press, 1998.

[119] T. Meurer and J. Qu, “Wave propagation in nonlinear and hysteretic media — a numerical study,” *International journal of solids and structures*, vol. 39, no. 21-22, pp. 5585–5614, 2002.

[120] K. Van Den Abeele, A. Sutin, and J. Carmeliet, “Micro-damage diagnostics using nonlinear elastic wave spectroscopy (NEWS),” *NDT & E International*, vol. 34, no. 4, pp. 239–248, 2001.

[121] B. Van Damme, *Optimisation of nonlinear elastic wave spectroscopy for diagnostic nondestructive testing and imaging.* PhD thesis, KU Leuven, 2011.

[122] J.-Y. Kim, A. Baltazar, J. Hu, and S. I. Rokhlin, “Hysteretic linear and nonlinear acoustic responses from pressed interfaces,” *International Journal of Solids and Structures*, vol. 43, no. 21, pp. 6436–6452, 2006.

[123] P. Delsanto and M. Scalerandi, “Modeling nonclassical nonlinearity, conditioning, and slow dynamics effects in mesoscopic elastic materials,” *Physical Review B*, vol. 68, no. 6, pp. 1–9, 2003.

[124] I. Solodov, N. Krohn, and G. Busse, “CAN: an example of nonclassical acoustic nonlinearity in solids,” *Ultrasonics*, vol. 40, no. 1-8, pp. 621–625, 2002.

[125] J. Chen, D. Zhang, and Y. Mao, “Contact acoustic nonlinearity in a bonded solid-solid interface.,” *Ultrasonics*, vol. 44 Suppl 1, pp. e1355–8, 2006.

[126] D. Yan, B. W. Drinkwater, and S. A. Neild, “Measurement of the ultrasonic nonlinearity of kissing bonds in adhesive joints,” *NDT & E International*, vol. 42, no. 5, pp. 459–466, 2009.

[127] R. A. Guyer and P. A. Johnson, *Nonlinear Mesoscopic Elasticity: The Complex Behaviour of Rocks, Soil, Concrete.* John Wiley & Sons, Inc., 2009.

[128] V. Aleshin, W. Desadeleer, M. Wevers, and K. Van Den Abeele, “Characterization of hysteretic stress–strain behavior using the integrated Preisach density,” *International Journal of Non-Linear Mechanics*, vol. 43, no. 3, pp. 151–163, 2008.

[129] N. N. Davidenkov, “Energy dissipation in vibrations,” *Journal of Technical Physics*, vol. 8, no. 6, p. 483, 1938.

[130] V. E. Nazarov, A. V. Radostin, L. A. Ostrovsky, and I. Soustova, “Wave processes in media with hysteretic nonlinearity. Part I,” *Acoustical Physics*, vol. 49, no. 3, pp. 344–353, 2003.

[131] N. G. W. Cook and K. Hodgson, “Some detailed stress-strain curves for rock,” *Journal of Geophysical Research*, vol. 70, no. 12, pp. 2883–2888, 1965.

[132] V. E. Nazarov, A. B. Kolpakov, and A. V. Radostin, “Experimental Study of Nonlinear Acoustical Effects in Limestone,” *Acoustical Physics*, vol. 53, no. 2, pp. 217–225, 2007.

[133] E. Barbieri, M. Meo, and U. Polimeno, “Nonlinear wave propagation in damaged hysteretic materials using a frequency domain-based PM space formulation,” *International Journal of Solids and Structures*, vol. 46, no. 1, pp. 165–180, 2009.

[134] K. R. McCall and R. A. Guyer, “Equation of state and wave propagation in hysteretic nonlinear elastic materials,” *Journal of Geophysical Research*, vol. 99, no. B12, pp. 23887–23897, 1994.

[135] K. Helbig and P. N. J. Rasolofosaon, “A theoretical paradigm for describing hysteresis and nonlinear elasticity in arbitrary anisotropic rocks,” *Anisotropy*, pp. 383–398, 2000.

[136] K. Van Den Abeele, “Multiscale approach and simulations of wave propagation and resonance in media with localized microdamage: 1D and 2D cases,” in *The Universality of Nonclassical Nonlinearity: Applications to Non-Destructive Evaluations and Ultrasonics* (P. P. Delsanto, ed.), pp. 1–25, New York: Springer Science+ Business Media, Incorporated, 2007.

[137] L. Straka, Y. Yagodzinskyy, M. Landa, and H. Hanninen, “Detection of structural damage of aluminum alloy 6082 using elastic wave modulation spectroscopy,” *NDT & E International*, vol. 41, no. 7, pp. 554–563, 2008.

[138] P. Liu, H. Sohn, T. Kundu, and S. Yang, “Noncontact detection of fatigue cracks by laser nonlinear wave modulation spectroscopy (LNWMS),” *NDT & E International*, vol. 66, pp. 106–116, sep 2014.

[139] K. Van Den Abeele, P.-Y. Le Bas, S. Vanaverbeke, T. Katkowski, and W. Desadeleer, “Nonlinear Elastic Wave Spectroscopy (NEWS): a diagnostic tool to detect microdamage with high potential for nondestructive testing,” in *Proceedings of the 8th Congres Francais d’Acoustique*, (Tours), pp. 167–174, 2006.

[140] M. Scalerandi, A. S. Gliozzi, C. L. E. Bruno, and K. Van Den Abeele, “Nonlinear acoustic time reversal imaging using the scaling subtraction method,” *Journal of Physics D: Applied Physics*, vol. 41, p. 215404, nov 2008.

[141] M. Scalerandi, A. S. Gliozzi, C. L. E. Bruno, D. Masera, and P. G. Bocca, “A scaling method to enhance detection of a nonlinear elastic response,” *Applied Physics Letters*, vol. 92, no. 10, p. 101912, 2008.

[142] C. L. E. Bruno, A. S. Gliozzi, M. Scalerandi, and P. Antonaci, “Analysis of elastic nonlinearity using the scaling subtraction method,” *Physical Review B*, vol. 79, no. 6, p. 064108, 2009.

[143] P. Antonaci, C. L. E. Bruno, A. S. Gliozzi, M. Scalerandi, and P. G. Bocca, “Monitoring evolution of compressive damage in concrete with linear and nonlinear ultrasonic methods,” *Cement and Concrete Research*, vol. 40, no. 7, pp. 1106–1113, 2010.

[144] C. L. E. Bruno, M. Scalerandi, A. S. Gliozzi, and P. Antonaci, “Break of reciprocity principle induced by cracks in concrete: experimental evidence and applications to nonlinear tomography,” in *Proceedings of XV International Conference on Nonlinear Elasticity in Materials*, (Otranto), 2010.

[145] D. C. Worlton, “Ultrasonic testing with Lamb waves,” *Non-Destructive Testing*, vol. 15, pp. 218–222, 1957.

[146] D. C. Worlton, “Experimental confirmation of Lamb waves at megacycle frequencies,” *Journal of Applied Physics*, vol. 32, no. 6, pp. 967–971, 1961.

[147] T. N. Grigsby and E. J. Tajchman, “Properties of Lamb Waves Relevant to the Ultrasonic Inspection of Thin Plates,” *IRE Transactions on Ultrasonic Engineering*, vol. 8, no. 1, pp. 26–33, 1960.

[148] I. A. Viktorov, *Rayleigh and Lamb Waves: Physical Theory and Applications.* Springer US, 1 ed., 1967.

[149] D. N. Alleyne, *The nondestructive testing of plates using ultrasonic Lamb waves.* PhD thesis, Imperial College of Science, Technology and Medicine, 1991.

[150] D. Ball and D. Shewring, “Some problems in the use of Lamb waves for the inspection of cold-rolled steel sheet and coil,” *Non-Destructive Testing*, vol. 6, no. 3, pp. 138–145, 1973.

[151] T. L. Mansfield, “Lamb Wave Inspection of Aluminium Sheet,” *Materials Evaluation*, vol. 33, no. 4, pp. 96–100, 1975.

[152] D. N. Alleyne, P. Cawley, A. M. Lank, and P. J. Mudge, “The Lamb wave inspection of chemical plant pipework,” *Review of Progress in Quantitative Nondestructive Evaluation*, vol. 16, pp. 1269–1276, 1997.

[153] M. J. S. Lowe, D. N. Alleyne, and P. Cawley, “Defect detection in pipes using guided waves,” *Ultrasonics*, vol. 36, no. 1-5, pp. 147–154, 1998.

[154] M. K. Yucel, M. Legg, M. Livadas, V. Kappatos, and T.-h. Gan, “Identification and Utilisation of Ultrasonic Guided Waves for Inspection of ACSR Cables,” in *Proceedings of ECNDT 2014*, (Prague), 2014.

[155] P. W. Tse and J. M. Chen, “Effective Guided Wave Technique for Performing Non-destructive Inspection on Steel Wire Ropes that Hoist Elevators,” in *Engineering Asset Management - Systems, Professional Practices and Certification* (P. W. Tse, J. Mathew, K. Wong, R. Lam, and C. N. Ko, eds.), pp. 309–320, Springer International Publishing, 2014.

[156] R. Raišutis, R. Kažys, L. Mažeika, E. Žukauskas, V. Samaitis, and A. Jankauskas, “Ultrasonic guided wave-based testing technique for inspection of multi-wire rope structures,” *NDT & E International*, vol. 62, pp. 40–49, 2014.

[157] R. P. Dalton, P. Cawley, and M. J. S. Lowe, “The potential of guided waves for monitoring large areas of metallic aircraft fuselage structure,” *Journal of Nondestructive Evaluation*, vol. 20, no. 1, pp. 29–46, 2001.

[158] X. Zhao, H. Gao, G. Zhang, B. Ayhan, F. Yan, C. Kwan, and J. L. Rose, “Active health monitoring of an aircraft wing with embedded piezoelectric sensor/actuator network: I. Defect detection, localization and growth monitoring,” *Smart Materials and Structures*, vol. 16, no. 4, pp. 1208–1217, 2007.

[159] L. Qiu and S. Yuan, “On development of a multi-channel PZT array scanning system and its evaluating application on UAV wing box,” *Sensors and Actuators A: Physical*, vol. 151, no. 2, pp. 220–230, 2009.

[160] D. P. Jansen and D. A. Hutchins, “Lamb wave tomography,” in *Ultrasonics Symposium*, pp. 1017–1020, 1990.

[161] W. Wright and D. A. Hutchins, “Air-coupled Lamb wave tomography,” *IEEE Transactions on Ultrasonics, Ferroelectrics and Frequency Control*, vol. 44, no. 1, pp. 53–59, 1997.

[162] M. K. Hinders, E. V. Malyarenko, and J. C. P. McKeon, “Contact scanning Lamb wave tomography,” *The Journal of the Acoustical Society of America*, vol. 104, no. 3, p. 1790, 1998.

[163] J. C. P. McKeon and M. K. Hinders, “Parallel projection and crosshole Lamb wave contact scanning tomography,” *The Journal of the Acoustical Society of America*, vol. 106, no. 5, pp. 2568–2577, 1999.

[164] E. V. Malyarenko and M. K. Hinders, “Fan beam and double crosshole Lamb wave tomography for mapping flaws in aging aircraft structures.,” *The Journal of the Acoustical Society of America*, vol. 108, no. 4, pp. 1631–9, 2000.

[165] E. V. Malyarenko and M. K. Hinders, “Ultrasonic Lamb wave diffraction tomography,” *Ultrasonics*, vol. 39, no. 4, pp. 269–281, 2001.

[166] K. R. Leonard, E. V. Malyarenko, and M. K. Hinders, “Ultrasonic Lamb wave tomography,” *Inverse Problems*, vol. 18, no. 6, pp. 1795–1808, 2002.

[167] J. Hou, K. R. Leonard, and M. K. Hinders, “Automatic multi-mode Lamb wave arrival time extraction for improved tomographic reconstruction,” *Inverse Problems*, vol. 20, no. 6, pp. 1873–1888, 2004.

[168] X. Zhao, R. L. Royer, S. E. Owens, and J. L. Rose, “Ultrasonic Lamb wave tomography in structural health monitoring,” *Smart Materials and Structures*, vol. 20, no. 10, pp. 105002–105012, 2011.

[169] X. Liu, C. Zhou, and Z. Jiang, “Damage localization in plate-like structure using built-in PZT sensor network,” *Smart Structures and Systems*, vol. 9, no. 1, pp. 21–33, 2012.

[170] V. Giurgiutiu, “Lamb wave generation with piezoelectric wafer active sensors for structural health monitoring,” in *SPIE’s 10th Annual International Symposium on Smart Structures and Materials*, (San Diego), pp. 1–11, 2003.

[171] T. E. Michaels and J. E. Michaels, “Integrating monitoring and inspection with attached ultrasonic transducers,” in *Health Monitoring and Smart Nondestructive Evaluation of Structural and Biological Systems V. Proceedings of the SPIE* (T. Kundu, ed.), vol. 6177, pp. 136–147, 2006.

[172] J. E. Michaels and T. E. Michaels, “Guided wave signal processing and image fusion for in situ damage localization in plates,” *Wave Motion*, vol. 44, no. 6, pp. 482–492, 2007.

[173] J. E. Michaels, “Imaging algorithms for locating damage via in situ ultrasonic sensors,” *SAS 2008 - IEEE Sensors Applications Symposium*, vol. 2, 2008.

[174] J. E. Michaels, “Detection, localization and characterization of damage in plates with an in situ array of spatially distributed ultrasonic sensors,” *Smart Materials and Structures*, vol. 17, no. 3, p. 035035, 2008.

[175] H. Gao, Y. Shi, and J. L. Rose, “Guided wave tomography on an aircraft wing with leave in place sensors,” *Review of Quantitative Nondestructive Evaluation*, vol. 24, pp. 1788–1795, 2005.

[176] T. R. Hay, R. L. Royer, H. Gao, X. Zhao, and J. L. Rose, “A comparison of embedded sensor Lamb wave ultrasonic tomography approaches for material loss detection,” *Smart Materials and Structures*, vol. 15, no. 4, pp. 946–951, 2006.

[177] A. A. Baker, S. Dutton, and D. W. Kelly, *Composite materials for aircraft structures*. Reston: American Institute of Aeronautics and Astronautics, Inc., 2nd ed., 2004.

[178] F. A. Administration, *Aviation Maintenance Technician Handbook - Airframe*, vol. 1. U.S. Department of Transportation, Federal Aviation Administration, 2012.

[179] A. Corigliano, “Damage and Fracture Mechanics Techniques for Composite Structures,” in *Comprehensive Structural Integrity*, pp. 459–539, Elsevier, 2003.

[180] C. Ibarra-Castanedo, M. Genest, S. Guibert, J.-M. Piau, X. P. V. Maldague, and A. Bendada, “Inspection of aerospace materials by pulsed thermography, lock-in thermography, and vibrothermography: a comparative study,” in *Defense and Security Symposium*, vol. 6541, pp. 654116–654116, 2007.

[181] R. Smith, “Composite Defects and Their Detection,” *Materials Science and Engineering*, vol. III, p. 14, 1997.

[182] W. Cantwell and J. Morton, “Comparison of the low and high velocity impact response of cfrp,” 1989.

[183] J. Hou, N. Petrinic, C. Ruiz, and S. R. Hallett, “Prediction of impact damage in composite plates,” *Composites Science and Technology*, vol. 60, no. 2, pp. 273–281, 2000.

[184] J. Stein, P. J. Withers, and A. Wilkinson, “An Innovative Use of X-Ray Computed Tomography in Composite Impact Damage Characterisation,” in *ECCM-16th European conference on composite materials*, (Seville), pp. 22–26, 2014.

[185] U. Polimeno, M. Meo, D. P. Almond, and S. L. Angioni, “Detecting low velocity impact damage in composite plate using nonlinear acoustic/ultrasound methods,” *Applied Composite Materials*, vol. 17, no. 5, pp. 481–488, 2010.

[186] D. J. Bull, L. Helfen, I. Sinclair, S. M. Spearing, and T. Baumbach, “A comparison of multi-scale 3D X-ray tomographic inspection techniques for assessing carbon fibre composite impact damage,” *Composites Science and Technology*, vol. 75, pp. 55–61, 2013.

[187] K. T. Tan, N. Watanabe, and Y. Iwahori, “X-ray radiography and micro-computed tomography examination of damage characteristics in stitched composites subjected to impact loading,” *Composites Part B: Engineering*, vol. 42, no. 4, pp. 874–884, 2011.

[188] F. Aymerich and S. Meili, “Ultrasonic evaluation of matrix damage in impacted composite laminates,” *Composites Part B: Engineering*, vol. 31, no. 1, pp. 1–6, 2000.

[189] P. D. Wilcox, M. J. S. Lowe, and P. Cawley, “Mode and Transducer Selection for Long Range Lamb Wave Inspection,” *Journal of Intelligent Materials Systems and Structures*, vol. 12, no. 8, pp. 553–565, 2001.

[190] D. W. Greve, J. J. Neumann, J. H. Nieuwenhuis, I. J. Oppenheim, and N. L. Tyson, “Use of Lamb Waves to Monitor Plates: Experiments and Simulations,” *Proceedings of SPIE*, vol. 5765, pp. 281–292, 2005.

[191] Z. Khodaei, L. Qu, and M. H. Aliabadi, “Influence of adhesive layer on actuation of Lamb wave signals,” *Key Engineering Materials*, vol. 525-526, pp. 617–620, 2013.

[192] H. M. Matt, *Structural diagnostics of CFRP composite aircraft components by ultrasonic guided waves and built-in piezoelectric transducers.* PhD thesis, University of California, San Diego, 2007.

[193] J. H. Nieuwenhuis, J. J. Neumann, D. W. Greve, and I. J. Oppenheim, “Generation and detection of guided waves using PZT wafer transducers I .

Introduction II . Emission of ultrasonic waves," *Computer*, vol. 52, no. 11, pp. 2103–2111, 2005.

[194] L. Wang and F. Yuan, "Group velocity and characteristic wave curves of Lamb waves in composites: Modeling and experiments," *Composites Science and Technology*, vol. 67, no. 7-8, pp. 1370–1384, 2007.

[195] L. Zeng, J. Lin, J. D. Hua, and W. Shi, "Interference resisting design for guided wave tomography," *Smart Materials and Structures*, vol. 22, no. 5, p. 055017, 2013.

[196] D. N. Alleyne and P. Cawley, "Optimization of lamb wave inspection techniques," *NDT & E International*, vol. 25, no. 1, pp. 11–22, 1992.

[197] X. Jia, "Modal analysis of Lamb wave generation in elastic plates by liquid wedge transducers," *The Journal of the Acoustical Society of America*, vol. 101, no. 2, pp. 834–842, 1997.

[198] J. Rose, S. Pelts, and M. Quarry, "A comb transducer model for guided wave NDE," *Ultrasonics*, vol. 36, no. 1-5, pp. 163–169, 1998.

[199] S. Dixon, C. Edwards, and S. Palmer, "The optimization of lamb and Rayleigh wave generation using wideband-low-frequency EMATs," *Review of Quantitative Nondestructive Evaluation*, vol. 22, pp. 297–304, 2003.

[200] D. A. Hutchins, W. M. D. Wright, G. Hayward, and A. Gachagan, "Air-coupled piezoelectric detection of laser-generated ultrasound," 1994.

[201] P. Hess, A. M. Lomonosov, and A. P. Mayer, "Laser-based linear and nonlinear guided elastic waves at surfaces (2D) and wedges (1D)," *Ultrasonics*, vol. 54, no. 1, pp. 39–55, 2014.

[202] H. Sohn, D. Dutta, J. Y. Yang, H. J. Park, M. DeSimio, S. Olson, and E. Swenson, "Delamination detection in composites through guided wave field image processing," *Composites Science and Technology*, vol. 71, no. 9, pp. 1250–1256, 2011.

[203] K. Luangvilai, *Attenuation of Ultrasonic Lamb Waves with Applications to Material Characterization and Condition Monitoring.* PhD thesis, Georgia Institute of Technology, 2007.

[204] P. D. Wilcox, "A rapid signal processing technique to remove the effect of dispersion from guided wave signals," *IEEE Transactions on Ultrasonics, Ferroelectrics, and Frequency Control*, vol. 50, no. 4, pp. 419–427, 2003.

[205] K. Xu, D. Ta, P. Moilanen, and W. Wang, "Mode separation of Lamb waves based on dispersion compensation method," *The Journal of the Acoustical Society of America*, vol. 131, no. 4, pp. 2714–2722, 2012.

[206] J. S. Hall, *Adaptive dispersion compensation and ultrasonic imaging for structural health monitoring.* PhD thesis, Georgia Institute of Technology, 2011.

[207] R. Sicard, J. Goyette, and D. Zellouf, “A numerical dispersion compensation technique for time recompression of Lamb wave signals,” *Ultrasonics*, vol. 40, no. 1-8, pp. 727–732, 2002.

[208] L. De Marchi, A. Marzani, N. Speciale, and E. Viola, “A passive monitoring technique based on dispersion compensation to locate impacts in plate-like structures,” *Smart Materials and Structures*, vol. 20, no. 3, p. 035021, 2011.

[209] J. Pohl and G. Mook, “Laser-vibrometric analysis of propagation and interaction of lamb waves in CFRP-plates,” *CEAS Aeronautical Journal*, vol. 4, no. 1, pp. 77–85, 2013.

[210] K. Ono and A. Gallego, “Attenuation of Lamb Waves in CFRP Plates,” *Journal of Acoustic Emission*, vol. 30, pp. 109–124, 2012.

[211] D. N. Alleyne and P. Cawley, “The interaction of Lamb waves with defects.,” *IEEE Transactions on Ultrasonics, Ferroelectrics and Frequency Control*, vol. 39, no. 3, pp. 381–397, 1992.

[212] Y. Cho, “Estimation of ultrasonic guided wave mode conversion in a plate with thickness variation,” *IEEE Transactions on Ultrasonics, Ferroelectrics and Frequency Control*, vol. 47, no. 3, pp. 591–603, 2000.

[213] F. Benmeddour, S. Grondel, J. Assaad, and E. Moulin, “Study of the fundamental Lamb modes interaction with asymmetrical discontinuities,” *NDT & E International*, vol. 41, no. 5, pp. 330–340, 2008.

[214] R. Benz, M. Niethammer, S. Hurlebaus, and L. J. Jacobs, “Localization of notches with Lamb waves,” *The Journal of the Acoustical Society of America*, vol. 114, no. 2, pp. 677–685, 2003.

[215] K. Xu, D. Ta, Z. Su, and W. Wang, “Transmission analysis of ultrasonic Lamb mode conversion in a plate with partial-thickness notch.,” *Ultrasonics*, vol. 54, no. 1, pp. 395–401, 2014.

[216] C. A. C. Leckey, M. D. Rogge, C. A. Miller, and M. K. Hinders, “Multiple-mode Lamb wave scattering simulations using 3D elastodynamic finite integration technique.,” *Ultrasonics*, vol. 52, no. 2, pp. 193–207, 2012.

[217] N. Guo and P. Cawley, “The interaction of Lamb waves with delaminations in composite laminates,” *The Journal of the Acoustical Society of America*, vol. 94, no. 4, pp. 2240–2246, 1993.

[218] T. Hayashi and K. Kawashima, “Multiple reflections of Lamb waves at a delamination,” *Ultrasonics*, vol. 40, no. 1-8, pp. 193–197, 2002.

[219] C. Ramadas, K. Balasubramaniam, M. Joshi, and C. V. Krishnamurthy, “Interaction of the Primary Anti-symmetric Lamb Mode (A0) With Symmetric Delaminations: Numerical and Experimental Studies,” *Smart Materials and Structures*, vol. 18, no. 8, pp. 085011–085017, 2009.

[220] C. Ramadas, K. Balasubramaniam, M. Joshi, and C. V. Krishnamurthy, “Interaction of guided Lamb waves with an asymmetrically located delamination in a laminated composite plate,” *Smart Materials and Structures*, vol. 19, no. 6, pp. 065009–065011, 2010.

[221] Y. Okabe and K. Fujibayashi, “Delamination detection in composite laminates using dispersion change based on mode conversion of Lamb waves,” *Smart Materials and Structures*, vol. 19, pp. 1–12, 2010.

[222] C. T. Ng and M. Veidt, “Scattering analysis of fundamental anti-symmetric lamb wave at delaminations in composite laminates,” *Australian Journal of Mechanical Engineering*, vol. 8, no. 2, pp. 197–206, 2011.

[223] C. T. Ng, M. Veidt, L. R. F. Rose, and C. H. Wang, “Analytical and finite element prediction of Lamb wave scattering at delaminations in quasi-isotropic composite laminates,” *Journal of Sound and Vibration*, vol. 331, no. 22, pp. 4870–4883, 2012.

[224] F. Ricci, E. Monaco, L. Maio, N. D. Boffa, and A. K. Mal, “Guided waves in a stiffened composite laminate with a delamination,” *Structural Health Monitoring*, vol. 15, no. 3, pp. 351–358, 2016.

[225] C. A. C. Leckey, M. D. Rogge, and F. Raymond Parker, “Guided waves in anisotropic and quasi-isotropic aerospace composites: Three-dimensional simulation and experiment,” *Ultrasonics*, vol. 54, no. 1, pp. 385–394, 2014.

[226] V. N. Smelyanskiy, V. Hafiychuk, D. G. Luchinsky, R. Tyson, J. Miller, and C. Banks, “Modeling wave propagation in Sandwich Composite Plates for Structural Health Monitoring,” in *Annual Conference of the Prognostics and Health Management Society*, pp. 1–10, 2011.

[227] S. M. H. Hosseini and U. Gabbert, “Numerical simulation of the Lamb wave propagation in honeycomb sandwich panels: A parametric study,” *Composite Structures*, vol. 97, pp. 189–201, 2013.

[228] H. Baid, C. Schaal, H. Samajder, and A. Mal, “Dispersion of Lamb waves in a honeycomb composite sandwich panel,” *Ultrasonics*, vol. 56, pp. 409–416, 2015.

[229] F. Song, G. L. Huang, and G. K. Hu, "Online Guided Wave-Based Debonding Detection in Honeycomb Sandwich Structures," *AIAA Journal*, vol. 50, no. 2, pp. 284–293, 2012.

[230] S. Mustapha, L. Ye, D. Wang, and Y. Lu, "Debonding Detection in Composite Sandwich Structures Based on Guided Waves," *AIAA Journal*, vol. 50, no. 8, pp. 1697–1706, 2012.

[231] N. Chakraborty, V. Rathod, D. Roy Mahapatra, and S. Gopalakrishnan, "Guided Wave based Detection of Damage in Honeycomb Core Sandwich Structures," *NDT & E International*, vol. 49, pp. 27–33, 2012.

[232] S. Sikdar, S. Banerjee, and G. Ashish, "Ultrasonic guided wave propagation and disbond identification in a honeycomb composite sandwich structure using bonded piezoelectric wafer transducers," *Journal of Intelligent Material Systems and Structures*, pp. 1–13, 2015.

[233] E. B. Flynn, S. Y. Chong, G. J. Jarmer, and J.-R. Lee, "Structural imaging through local wavenumber estimation of guided waves," *NDT & E International*, vol. 59, pp. 1–10, 2013.

[234] P. D. Juarez and C. A. C. Leckey, "Multi-frequency local wavenumber analysis and ply correlation of delamination damage," *Ultrasonics*, vol. 62, pp. 56–65, 2015.

[235] L. Yu, Z. Tian, and C. A. C. Leckey, "Crack Imaging and Quantification in Aluminum Plates with Guided Wave Wavenumber Analysis Methods," *Ultrasonics*, 2015.

[236] O. Mesnil, H. Yan, M. Ruzzene, and K. Paynabar, "Fast wavenumber measurement for accurate and automatic location and quantification of defect in composite," *Structural Health Monitoring*, vol. 15, no. 2, pp. 223–234, 2016.

[237] F. Albiruni, Y. Cho, J.-H. Lee, and B.-Y. Ahn, "Non-Contact Guided Waves Tomographic Imaging of Plate-Like Structures Using a Probabilistic Algorithm," *Materials Transactions*, vol. 53, no. 2, pp. 330–336, 2012.

[238] J. D. Hua, L. Zeng, J. Lin, and W. Shi, "Ultrasonic Guided Wave Tomography for Damage Detection in Harsh Environment," *Key Engineering Materials*, vol. 569-570, pp. 1005–1012, 2013.

[239] B. Sheen and Y. Cho, "A study on quantitative lamb wave tomogram via modified RAPID algorithm with shape factor optimization," *International Journal of Precision Engineering and Manufacturing*, vol. 13, no. 5, pp. 671–677, 2012.

[240] T. Cicero, *Signal processing for guided wave structural health monitoring.* PhD thesis, Imperial College London, 2009.

[241] A. J. Croxford, J. Moll, P. D. Wilcox, and J. E. Michaels, “Efficient temperature compensation strategies for guided wave structural health monitoring,” *Ultrasonics*, vol. 50, no. 4-5, pp. 517–528, 2010.

[242] T. Clarke, F. Simonetti, and P. Cawley, “Guided wave health monitoring of complex structures by sparse array systems: Influence of temperature changes on performance,” *Journal of Sound and Vibration*, vol. 329, no. 12, pp. 2306–2322, 2010.

[243] S. Delrue and K. Van Den Abeele, “Three-dimensional finite element simulation of closed delaminations in composite materials.,” *Ultrasonics*, vol. 52, no. 2, pp. 315–324, 2012.

[244] S. Delrue, *Simulations as a guidance to support and optimize experimental techniques for ultrasonic non-destructive testing.* PhD thesis, KU Leuven, 2011.

[245] Z. Tian, L. Yu, and C. A. C. Leckey, “Delamination detection and quantification on laminated composite structures with Lamb waves and wavenumber analysis,” *Journal of Intelligent Material Systems and Structures*, 2014.

[246] I. Solodov, J. Bai, S. Bekgulyan, and G. Busse, “A local defect resonance to enhance acoustic wave-defect interaction in ultrasonic nondestructive evaluation,” *Applied Physics Letters*, vol. 99, no. 21, pp. 1–4, 2011.

[247] I. Solodov, “Local Defect Resonance as a Mechanism of Highly-Efficient and Frequency-Selective Ultrasonic Thermography,” in *NDCM-XIII 2013*, (Le Mans), 2013.

[248] W. Thomson, *Theory of Vibration with Applications.* Taylor & Francis, 1996.

[249] L. D. Landau and E. M. Lifshitz, *Theory of Elasticity.* Butterworth-Heinemann, 3rd ed., 1985.

[250] I. Solodov, M. Rahammer, and N. Gulnizkij, “Highly-Sensitive and Frequency-Selective Imaging of Defects via Local Defect Resonance,” in *11th ECNDT*, (Prague), 2014.

[251] I. Solodov, M. Rahammer, D. Derusova, and G. Busse, “Highly-efficient and noncontact vibro-thermography via local defect resonance,” in *QIRT2014 Conference*, 2014.

[252] I. Solodov, “Resonant acoustic nonlinearity of defects for highly-efficient nonlinear NDE,” *Journal of Nondestructive Evaluation*, vol. 33, no. 2, pp. 252–262, 2014.

[253] I. Solodov, “Resonant ultrasonic imaging of defects for advanced non–linear and thermosonic applications,” *International Journal of Microstructure and Materials Properties*, vol. 9, no. 3-5, pp. 261–273, 2014.

[254] I. Solodov, D. Derusova, and M. Rahammer, “Thermosonic Chladni figures for defect-selective imaging,” *Ultrasonics*, vol. 60, pp. 1–5, 2015.

[255] I. Solodov, “Resonant acoustic nonlinearity for defect-selective imaging and NDT,” in *AIP Conference Proceedings*, vol. 1685, (Écully), 2015.

[256] J. H. Cantrell and W. T. Yost, “Nonlinear ultrasonic characterization of fatigue microstructures,” *International Journal of Fatigue*, vol. 23, pp. 487–490, 2001.

[257] K. Van Den Abeele, J. Carmeliet, J. A. Ten Cate, and P. A. Johnson, “Nonlinear elastic wave spectroscopy (NEWS) techniques to discern material damage, Part II: single-mode nonlinear resonance acoustic spectroscopy,” *Research in Nondestructive Evaluation*, vol. 12, no. 1, pp. 31–42, 2000.

[258] C. Homma, M. Rothenfusser, J. Baumann, and R. Shannon, “Study of the Heat Generation Mechanism in Acoustic Thermography,” *AIP Conference Proceedings*, vol. 820, no. 1, pp. 566–573, 2006.

[259] J. Renshaw, S. D. Holland, and D. J. Barnard, “Viscous material-filled synthetic defects for vibrothermography,” *NDT & E International*, vol. 42, no. 8, pp. 753–756, 2009.

[260] J. Renshaw, J. C. Chen, S. D. Holland, and R. Bruce Thompson, “The sources of heat generation in vibrothermography,” *NDT & E International*, vol. 44, no. 8, pp. 736–739, 2011.

[261] R. Montanini and F. Freni, “Investigation of heat generation sources in sonic infrared thermography using laser Doppler vibrometry,” in *11th International Conference on Quantitative InfraRed Thermography*, 2012.

[262] T. Zweschper, A. Dillenz, G. Riegert, D. Scherling, and G. Busse, “Ultrasound excited thermography using frequency modulated elastic waves,” *Insight: Non-Destructive Testing and Condition Monitoring*, vol. 45, no. 3, pp. 178–182, 2003.

[263] I. Solodov, J. Bai, and G. Busse, “Resonant ultrasound spectroscopy of defects: Case study of flat-bottomed holes,” *Journal of Applied Physics*, vol. 113, no. 22, p. 223512, 2013.

[264] S. Timoshenko, *Vibration problems in engineering.* New York: D. Van Nostrand Company, Inc., 2 ed., 1937.

[265] MATLAB, *version R2014a.* Natick, Massachusetts: The MathWorks Inc., 2014.

[266] N. Otsu, “A Threshold Selection Method from Gray-Level Histograms,” *IEEE Transactions on Systems, Man and Cybernetics*, vol. 9, no. 1, pp. 62–66, 1979.

[267] R. C. Gonzalez and R. C. Woods, *Digital Image Processing Using Matlab.* Gatesmark Publishing, 2nd ed., 2009.

[268] R. J. Varley, “Ionomers as self healing polymers.,” *Springer Series in Materials Science*, vol. 100, pp. 95–114, 2007.

[269] R. J. Varley and S. van der Zwaag, “Towards an understanding of thermally activated self-healing of an ionomer system during ballistic penetration,” *Acta Materialia*, vol. 56, no. 19, pp. 5737–5750, 2008.

[270] R. J. Varley and S. van der Zwaag, “Autonomous damage initiated healing in a thermo-responsive ionomer,” *Polymer International*, vol. 59, no. 8, pp. 1031–1038, 2010.

Curriculum

Jan Hettler

Curriculum Vitae

Education

2012–2016	**PhD in Physics**, *KU Leuven*, Belgium. Faculty of physics and astronomy
2010–2012	**Master in Physical engineering (Ing.)**, *Czech Technical University*, Prague, *graduated with honours*. Faculty for Nuclear Science and Physical Engineering, Department of Materials
2007–2010	**Bachelor in Physical engineering (Bc.)**, *Czech Technical University*, Prague, . Faculty for Nuclear Science and Physical Engineering, Department of Materials

Master thesis

Title	*C-imaging of defects by means of nonlinear ultrasonic spectroscopy (in czech)*
Supervisors	Ing. Zdeněk Převorovský, Csc.
Description	The present work deals with the design and realization of the experiment using non-linear wave modulation spectroscopy for the damage zone localization in larger concrete samples. The 3D ultrasonic scanner is used as a motion platform for this experiment. A special attention is paid to the generation of the intermodulation frequency components as a sign of a non-linearity and damage in the sample. The applicability of the scaling subtraction method and harmonics analysis for the damage assessment of concrete samples is further investigated as a second objective of the presented work.

Experience

Vocational

2012–2016	**Doctoral researcher**, *Laboratory of Linear and Nonlinear Ultrasonic Spectroscopy, KU Leuven*, Kortrijk, Belgium.
2009–2012	**Student researcher**, *Laboratory of Non-Destructive Testing, Institute of Thermomechanics, The Academy of Sciences of the Czech Republic*, Prague, Czech Republic.

Languages

Czech	Native speaker
English	fluent, IELTS certificate, overall score 7.5
German	good, Goethe B2 certificate, grade: good

Havlickova 406 – 34012 Svihov – Czech Republic
☎ *+4915251503135* • ✉ *jan.hettler@gmail.com* • in *Jan Hettler*
hettljan

Computer skills

Programming languages	MATLAB, LabVIEW (CLAD), Python, NI DIAdem, BASH
Graphics	Inkscape, Gimp, VisIT, pyplot/matplotlib
FEM & CAD	COMSOL Multiphysics, Marc.Mentat, SolidEdge
Office	Word, Excel, Powerpoint, LaTeX
OS	Windows, Linux

Additional Skills

- Driving license, class B
- Laser vibrometry
- Infrared thermography
- Hardware control using LabVIEW and Matlab
- Ultrasonic measurements - contact, immersion, laser
- Design of experiments
- Signal processing

Interests

- cycling
- travelling
- hiking

References

- Koen Van Den Abeele, KU Leuven Kulak, Belgium
- Herbert De Gersem, TU Darmstadt, Germany
- Zdeněk Převorovský, IT CAS, Czech Republic

List of Publications

[1] J. Hettler, M. Tabatabaeipour, S. Delrue, and K. Van Den Abeele, "Linear and nonlinear guided wave imaging of impact damage in CFRP using a probabilistic approach," *Materials*, vol. 9, no. 9, 2016. Accepted.

[2] J. Hettler, M. Tabatabaeipour, S. Delrue, and K. Van Den Abeele, "Guided wave tomography based inspection of CFRP plates using a probabilistic reconstruction algorithm," in *Emerging Technologies in Non-Destructive Testing VI - Proceedings of the 6th International Conference on Emerging Technologies in Nondestructive Testing, ETNDT 2016*, 2016.

[3] J. Hettler, M. Tabatabaeipour, S. Delrue, and K. Van Den Abeele, "Guided Wave Tomography Based Inspection of CFRP Plates Using a Probabilistic Reconstruction Algorithm," in *Emerging Technologies in Non-Destructive Testing VI.* (D. Aggelis,

D. Van Hemelrijck, S. Vanlanduit, A. Anastasopoulos, and T. Philippidis, eds.), no. 2015, (Brussels), pp. 117–123, Leiden: CRC Press/Balkema, 2015.

[4] J. Hettler, M. Tabatabateipour, S. Delrue, and K. Van Den Abeele, "Application of a Probabilistic Algorithm for Ultrasonic Guided Wave Imaging of Carbon Composites," *Physics Procedia*, vol. 70, pp. 664–667, 2015.

[5] E. Monaco, N. D. Boffa, V. Memmolo, F. Ricci, N. Testoni, L. De Marchi, A. Marzani, J. Hettler, M. Tabatabaeipour, S. Delrue, and V. D. A. Koen, "Methodologies for Guided Wave-Based SHM System Implementation on Composite Wing Panels: Results and Perspectives from SARISTU Scenario 5," in *Smart Intelligent Aircraft Structures (SARISTU)* (P. C. Wölcken and M. Papadopoulos, eds.), pp. 495–527, Cham: Springer International Publishing, 2016.

[6] S. Delrue, M. Tabatabaeipour, J. Hettler, and K. Van Den Abeele, "Non-Destructive Evaluation of Kissing Bonds using Local Defect Resonance (LDR) Spectroscopy: A Simulation Study," *Physics Procedia*, vol. 70, pp. 648–651, 2015.

[7] S. Delrue, M. Tabatabaeipour, J. Hettler, and K. Van Den Abeele, "Applying a nonlinear, pitch-catch, ultrasonic technique for the detection of kissing bonds in friction stir welds," *Ultrasonics*, vol. 68, pp. 71–79, 2016.

[8] A. Rigolle, I. Foubert, J. Hettler, E. Verboven, R. Demuynck, and K. Van Den Abeele, "Development of an ultrasonic shear reflection technique to monitor the crystallization of cocoa butter," *Food Research International*, vol. 75, 2015.

[9] A. Rigolle, I. Foubert, J. Hettler, E. Verboven, A. Martens, R. Demuynck, and K. Van Den Abeele, "Insight in ultrasonic shear reflection parameters by studying temperature and limonene influence on cocoa butter crystallization," *Innovative Food Science & Emerging Technologies*, vol. 33, pp. 289–297, 2016.

[10] M. Tabatabaeipour, J. Hettler, S. Delrue, and K. Van Den Abeele, "Nonlinear ultrasonic inspection of friction stir welds," in *Emerging Technologies in Non-Destructive Testing VI - Proceedings of the 6th International Conference on Emerging Technologies in Nondestructive Testing, ETNDT 2016*, 2016.

[11] M. Tabatabaeipour, J. Hettler, S. Delrue, and K. Van Den Abeele, "Nondestructive Ultrasonic Inspection of Friction Stir Welds," *Physics Procedia*, vol. 70, pp. 660–663, 2015.

[12] M. Tabatabaeipour, J. Hettler, S. Delrue, and K. Van Den Abeele, "Non-destructive ultrasonic examination of root defects in friction stir welded butt-joints," *NDT & E International*, vol. 80, pp. 23–34, 2016.

[13] M. Tabatabaeipour, J. Hettler, and S. Delrue, "Reconstruction Algorithm for Probabilistic Inspection of Damage (RAPID) in Composites," in *Proceedings of ECNDT*, (Prague), 2014.

[14] K. Van Den Abeele, J. Hettler, M. Tabatabaeipour, and S. Delrue, "Pulse inversion and scaling subtraction signal processing for nonlinearity based defect detection,"

The Journal of the Acoustical Society of America, vol. 138, pp. 1836–1836, sep 2015.

[15] D. Yan, S. Avramidis, D. Liaptsis, M. Lindop, I. Cooper, S. Michau, A. Nguyen-Dinh, J. Hettler, M. Tabatabaeipour, S. Delrue, K. Van Den Abeele, and F. Perrier, "Development of an ultrasonic inspection system to detect kissing bonds in friction stir welded components," in *NDT 2014 - 53rd Annual Conference of the British Institute of Non-Destructive Testing*, 2014.

FACULTY OF SCIENCE
SUBFACULTY OF PHYSICS AND ASTRONOMY
WAVE PROPAGATION AND SIGNAL PROCESSING
Etienne Sabbelaan 53
B-8500 Kortrijk